ANALYSIS AND DESIGN OF PIPE RAMMING INSTALLATIONS

Final Report

SPR 710

Oregon Department of Transportation

ANALYSIS AND DESIGN OF PIPE RAMMING INSTALLATIONS

Final Report

SPR 710

by

Armin W. Stuedlein, PhD, PE
Tadesse Meskele
Geotechnical Engineering Group
School of Civil and Construction Engineering
Oregon State University
220 Owen Hall
Corvallis, OR 97331

for

Oregon Department of Transportation
Research Section
555 13th Street, Suite 1
Salem OR 97301

and

Federal Highway Administration
400 Seventh Street, SW
Washington, DC 20590-0003

November 2013

Technical Report Documentation Page

1. Report No.	2. Government Accession No.	3. Recipient's Catalog No.
FHWA-OR-RD-XX		

4. Title and Subtitle	5. Report Date
Analysis And Design Of Pipe Ramming Installations	November 2013
	6. Performing Organization Code

7. Author(s)	8. Performing Organization Report No.
Armin W. Stuedlein, PhD, PE, Tadesse Meskele	SPR 710

9. Performing Organization Name and Address	10. Work Unit No. (TRAIS)
Oregon Department of Transportation Research Section 555 13th Street, Suite 1 Salem, OR 97301	11. Contract or Grant No.

12. Sponsoring Agency Name and Address		13. Type of Report and Period Covered
Oregon Department of Transportation Research Section 555 13th Street, Suite 1 Salem, OR 97301	and Federal Highway Administration 400 Seventh Street, SW Washington, DC 20590-0003	Final Report 14. Sponsoring Agency Code

15. Supplementary Notes

16. Abstract

The trenchless technology known as pipe ramming for construction of culverts and buried pipes under roadways or other infrastructure has gained significant popularity due to its cost-effectiveness and ability to alleviate surface disruptions associated with open-cut trenching. Although the experience with pipe ramming is increasing, there has been remarkably little technical guidance available for engineers to appropriately specify aspects of a pipeline or culvert installation, including the planning of feasible layouts, rates of penetration, pipe diameters, and hammers. This research provides a comprehensive engineering framework for evaluation of culvert installations at the planning phase to address the gaps in knowledge associated with pipe ramming.

Presently there are no existing and proven techniques for prediction of settlement, vibration, driving stresses, soil resistance to ramming, and drivability for pipe ramming installations. This study has adopted existing drivability, soil resistance, settlement, and vibration prediction models from pipe jacking, microtunneling, and pile driving models and examined their applicability in pipe ramming installations, resulting in new and technology-specific design guidance. The development of this comprehensive engineering guidance is based on engineering calculations empirically tuned using a database of actual performance measurements. Field observations of five production installations and a full-scale experiment were conducted to form the performance database employed to understand the mechanics associated with pipe ramming installations, ranging from vertical ground movements, ground vibrations, and installation performance.

Settlement prediction was evaluated using the inverted normal probability distribution based models, and these methods over-estimated the observed settlements close to the center of the pipes and under-estimated settlements at radial distances away from the pipe. A pipe-ramming-specific hyperbolic model was developed for better prediction of the vertical settlement induced by pipe ramming in granular soils. Attenuation of observed pipe ramming-induced vibrations was modeled using a simple semi-empirical approach, and the calibrated model resulted in reasonable predictions of the ground vibrations for granular soils. The static soil resistance to ramming was evaluated using the traditional quasi-static pipe jacking models and the models resulted in inaccurate predictions for instrumented pipe ramming installations. Therefore pipe ramming-specific static soil resistance models were developed for both the face and casing resistance in granular soils. Principles of stress wave theory routinely applied in the drivability analyses for pile foundations were adopted for the evaluation of the dynamic response of pipes during ramming. Reliable estimates of the static soil resistance and dynamic soil parameters were obtained through signal matching processes. Data-informed drivability analysis were performed to simulate the magnitude of driving stresses and develop drivability curves which relate the penetration resistance of a given pipe and hammer to the range of static soil resistances. The study culminates in the first comprehensive framework and recommendations for the installation of pipes by ramming, and should help owners, consultants, and contractors to appropriately plan pipe ramming installations.

17. Key Words	18. Distribution Statement
Trenchless, Pipe Ramming, Culverts, Settlement, Vibration, Driving Stresses, Soil Resistance, Drivability	Copies available from NTIS, and online at http://www.oregon.gov/ODOT/TD/TP_RES/

19. Security Classification (of this report)	20. Security Classification (of this page)	21. No. of Pages	22. Price
Unclassified	Unclassified	XXX	

Technical Report Form DOT F 1700.7 (8-72) Reproduction of completed page authorized Printed on recycled paper

SI* (MODERN METRIC) CONVERSION FACTORS

APPROXIMATE CONVERSIONS TO SI UNITS

Symbol	When You Know	Multiply By	To Find	Symbol
		LENGTH		
in	inches	25.4	millimeters	mm
ft	feet	0.305	meters	m
yd	yards	0.914	meters	m
mi	miles	1.61	kilometers	km
		AREA		
in^2	square inches	645.2	millimeters squared	mm^2
ft^2	square feet	0.093	meters squared	m^2
yd^2	square yards	0.836	meters squared	m^2
ac	acres	0.405	hectares	ha
mi^2	square miles	2.59	kilometers squared	km^2
		VOLUME		
fl oz	fluid ounces	29.57	milliliters	ml
gal	gallons	3.785	liters	L
ft^3	cubic feet	0.028	meters cubed	m^3
yd^3	cubic yards	0.765	meters cubed	m^3
NOTE: Volumes greater than 1000 L shall be shown in m^3.				
		MASS		
oz	ounces	28.35	grams	g
lb	pounds	0.454	kilograms	kg
T	short tons (2000 lb)	0.907	megagrams	Mg
		TEMPERATURE (exact)		
°F	Fahrenheit	(F-32)/1.8	Celsius	°C

APPROXIMATE CONVERSIONS FROM SI UNITS

Symbol	When You Know	Multiply By	To Find	Symbol
		LENGTH		
mm	millimeters	0.039	inches	in
m	meters	3.28	feet	ft
m	meters	1.09	yards	yd
km	kilometers	0.621	miles	mi
		AREA		
mm^2	millimeters squared	0.0016	square inches	in^2
m^2	meters squared	10.764	square feet	ft^2
m^2	meters squared	1.196	square yards	yd^2
ha	hectares	2.47	acres	ac
km^2	kilometers squared	0.386	square miles	mi^2
		VOLUME		
ml	milliliters	0.034	fluid ounces	fl oz
L	liters	0.264	gallons	gal
m^3	meters cubed	35.315	cubic feet	ft^3
m^3	meters cubed	1.308	cubic yards	yd^3
		MASS		
g	grams	0.035	ounces	oz
kg	kilograms	2.205	pounds	lb
Mg	megagrams	1.102	short tons (2000 lb)	T
		TEMPERATURE (exact)		
°C	Celsius	1.8C+32	Fahrenheit	°F

*SI is the symbol for the International System of Measurement

ACKNOWLEDGEMENTS

This project was funded by the Oregon Department of Transportation (ODOT) and Federal Highway Administration (FHWA) through Research Contract SPR-710, which is gratefully acknowledged. The authors thank the research coordinator Dr. Matthew Mabey, and the Technical Advisory Committee: Jan L. Six, Bernard D. Kleutsch, Robert E. Trevis, Jonathan N. Guido, Dusting J. Haas, and Tim Rogers for their review and input into the project scope and target outcomes. The significant help by undergraduate students is gratefully acknowledged, including Mitch Madsen, Lee Bissinger, Atanas (Nick) Atanasov, Andrew Strahler, and James Walters. Technical assistance with logistics and data acquisition provided by James Batti and Michael Dyson of Oregon State University and Andrew Banas and Robert Miner of RMDT, Inc., is appreciated. This work was significantly aided by discussions with Kim Staheli of Staheli Trenchless Consultants. Collins Orton and George Mallakis of Trenchless Technologies provided important background information for this work. Thanks are due to Gookin Software for the free use of their boring log software.

This research was made possible in part by the outstanding collaborative effort contributed by members of the Oregon and Southwest Washington Chapter of the National Utility Contractor Association (NUCA) for the full-scale field experiment. Special thanks are due to Lyle Schellenberg and Tim O'Neill of Armadillo Underground, Jim Gonzales of Gonzales Boring and Tunneling, Bill Martinak and John Moore of Emery & Sons, Inc., John Fowler of JW Fowler Construction, Bob Stichman and Stuart Krause of Wyo-Ben, Inc., Donald Wiseman and Isaac Malson of RDO Equipment, Jim Moore of Moore Excavation, and Peterson Machinery. Their significant donation of time, labor, and equipment is gratefully acknowledged.

Data associated with the production installations described in this report was made available by a significant number of agencies, firms, and individuals. Their willingness to share their project data is appreciated. Case 1 was carried out with the cooperation of the Wildish Sand and Gravel Company and Gonzales Boring and Tunneling. Case 2 was carried out with the cooperation of David Staseff and Ian Aseltine of the Ontario Ministry of Transportation (MTO), Dirka Prout of Golder Associates, and Jim Robinson Contracting. Case 3 information and data was provided by Matthew Mabey of the Oregon DOT, Bert Miner of Robert Miner Dynamic Testing Inc., (RMDT), and J.W. Fowler Construction. Daryl Poduska and Todd Wanless of URS Corporation provided photographs and background information for Case 4. Background information, photographs, installation reports, and data for Case 5 was provided by Alan Jackson Aerojet, David Bennett of Bennett Trenchless Engineers, and Ken Sorenson of Kleinfelder, Inc.

DISCLAIMER

This document is disseminated under the sponsorship of the Oregon Department of Transportation and the United States Department of Transportation in the interest of information exchange. The State of Oregon and the United States Government assume no liability of its contents or use thereof.

The contents of this report reflect the view of the authors who are solely responsible for the facts and accuracy of the material presented. The contents do not necessarily reflect the official views of the Oregon Department of Transportation or the United States Department of Transportation.

The State of Oregon and the United States Government do not endorse products of manufacturers. Trademarks or manufacturers' names appear herein only because they are considered essential to the object of this document.

This report does not constitute a standard, specification, or regulation.

TABLE OF CONTENTS

1 INTRODUCTION 1

1.1 BACKGROUND 1
1.2 NEED FOR THIS RESEARCH 1
1.3 OBJECTIVES OF THE STUDY 2
1.4 SCOPE OF WORK 3
1.5 ORGANIZATION OF THIS REPORT 4

2 LITERATURE REVIEW 5

2.1 OVERVIEW OF PIPE OR CULVERT INSTALLATION 5
2.1.1 Brief Review of Open-cut Methods 5
2.1.2 Review of Trenchless Technology 5
2.1.3 Suitable Ground Conditions 9
2.1.4 Advantages and Disadvantages of Trenchless Technology 10
2.1.5 Consideration of Traffic Disruption 11
2.2 OVERVIEW OF THE PIPE RAMMING METHOD 12
2.2.1 Geotechnical Investigation 12
2.2.2 General Considerations for Construction 12
2.2.3 Pipe Ramming Hammers 16
2.2.4 Cutting Shoes 18
2.2.5 Lubrication of Culverts 19
2.2.6 Spoil Removal 20
2.2.7 Construction Observation of Pipe Ramming 21
2.2.8 Advantages and Limitations of Pipe Ramming 21
2.3 STATIC SOIL RESISTANCE TO RAMMED CULVERTS 22
2.3.1 Pipe Jacking-based Methods to Determine Face Resistance 23
2.3.2 Methods for the Determination of Normal Stress on Culverts 26
2.3.3 Methods for the Determination of Casing Resistance 31
2.4 GROUND VIBRATIONS ASSOCIATED WITH PIPE RAMMING 37
2.5 GROUND DEFORMATIONS ASSOCIATED WITH CULVERT INSTALLATION 42
2.6 CASE HISTORIES 47
2.6.1 Introduction 47
2.6.2 Overview of Reported Case Histories 47
2.6.3 Discussion of Selected Case Histories 48
2.7 SUMMARY OF LITERATURE REVIEW AND IDENTIFICATION OF KNOWLEDGE GAPS 53

3 OBSERVATION SITES AND CASE HISTORIES 55

3.1 PRODUCTION INSTALLATIONS 55
3.1.1 Case 1: Pressurized water pipe Installation, Wildish Sand and Gravel Co. Site, Eugene, Oregon 55
3.1.2 Case 2: Corrugated Metal Pipe (CMP) replacement project under Highway 21 at Allan's Creek, Ontario 60
3.1.3 Case 3: Culvert replacement project under Interstate Highway 84 at Perham Creek, Oregon 64
3.1.4 Case 4: Ramsey Town Center Storm water Conveyance Installation, Ramsey, Minnesota (Jensen et al. 2007) 66
3.1.5 Case 5: Water main Installation under US Highway 50, Rancho Cordova, California 69
3.1.6 Full-scale Pipe Ramming Experiment at Emery & Sons, Inc., Yard in Salem, Oregon (Case 6) 73
3.2 SUMMARY 85

4 ANALYSIS OF SETTLEMENT 86

4.1 CASE 1: PRESSURIZED WATER PIPE INSTALLATION, WILDISH SAND AND GRAVEL CO. SITE, EUGENE, OREGON 87
4.2 CASE 4: RAMSEY TOWN CENTER STORM WATER CONVEYANCE INSTALLATION, RAMSEY, MINNESOTA (*JENSEN ET AL. 2007*) 92
4.3 CASE 5: WATER MAIN INSTALLATION UNDER US HIGHWAY 50, RANCHO CORDOVA, CALIFORNIA 96
4.4 CASE 6: FULL-SCALE PIPE RAMMING EXPERIMENT AT EMERY & SONS SITE NEAR SALEM, OREGON 104
4.5 EVALUATION AND DEVELOPMENT OF SETTLEMENT MODELS 108
4.5.1 Global Accuracy of Selected Settlement Models 108
4.5.2 Development of a Pipe Ramming-specific Settlement Model 110
4.5.3 Parametric Analysis of Proposed Settlement Model 113
4.5.4 Estimation of Settlement Based on In-situ tests 115
4.6 SUMMARY 116

5 ANALYSIS OF GROUND VIBRATIONS 117

5.1 GROUND VIBRATION IN THE TIME DOMAIN 117
5.2 GROUND VIBRATIONS IN THE FREQUENCY DOMAIN 121
5.3 ATTENUATION OF PIPE RAMMING-INDUCED VIBRATIONS 124
5.4 SUMMARY 129

6 ANALYSIS OF PIPE RAMMING DYNAMICS 131

6.1 INTRODUCTION 131
6.2 WAVE PROPAGATION ANALYSIS 131
6.2.1 Basics of Stress Wave Equation 131
6.2.2 Smith's Idealization of Wave Equation 133
6.2.3 Modeling Soil Resistance 134
6.2.4 One-Dimensional Wave Equation Models 136
6.3 ANALYSIS OF STRESS WAVE OBSERVATIONS 141
6.3.1 Theoretical Background 141
6.3.2 Case Method Analysis of Field Observations 144
6.4 BACK-ANALYSIS OF SOIL RESISTANCE TO RAMMING 151
6.4.1 Theoretical Background 151
6.4.2 CAPWAP Analysis of Field Observations 154
6.4.3 Comparison of CAPWAP, Case Method, and Traditional Jacking Methods 160
6.5 SUMMARY 166

7 DRIVABILITY ANALYSIS OF PIPE RAMMING INSTALLATIONS 168

7.1 INTRODUCTION 168
7.2 DEVELOPMENT OF A PIPE RAMMING-SPECIFIC STATIC SOIL RESISTANCE MODEL 168
7.2.1 Face Soil Resistance Model 169
7.2.2 Casing Soil Resistance Model 170
7.2.3 Global Performance of New Total Static Soil Resistance Model 174
7.3 DYNAMIC SOIL MODEL PARAMETERS (QUAKE AND DAMPING) 175
7.4 PIPE RAMMING HAMMER–PIPE ENERGY TRANSFER EFFICIENCY 178
7.5 SENSITIVITY ANALYSIS OF WAVE PROPAGATION MODELING 184
7.6 DRIVABILITY ANALYSIS OF FIELD OBSERVATIONS 187
7.6.1 Case 1: Pressurized Water Pipe Installation, Wildish Sand and Gravel Co. Site, Eugene, Oregon .188
7.6.2 Case 2: Corrugated Metal Pipe (CMP) replacement project under Highway 21 at Allan's Creek, Ontario 191

7.6.3 Case 3: Culvert replacement project under Interstate Highway 84 at Perham Creek, Oregon 193
7.6.4 Case 6: Full-scale Pipe Ramming Experiment at Emery & Sons, Inc., yard in Salem, Oregon.....195
7.7 RECOMMENDATIONS FOR CONDUCTING DRIVABILITY ANALYSES 201
7.8 SUMMARY 203
8 SUMMARY AND CONCLUSIONS 205
8.1 SUMMARY 205
8.2 CONCLUSIONS 205
8.2.1 Vertical Ground Movements.....205
8.2.2 Ground Vibration.....206
8.2.3 Dynamics of Pipe Ramming.....206
8.2.4 Static Soil Resistance to Ramming.....206
8.2.5 Drivability Analysis 207
8.2.6 Recommendations for Future Study.....207
9 REFERENCES..... 209

LIST OF TABLES

Table 2.1: Suitability of trenchless road crossing methods (adapted and modified from Najafi et al. 2004). 10
Table 2.2: Statistical evaluation of unit face resistance for 69 microtunneling case histories with auger spoil removal (adapted from ISTT 1994). 26
Table 2.3: Soil parameters used to compute the normal stress (adopted and modified from Pellet-Beaucour and Kastner 2002). 30
Table 2.4: Summary of interface shear testing at a normal stress of 80 kPa and relative density of 80 % (adapted from Iscimen 2004). 32
Table 2.5: Pipe-soil interface friction coefficients, μ = tan δ reported by Potyondy (1961). Note, w = the natural moisture content. 33
Table 2.6: Pipe-soil interface friction coefficients, μ = tan δ reported in NAVFAC (1986). 33
Table 2.7: Typical values of unit skin resistance/adhesion for cohesive soils (adapted from Craig 1983).....34
Table 2.8: Range of P- and S-wave velocities at small strains for different soil type (*adapted from Massarch and Fellenius 2008*). 39
Table 2.9: Coefficient of radiation damping (*adapted from Kim and Lee 2000*).....39
Table 2.10: Classification of earth material by attenuation coefficient (*adapted from Woods 1997*).....39
Table 2.11: Summary of pipe ramming case histories. 50
Table 3.1: Summary of case histories 85
Table 4.1: Measured total settlements for the Case 4, 2180 mm pipe installation. 93
Table 4.2: Measured total settlements for the Case 4, 1980 mm twin pipe installation. 94
Table 4.3: Measured total settlements for at cross sections in the transversal direction for 760 mm casing installation. 97
Table 4.4: Measured total settlements by the reflectors along the centerline in the longitudinal direction. 97
Table 6.1: Statistical summary of Case Method derived maximum energy transfer. 150
Table 6.2: Statistical summary of Case Method derived compressive stress. 150
Table 6.3: Parameters employed in static soil resistance calculations. 161
Table 7.1: Summary of static and dynamic soil parameters from the CAPWAP and CASE analyses. 176
Table 7.2: Statistical summary of dynamic soil parameters (quake and damping) excluding Case 3. 178
Table 7.3: Hammers and type of connections used for the case histories. 179
Table 7.4: Statistical summary of energy transfer efficiency for the case histories. 184
Table 7.5: CAPWAP and Case Method energy transfer efficiencies (note, the rated hammer energy was 6.4 kN-m for segments 1 through 5 and 18.6 kN-m for segment 6). 196
Table 7.6: Computed driving times for blows of Case 6. 199

LIST OF FIGURES

Figure 1.1: Flow chart representing engineering guidance for pipe ramming installations. 3
Figure 2.1: Trenchless culvert installation methods (*adapted from Iseley and Gokhale 1997*). 6
Figure 2.2: Overview of the pipe jacking method (*C. Price, personal communication, 2013*). 7
Figure 2.3: HDD pipe pulling (adapted from Hashash and Javier 2011). 8
Figure 2.4: Typical pipe ramming setup for embankment (*after Piehl 2005*). 14
Figure 2.5: Typical pipe ramming setup; view from one of the study sites. 14
Figure 2.6: Photograph of 400 mm pneumatic hammer driving 600 mm diameter pipe pipe (corresponding to Case 1, described in Chapter 3). 16
Figure 2.7: Hydraulic Hammer driving 3050 mm diameter pipe (*after Piehl 2005*). 17
Figure 2.8: T1 cutting shoe being welded to 1060 mm diameter pipe pipe (corresponding to Case 6, described in Chapter 3). 18
Figure 2.9: Auger boring machine removing spoil from 1060 mm pipe (corresponding to Case 6, described in Chapter 3). 20
Figure 2.10: Typical sources of pipe jacking resistance. 23
Figure 2.11: Coefficient of face bearing resistance as a function of friction angle. 24
Figure 2.12: Conceptual correlation of earth pressures to surface deformation (*adapted from Stein 2005*). 26
Figure 2.13: Conceptual and computational schematic for computation of earth pressures on culverts: (a) Terzaghi's trap door model (*adopted from Terzaghi 1943*), (b) vertical and horizontal stress acting on the pipe (*adopted from Stein 2005*). 29
Figure 2.14: Geometric derivation of the trapdoor width (*adapted from Staheli 2006*). 30
Figure 2.15: Variation of stress reduction factor with normalized depth of embedment (h/D); upper bound curves given by ϕ = 30°, lower bound curves given by ϕ = 45°. 31
Figure 2.16: Frictional response at interface of steel pipe against Ottawa 20/30 sand at a normal stress of 80 kPa and a relative density of 80 % (*adapted from Iscimen 2004*). 33
Figure 2.17: Haslem (1986) model for pipe-soil interaction in "stable" cohesive soil (after Marshall 1998). 35
Figure 2.18: Progress of the total jacking force for a project in Champigny, France, showing increase of the jacking load after stoppages (*adopted from Pellet-Beaucour and Kastner 2002*). 36
Figure 2.19: Summary of unit jacking forces in different projects (*after Borghi 2006*). 37
Figure 2.20: Attenuation of surface waves (β = 0.5, r_1 = 10 m) (*adopted from Massarch and Fellenius 2008*). 40
Figure 2.21: Peak vertical particle velocity versus scaled distance (*adopted from Woods 1997*). 41
Figure 2.22: Safe vibration criteria based the USBM and OSM criteria. 42
Figure 2.23: Ground vibrations associated with pipe bursting: (a) peak particle velocity versus frequency plot for pneumatic pipe bursting, and (b) velocity versus distance from the bursting head (*after Atalah 1998*). 42
Figure 2.24: Conceptual sketch of 3-D settlement during pipe jacking (*adopted from Attewell 1988*). 44
Figure 2.25: Settlement behavior due to pipe jacking and microtunneling a) idealized transverse settlement trough (b) centrifuge modeling result that shows displacement vectors (*after Farrell 2011*). 44
Figure 2.26: Relation between settlement trough width and tunnel depth for different grounds (*adopted from Peck 1969*). 45
Figure 2.27: Idealized heave in transversal direction (*adopted from Bennett and Wallin 2010*). 47
Figure 3.1: Location of the Case 1 project site (Source: USGS Earth Explorer). 56
Figure 3.2: Photographs showing construction activities for the Case 1 pipe ramming project: (a) the first segment of the pipe with cutting shoe welded at the leading edge and situated steel auger boring tracks, (b) the ramming process under the embankment, (c) welding the second segment of the pipe, and (d) spoil removal using auger boring. 57
Figure 3.3: Grain size distribution of the soil sample taken from the project site. 58
Figure 3.4: Profile and plan view of the access road and conveyer belt embankment and settlement monitoring points. 59
Figure 3.5: Photographs showing (a) pile driving analyzer (PDA), and (b) high frequency strain gage and accelerometer attached to the pipe. 60
Figure 3.6 Location of the Case 2 project site (Source: USGS Earth Explorer). 61
Figure 3.7 (a) Photograph showing installation of the new 2440 mm culvert parallel to the failing CMP culvert, and (b) geometry of the cutting shoe. 62

Figure 3.8 Profile along the centerline of the culvert showing location of borings (*Golder Associates 2010*). 63
Figure 3.9 Two pairs of accelerometers and strain gages mounted to the pipe. 64
Figure 3.10 Location of the Case 3 project site (Source: USGS Earth Explorer). 65
Figure 3.11 Photos showing activities related to Perham Creek culvert replacement project: (a) pipe ramming operation under Interstate 84, (b) launch pit set-up, (c) 800 mm pneumatic Grundoram Apollo hammer (*J.W. Fowler, personal communication, 2012*), and (d) 915 mm hydraulic IHC S-280 hammer (*ODOT 2010*). 66
Figure 3.12 Location of the Case 4 project site (Source: USGS Earth Explorer). 67
Figure 3.13 Boring location relative to the casing crossings (*adapted from Jensen et al. 2007*).....68
Figure 3.14: Cross section of the boring along the 2180 mm casing (*adapted from Jensen et al. 2007*). 68
Figure 3.15: Ground deformation monitoring point layout plan (*adapted from Jensen et al. 2007*). 69
Figure 3.16: Location of the Case 5 project site (Source: USGS Earth Explorer). 70
Figure 3.17: Pipe ramming in progress for 760 mm casing installation (*Bennett Trenchless 2010a*). 71
Figure 3.18: Spoil obtained from inside of the pipe: (a) spoils from 0 to 3 m penetration in foreground and from 3 to 6 m in background, and (b) augers approximately 8 m into the casing (*Bennett Trenchless 2010b*). 72
Figure 3.19: Location of ground deformation monitoring points (GDMPs) (*adapted from Stantec 2010*). 73
Figure 3.20: Location of the Case 6 project site (Source: USGS Earth Explorer). 74
Figure 3.21: Exploration plan and cross-section of subsurface for Case 6. 75
Figure 3.22: In-situ testing at the site including (a) Standard Penetration Testing (SPT) , and (b) Cone Penetration Testing (CPT).....75
Figure 3.23: Representative photographs indicating soil stratigraphy: (a) soil augured out of the pipe, and (b) soil exposed along the pipe following installation. 76
Figure 3.24: Grain size distribution (GSD) curve for a soil sample taken from experimental site. 77
Figure 3.25: Triaxial test results for Case 6 (a) principal stress difference versus axial strain (b) volumetric strain versus axial strain (c) Peak Mohr-Coulomb failure envelopes (d) Residual Mohr-Coulomb failure envelopes. 77
Figure 3.26: Location of the strain gages on each pipe segment. 78
Figure 3.27: Pipe instrumentation with strain gages; note, pairs of gages were installed to provide redundancy. 78
Figure 3.28: Photos showing site preparation activities for the field experiment: (a) transportation of the instrumented pipe the experiment site, (b) excavation of the insertion pit, (c) dewatering the insertion pit, and (d) steel tracks on the leveled gravel bed and steel sheets.....79
Figure 3.29: Photographs showing experiment activities: (a) welding of the T1 steel cutting shoe to the first pipe segment, (b) pipe ramming in progress, (c) spoil removal using auger boring, and (d) bentonite mixing and field testing of viscosity. 81
Figure 3.30: Photos showing field instrumentation: (a) Minimate Plus seismograph with standard geophone and a sandbag (b) Pile Driving Analyzer (PDA), and (c) high frequency strain gauges and accelerometers attached to the pipe. 83
Figure 3.31: Location of the ground deformation monitoring points. 84
Figure 3.32: Location of ground vibration monitoring points. 84
Figure 4.1: Observed and calculated ground movement profiles transverse to the advancing pipe for Case 1, at Section 1, considering (a) entire overcut volume, and (b) half of the overcut volume. 88
Figure 4.2: Observed and calculated ground movement profiles transverse to the advancing pipe for Case 1, at Sections 2,3 and 4, considering (a) entire overcut volume, and (b) half of the overcut volume. 90
Figure 4.3: Case 1 observed vertical ground movements and calculated settlement profiles. The vertical ground movement calculations represent the centerline of the pipe in the longitudinal direction considering (a) entire overcut volume, and (b) half-overcut volume. The settlement measurements were observed along the center and offset distances of 0.75*D*, 1.5*D* and 3*D* (e.g., L1 = offset left 0.75*D*, R2 = offset right 1.5*D*). 91
Figure 4.4: Sample biases for vertical ground deformation estimates for Case 1 considering (a) entire overcut volume, and (b) half of the overcut volume. 92
Figure 4.5: Observed and calculated ground movement profiles transverse to the advancing 2180 mm diameter pipe for Case 4, considering (a) entire overcut volume, and (b) half of the overcut volume. 94
Figure 4.6: Observed and calculated ground movement profiles transverse to the advancing twin 1980 mm diameter pipes for Case 4, considering (a) entire overcut volume, and (b) half of the overcut volume. 95
Figure 4.7: Sample biases for vertical ground deformation estimates for Case 4 considering (a) entire overcut volume, and (b) half of the overcut volume. 96

Figure 4.8: Observed and calculated ground movement profiles transverse to the advancing pipe for Case 5, at Southern ROW and Southern K-Rail, considering (a) entire overcut volume, and (b) half of the overcut volume.....99
Figure 4.9: Observed and calculated ground movement profiles transverse to the advancing pipe for Case 5, at Northern ROW, considering (a) entire overcut volume, and (b) half of the overcut volume.....100
Figure 4.10: Observed and calculated ground movement profiles transverse to the advancing pipe for Case 5, at East and West Bound, considering (a) entire overcut volume, and (b) half of the overcut volume.....101
Figure 4.11: Case 5 observed vertical ground movements and calculated settlement profiles. The vertical ground movement calculations represent the centerline of the pipe in the longitudinal direction considering (a) entire overcut volume, and (b) half-overcut volume. The settlement measurements were observed along the center and offset distances of 2*D* and 4*D* (e.g., L1 = offset left 2*D*, R2 = offset right 4*D*).....102
Figure 4.12: Sample biases for vertical ground deformation estimates for Case 5 considering (a) entire overcut volume, and (b) half of the overcut volume.....103
Figure 4.13: Observed and calculated ground movement profiles transverse to the advancing pipe for Case 6, considering (a) entire overcut volume, and (b) half of the overcut volume.....105
Figure 4.14: Case 6 observed vertical ground movements and calculated settlement profiles. The vertical ground movement calculations represent the centerline of the pipe in the longitudinal direction considering (a) entire overcut volume, and (b) half-overcut volume. The settlement measurements were observed along the center and offset distances of 0.5*D*, 1.5*D* and 3*D* (e.g., L1 = offset left 0.5*D*, R2 = offset right 1.5*D*).....106
Figure 4.15: Sample biases for vertical ground deformation estimates for Case 6 considering (a) entire overcut volume, and (b) half of the overcut volume.....107
Figure 4.16: Settlement observation and model estimations based on O'Reilly and New (*1982*) considering (a) entire overcut volume and (b) half overcut volume; Mair and Taylor (*1997*) considering (c) entire overcut volume and (d) half overcut volume; Cording and Hansmire (*1975*) considering (e) entire overcut volume and (f) half overcut volume.....109
Figure 4.17: Settlement observation and proposed model estimates at (a) Section 1 for Case 1 (b) Section 2, 3 and 4 for Case 1 (c) South and North track for Case 4 (d) Southern K-Rail and ROW for Case 5(e) Northern ROW for Case 5 (f) East- and West bound lanes for Case 5, and (g) Sections 1 through 6 for Case 6.....112
Figure 4.18: Proposed model biases for the entire database.....113
Figure 4.19: Parametric analysis of settlement prediction by varying (a) depth of cover above the crown of the pipe (b) diameter of the pipe, and (c) diameter of the cutting shoe.....114
Figure 4.20: Regression model for the estimate of maximum settlement based on SPT *N* blow counts.....115
Figure 5.1: Sign convention of the ground vibration in orthogonal directions.....117
Figure 5.2: Transverse, vertical and longitudinal particle velocity at Section 2 directly above the center of the pipe.....118
Figure 5.3: Particle motion at Section 2 directly above the center of the pipe (a) transverse versus vertical particle motion (b) longitudinal versus vertical particle motion, and (c) three dimensional particle motion.....119
Figure 5.4: Transversal, vertical, and longitudinal particle velocity at Section 3 directly above the center of the pipe.....120
Figure 5.5: Particle motion at Section 3 directly above the center of the pipe (a) transverse versus vertical particle motion, (b) longitudinal versus vertical particle motion, and (c) three dimensional particle motion.....121
Figure 5.6: Schematic showing vibration propagation induced by pipe ramming.....122
Figure 5.7: Peak vector sum velocities versus dominant frequency of Forward propagating vibration using the 400 mm HammerHead hammer.....123
Figure 5.8: Peak vector sum velocities versus dominant frequency of Forward propagating vibration using the 610 mm Grundoram Taurus hammer.....123
Figure 5.9: Peak vector sum velocities versus dominant frequency of lateral propagating vibration.....124
Figure 5.10: Observed vibrations versus scaled distance and calibration of attenuation model based on the Case 6 vibration observations: (a) Scenario 1, forward propagation and source of energy at the face of the pipe, (b) Scenario 2, forward propagation and source of energy at the rear end the pipe, (c) Scenario 3, lateral propagation and source of energy at the rear end of the pipe.....126
Figure 5.11: Distribution of sample bias with scaled distance for the vibration attenuation model (a) Scenario 1, forward propagation and source of energy at the face of the pipe, (b) Scenario 2, forward propagation and source of energy at the rear end the pipe, (c) Scenario 3, lateral propagation and source of energy at the rear end of the pipe.....127

Figure 5.12: Vibration contour and surface maps in mm/s: (a) and (b) for HammerHead hammer; (c) and (d) for Grundoram Taurus hammer. 128
Figure 6.1: Infinitesimal pipe element subjected to a compressive wave. 131
Figure 6.2: Smith's pipe discretization for pipe ramming and soil resistance model. 133
Figure 6.3: Smith's soil resistance models (a) casing resistance model (b) face resistance model (c) linear elastic perfectly plastic load-displacement relationship for static soil resistance, and (d) load-velocity relationship for dynamic soil resistance. 136
Figure 6.4: WEAP numerical procedure and integration (a) List of Numerical Equations and (b) Flow chart for the Predictor-Corrector analysis (*adapted from GRLWEAP ® 2010*). 138
Figure 6.5: Numerical analysis procedures for WEAPRI. 140
Figure 6.6: Typical force and velocity traces for (a) minimal casing and face resistance condition, (b) significant face resistance conditions, and (c) significant casing resistance condition (*after Hannigan 1990*). 142
Figure 6.7: Case Method results indicating pipe performance for Case 1: (a) maximum transferred energy (b) maximum induced compressive stress in the pipe, and (c) total (static and dynamic) soil resistance. 145
Figure 6.8: Case Method results indicating pipe performance for Case 2: (a) maximum transferred energy (b) maximum induced compressive stress in the pipe and (c) total (static and dynamic) soil resistance. 146
Figure 6.9: Case Method results indicating pipe performance for Case 3: (a) maximum transferred energy (b) maximum induced compressive stress in the pipe, and (c) total (static and dynamic) soil resistance. 147
Figure 6.10: Case Method results indicating pipe performance for Case 6: (a) maximum transferred energy (b) maximum induced compressive stress in the pipe, and (c) total (static and dynamic) soil resistance. 149
Figure 6.11: Photo showing the bleeding loss of the lubricant due to the likely damage of the lubricant hose close to the insertion of the pipe. 150
Figure 6.12: General procedure for numerical simulation of measured stress wave signals (*adapted from Balthaus 1988*). 152
Figure 6.13: CAPWAP Iteration for the signal matching process (*adapted from Hannigan et al. 2006*). 153
Figure 6.14: CAPWAP results for the Case 1 installation: (a) static soil resistance, (b) quake values, and (c) Smith and Case damping constants. 156
Figure 6.15: CAPWAP results for the Case 2 installation: (a) static soil resistance, (b) quake values, and (c) Smith and Case damping constants. 157
Figure 6.16: CAPWAP results for the Case 3 installation: (a) static soil resistance, (b) quake values, and (c) Smith and Case damping constants. 158
Figure 6.17: CAPWAP results for the Case 6 installation: (a) static soil resistance, (b) quake values, and (c) Smith and Case damping constants. 159
Figure 6.18: CAPWAP and Case Method soil resistance comparisons for (a) Case 1, (b) Case 2, (c) Case 6, and (d) expanded view of Case 6 resistances. 161
Figure 6.19: Comparison of CAPWAP and jacking method soil resistance for Case 1 (a) face resistance (b) casing resistance using peak angle of friction, and (c) casing resistance using residual state angle of friction. Note: Staheli Method uses only residual angle of friction. 164
Figure 6.20: Comparison of CAPWAP and jacking method soil resistance for Case 2 (a) face resistance (b) casing resistance using peak angle of friction, and (c) casing resistance using residual state angle of friction. Note: Staheli Method uses only residual angle of friction. 164
Figure 6.21: CAPWAP and jacking method soil resistance comparisons for Case 3 (a) face resistance (b) casing resistance using peak angle of friction, and (c) casing resistance using residual state angle of friction. Note: Staheli Method uses only residual angle of friction. 164
Figure 6.22: CAPWAP-based and jacking method soil resistance comparisons for Case 6: (a) face resistance, (b) casing resistance using peak angle of friction, (c) expanded view of casing resistance using peak angle of friction, (d) casing resistance using of the residual friction angle, and (e) expanded view of casing resistance using the residual angle of friction. 165
Figure 6.23: CAPWAP-based and jacking method soil resistance comparisons for each Case 6 pipe segment: (a) Terzaghi (*1943*) method, (b) ATVA method, (c) PJA method, and (d) Staheli (*2006*) method. 166
Figure 7.1: Variation of coefficient of unit face resistance with soil friction angle for the case histories. 170
Figure 7.2: Comparison of CAPWAP and proposed model unit face resistances for the case histories. Note, many CAPWAP-based resistances coincide on this plot; the number of coincidental data is indicated. 170
Figure 7.3: Assumed shear surfaces for pipe ramming installations 172

Figure 7.4: Comparison of CAPWAP and proposed model unit casing resistances for the observed case histories considering (a) data without lubrication (b) data with lubrication. Note, many CAPWAP-based resistances coincide on this plot; the number of coincidental data is indicated.....174
Figure 7.5: Comparison of CAPWAP and proposed model total static soil resistance (a) expanded view showing Case 1, 2 and 6, and (b) full range of resistance showing all of the case histories.....175
Figure 7.6: Normalized face resistances versus back-calculated dynamic soil parameters. 177
Figure 7.7: Normalized casing resistances versus back-calculated dynamic soil parameters.....177
Figure 7.8: Back calculated soil stiffness for the case histories.....178
Figure 7.9: Hammer-pipe connections (a) collets showing moderate wear or damage (b) pipe ram collar and collets, the latter showing significant wear (c) pipe reducing cone/adapter, and (d) cotter segments (e) ram cone and cotter segments, and (f) ram cone. 180
Figure 7.10: Hammer–pipe connection for Case 1: (a) the 400 mm diameter HammerHead hammer, and (b) observed hammer–pipe energy transfer efficiency distribution. 181
Figure 7.11: Hammer–pipe connection for Case 6. (a) a 400 mm diameter HammerHead hammer (b) observed hammer–pipe energy transfer efficiency distribution.....181
Figure 7.12: Hammer–pipe connection for Case 2. (a) a 800 mm diameter Grundoram Apollo hammer (b) observed hammer–pipe energy transfer efficiency distribution.....182
Figure 7.13: Hammer–pipe connection for Case 3. (a) a 915 mm diameter IHC S-280 hammer (b) observed hammer–pipe energy transfer efficiency distribution.....183
Figure 7.14: Hammer–pipe connection for Case 6. (a) a 610 mm diameter Grundoram Taurus hammer (b) observed hammer–pipe energy transfer efficiency distribution.....183
Figure 7.15: Sensitivity analysis of drivability modeling indicating the variation in blow count in blows per meter (b/m) as a function of static soil resistance, by varying (a) the percentage of casing resistance (b) casing damping (c) face damping (d) casing quake (e) face quake, (f) hammer-pipe energy transfer efficiency, and (g) line force. 186
Figure 7.16: Observed and simulated force traces and drivability estimates: (a) force traces for blow #42, (b) drivability graph for blow #42, (c) force traces for blow #3304, and (d) drivability graph for blow #3304....189
Figure 7.17: Comparison of observed penetration resistance to the average, lower- and upper-bound drivability curves simulated for blow #42 and #3304.....190
Figure 7.18: Maximum compressive stresses obtained from the Case Method solution to the PDA observations and those estimated using the drivability analyses for blow #42 and #3304. 190
Figure 7.19: Observed and simulated force traces and drivability estimates: (a) force traces for blow #14, (b) drivability graph for blow #14, (c) force traces for blow #1885, and (d) drivability graph for blow #1885....192
Figure 7.20: Comparison of observed penetration resistance to the average, lower- and upper-bound drivability curves simulated for blow #14 and #1885.....192
Figure 7.21: Maximum compressive stresses obtained from the Case Method solution to the PDA observations and those estimated using the drivability analyses for blow #14 and #1885 of production Case 2. 193
Figure 7.22: Observed and simulated force traces and drivability estimates: (a) force traces for blow #4, (b) drivability graph for blow #4, (c) force traces for blow #3676, and (d) drivability graph for blow #3676.....194
Figure 7.23: Comparison of observed penetration resistance to the average, lower- and upper-bound drivability curves simulated for blow #4 and #3676.....194
Figure 7.24: Observed and simulated force traces and drivability estimates of pipe segment 3 (a) force traces for blow #200 (b) drivability graph for blow #200 (c) force traces for blow #1991 (d) drivability graph for blow #1991.....197
Figure 7.25: Observed and simulated force traces and drivability estimates of pipe segment 6: (a) force traces for blow #40, (b) drivability graph for blow #40, (c) force traces for blow #2404, and (d) drivability graph for blow #2404.....198
Figure 7.26: Comparison of observed penetration resistance to the average, lower- and upper-bound drivability curves simulated for blow #200 and #1991 of pipe segment 3. 198
Figure 7.27: Comparison of observed penetration resistance to the average, lower- and upper-bound drivability curves simulated for blow #40 and #2404 of pipe segment 6. 199
Figure 7.28: Pipe ramming log showing observed and simulated blow counts per meter.....200
Figure 7.29: Maximum compressive stresses obtained from the Case Method solution to the PDA observations and those estimated using the drivability analyses. 201
Figure 7.30: Conceptual sketch indicating target range of efficient penetration for pipe ramming.....202

1 INTRODUCTION

1.1 BACKGROUND

Culverts are an essential component of roadway drainage systems that transport storm runoff and stream channels from one side of a road to the other. The majority of culverts installed in the 1950s and 1960s are reaching the end of their functional lives and need replacement due to structural deterioration, scour, corrosion, erosion, separation, or increased hydraulic requirements *(Najafi 2008)*. Additionally, a significant number of culverts that are buried under a dense network of public roads (more than 6.2 million km) in the United States serving over 200 million vehicles need rehabilitation or replacement *(National Research Council 1997)*. The Federal Highway Administration (FHWA) estimated more than six percent of a total of 132,110 culverts needed replacement as of December 2011 *(FHWA 2011)*.

The traditional open cut method is the most widely used method for installation or rehabilitation of underground pipelines, conduits, and culverts. However, the open-cut method requires time-consuming excavation, installation and back-filling, which can impose an adverse impact on the daily life of society by creating road or rail closures, traffic delays, detours, loss of access to homes and businesses, and undesirable noises *(Ariaratnam et al. 2006)*. Thus, engineers and contractors are gradually abandoning open trench cutting and embracing trenchless methods of pipe installation. These trenchless methods can mitigate many of the logistical issues associated with traditional approaches. In particular, pipe ramming, which is a simple non-steerable trenchless construction technique, is becoming an emerging method of pipe installation, because it allows installation of casings in soils with large cobbles and boulders, which are ground conditions that may pose greater difficulty to other trenchless techniques. Pipe ramming is also a commonly chosen technique for shallow pipe or culvert installation under roads and railways, where other trenchless methods could cause unacceptable ground settlement or heave.

1.2 NEED FOR THIS RESEARCH

Despite the growing popularity and experience with pipe ramming, there is surprisingly little technical guidance available for engineers to plan pipe ramming installations appropriately. Although Simicevic and Sterling (*2001a*) and Najafi (*2008*) provide helpful information for planning pipe ramming projects, currently there exists no detailed technical guidance for engineering design of pipe ramming installation. Stuedlein and Meskele (*2012*) presented a preliminary, baseline engineering framework for the design of pipe ramming installations. An engineered pipe ramming installation requires the assessment of the constructability of the required length and diameter of pipe with a given hammer, and the evaluation of the likelihood of damage to the pipe due to excessive driving stress. In addition, the potential ground deformation and vibration associated with the installation of rammed pipes must be considered; particularly in proximity to existing adjacent structures and buried utilities. At present, there are no proven existing techniques for estimating the driving stresses, selection of optimal impact hammers, pipe wall thickness, and predicting the ground deformation and vibration associated

with pipe ramming installations (*Stuedlein and Meskele 2012*). Thus the purpose of this research is to develop a comprehensive engineering framework for design and evaluation of pipe ramming projects to improve the confidence of engineers in specifying all aspects of a pipeline or culvert installation.

1.3 OBJECTIVES OF THE STUDY

The main objective of this research is to study the mechanics of pipe ramming and to develop a rational engineering framework for the optimal design and specification of pipe ramming installations. Reliable estimates of the soil resistance, ground deformations, and ground vibrations associated with pipe ramming are essential for the successful installation of culverts. This study evaluates the accuracy and application of existing soil resistance, settlement, and vibration prediction models that have been used and adapted from existing pipe jacking, microtunneling, and pile driving models for rammed culverts. This study also appraises the suitability of an existing simplified one-dimensional wave equation model for dynamic analysis of pipe ramming installations. New semi-empirical approaches have been developed to improve prediction accuracy of design models.

The work described herein is intended to provide reliable engineering guidance to evaluate culvert installations at the planning phase, which could result in significant cost savings, increased efficiency, and safe construction. A framework of the proposed engineering approach is shown in Figure 1.1. Assessment of pipe drivability using the proposed hammer-pipe-soil combination, selection of the optimal hammer, and evaluation of the safe driving stresses should be based on analysis of stress wave propagation. The stress wave propagation analysis requires specification of the model inputs such as pipe properties (diameter, length, modulus, and mass density), hammer properties (rated energy, hammer efficiency) and soil properties (face and casing soil resistance, quake, and damping). The proposed framework incorporates the components that represent commonly employed hammers, soil resistance and dynamic soil parameters for pipe ramming installations. The proposed framework necessarily addresses the potential for ground settlement and vibration to assess the safety of nearby existing structures (e.g. buildings, roadway pavements, railways) and buried utilities during the ramming operation.

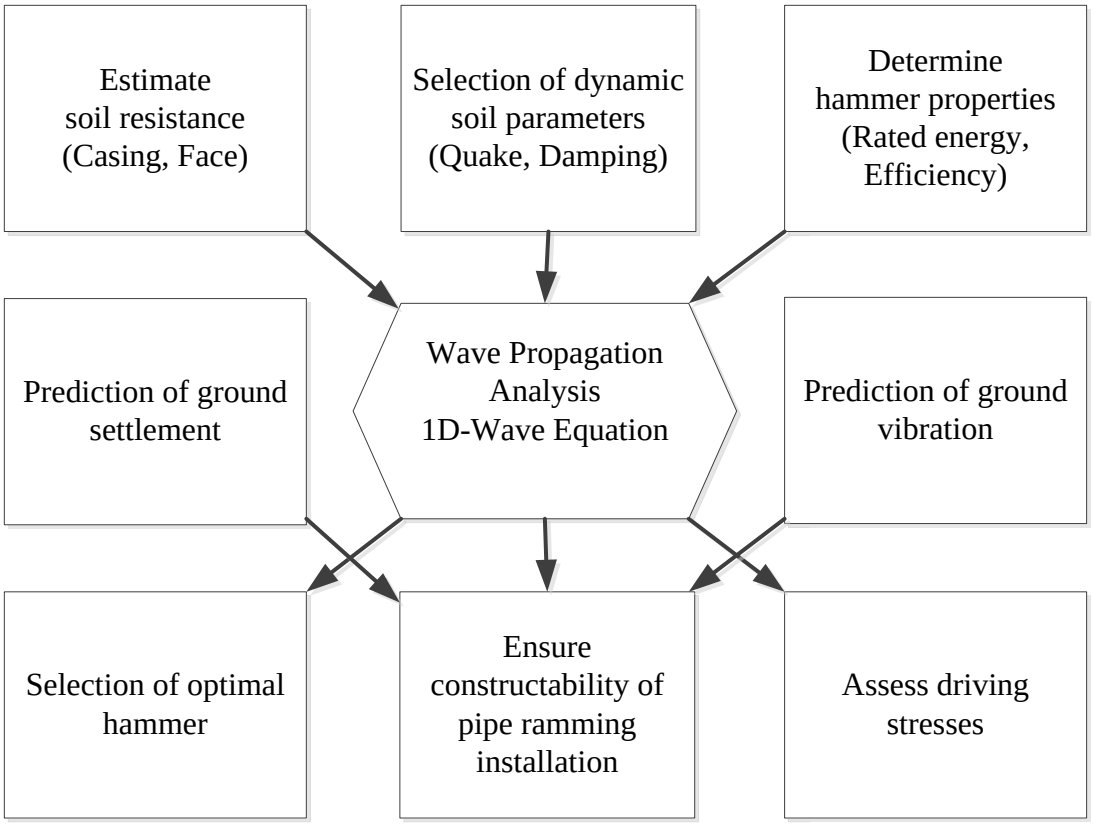

Figure 1.1: Flow chart representing engineering guidance for pipe ramming installations.

1.4 SCOPE OF WORK

This research is primarily intended to provide baseline technical guidance for the planning and design of pipe ramming installations. The scope of work for this study includes:

- Reviewing the literature on pipe ramming and other related techniques to summarize the state-of-practice and to determine the knowledge gaps that must be addressed;
- Performing an instrumented, full scale field experiment and observing various production pipe ramming projects;
- Analyzing pipe and culvert installation performance data and supporting laboratory-based soil testing;
- Evaluation of tunneling-based ground deformation models and their application to pipe ramming;
- Assessment of ground vibration models in construction and their application to pipe ramming;
- Assessing the accuracy of existing estimation methods for static soil resistance for face and shaft resistance developed from pipe jacking and microtunneling methods;

- Proposing new semi-empirical methods to estimate static soil resistance to ramming;
- Observing and recommending suitable dynamic soil properties for drivability studies; and,
- Development of a methodology for performing drivability studies that will result in the selection of adequate hammer energy, estimation of maximum hammer-induced stress, and selection of the appropriate pipe wall thicknesses.

1.5 ORGANIZATION OF THIS REPORT

This report is organized into several chapters. The contents of each chapter include:

- Chapter 2 reviews the available literature relevant to pipe ramming installations and related technologies. Existing methods to estimate soil resistance, ground deformations, and vibrations that were typically developed for pipe jacking, microtunneling and pile driving techniques were reviewed and discussed with intent of investigating their applicability for pipe ramming installations.
- Chapter 3 presents the details of the pipe ramming case histories considered in this study. The discussion includes the site investigation, laboratory testing, project set-up and field instrumentation used to monitor the performance of the installed pipe(s), ground movements, and ground vibrations, where applicable.
- Chapter 4 presents an analysis of the settlement observations obtained from the case histories. This section explores existing empirical approaches based on the inverted normal probability distribution curve models for prediction of vertical ground movements and presents a pipe ramming-specific settlement model.
- Chapter 5 assesses observed pipe ramming-induced ground vibration data collected during a full-scale experimental pipe installation. An existing vibration-attenuation model is calibrated for use with pipe ramming.
- Chapter 6 presents the dynamics of pipe ramming installations based on the basic theory of stress wave propagation analysis and dynamic measurements gathered during pipe ramming. Pipe performance metrics, including the energy transferred to the pipe, the induced compressive stresses, and the total soil resistance to ramming are presented. Existing methods for the prediction of static soil resistance to pipe jacking and microtunneling are evaluated against the observed static soil resistance.
- Chapter 7 presents the development of static soil resistance models for pipe ramming installations, including a new face and casing resistance model. The drivability analysis for pipe ramming installations are discussed using the framework of wave equation models, and the relationship between the static soil resistances to ramming and the dynamic pipe penetration resistances at the time of driving is established. Recommendations for performing pipe drivability analyses are described.
- Chapter 8 summarizes this report, and presents a list of conclusions based on the work performed in this study. Specific recommendations for future research are provided based on the findings of this study.

2 LITERATURE REVIEW

2.1 OVERVIEW OF PIPE OR CULVERT INSTALLATION

Underground conduits are an integral part of subsurface infrastructure used in diverse applications such as culverts, sewer lines, water mains, gas lines, telephone and electrical conduits, oil pipelines, and heat distribution lines. Culvert construction in the United States became increasingly necessary with the growth in highway construction. Safe installation of pipelines requires careful planning of the construction process. The conventional installation of pipelines is performed using the open-cut technique, which consists of excavating a trench, placing the pipeline, and then back-filling the trench. However, the traditional open-cut method is becoming undesirable, because it involves long duration of excavation, installation and back-filling, and creates road or rail closures. Trenchless technologies have been developed to avoid disturbance to surface activities by allowing the installation of pipelines in a minimaly-disruptive or non-disruptive manner. Trenchless techniques range from simple percussive drilling methods to highly sophisticated operations that can include the excavation or displacement of ground ahead of the leading edge of the new pipeline (*Chapman et al. 2007*).

2.1.1 Brief Review of Open-cut Methods

Open-cut pipeline construction is a traditional and widely-used method for the installation, rehabilitation, and replacement of underground utilities. The open-cut trenching method involves manual labor, excavation with heavy equipment, shoring, and de-watering when working below the groundwater table. These elements are required across the entire culvert alignment. Because the construction process requires an excavation of a trench across the roadway, the road surface must be maintained during and restored following construction. The installation operation requires occupancy of the roadway and disruption to traffic. Trenchless methods have been developed and implemented over the past 70 years as our understanding of soil behavior and the awareness of the impact of open-trench methods has increased.

2.1.2 Review of Trenchless Technology

The option of trenchless technology is becoming more desirable due to the density of existing civil infrastructure, and social and environmental considerations. Trenchless technology can be used to replace, refurbish, or install new pipe below the ground surface with minimal excavation by means of specialized equipment, materials, and methods. As shown in Figure 2.1, trenchless construction methods are categorized as a function of personnel entry requirements, subsequently branching into three main categories: (1) pipe jacking; (2) horizontal earth boring, and (3) utility tunneling. Although this study focuses mainly on pipe ramming, an overview of trenchless technology is provided to set the context of the application of pipe ramming.

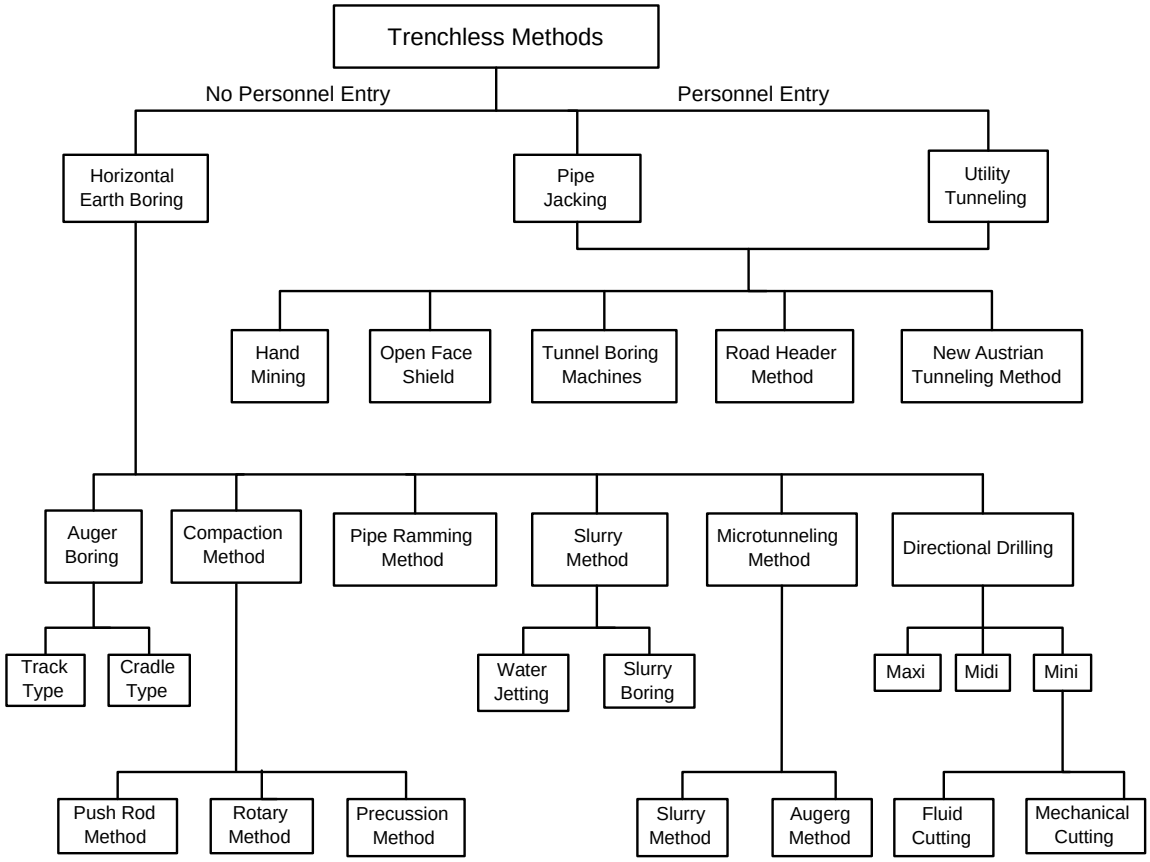

Figure 2.1: Trenchless culvert installation methods (*adapted from Iseley and Gokhale 1997*).

2.1.2.1 Pipe Jacking

Pipe jacking utilizes hydraulic jacks that push segments of prefabricated steel, reinforced concrete, or centrifugally cast fiber reinforced polymer pipe (CCFRPM) through embankments or earth structures for pipes up to 2400 mm (96 in) diameter and lengths up to 183 m (600 ft) (*Najafi et al. 2004*). Working pits are typically developed to set up the jacking and spoil removal operation. The process requires installation of pipe sections in segments where upon the hydraulic rams are retracted after installing the first segment, and a new section of pipe is joined with the proper connection, allowing the jacking process to proceed. The design of pipe joints requires special attention and is based on an evenly distributed horizontal thrust zone around the internal jacking face (*Howitt 2004*). Joints are designed to improve the jacking load carrying capacity by transmitting the loads through the center of the culvert wall rather than edges. A picture illustrating a typical jacking operation is shown in Figure 2.2.

Figure 2.2: Overview of the pipe jacking method (*C. Price, personal communication, 2013*).

2.1.2.2 Horizontal Directional Drilling (HDD)

Horizontal Directional Drilling (HDD) utilizes steerable drilling machines capable of drilling large and small diameter holes. Drilling machines are mechanical cutting devices using drill bits or high pressure jets that drill by fluid cutting. HDD is a unique system because of its capability to keep track of the drilling path and adjust the location of the drill bit. Most applications require a three-stage process. First, a small diameter pilot hole is drilled along the desired centerline of the culvert or pipeline. Then, the second stage enlarges the pilot hole to the desired diameter using a reamer appropriate for the new utility and the third stage involves pulling in the pipe through the drilled hole (Figure 2.3). HDD can drill lengths up to 1524 m (5000 ft) for diameters of 100 to 1500 mm (4 to 60 in). Due to its steering capability, installations can be performed in a shallow arc (*Piehl 2005*). The pipe materials installed with HDD vary from high-density polyethylene (HDPE), steel, polyvinyl chloride (PVC), and ductile iron. The accuracy of the borehole can be very high depending on the quality of the tracking equipment and geotechnical analysis (*Najafi et al. 2004*).

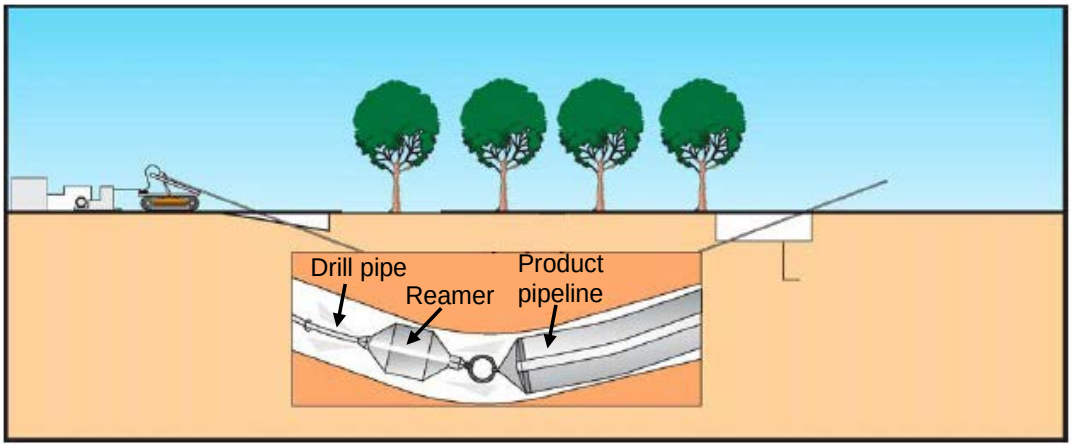

Figure 2.3: HDD pipe pulling (adapted from Hashash and Javier 2011).

2.1.2.3 Microtunneling

Microtunneling is a trenchless technology that is conventionally used for smaller tunnels over long runs (*Piehl 2005*). The process consists of a tunnel boring machine in the front with a guided remote-control method of jacking pipe. Characteristics of the microtunneling method include: (1) boring machines operated via remote control, (2) use of lasers to guide the tunneling alignment (3) installation of the culvert with a jacking system, and (4) the balancing of earth and groundwater pressures with constant face pressure via the slurry within tunnel boring machine (TBM). Spoils are removed through a pressurized slurry system for transportation to the working pit. Hydraulic systems are generally used for conveyance of spoils. Soil types or flow conditions dictate the type of removal method. A TBM is made of two segments connected with an articulating joint. The front portion comprises the boring head and is followed by the trailing shield in the rear section. Hydraulic actuators are attached from the trailing shield to the bore head. These actuators cylinders pivot the head to the desired alignment and grade for proper installation.

2.1.2.4 Auger Boring

Auger boring is the most widely used trenchless method for culvert installation under road and railway embankments (*K. Staheli, personal communication, 2013*). Auger boring creates a horizontal borehole through the ground from an insertion pit to a receiving pit using a rotating cutting head for installation of a pipe (*Iseley and Gokhale 1997*). The cutting head is normally attached to the leading face of the auger string and facilitates the cutting of the ground simultaneously transporting the spoil to the insertion pit through the rotation of helical-wound auger flights (*Iseley and Gokhale 1997*). The auger boring can be performed based on either a track or cradle system. The track system is the most commonly used auger boring technique, whereas the cradle system is limited primarily to oil and gas pipeline crossings (*Iseley and Gokhale 1997*). Auger boring is commonly used to install pipe diameters ranging from 200 mm to 900 mm (*Iseley and Gokhale 1997*). The major problem associated with auger boring is the subsidence or settlement of the ground above the borehole. The cutter at the leading face of the augers

generally excavates a borehole larger than the size of the casing; therefore, settlement is a major concern, particularly for non-cohesive soils (*Iseley and Gokhale 1997*).

2.1.2.5 Pipe Ramming

Unlike HHD and microtunneling, pipe ramming is a non-steerable trenchless construction technique used primarily in horizontal applications. The accuracy of drive in pipe ramming depends on the initial alignment of the ram and pipe and contractor care. Ramming utilizes a pneumatic or hydraulic hammer to drive a culvert or casing through an embankment. The end of the culvert may be left open or fitted with a cutting shoe depending on the soils and the length penetrated. In an open end application (described in detail in subsequent sections), the leading face of the culvert is usually accompanied with a cutting edge to reduce the resistance along the pipe as it moves through the ground. The spoil enters the cavity of the culvert as forward movement progresses. Depending on the length of the pipe and impact energy provided by the ram, the spoil can be left in the pipe or removed though auger boring, compressed air, or pressurized water.

Ramming can accommodate pipe diameters of 102 to 3600 mm (4 to 144 in) and lengths of up to 122 m (400 ft). Pipe material is generally limited to steel due to the large forces transferred to the pipe during the process. However, other materials such as vitrified clay, reinforced concrete, and High Density Polyethylene (HDPE) have been used. The functions of these pipes range from gas and sewer lines, air intake pipes, casings for utilities, and drainage. The rammed pipe can act as a utilidor or casing for other utilities (e.g, smaller pipelines) to travel through (*Wetter et al. 2009, Schrank et al. 2009, Currey et a., 2009, Staheli et al, 2006*).

Ramming can also be accomplished in the vertical direction and is referred to as pipe driving. This has been done to support foundations in soft soils, susceptible to large settlements, or unable to carry temporary loads associated with construction. For instance, if the bridge's load carrying capacity is not adequate to support equipment loads such as cranes during installation of vertical supporting piles in a conventional way, pipe driving can present a practical construction alternative (*Simicevic and Sterling 2001a*).

2.1.3 Suitable Ground Conditions

Each trenchless method is best utilized when paired with the appropriate soil type, pipe material, length, and diameter of pipe. Najafi et al. (*2004*) summarized the ground conditions that are suitable for pipe jacking, microtunneling, HDD, and pipe ramming, as shown in Table 2.1. The various culvert installation methods are rated as follows:

- Yes: generally suitable by experienced contractor with appropriate equipment;
- Marginal: difficulties may occur; some modifications of equipment or procedure may be required; and,
- No: substantial problems, generally unsuitable or unintended for the conditions.

Table 2.1: Suitability of trenchless road crossing methods (adapted and modified from Najafi et al. 2004).

Ground Conditions	Pipe Ramming	HDD	Micro-tunneling	Pipe Jacking
Soft to very soft clays, silts & organic deposits	Yes	Yes	Yes	Marginal
Medium stiff to very stiff clays and silts	Yes	Yes	Yes	Yes
Hard clays and highly weathered shales	Marginal	Yes	Yes	Yes
Very loose to loose sand above the water table	Yes	Yes	Yes	Marginal
Medium to dense sands below the water table	Yes*	Yes	Yes	No
Medium to dense sands above the water table	Yes	Yes	Yes	Yes
Gravels & cobbles less than 50-100 mm diameter	Yes	Marginal	Marginal	Yes
Soils with cobbles, boulders or obstructions larger than 100-150 mm diameter	Yes	Marginal	No	Marginal
Weathered rocks, marls, chalks and firmly cemented soils	Yes*	Yes	Yes	Marginal
Slightly weathered to unweathered rocks	Marginal*	Marginal	Marginal	No

*Modified based on contractor experience (*K. Staheli, personal communication, 2013*).

2.1.4 Advantages and Disadvantages of Trenchless Technology

Trenchless technology has become an attractive alternative to conventional trenching techniques for pipeline construction and should be evaluated when considering open-cut and traditional tunneling methods. Owners, engineers and contractors have relied on open-cut methods for years and these methods have proved successful in many cases. Nevertheless, the problems typically associated with open-cut methods can be less severe when using trenchless methods due to the minimization of excavation and rehabilitation of the area where a culvert needs to be installed. Major problems associated with open-cut trenching are outlined below (*after Rogers and Chapman 1995*):

- High amounts of traffic congestion can occur in urban areas during the trenching operation;
- Social cost associated with the traffic delays;
- Potential damage to existing road pavement structures and existing utilities; and,
- Reduction in the structural life of the roadway and utilities.

In addition, the open-cut method involves costly excavation of a large volume of soil and design and construction of shoring for culverts, since they are generally located at the bottom of embankments.

The demand for new methods for the installation of pipe has been driven by the following factors (*Piehl 2005*):

- The culverts installed in the 1950's and 1960's are reaching their intended and/or extended service life;
- The deterioration of culverts is occurring due to corrosion, scour, erosion, and separation of joints;
- The hydraulic capacity of existing culverts is no longer able to handle maximum flow events or meet updated standards;
- Construction constraints (e.g., environmental concerns) require shorter construction periods and limited damage to surrounding soils and water bodies; and,
- The need for enlarged culverts to enhance the passage of aquatic organisms and other animals, and large debris.

Significant cost savings are possible with proper trenchless technology implementation. Additionally, for instances of increased expense to complete an installation using a trenchless alternative, the best approach still may require trenchless technology due to the following advantages (*Piehl 2005*):

- *Environmental effects:* environmental impacts can be reduced substantially with less soil disruptions around the project site;
- *Social impacts:* deep trenchless culvert construction reduces or eliminates traffic delays for virtually all traffic loading. Shallower work still nearly eliminates traffic disruptions;
- *Project completion rate*: with proper site analysis trenchless construction can be faster to complete than open-cut methods and other viable trenchless methods;
- *Safety:* worker exposure to traffic, steep slopes, and labor inside trench boxes can be reduced or eliminated;
- *Less engineering:* avoidance of open-cut methods can reduce site surveying, reduce cut/fill calculations, and result in less specifications and drawings;
- *Contingencies minimized:* ground displacement is minimized so less precautionary measures need to be taken to account for unforeseen occurrences; and,
- *Areas of application:* deeper tunneling depths and tighter working space constraints can be accomplished with trenchless technology.

Traditional open-cut excavations can be more cost effective in areas of shallow application and low traffic flows (*Piehl 2005*). In addition, project changes after the installation has been already started can be difficult in some cases. For instance, if decisions that affect grade or alignment are made after the start of installation, correction for new requirements might not be possible (*Piehl 2005*).

2.1.5 Consideration of Traffic Disruption

Traditional open-cut methods cause large social impacts to the surrounding community, and the most notable is traffic disruption. Open-cut is proven as a reliable method for installing culverts and pipelines, but results from studies have indicated that this is an extremely time consuming method for pipe installation. When comparing the costs and time related to traditional methods

of culvert installation, the social and environmental costs that are not usually included within the bids will surpass the estimated bid for the project (*Gangavarapu et al. 2003*). The Texas Transportation Institute study showed that in 1999 the average person spent 36 hours per year in their car sitting in traffic due to traffic congestion. The study also concluded that traffic congestion within the nation consumes 6.8 billion gallons of fuel, 4.5 billion hours of travel time, and $78 billion dollars per year. Open-cut trenching increases these numbers and creates traffic disruptions along the detour route along with the project site. Major categories of social costs related to traffic disruptions include (*Bush and Simonsen 2001*):

- Project length;
- Fuel costs;
- Related travel time costs;
- Damage to detour roads and project area;
- Wear on vehicles;
- Loss of revenue to local business; and,
- Noise and vibrations.

Trenchless methods are capable of installing pipelines below grade without the use of an open-cut trench (*Iseley et al. 1999*). Although trenchless technology may be the best option for soil conditions and time constraints, the cost savings to the public through utilizing a trenchless method can significantly impact the selection of a method of installation. Site specific studies will help determine social costs. In situations with medium to low traffic volumes, the detour route could have serious environmental implications. Use of a trenchless technology can limit social costs by saving time, money, and the overall physical and social disruption related to open-cuts.

2.2 OVERVIEW OF THE PIPE RAMMING METHOD

2.2.1 Geotechnical Investigation

In order to successfully perform a pipe ramming operation, the owner or the design consultant should perform a geotechnical investigation along the proposed alignment. The site investigation should include a review of the existing construction records or site history, geologic maps, historical photographs including aerial imagery, specifications, and as-built drawings. If required, new explorations should be performed, including but not limited to test pits, mud-rotary or auger borings with sampling, and/or cone penetration tests. Undisturbed and disturbed samples should be analyzed in the laboratory to determine index properties and strength parameters. This information forms the basis for the design of the pipe wall thickness, selection of a cutting shoe and/or lubrication, estimation of the required ram energy, and estimation of the potential for settlement. Refer to Mayne et al. (*2002*) for specific recommendations regarding subsurface investigations for geotechnical site characterization.

2.2.2 General Considerations for Construction

The installation of a culvert with pipe ramming methods begins with the construction of insertion and receiving pits, if necessary. If conditions permit, such as on the sides of an embankment

with adequate room to perform the operation, construction of a working pit may not be required. The next step is to set the pipe and ram in the correct alignment and grade. This is an important part of the pipe ramming setup, as correcting the alignment after 1.2 m (4 ft) of insertion is extremely difficult (*Najafi 2008*). Some limited steering is possible following removal of spoils and welding of steering wedges to the cutting shoe, however, this practice requires significant experience to be performed reliably. When misalignment requires pullback of the pipe, loose soil at the insertion face prevents the installation proceeding at the proper line and grade (*Najafi 2008*). Operations must progress very slowly so that grades can be monitored every foot of increased depth (*Najafi 2008*). The ram can be directly attached to the rear end of the culvert through the use of connections (e.g., adjustment collets, ram cones, cotter segments) that usually downsize the diameter of the pipe (*Clarke 2007*). As ramming commences, the ram advances the culvert into the ground while simultaneously pulling itself along with the pipe. Depending on the project requirement and the proximity of sensitive structures, it may be required to establish a surface monitoring system to observe surface heave, settlements, or ground distortion. Examples of general pipe ramming operations are depicted in Figure 2.4 and Figure 2.5.

The location of working pits will be based on the "job requirements, right of way access, and regulations of the governing municipal agency" (*Simicevic and Sterling 2001a*). Culvert installation length, ram size, and ancillary equipment (e.g. compressors, mixers, and pumps) will need to be considered when constructing working pits. Maximizing the length of the insertion pit will benefit the project by allowing the installation of longer sections and reducing the time and labor associated with welding pipe segments. If an open cut along the embankment side slope cannot be made, an appropriate method, such as the sheet piling or soldier pile and lagging, will need to be installed to shore the pit. In order to ensure the correct grade of the pipe, the floor of the pit must be graded to match the design slope of the culvert. Crushed rock placed and compacted on the working pit floor, occasionally capped with a thin cement mat, can help maintain the accuracy of the alignment and the stability of the ram during operation. Guide rails may be installed on the working mat to increase the alignment and grade accuracy. If the construction of an insertion pit is not feasible, a special cradle can be used to allow pipe ramming on a slope face (*Simicevic and Sterling 2001a*).

For shorter installation lengths, spoils may be left in the casing and removed when ramming is completed. For long driving distances with multiple pipe segments, it may be necessary to remove spoils prior to the attachment of new culvert segments. Spoil removal is performed to: (1) ensure clear passage for subsequent utility lines, (2) remove weight and internal soil friction to maintain the rate of installation, and (3) maintain the grade in soft and weak soils, which can be affected by the weight of the pipe.

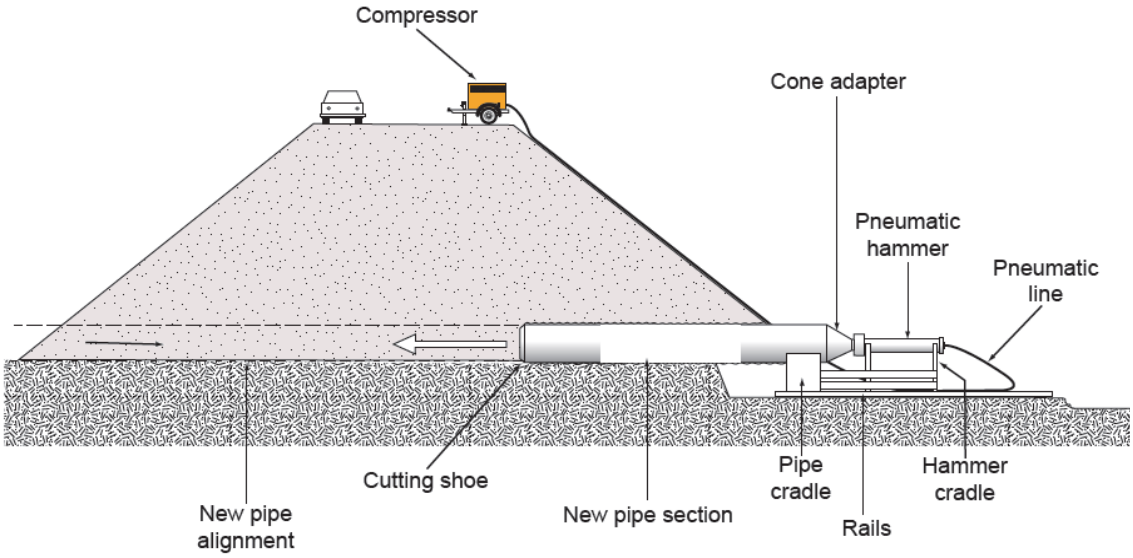

Figure 2.4: Typical pipe ramming setup for embankment (*after Piehl 2005*).

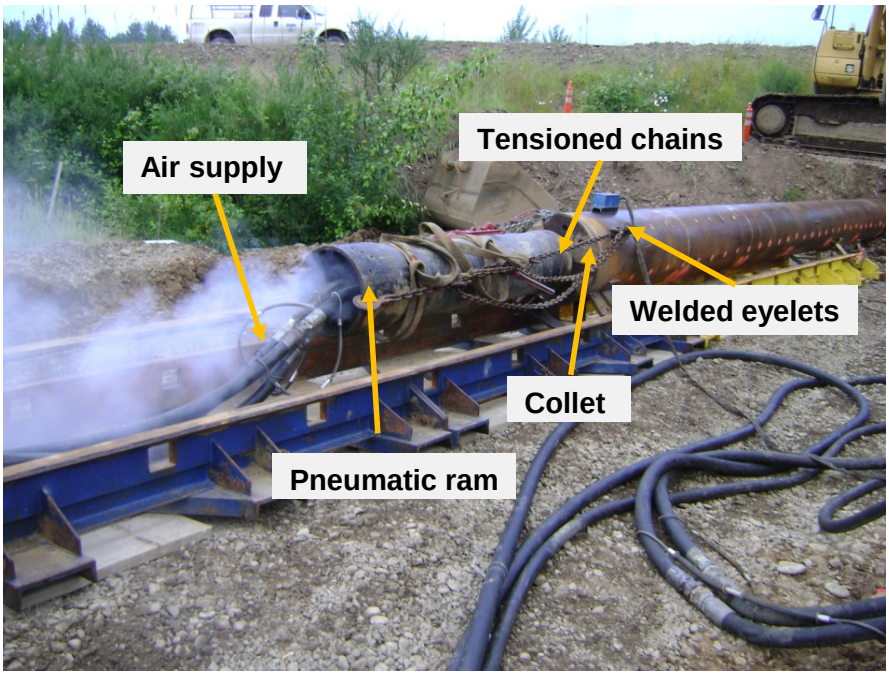

Figure 2.5: Typical pipe ramming setup; view from one of the study sites.

2.2.2.1 Route Layout

Ground movement and vibrations created during the pipe ramming installations require the proper route selection to avoid damaging surrounding utilities. Because pipe ramming is a non-steerable trenchless technology, the path of culvert must be installed in a straight line. Initial installation accuracy is paramount to avoid misalignment. Vertical and horizontal tolerances in alignment should not exceed 1 percent deviation. With proper initial set up, an accuracy of 0.5 percent can be achieved (*Simicevic and Sterling 2001a*).

2.2.2.2 Depth and Length of Pipe Ramming Installation

Pipe ramming is typically selected for deeper installations where the open-cut method would prove difficult due to ground conditions or the large volume of material to be excavated. Typical depths range from 3.05 to 6.10 m (10 to 20 ft), although shallower depths, ranging from 0.46 to 3.05 m (1.5 to 10 ft) have been accomplished (*Simicevic and Sterling 2001a*). The lengths of culvert segments suitable for pipe ramming are selected based on the dimensions of the insertion and receiving pits. If the working pit is large enough to accommodate the entire pipe ramming setup, the culvert can be installed in a single run without the need of breaking the operation into segments. Lengths between 3.05 to 18.3 m (10 to 60 ft) are appropriate for the installation of a culvert in a single section. The length of pipe segments to be installed is determined by the contractor or site constraints (*Simicevic and Sterling 2001a*).

2.2.2.3 Pipe Design Considerations

The ramming energy and associated forces delivered to the pipe require the culvert to be made of steel. A139 Grade B smooth wall carbon steel pipe with minimum yield strength of 241 MPa (35,000 psi) should be used; however, drivability analyses described in this study should provide the basis for the selection of the minimum yield strength. Likewise, the pipe wall thickness is based on the maximum anticipated installation stresses during the construction phase and can be evaluated with drivability analyses. The potential for pipe buckling is typically investigated during the culvert design. Geotechnical investigations could reveal potential obstructions in the proposed path of the culvert that could alter the pipe design (*Simicevic and Sterling 2001a*).

Connecting segments of culverts can be accomplished by welding or by using proprietary joint systems such as those provided by Permalok®. Full-penetration welds are required to provide adequate strength and transfer of the wave energy during the ramming process. Breaking and cracking of the welds can occur if full-penetration welds are not used. Welding can contribute to increased installation durations, resulting in up to 12 hours to disconnect the ram, set the next section properly, and weld the sections together. Permalok® connections can reduce this time to 2 to 4 hours. The Permalok® system utilizes mechanically pressed fit joints that are watertight and do not require welding (*Simicevic and Sterling 2001a*).

2.2.3 Pipe Ramming Hammers

2.2.3.1 Introduction to Pipe Hammers

Impact hammers consist of a pneumatically or hydraulically powered reciprocating piston within a specially designed steel shell. The piston strikes the inside of the shell, which is in turn connected to the culvert, and moves the hammer/pipe system into the ground in a hysteretic manner. Pipe ramming technology was developed during World War I by the military for use as a hidden weapons delivery system. At the time, explosives were too volatile to withstand the vibrations caused during movement. Later, engineers in Russia designed the first working models of a pipe hammer for installation of buried service utilities (*Clarke 2007*). The accuracy of these first models proved unreliable for pipeline installation. Advancements in technology and understanding of ground behavior in the last couple of decades have resulted in reliable, strong, and accurate ramming machines (*Clarke 2007*).

2.2.3.2 Pneumatic Hammers

Pneumatic hammers (Figure 2.6) are the most common type of impact hammer, and they employ compressed air to drive the piston (*Schrank et al. 2009, Currey et al. 2009, Yin et al. 2003*). These hammers require a large external air compressor to provide the air supply to the ram. The rams are fitted into a cradle or on a rail system, which allows the hammer to move with the advancing culvert. Once the culvert is driven in the ground, some hammers may be operated in reverse to detach the connection to the culvert, increasing the efficiency of the operation. Varying impact energy quantities and frequency rates are possible during the operation by changing the air pressure supplied to the hammer and the rate at which it flows within the hammer casing.

Figure 2.6: Photograph of 400 mm pneumatic hammer driving 600 mm diameter pipe pipe (corresponding to Case 1, described in Chapter 3).

2.2.3.3 Hydraulic Hammers

Hammers using hydraulic fluids operate on a similar principle as pneumatic hammers. Typically, a hydraulic ram system (Figure 2.7) consists of a hydraulic hammer, hydraulic power unit, adaptors, and a support device for the hammer to rest and glide. Differences between hydraulic and pneumatic designs exist due to the operating fluid powering the ram's piston and gas within its accumulator system. The use of hydraulic fluid in a ram allows for an overall smaller ram and hydraulic power unit that weighs less than pneumatic systems. Hydraulic oil lubricates moving parts within the machine, decreasing frictional wear and therefore increasing reliability and service life. However hydraulic hammers are generally more expensive than pneumatic hammers.

The use of a hydraulic hammer allows for increased operational efficiency of the ramming system. Hydraulic systems need 25 to 50 percent of the energy required to operate pneumatic systems. Reduced frictional components, smaller dimensions, and decreased internal components allow for a more efficient transfer of energy throughout the operation. Blow energy and frequency can easily be changed with adjustments to the charge pressure of the gas within the accumulator or flow rate of hydraulic fluid depending on soil conditions, size of pipe, and other consideration (*Yin et al. 2003*).

Figure 2.7: Hydraulic Hammer driving 3050 mm diameter pipe (*after Piehl 2005*).

2.2.4 Cutting Shoes

Cutting shoes are often used in pipe ramming applications, and are intended to: (1) reduce frictional drag around the culvert by creating an overcut within the borehole slightly larger than the diameter of the culvert being installed, (2) reinforce the leading edge to assist in the breakup of boulders and cobbles, and resist the hoop stress created from uneven stress distribution due to boulders (3) direct spoil into the culvert, and (4) promote better directional control. The leading edge of the first segment to be installed is fitted with the cutting shoe (Figure 2.8) and is often accompanied by steel bands welded around the outer and inner faces of the culvert. The steel bands used are typically recessed behind the leading edge of the culvert to compact the annular soil around the pipe, relieve skin friction, and stiffen the leading head of the cutting shoe in breaking the boulders and cobbles. Shoes are continued past the leading edge of the culvert in a beveled design to also promote better directional control for the advancement of the pipe and directing spoil into the overcut and culvert. Cutting shoes may also be outfitted with special fins for increased directional control and to prevent rolling (*Tolouli et al. 2009*). In cemented soils, which are the most challenging soils for pipe ramming, shoes with a beveled edge may be used and combined with auger teeth welded to edge of the pipe. Inner surface bands provide the same advantages of the outer band but also create clearance for the soil within the culvert. This improved soil clearance assists in spoil removal and reduces frictional drag within the culvert (*Najafi 2008*).

Figure 2.8: T1 cutting shoe being welded to 1060 mm diameter pipe pipe (corresponding to Case 6, described in Chapter 3).

2.2.5 Lubrication of Culverts

2.2.5.1 Purpose of Lubrication

Another way to reduce friction along the outer and inner pipe surface is to use lubrication. The use of lubrication is generally recommended for all soil types, though may not be required, depending on the casing diameter, length of penetration, and hammer energy supplied. A lubrication system requires external mixing and pumping systems which usually share a chassis located in or near the working pit. The lubrication is transferred and applied to the outer surface of the culvert by a series of hardline tubes, hoses, and threaded ports installed on the culvert. Cutting shoes can be designed to incorporate the release system for the lubrication (*Akkerman 2006*). Theoretically, the minimum flow rate of lubrication required may be computed by multiplying the cross-sectional area of the overcut with the anticipated rate of installation. However, the amount calculated will typically be less than the actual demand due to seepage into the surrounding soils. Additionally, Simicevic and Sterling (*2001a*) indicate a propensity for lubrication to run towards the face of the insertion pit.

Lubrication is used to reduce skin friction acting against the inner and outer pipe surfaces during the ramming operation. Although the reduction of friction is the main purpose the system, it can also provide water to assist in removal of spoil and to saturate the surrounding soil. Depending on the soils being penetrated, the combination of lubrication and water applied in the ramming process can help to maintain the integrity of the hole being created. This is especially true in sands where the bentonite platelets that travel within the water fill the pore space to form a “filter cake” layer. This in turn reduces the effective porosity and therefore permeability of sands (*Najafi 2008*).

In general, the forces resisting ramming increase as the length of culvert penetration increases. The aim of lubrication use is to decrease the resistance that the pipe and hammer has to overcome to penetrate the ground (*Najafi 2008, Currey et al. 2009*). The use of lubrication for reduction of friction will be effective only if a distinct layer of lubricant is kept within the overcut space provided by the cutting shoe. Lubricants can provide adequate internal pressure to the soil that may move into the overcut and prevent the collapse of the annular space. The consistency of the lubricant will be important to prevent excessive bleeding and counter pore water pressures. Proper mix design and implementation of the lubricants may also help to reduce the settlement above the pipe and help reduce frictional characteristics (*Marshall 1998*).

2.2.5.2 Types of Lubrication

Substances used as a lubricant include bentonite, polymers, and water. Bentonite lubrication is a mixture of powdered montmorillonite clay minerals and water (*Najafi 2008*). The bentonite-water mixture is mixed to the required specifications in a high-shear mixer, resulting in the minerals separating into flat, thin, and individual particles. When mixed with water, bentonite acts as a thixotropic material: when the bentonite is agitated it acts like a liquid, but when left to rest it becomes a gel like substance. The mixture needs several hours for separation to fully occur and the substance to swell to the

proper gel consistency (*Marshall 1998*). During the lubrication process these platelets act as patches that seal the pore spaces along the borehole wall forming a filter cake (*Najafi 2008*). This quality makes bentonite a good candidate for use with low cohesion soils with natural void space the bentonite can fill. (*Marshal 1998*)

The use of polymeric lubricants is preferred for pipe ramming installations through highly plastic cohesive soils and shale to avoid the tendency for swelling and reduce the sticking nature of plastic clays (*Najafi 2008*). Polymers are very dilute water-based solutions that are used as lubricants either alone or in combination with other chemical components or bentonite (*Borghi 2006*). Although the cost of most polymer additives is expensive compared to bentonite, the lubrication quality is excellent and very effective.

2.2.6 Spoil Removal

Open-face ramming results in the movement of soil into the culvert; removal of the spoil may be necessary during the process for longer pipe installations or soils with a high frequency of boulders and cobbles, as these occurrences will increase the total weight of the pipe and reduce the rate of penetration. Limited spoil removal in proximity to the insertion pit is necessary on all installations so that welding of subsequent pipe sections can be accomplished. For ramming in loose, saturated granular soils and soft cohesive soils, the additional weight in the pipe may result in the downward movement of the pipe relative to the intended grade. Spoil removal is accomplished using water pressure, air pressure, augers, or scrapers, depending on the diameter of the pipe; soil type, and accessibility. Auger boring is commonly used for large diameter installations (i.e. greater than 200 mm) while compressed air is utilized for smaller diameter culverts. Auger boring uses solid stem augers with wide flanges that excavate the pipe cavity with rotation of the drill. Relatively short installations may allow soil removal following installation of the entire casing. As shown in Figure 2.9, auger boring requires the use of an auger boring machine resting on guidance tracks.

Figure 2.9: Auger boring machine removing spoil from 1060 mm pipe (corresponding to Case 6, described in Chapter 3).

2.2.7 Construction Observation of Pipe Ramming

As with any construction operation, owners should observe the installation to document progress and to provide information for comparison to the design and baseline documents (e.g., geotechnical data report). Contractor submittals should include the following (after *Simicevic and Sterling 2001a*):

- Pre-construction surveys, as-built drawings;
- Construction logs;
- Material certifications and quantities;
- Cause and extent of delay (if any);
- Locations of disturbed areas (if any); and,
- Any unusual or unexpected conditions.

Simicevic and Sterling (*2001a*) recommend that a construction log of a pipe ramming operation should consist of the following:

- The position of the pipe in relation to the design alignment and grade;
- Date and time of start and finish;
- Pipe inclination and advance rates;
- Hammer performance (blow rate, bpm; blow count, bpf or blows per 0.3 m);
- Operating pressure of air compressor or hydraulic pump;
- Spoil quantities removed; and,
- A separate log tracking quantity and quality (e.g., viscosity) of lubricant used and pressure of lubricant delivery system.

Regardless of the method pipe installation, uncertainties in the soil stratigraphy and characterization, groundwater levels, operation of construction equipment, surcharge and traffic loading, and other variables exist. Although surface disruptions are generally minimal for pipe ramming installations (*Simicevic and Sterling 2001a*), the observation of construction operations is required to adequately document the installation in the event uncertainties produce undesirable production rates or outcomes (i.e, damage). In some instances, owners may require detailed construction observation, such as for installations beneath railways and highways. Sensitive utilities that may lie in close proximity to the new installation may trigger the incorporation of an instrumentation and monitoring plan. Instrumentation programs can range from simple leveling surveys to complex systems whereby strains within the culvert, pore pressures within the ground, and displacement monitoring points are recorded in automated real-time acquisition systems. Generally, the sophistication of the instrumentation program implemented varies with the complexity of the site (density of potential hazards) and risk of the operation.

2.2.8 Advantages and Limitations of Pipe Ramming

The most significant benefit in the use of pipe ramming is the cost-effectiveness of the operation. When compared to other trenchless technologies, ramming equipment requires the simplest design and equipment. Compared to the rotating cutting heads and jacking actuators, associated with microtunneling and HDD, the moving parts required for installing the pipe are significantly

reduced with pipe ramming equipment. Therefore, the maintenance costs throughout the project are lowered, resulting in a potential decrease in installation time. Smaller work crews and less heavy equipment are needed in pipe ramming operations, reducing operational costs associated with the culvert installment.

Surface settlements are minimal or negligible in both open- and closed-end applications. Ramming is possible in a wide variety of soils including cobbles and boulders, stable (non-flowing) and unstable (flowing) ground conditions (*Schrank et al 2009*). Large boulders and obstacles of considerable size can be traversed, as long as their diameter is smaller than that of the culvert or they are broken up by the ramming action of the pipe. When using open faced ramming, the spoil moves steadily into the cavity of the pipe, reducing damage, deviations in alignment, creation of void, and surface disruptions (*Simicevic and Sterling 2001a*).

Pipe ramming restricts the pipe material to steel due to the installation forces. However, the advantages of using steel tend to outweigh the disadvantage of limited material alternatives. The use of steel minimizes the damage to the leading edge of the culvert. A reduction in the damage to joints is achieved through the use of steel. If boulders or cobbles are encountered, directional changes are less likely than with other materials. Steel joints are more rigid and allow even distributions of thrust forces from one section to another. The service life of steel is greater than other materials such as reinforced concrete or vitrified clay.

One of the main limitations of pipe ramming is directional control. Changing direction of a pipe ramming installation during operation is difficult or impossible once an installation passes a pre-determined depth based on soil-pipe interactions. Thus, setting the grade and alignment of the initial pipe segment is the most critical aspect of the construction preparation as correcting the alignment after approximately 1.2 m of insertion is extremely difficult (*Najafi 2008*). In addition, pipe ramming might pose some social impacts related to high noise levels. The level of noise associated with a pipe ramming operation can cause annoyance and discomfort to people at noise-sensitive sites (e.g. residences, hospitals, schools etc.).

2.3 STATIC SOIL RESISTANCE TO RAMMED CULVERTS

The accurate prediction of static soil resistance on culverts during installation is critical from the standpoint of structural design and constructability. Accurate prediction of soil resistance guides the selection of equipment with the goal of providing the required thrust or ramming energy (or forces) to complete the installation without damage to the pipe. A review of the literature indicates that studies on soil resistance to pipe ramming are very limited. However, studies on the soil resistance developed during pipe jacking by Auld (*1982*), Norris (*1992*), Bennett (*1998*), Marshall (*1998*), Chapman and Ichioka (*1999*), and Staheli (*2006*) provide a starting point for assessing the static forces developed during pipe ramming. Therefore, the literature related to static pipe jacking theory is discussed to set the stage for the pipe ramming investigations.

Pipe jacking refers to the trenchless construction method whereby a pseudo-static jacking force is applied to a pipe to facilitate movement of the pipe into an embankment or subgrade, as discussed in Section 2.1.2. The jacking force depends on the force required to overcome the face resistance at the leading edge of the pipe and the frictional resistance along the length of the pipe.

In general, the required jacking force, R_{req}, should be greater than the sum of the penetration resistance of the face and the frictional resistance along the surface of the casing (Figure 2.10):

$$R_{req} \geq R_f + R_s \quad \textbf{(2.1)}$$

where R_f = face resistance, and R_s = casing resistance along the pipe length.

The jacking force depends on a number of factors including the type of jacking technique (e.g., static jacking, microtunneling, etc.). A predictive model for the required jacking force should take into account the following parameters (*Norris 1992, Ripley 1989, Zhou 1998, Stein 2005*):

- Surface loading above culvert including surcharges, transient loads and water pressures;
- Type, strength, relative density or consistency, and stratigraphy of soil layers along the pipeline;
- The length, diameter and self-weight of the culvert;
- Amount of overcut during excavation;
- Misalignment of pipe; and,
- Type and amount of lubricant.

In the case of pipe ramming, the hammer energy, the pipe-hammer connection, and rate of impact should be accounted for in addition to the parameters listed for pipe jacking above.

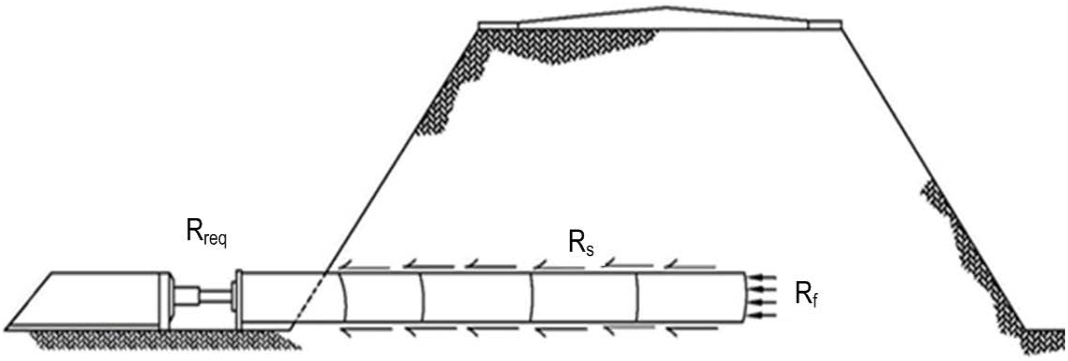

Figure 2.10: Typical sources of pipe jacking resistance.

2.3.1 Pipe Jacking-based Methods to Determine Face Resistance

To date, the discussion of face resistance in the literature review appears to be centered on microtunneling techniques, in which the goal is to maintain face stability at the interface of the TBM and the subgrade. Although the determination of face resistance for microtunneling is not directly applicable to pipe ramming operations, a review is provided with the intent of informing considerations of face resistance for pipe ramming. The amount of face resistance encountered during pipe jacking depends on the method of jacking (static jacking or microtunneling), and may include cutting edge resistance, contact pressure force, and support force (*Stein 2005*). In general, jacking penetration resistance is solely due to the cutting edge resistance of the tunneling shield and the friction acting on the external surface of the shield (*Auld 1982*). The

cutting edge resistance greatly depends on the type of soil, the type of deformation in front of the cutter, and the type and position of cutting tools.

The total face resistance, R_f, in the direction of the excavation can be estimated as (*Stein 2005*):

$$R_f = r_f \cdot A_f \tag{2.2}$$

where A_f is area of the bore head and r_f is the unit face resistance at the bore head.

The unit face resistance can be estimated using an approach proposed by Weber and Hurtz (*1981*) and summarized by Stein (*2005*) for jacking load predictions of microtunneling machines. Based on statistical evaluation of instrumented case histories and laboratory tests, Weber and Hurtz (*1981*) proposed the unit face resistance equal to:

$$r_f = \lambda\left(c + \gamma\left(h + \frac{D}{2}\right)\tan\phi'\right) \tag{2.3}$$

where c is the soil cohesion, γ is the unit weight of the soil, h is the height of soil cover above the pipe crown, D is the bore diameter, ϕ' is the effective soil friction angle, and λ is an empirical coefficient of face bearing resistance. The relationship for λ generated by Weber and Hurtz (*1981*) is shown in Figure 2.11 and may be approximated for $\phi' \leq 45°$ by the relationship (*Stuedlein and Meskele 2012*):

$$\lambda = \frac{3\pi}{2} e^{\pi \tan\phi'} \tag{2.4}$$

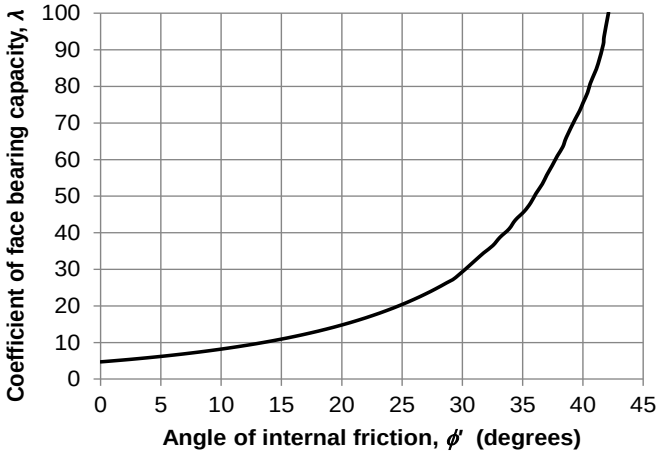

Figure 2.11: Coefficient of face bearing resistance as a function of friction angle.

In microtunneling, the face resistance takes in to account the contact pressures and the earth pressure required to maintain the stability of the ground. The support force at the working face should be applied in a manner to avoid subsidence and heaving of ground surface above the culvert installation. In the former case, sufficient face pressure is applied by the TBM to the face to exceed the active earth pressure, whereas in the latter case, heaving is avoided by maintaining face pressure below the passive earth pressure. From consideration of earth pressure theory, the optimum face resistance likely corresponds to the earth pressure at rest (*Stein 2005*). The coefficients of the lateral earth pressure are determined as a function of the inclination of the ground, angle of internal friction, and wall friction angles (e.g., NAVFAC 1986). Thus, the minimum and maximum allowable *unit* face resistances are calculated, respectively, as (*Stein 2005*):

$$r_{f,min} = \gamma \cdot \left(h + \frac{D}{2} \right) \cdot K_a - 2 \cdot c \cdot \sqrt{K_a} \qquad \textbf{(2.5)}$$

$$r_{f,max} = \gamma \cdot \left(h + \frac{D}{2} \right) \cdot K_p + 2 \cdot c \cdot \sqrt{K_p} \qquad \textbf{(2.6)}$$

where h equals the depth of cover, D equals the external diameter of the pipe or TBM, γ equals the unit weight the soil, c equals the cohesion of the soil, and K_a and K_p equals the coefficient of lateral active and passive earth pressure, respectively. The concept is illustrated in Figure 2.12.

Stein (*2005*) also provides an overview of several limit-equilibrium methods that incorporate an assumed failure volume and associated 3D slip surface. Although these face resistance models appear theoretically robust, it appears that none have been sufficiently compared against actual case histories. Furthermore, these models are not directly applicable to open-ended pipe ramming operations. In an indication of the acceptance of model uncertainty, a working group at the International Society for Trenchless Technology (*ISTT 1994*) applied a statistical assessment of 238 microtunneling case histories. For diameters ranging from 250 to 1000 mm (10 to 39.4 in), the working group recommended applying the average face resistance, R_f, of 65, 94, or 134 kN (15, 21, and 30 kips) for clay, sand, and sand-gravel mixtures, respectively. The working group also analyzed a subset of the data to determine the average and upper-bound unit face resistance, r_f, for diameters ranging from 250 to 700 mm (10 to 27.6 in), as shown in Table 2.2.

In regard to open-ended pipe ramming, the soil spoils within the pipe immediately adjacent to the face should provide some counterbalance to the earth pressure resisting the advance of the pipe. Although this effect may be small for deep installations, the efficiency of the spoil is expected to increase with decreasing depth of cover. Additionally, the overall face resistance for open-ended pipes should not reflect that of a closed-end pipe or TBM; rather, the resistance is anticipated to resemble that of an unplugged open-end pipe pile, albeit with a gradient of increasing resistance from the top to the bottom of the pipe.

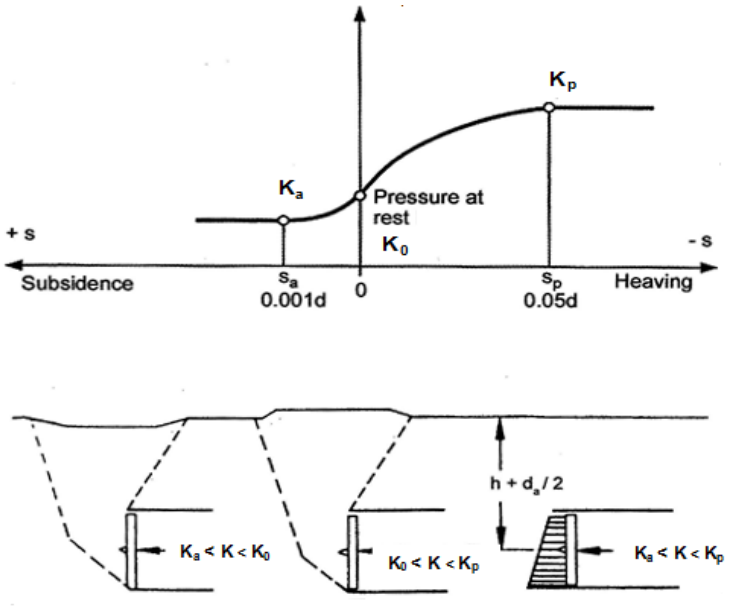

Figure 2.12: Conceptual correlation of earth pressures to surface deformation (*adapted from Stein 2005*).

Table 2.2: Statistical evaluation of unit face resistance for 69 microtunneling case histories with auger spoil removal (adapted from ISTT 1994).

r_f (kN/m^2)	Clay	Sand, Sand-Gravel mixture
Mean value	328	485
80% quantile	500	700

2.3.2 Methods for the Determination of Normal Stress on Culverts

The normal load imposed on culverts during pipe jacking (and ramming) depends on the ground conditions, concentrated and/or surcharge loads (e.g., crane outriggers or foundations, respectively) and live loads (e.g., traffic loads). The normal stress acting radially on the pipe is a function of the vertical and horizontal stress on the pipe and can be obtained using the Mohr's circle of stress (and assumed level ground conditions) as:

$$\sigma_n = \frac{(\sigma_v + \sigma_h)}{2} + \frac{(\sigma_v - \sigma_h)}{2}\cos 2\theta \qquad \textbf{(2.7)}$$

where σ_v = vertical stress, σ_h = horizontal stress, θ = orientation of the elemental soil surface with the horizontal axis. The horizontal stress acting on any point on the surface of the pipe is also a function of vertical stress and is given by:

$$\sigma_h = K_h \cdot \sigma_v \qquad \textbf{(2.8)}$$

where K_h = coefficient of horizontal earth pressure and is considered to be equal to the coefficient of earth pressure at rest, given by $K_h = 1 - \sin\phi'$ for normally consolidated soils.

Typically, the horizontal stress acting at the springline of the pipe is assumed to act uniformly over the diameter of the pipe (Figure 2.13); it is calculated as:

$$\sigma_h = K_h \cdot \sigma_v + \gamma \cdot \frac{D}{2} \qquad \textbf{(2.9)}$$

where α= the unit weight of the soil. The error due to the use of uniform horizontal mean stress acting on the pipe for small or deep pipes is likely minimal. However, for large culverts near the ground surface, there may be significant error resulting from the use of the horizontal mean earth pressure at the springline.

The most widely used model to estimate the vertical stress acting at the top of a pipe is given by Terzaghi's (*1943*) trapdoor theory. According to Terzaghi, the soil above a trapdoor (or a culvert, in the present case) of certain width, b , is assumed to move downward between two potential vertical shear planes by transferring the yielding soil mass pressure onto adjacent unyielding stationary parts (Figure 2.13). As the soil column moves downward, friction mobilizes on assumed vertical shear surfaces, resulting in an induced compressive stress along the borders of the parallelepiped soil column. Because of the transfer of the weight of the soil prism and the upward shear stress developed on the vertical planes, the overburden stress at the crown of the pipe reduces. This behavior is termed soil arching, which is presumed to occur during the installation of culverts with pipe jacking (and ramming) methods, particularly if an overcut is specified (i.e., a cutting shoe is used).

The reduced vertical stress due to soil arching can be derived based on the equilibrium of the forces above the trapdoor. At equilibrium, the sum of vertical forces on an infinitesimal element of a soil equals zero. The differential form of the vertical force equilibrium is given by (*Stein 2005*):

$$\frac{\partial \sigma_v}{\partial z} = \gamma - \frac{2c}{b} - 2K\sigma_v \frac{\tan\delta}{b} \qquad \textbf{(2.10)}$$

where c = cohesion, $\delta = \alpha'$ for soil-to-soil shearing surfaces, γ = the unit weight of the soil, K = the coefficient of earth pressure above the pipe, and σ_v = the vertical overburden soil pressure. Integration of the differential equation for the case when the depth, z, equals the depth of cover, h, results in an expression for the vertical stress at the top of the pipe:

$$\sigma_v = \frac{b\left(\gamma - \frac{2c}{b}\right)}{2K\tan\delta}\left[1 - e^{-2K\frac{h}{b}\tan\delta}\right] \qquad \textbf{(2.11)}$$

For deep culverts, *h* increases to infinity and Equation 2.11 approaches:

$$\sigma_v = \frac{b\left(\gamma - \frac{2c}{b}\right)}{2K\tan\delta} \qquad \textbf{(2.12)}$$

For cohesionless soils, the vertical stress formulation at the crown of the pipe can be rewritten in a simplified form as:

$$\sigma_v = k \cdot \gamma \cdot h \qquad \textbf{(2.13)}$$

where *k* = the stress reduction factor contributed by the loosening of the ground around the pipe and given by:

$$k = \frac{1 - e^{-2K\frac{h}{b}\tan\delta}}{2K\frac{h}{b}\tan\delta} \qquad \textbf{(2.14)}$$

where *h* is the height of cover above the pipe crown, γ is unit weight of the soil, *K* is lateral coefficient of the soil pressure above the pipe crown, *b* is the trap width that influence the soil above the pipe, and δ is wall friction angle in the vertical shear plane. The stress reduction factor given in Equation 2.14 involves the parameters *K*, *b* and δ which are considered differently by various researchers and design codes. Staheli (*2006*) suggested that observed planes of shear above pipelines constructed with an overcut resembled the failure angles implied by the Mohr failure criterion (shown in Figure 2.14), and proposed that the use of Equation 2.15, in which the trapdoor width is expressed as:

$$b = D \cdot \cos\left(\frac{\pi}{4} + \frac{\phi'}{2}\right) \qquad \textbf{(2.15)}$$

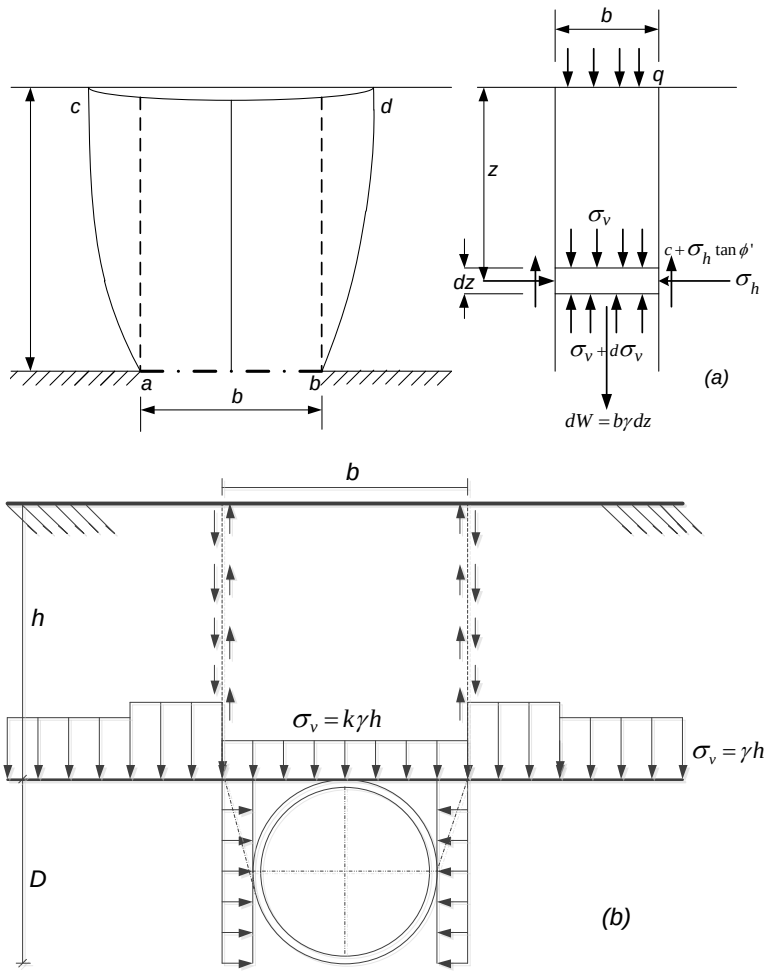

Figure 2.13: Conceptual and computational schematic for computation of earth pressures on culverts: (a) Terzaghi's trap door model (*adopted from Terzaghi 1943*), (b) vertical and horizontal stress acting on the pipe (*adopted from Stein 2005*).

Substituting Equation 2.15 into Equation 2.11 with $K = 1.0$, $\delta = \phi'$, and $h = \infty$ (*recommended by Staheli 2006, per Terzaghi 1943*) yields the following expression of vertical stress for cohesionless soils:

$$\sigma_v = \frac{\gamma \cdot D \cdot \cos\left(\frac{\pi}{4} + \frac{\phi}{2}\right)}{2 \cdot \tan\phi} \qquad \textbf{(2.16)}$$

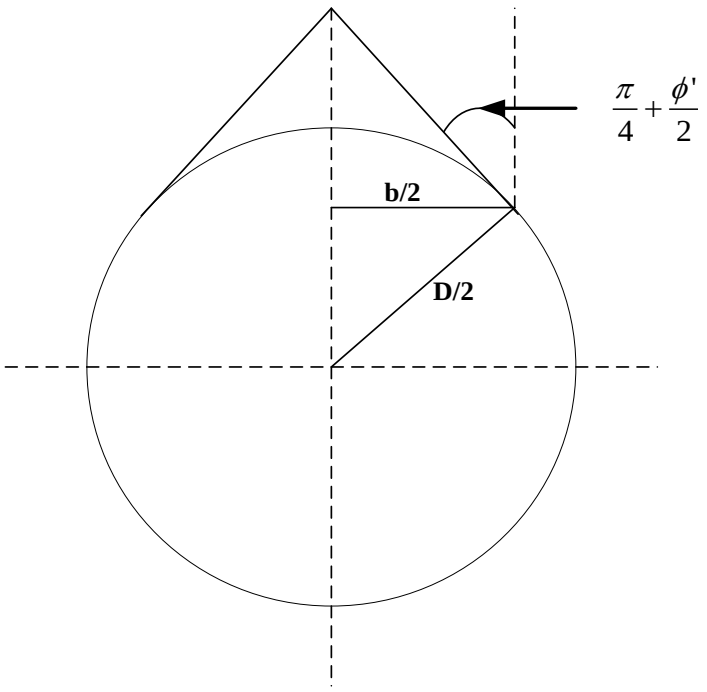

Figure 2.14: Geometric derivation of the trapdoor width (*adapted from Staheli 2006*).

The recommendations of other researchers and design codes for physical parameters of *K*, *b*, and δ are summarized on Table 2.3. The stress reduction factor, *k*, is plotted as a function of friction angle and the ratio of depth of cover to diameter (*h/D*) in Figure 2.15. As shown in the figure, *k* can vary dramatically from method to method for a given friction angle.

Table 2.3: Soil parameters used to compute the normal stress (adopted and modified from Pellet-Beaucour and Kastner 2002).

Soil Parameter	**Terzaghi (*1943*)**	**ATV**	**PJA**	**Staheli (*2006*)**
b	$D+2D\cdot\tan\left(\frac{\pi}{4}-\frac{\phi'}{2}\right)$	$D\sqrt{3}$	$D\cdot\tan\left(\frac{3\pi}{8}-\frac{\phi'}{4}\right)$	$D\cdot\cos\left(\frac{\pi}{4}+\frac{\phi'}{2}\right)$
δ	ϕ'	$\phi'/2$	ϕ'	ϕ'
K	1	0.5	$\frac{1-\sin\phi'}{1+\sin\phi'}$	1

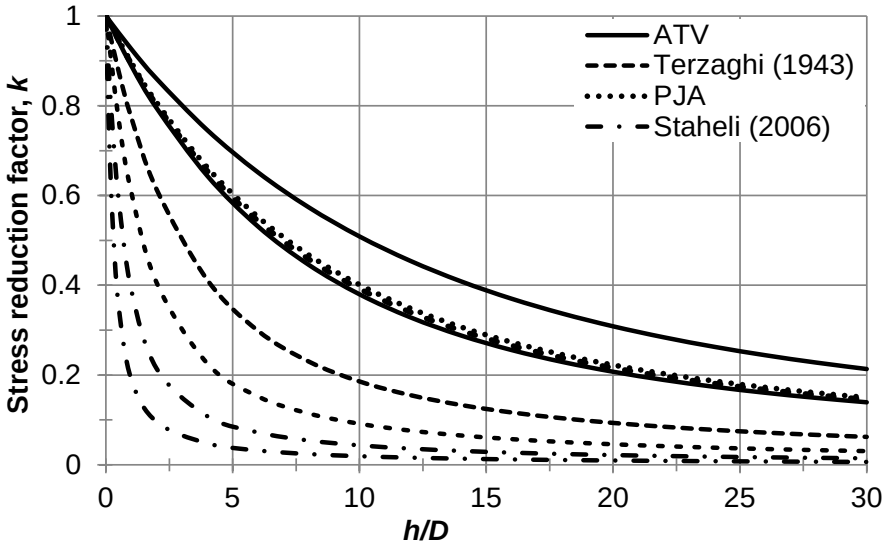

Figure 2.15: Variation of stress reduction factor with normalized depth of embedment (h/D); upper bound curves given by ϕ = 30°, lower bound curves given by ϕ = 45°.

2.3.3 Methods for the Determination of Casing Resistance

2.3.3.1 Overview of Casing Resistance

The resistance, R_c, along the length of the casing can account for a majority of the jacking force required to install the culvert, particularly as penetration increases along an alignment. The casing resistance per unit area, r_c, of the culvert depends in part on whether the excavation results in an arching soil behavior (termed a "stable condition" in the tunneling industry). In the case of a stable condition, the casing resistance is mainly associated with the buoyant weight of the culvert and its relatively smaller contact area with the surrounding soil (*Borghi 2006*); on the other hand, the surrounding soil may lie in full contact with the pipe with ground in an unstable condition. This latter condition may increase the contact area of the soil on the culvert resulting in larger total frictional forces. The specification of an overcut, through the use of cutting shoes in pipe ramming applications, should promote the generation of a soil arch: as the soil behind the cutting shoe moves into the annulus generated between the surrounding soil and pipe by the shoe, the vertical soil load is transferred to the side walls (i.e., shear planes) of the presumed soil column. The use of lubrication may also serve to reduce the frictional forces acting on a culvert.

In general, the casing resistance, R_c, is obtained by the integration of the unit casing resistance, r_c, acting on the external surface area of the pipe, A_c. One method to compute the casing resistance assumes that soil is in contact with the entire surface area of the pipe. The friction force due to the normal stress of ground pressure is given by:

$$R_c = \mu \cdot 2 \cdot \int_o^L \int_0^\pi \sigma_n \frac{D}{2} d\theta dL \qquad \textbf{(2.17)}$$

where σ_n = the normal stress acting on the pipe and L = length of the pipe. The normal stress acting on the pipe is computed based on discussion in Section 2.3.2 and Equation 2.7, which is the function of vertical and horizontal stresses. However, the jacking frictional resistance model proposed by Staheli (*2006*) applies the vertical stress in Equation 2.16 instead of the normal stress and utilizes the critical state angle of internal friction.

The coefficient of friction, α, varies as a function of the interface friction angle (α, such that $\alpha = \tan \delta$), which ranges from $0.25\alpha'$ to $0.75\alpha'$ depending on the roughness of the soil-pipe interface and use of lubricant (*Pellet-Beaucour and Kastner 2002*). The casing resistance may result from the relatively drained resistance in cohesionless soils or relatively undrained resistance in cohesive soils. The following discussion addresses these two sources of casing resistance.

2.3.3.2 Determination of Casing Resistance in Cohesionless Soils

For drained conditions, the computation of unit casing resistance is based on the usual formulation of friction and is given by:

$$r_c = \mu \cdot \sigma_n = \sigma_n \cdot \tan \delta \qquad \textbf{(2.18)}$$

where σ_n is the unit radial stress surrounding the external surface of the pipe. The behavior of soil-pipe interfaces varies as a function of surface roughness, normal stress, particle mineralogy and angularity, relative density, and moisture content. Iscimen (*2004*) performed direct shear tests on several pipe materials with two sand types, and under several normal stresses, to determine the interface strength as a function of relative shear displacement. Iscimen (*2004*) found that the peak and residual interface friction coefficient slightly decreased as a function of normal stress up to approximately 80 kPa, whereupon the interface friction coefficient remained relatively constant. A typical plot of Ottawa 20/30 sand against a Permalok® steel pipe is shown in Figure 2.16; a summary of the test results by Isicimen (*2004*) is given in Table 2.4.

Table 2.4: Summary of interface shear testing at a normal stress of 80 kPa and relative density of 80 % (adapted from Iscimen 2004).

Pipe Material	Average Roughness [μ m]	Coefficient of Friction, σ_n = 80 kPa			
		Ottawa 20/30 [$\phi' = 38.9^0$, $\phi_r' = 27.9^0$]		Atlanta Blasting [$\phi' = 43.1^0$, $\phi_r' = 34.6^0$]	
		Peak μ	Residual μ_r	Peak μ	Residual μ_r
Hobas	6.5	0.50	0.44	0.58	0.56
Polycrete	16.9	0.49	0.43	0.53	0.49
Permalok Steel	18.7	0.62	0.44	0.73	0.58

Wet Cast Concrete	24.8	0.65	0.48	0.76	0.59
Packerhead Concrete	55.1	0.73	0.53	0.86	0.62
Vitrified Clay	93.8	0.63	0.48	0.77	0.61

In the absence of test data, the interface friction coefficient may derived from the angle of friction of the soil (α'), and a reduction factor applied to α', typically ranging from ¼ α' to ¾ α'. Table 2.5 and Table 2.6 provide interface friction coefficients reported by Potyondy (*1961*) and NAVFAC (*1986*), respectively, for steel surfaces. Staheli (*2006*) recommends the use of the residual friction, α_r' in the determination of σ_n and the residual interface friction coefficient, μ_r, in conjunction with Eqns. (2.18).

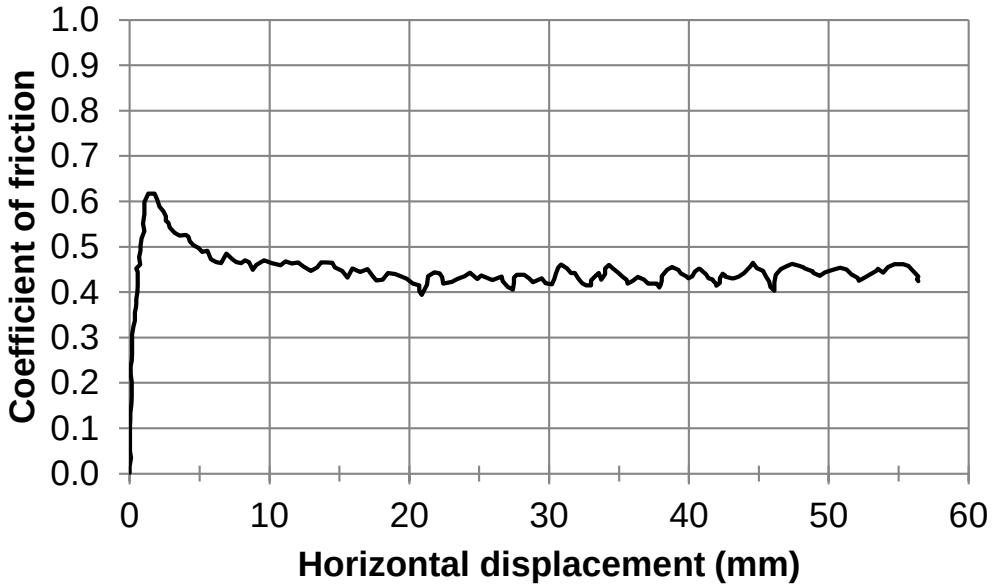

Figure 2.16: Frictional response at interface of steel pipe against Ottawa 20/30 sand at a normal stress of 80 kPa and a relative density of 80 % (*adapted from Iscimen 2004*).

Table 2.5: Pipe-soil interface friction coefficients, μ = tan δ reported by Potyondy (1961). Note, w = the natural moisture content.

Soil Type	Smooth Steel	Rough Steel
Dense dry sand	0.45	0.67
Dense saturated sand	0.43 to 0.46	-
Clay (w = 26.1 %)	0.11	0.10
Clay (w = 22.8 %)	0.16	0.18
Clay (w = 17.0 %)	0.13	0.18
Clay (w = 15.0 %)	0.15	0.23
Clay (w = 13.0 %)	0.18	0.33

Table 2.6: Pipe-soil interface friction coefficients, μ = tan δ reported in NAVFAC (1986).

Soil Type	Steel (sheet piling)
Clean gravel, gravel-sand mixtures, well-graded rockfill with spoils	0.40

Clean sand, silty sand-gravel mixtures, uniform hard rockfill	0.30
Silty sand, gravel or sand mixed with silt or clay	0.25
Fine sandy silt, non-plastic silt	0.20

2.3.3.3 Determination of Casing Resistance in Cohesive Soils

The computation of casing resistance for the rapid installation of culverts in cohesive soils is usually performed considering undrained conditions. Haslem (*1986*) studied the interaction of pipelines in cohesive soils and developed an adhesion model that applies the undrained shear strength, c_u, along the contact width, b, (Figure 2.17) of the pipe with the cavity. The contact width is determined using an elastic theory model developed by Roark and Young (*1976*). The unit casing resistance is given by:

$$r_c = \mathrm{A} \cdot c_u \qquad \textbf{(2.19)}$$

where A is the adhesion factor commonly used in pile design.

The total casing resistance in Figure 2.17 case can be determined using:

$$R_c = \sum_{\mathrm{i}=1}^{\mathrm{n}} r_{\mathrm{c,i}} \cdot b_{\mathrm{i}} \cdot \Delta \mathrm{L}_{\mathrm{i}} \qquad \textbf{(2.20)}$$

In practice, engineers develop and use empirical values of adhesion from years of experience on pipe jacking projects. The unit skin resistance, r_c, usually lies between 5 and 25 kPa. Typical values for the unit skin resistance are provided in Table 2.7 for different ground conditions (*Craig 1983*):

Table 2.7: Typical values of unit skin resistance/adhesion for cohesive soils (adapted from Craig 1983).

Soil type	Skin Resistance (kPa)
Boulder clay	5 to 18
Firm clay	5 to 20
Silt	5 to 20
Fill	up to 45

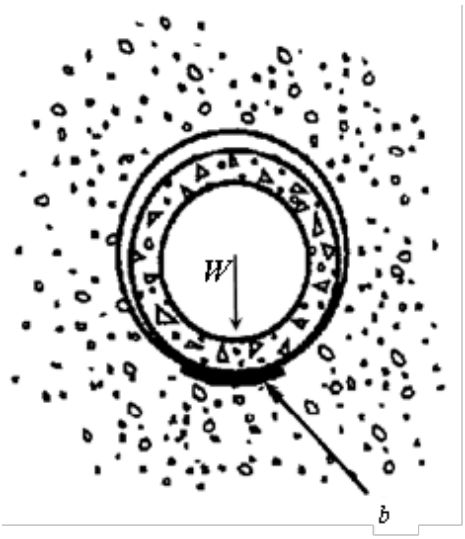

Figure 2.17: Haslem (1986) model for pipe-soil interaction in "stable" cohesive soil (after Marshall 1998).

2.3.3.4 Effect of Driving Interruption on Casing Resistance

Studies demonstrate that there is an increase in the jacking forces following pauses for nights and weekends. The jacking loads for a project in Champigny, France, provided in Figure 2.18, clearly show that much greater jacking force is required to mobilize the pipe when the jacking has stopped for a period of time. For example, an additional frictional stress of 2.4 kPa following 2.5 days of interruption, 2 kPa for daily interruption, and 0.8 kPa for short-length interruptions was required. The increase in jacking forces (i.e., $\Delta P = P_{\text{at start}} - P_{\text{last force before interruption}}$) is usually attributed to an increase in casing resistance, as the face resistance typically remains constant within uniform materials and overburden thicknesses. Pellet-Beaucour and Kastner (*2002*) identifies two phenomena that can result in an increase of the casing resistance during pauses as: (1) the surrounding soil may lie in full contact by flowing to the pipe, and (2) when the jacking force and lubricant supply ceases, the frictional forces will increase due to an increase in the effective stress following dissipation in positive excess pore water pressure. There is also a potential for the lubricant to change from a liquid state to a solid state which will increase the frictional resistance along the pipe. In cohesive soils, high adhesive resistances and potential for swelling may lead to an interruption or in extreme cases termination of the jacking operation. In such soils, jacking of pipes should take place with longer segments to avoid undue delay.

2.3.3.5 Effect of Cutting Shoes and Lubrication on Skin Resistance

Reducing the required ramming force during installation of culverts allows longer driving lengths, reduces installation times, and lessens potential damage to the culverts during installation. The reduction in ramming force can be achieved through the formation of a cavity such as that created by a cutting shoe. The cutting shoe may be described using an overbreak ratio (*Marshall 1998*):

$$OR = \frac{D_e - D}{D} \qquad \textbf{(2.21)}$$

where D_e is the excavated bore diameter and D is pipe diameter. In studies conducted at Loughborough University on 200 mm diameter pipes in dry granular soils with overbreak ratios varying from 0 to 0.14, it was observed that the optimum value was 0.04 (*as cited in Marshall 1998*). The ramming forces were observed to reduce with increasing overbreak ratio up to the optimum, however, the jacking forces significantly increased as the ratio approached to zero.

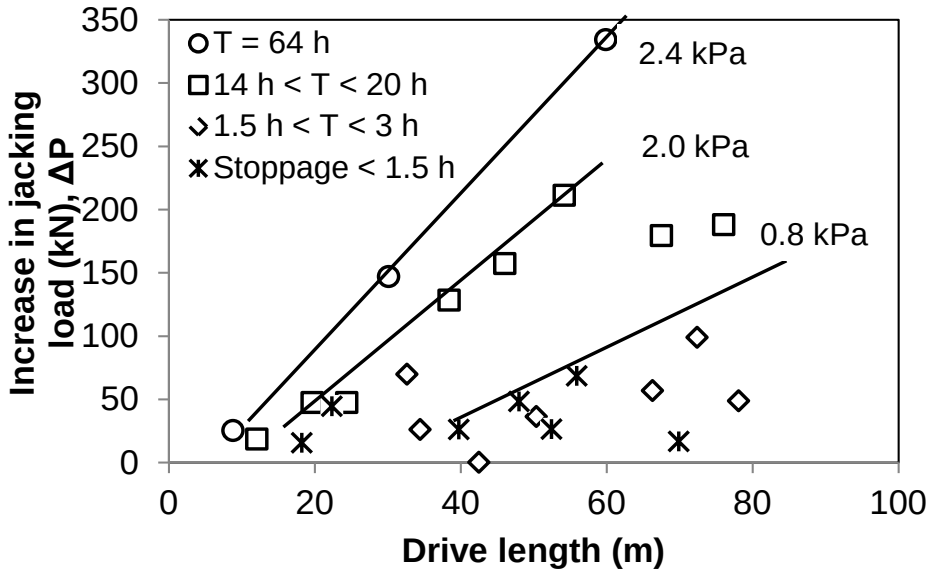

Figure 2.18: Progress of the total jacking force for a project in Champigny, France, showing increase of the jacking load after stoppages (*adopted from Pellet-Beaucour and Kastner 2002*).

Although the generated cavity may be stable (i.e, a stable "arch" develops resulting in reduced earth pressures), the stress relief and subsequent swelling of some soils may occur, such as overconsolidated and highly plastic clays, and result in high earth pressures and associated driving forces. Lubrication is used to decrease the driving forces by injection behind the overcut generated by a cutting shoe. The lubricant reduces the driving force by delaying the build-up of radial stress on the culvert, reducing the interface friction angle between the ground and the culvert, and achieving partial buoyancy of the culvert (*Borghi 2006*).

Injection of lubricant during the installation of culverts has been shown to decrease the jacking forces by up to 70 percent in both coarse-grained and fine-grained soils (*Bennett 1998, Milligan and Norris 1999, Marshall 2001*). Borghi (*2006*) summarized lessons learned in the field by studying the documentation of projects, quantifying the net effect of lubrication by comparing pipe jacking forces in lubricated and un-lubricated drives. The findings are summarized Figure 2.19 and demonstrate that the introduction of lubrication generally resulted in a significant decrease in the jacking force.

In addition to reducing the rate of jacking force increase, lubrication appears to reduce the total jacking force, suggesting that lubrication is effective over the entire length of the drive (*Borghi 2006*).

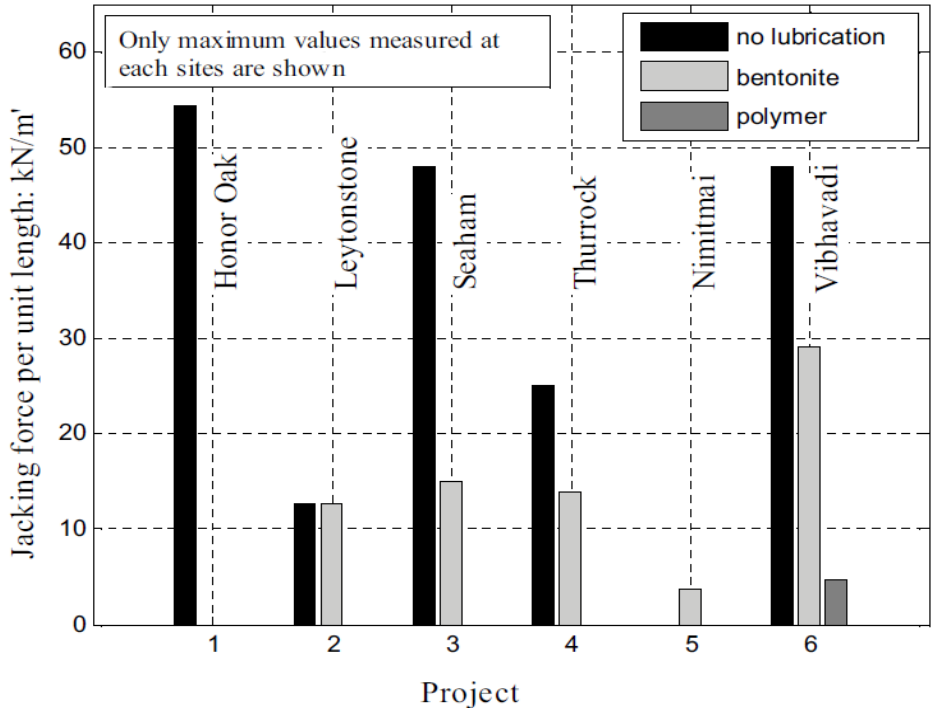

Figure 2.19: Summary of unit jacking forces in different projects (*after Borghi 2006*).

2.4 GROUND VIBRATIONS ASSOCIATED WITH PIPE RAMMING

Pipe ramming employs an impact hammer that induces stress waves within the pipe and results in the transfer of vibrations to the ground. Ground vibration can cause damage to buildings that can range from cosmetic cracks to serious structural cracks in the walls and floors, densification and settlement in sandy soils, and disturbance and annoyance to nearby people. The degree of vibration depends on the hammer type and hammer energy, the dynamic properties of the soil, and the distance between the source of energy and location of interest. During pipe ramming, the hammer imparts a compressive stress wave to the rear end of the pipe which travels to the leading edge of the pipe and partially reflects back after dissipating a portion of the energy due to material damping and soil resistance on the pipe. At the leading edge of the pipe, the stress wave propagates outward into the soil in the form of spherical P-waves, whereas along the pipe casing, it distributes outward in conical forms as polarized shear waves (S-waves) (*Massarch and Fellenius 2008*). The velocities of the compressive primary waves (i.e, P-waves, C_p) and shear secondary waves (i.e, S-waves, C_s) are controlled by the small strain elastic properties of the soil and can be derived based on three-dimensional equations of motions for an isotropic, linear, elastic solid, given by (*Kramer 1996*):

$$\rho \frac{\partial^2 u}{\partial t^2} = (\xi + \eta) \frac{\partial \bar{\varepsilon}}{\partial x} + \eta \cdot \nabla^2 u \qquad \textbf{(2.22)}$$

where u is the displacement in x-direction, ξ and η are Lamé's constants, ρ = the mass density, $\overline{\varepsilon} = \varepsilon_{xx} + \varepsilon_{yy} + \varepsilon_{zz}$ is volumetric strain and ∇^2 is the Laplace operator. Similar equations of motions can be stated for y- and z- directions. These equations can be manipulated to produce two equations for body waves (i.e. primary wave and secondary wave) that travel through an unbounded solid. The characteristic wave velocities are:

$$C_p = \sqrt{\frac{\xi + 2\eta}{\rho}} = \sqrt{\frac{E(1-\nu)}{\rho(1+\nu)(1-2\nu)}} \quad \textbf{(2.23)}$$

$$C_s = \sqrt{\frac{\eta}{\rho}} = \sqrt{\frac{G}{\rho}} = \sqrt{\frac{E}{2(1+\nu)\rho}} \quad \textbf{(2.24)}$$

where G is elastic shear modulus, and ν is Poisson's ratio.

Typical values for P- and S-waves can also be estimated from site-specific in-situ tests, such as down-hole or multi-channel analysis of surface wave (MASW) tests, which are recommended for projects where critical infrastructure may be impacted by ground vibration. Ranges of the P- and S-wave velocities at small strains are given in Table 2.8 for different soil types.

When P- and S-waves encounter the ground surface, part of their energy is reflected back into the ground, whereas the remainder convert to surface waves that consist of Rayleigh waves (R-waves), and in some limited cases, Love waves (L-waves) (*Kramer 1996*). These pipe ramming-induced vibrations attenuate with distance at a rate that depends on the energy delivered to the pipe, pipe geometry, and the ground conditions and geometry. The decay of the vibration amplitude at some distance can be attributed to radiation (geometric) damping and material damping (*Kim and Lee 2000*) and estimated using:

$$v_2 = v_1 \left(\frac{r_1}{r_2} \right)^{\beta} e^{-\alpha(r_2 - r_1)} \quad \textbf{(2.25)}$$

where v_1 and v_2 are peak particle velocities at distances of r_1 and r_2 respectively, and β and α are attenuation coefficients due to geometric and material damping, respectively (see Table 2.9 and Table 2.10). The results of the decay equation are depicted on Figure 2.20 for β = 0.5, r_1 = 10 m and various α values considered. The attenuation coefficient, α, varies with vibration frequency and wave propagation velocity and can be computing using: (*Massarsch 1992*):

$$\alpha = \frac{2\pi f \zeta}{c} \quad \textbf{(2.26)}$$

where ζ = the damping ratio of the soil , c = ground surface wave velocity and f = the frequency of vibration.

Table 2.8: Range of P- and S-wave velocities at small strains for different soil type (*adapted from Massarch and Fellenius 2008*).

Soil Type	P-wave Velocity (m/s)	S-wave Velocity (m/s)
Dry gravel	500-1000	250-400
Saturated gravel	1450	300-400
Dry sand	300-600	150-200
Saturated sand	1450	150-250
Silts and stiff clays	1450	100-200
Plastic clay	1450	50-100
Organic soils	1450	30-50

Table 2.9: Coefficient of radiation damping (*adapted from Kim and Lee 2000*).

Source location	Source type	Wave induces	β
Surface	Point	Body wave	2.0
		Surface wave	0.5
	Infinite line	Body wave	1.0
		Surface wave	0.0
At-depth	Point	Body wave	1.0
	Infinite line	Surface wave	0.5

Table 2.10: Classification of earth material by attenuation coefficient (*adapted from Woods 1997*).

Class	Material damping coefficient , α (1/m)		Description of material
	5 Hz	50 Hz	
I	0.01-0.03	0.1-0.3	Weak or soft soils (N_{SPT}<5)
II	0.003-0.01	0.03-0.1	Competent soils (5 < N_{SPT} < 15)
III	0.0003-0.003	0.003-0.03	Hard soils(15 < N_{SPT} < 50)
IV	<0.0003	<0.003	Hard competent rock (N_{SPT} > 50)

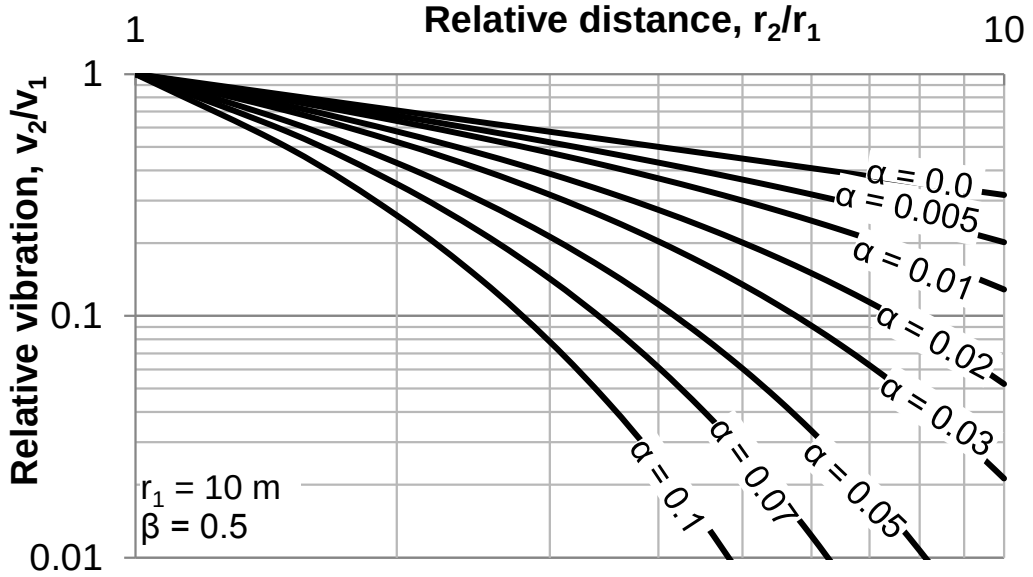

Figure 2.20: Attenuation of surface waves (β = 0.5, r_1 = 10 m) (*adopted from Massarch and Fellenius 2008*).

In another attempt to model the attenuation, a simplified version of the vibration attenuation model (pseudo-attenuation) was formulated by Wiss (*1981*) based on field observations of vibrations due to pile driving. The power law model relates the pile driving hammer energy, *E*, and radial distance, *r*, between the source of the energy and a location of interest to vibration by:

$$v = K_d \left[\frac{r}{\sqrt{E}} \right]^{-n} \qquad \textbf{(2.27)}$$

where K_d = intercept value of vibration amplitude at "scaled-distance" $r/\sqrt{E} = 1$ and n = attenuation rate. Woods and Jedele (*1985*) collected vibration data from different construction projects and developed vibration versus scaled distance chart based on Wiss (*1981*) model for various ground types as shown on Figure 2.21. The ground type is defined by the *n*- term of Wiss model and the sloping lines with n = 1.5 and n = 1.1 represent the Class II and Class III soils from Table 2.10.

In an effort to reduce structural damage, the U.S. Bureau of Mines (USBM) and the Office of Surface Mining (OSM) developed "safe" vibration criteria for residential structures based on frequency content and peak particle velocity. The safe vibration criteria use the peak vector sum (PVS) velocity, which is a vector sum of the peak particle velocities in the longitudinal, vertical, and transverse directions and the dominant frequency at the maximum particle velocity. Figure 2.22 shows the thresholds lines for corresponding to the USBM and OSM criteria. Note that the charts indicate that the potential for damage due to low-frequency vibrations (<10 Hz) is considerably higher than those of high-frequency vibrations (>30 Hz) and thus a lower threshold PVS should be adopted if the frequency of the vibrations is low.

Little, if any, field observations of the ground vibrations due to pipe ramming have been conducted and reported; the authors were unable to identify a case history in the literature. Simicevic and Sterling (*2001b*) suggest that ground vibrations due to pipe ramming could be compared to pneumatic pipe bursting due to the similarity of the equipment operation (e.g., blow

rate between 180 and 580 bpm). The ground vibration study performed by Atalah (*1998*) demonstrated that vibrations due to pipe bursting ranges between 30 and 100 Hz (Figure 2.23), which substantially exceeds the natural frequency of typical buildings (5 to 11 Hz) (*Simicevic and Sterling 2001b*). Simicevic and Sterling (*2001b*) suggest that buried structures are less susceptible to vibration damage compared to surface structures, and the threshold soil particle velocity of 130 mm/sec is considered to be the acceptable tolerance. However, vibrations of this amplitude are rarely accepted by owners or their representatives; rather, 25 mm/sec is considered the typical allowable limit. Simicevic and Sterling (*2001b*) stated that the vibrations from pipe bursting operations for 150 to 380 mm (6 to 15 in) diameter pipes conducted by Atalah (*1998*) are not likely to create problems unless the structures are located at very close distances (Figure 2.23).

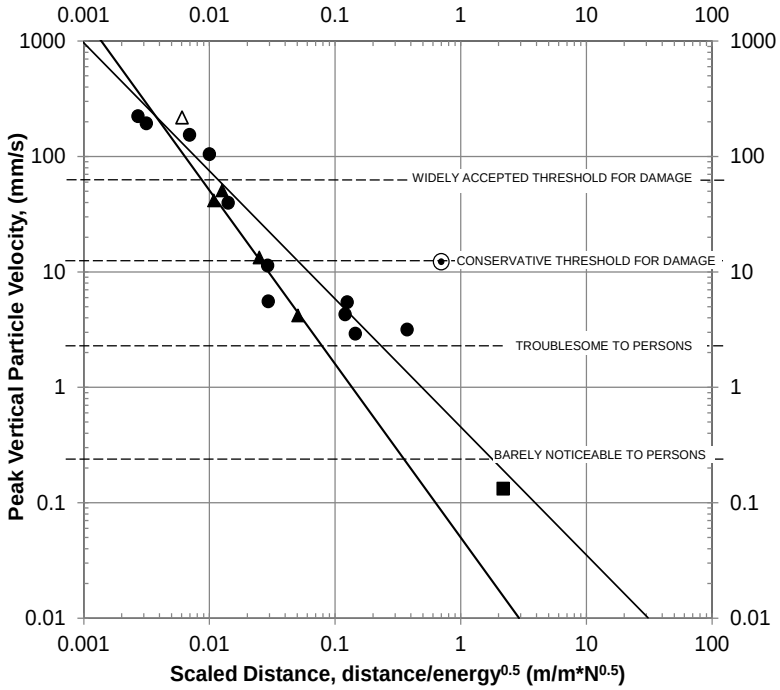

Figure 2.21: Peak vertical particle velocity versus scaled distance (*adopted from Woods 1997*).

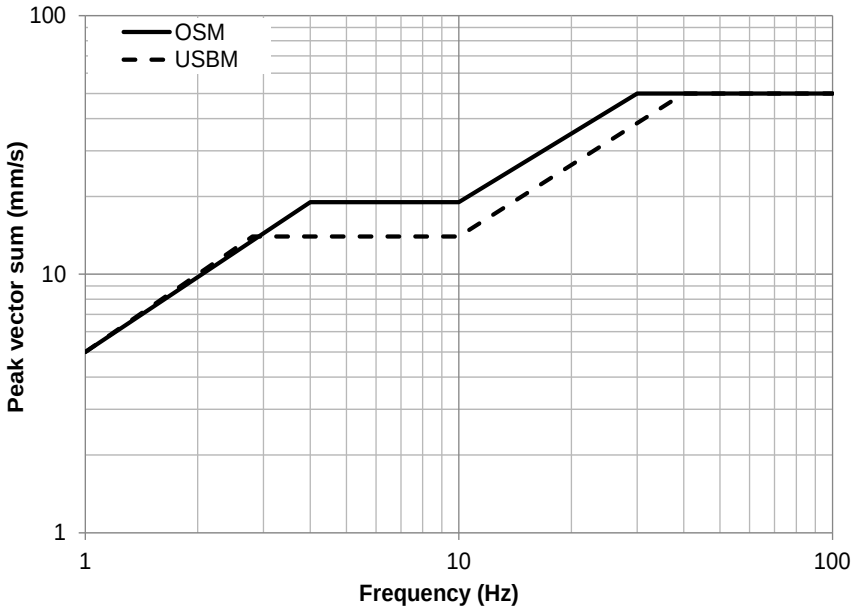

Figure 2.22: Safe vibration criteria based the USBM and OSM criteria.

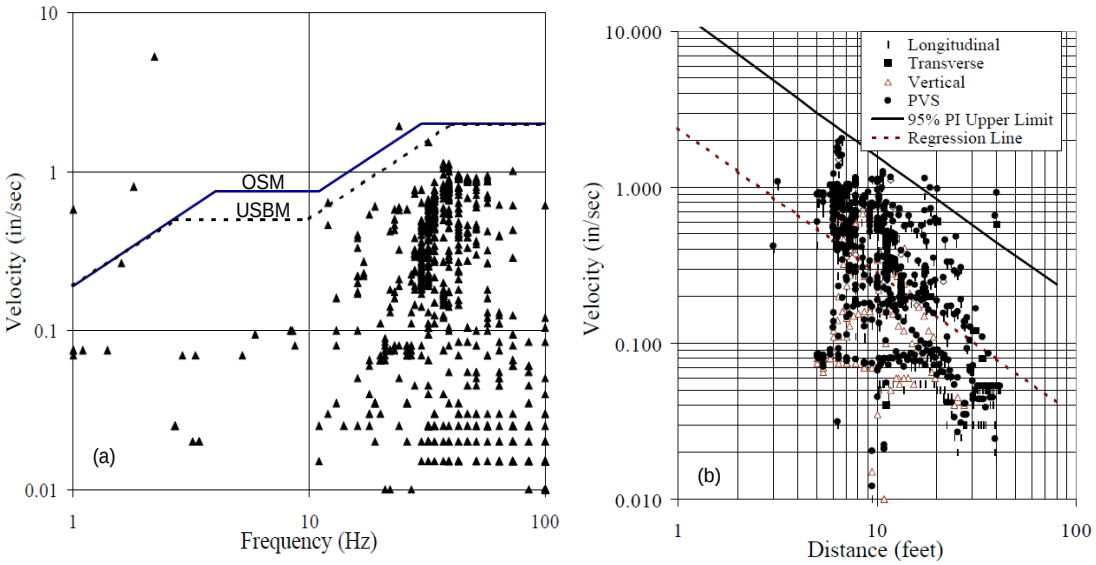

Figure 2.23: Ground vibrations associated with pipe bursting: (a) peak particle velocity versus frequency plot for pneumatic pipe bursting, and (b) velocity versus distance from the bursting head (*after Atalah 1998*).

2.5 GROUND DEFORMATIONS ASSOCIATED WITH CULVERT INSTALLATION

Analysis of the ground deformations associated with the installation of pipes and other underground conduits, particularly in urban areas or in proximity to adjacent structures where soil movement can induce structural damage in buildings, roadway pavements, railways, and buried structures, is critical for designers planning new construction. The nature and magnitude of soil displacement due to a new installation depends on the soil characteristics, groundwater conditions, depth and size of the culvert, and the construction technique (*Leca and New 2007*).

Soil deformation generally occurs due to a change in the position of soil particles resulting from shearing and volumetric strains imposed by the pipe; thus, the ground deformation during pipe ramming is a complex three-dimensional problem (Figure 2.24). Although displacement at the ground surface is typically perceived to be minimal for pipe ramming installations, some ground deformation is inevitable due to the collapse of the overcut and displacement of the soil by the cutting shoe. The magnitude of soil displacement must be kept within tolerable limits to avoid potential damage to existing adjacent buildings, structures, and utilities. Thus, understanding the nature and magnitude of ground deformations due to pipe ramming operations is important. The magnitude of ground deformation can be modeled using empirical, analytical, or numerical methods. The empirical approach proposed by Schmidt (*1969*) and Peck (*1969*) is commonly used to estimate the magnitude and extent of settlement resulting from tunneling. This method assumes that the shape of the transverse settlement profile immediately behind the advancing pipe follows an inverted normal probability distribution curve and symmetrical about the vertical axis normal to the longitudinal centerline through the pipe. The ground displacement due to a radial flow of material toward the culvert can be represented by (*Peck 1969*):

$$S_z(y) = S_{\max} e^{-\frac{y^2}{2i^2}} \tag{2.28}$$

where $S_z(y)$ is the vertical settlement at a distance y from the center line, S_{max} is the maximum centerline settlement, and i is the horizontal distance from the pipe axis to the inflection of the settlement trough (Figure 2.25). The maximum settlement S_{max} can be obtained by equating the total volume of settlement trough and the ground loss due to the over-cut, V_s:

$$V_s = \frac{\pi}{4}\left[D_c^2 - D^2\right] = \int_{-\infty}^{\infty} S_z(y)\, dy = \sqrt{2\pi} \cdot i \cdot S_{\max} \tag{2.29}$$

$$S_{\max} = \frac{V_s}{i\sqrt{2\pi}} \tag{2.30}$$

where V_s = volume of soil loss per unit of length, D_c = external diameter of the cutting shoe or excavated bore and D = external diameter of the pipe. The distance from the pipe axis to the inflection of the settlement trough, i, has been subject to many investigations. Peck (*1969*) suggested that the width of the settlement trough (i) can be described as function of the depth of the pipe below the ground surface (z_0) and diameter of the pipe (D) depending on ground conditions as described in Figure 2.26. Peck (*1969*) compiled data from field observations and fitted a trend line after categorizing them based on their soil types.

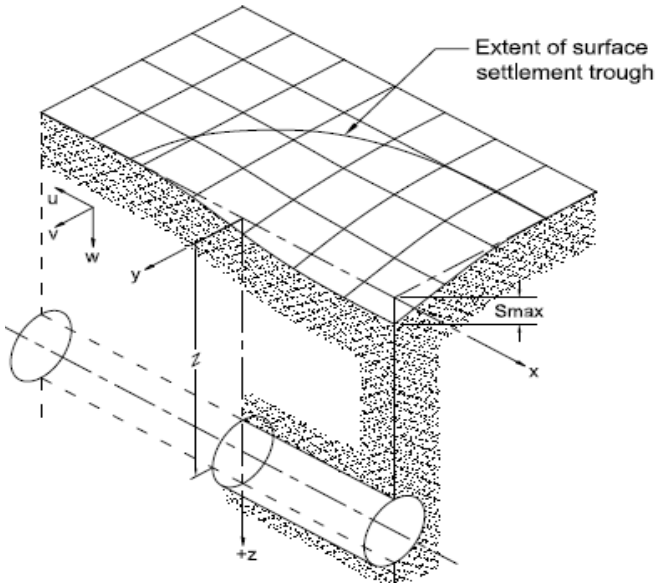

Figure 2.24: Conceptual sketch of 3-D settlement during pipe jacking (*adopted from Attewell 1988*).

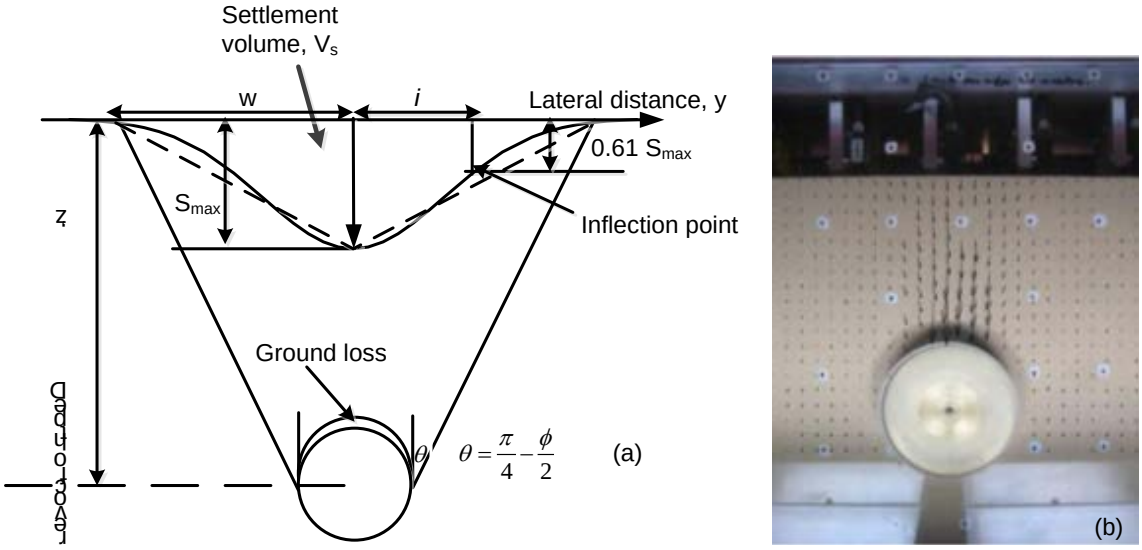

Figure 2.25: Settlement behavior due to pipe jacking and microtunneling a) idealized transverse settlement trough (b) centrifuge modeling result that shows displacement vectors (*after Farrell 2011*).

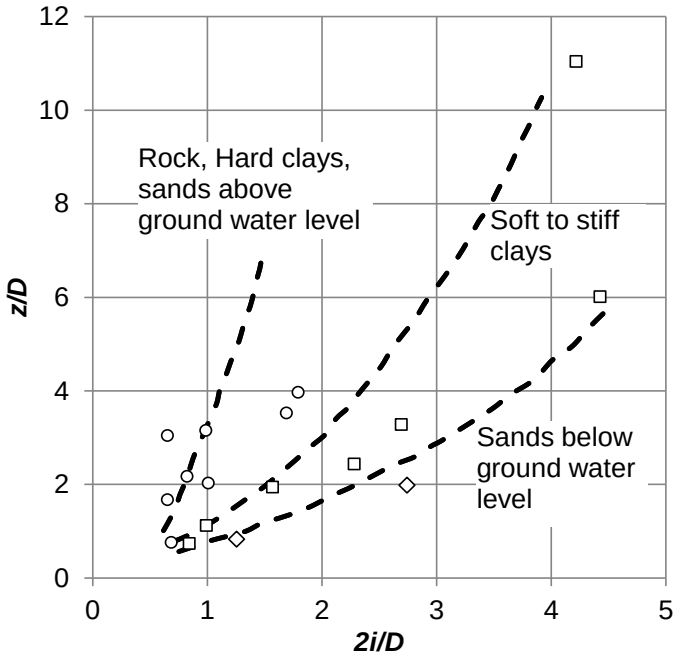

Figure 2.26: Relation between settlement trough width and tunnel depth for different grounds (*adopted from Peck 1969*).

Cording and Hansmire (*1975*) developed similar relationships by approximating the volume per unit length under inverted normal probability distribution curve with a triangular area:

$$V_s = \frac{1}{2} \cdot 2w \cdot S_{\max} \Rightarrow S_{\max} = \frac{V_s}{w} \qquad \textbf{(2.31)}$$

where w = the half-width of the settlement trough, as shown in Figure 2.25a. Cording and Hansmire (*1975*) formulated a relation between w and depth through a vertical angle, $\theta = 45\text{-}\frac{\phi}{2}$, which is given by:

$$w \approx 2.5i = \frac{D_c}{2} + z \cdot \tan\left(\frac{\pi}{4} - \frac{\phi}{2}\right) \qquad \textbf{(2.32)}$$

In general, the Cording and Hansmire (*1975*) models were observed to overestimate the settlement in tunneling by factor of 2.0 even in cases where only half-volume of the overcut is considered for settlement analysis (*K. Staheli, personal communication, 2013*).

O'Reilly and New (*1982*) generated another relationship for the width of the settlement trough as a function of the depth of the pipe. The method developed by O'Reilly and New (*1982*) was based on multiple linear regression on field data representative of cohesive and cohesionless soil; the results indicated that the width of the settlement trough could be modeled using $i = 0.28z_0 - 0.12$ for non-cohesive soils and $i = 0.43z_0 + 1.1$ for cohesive soils, where z_0 is the depth of cover to the center of the pipe in meters. For all practical purposes, the regression equations can be simplified to the form $i = p\ z_0$ where p is a trough width parameter ranging 0.25 to 0.45 for sandy

soils and 0.4 to 0.6 in clays (*Mair and Taylor 1997*). Generally the settlement risk associated with pipe ramming can be potentially high in loose or soft ground conditions since the soils are vibrated and disturbed during the ramming process.

Heave is also another possible ground deformation risk associated with pipe ramming because of the soil displaced by the casing and face of the cutting shoe. The modeling of heave can also be based on the empirical normal probability distribution curve with the peak of the curve directly above the centerline of the pipe crown (*Bennett and Wallin 2010*). Therefore, the normal probability distribution curve project upward for heave estimation unlike the inverted shape used to estimate settlement. Bennett and Wallin (*2010*) modified the Cording and Hansmire (*1975*) approach for heave by approximating the volume of the heave surface per unit length under the normal probability distribution curve with a triangular area:

$$V_{surface} = \frac{1}{2} \cdot 2w \cdot h_{\max} \Rightarrow h_{\max} = \frac{V_{surface}}{w} \quad \textbf{(2.33)}$$

where w = the half-width of the heave, as shown in Figure 2.27. Bennett and Wallin (*2010*) assume the volume of the heave surface projected upward to be two-thirds of volume of the cutting shoe. The width, w, is related to depth of cover through a vertical angle, $\theta = 45 + \phi/2$, which is given by:

$$w \approx 2.5i = \frac{D_c}{2} + z \cdot \tan\left(\frac{\pi}{4} + \frac{\phi}{2}\right) \quad \textbf{(2.34)}$$

The heave due to the soil displaced t can be represented by Bennett and Wallin (*2010*):

$$h_z(y) = h_{\max} e^{-\frac{y^2}{2i^2}} \quad \textbf{(2.35)}$$

where $h_z(y)$ is the vertical heave at a distance y from the center line, h_{max} is the maximum centerline heave.

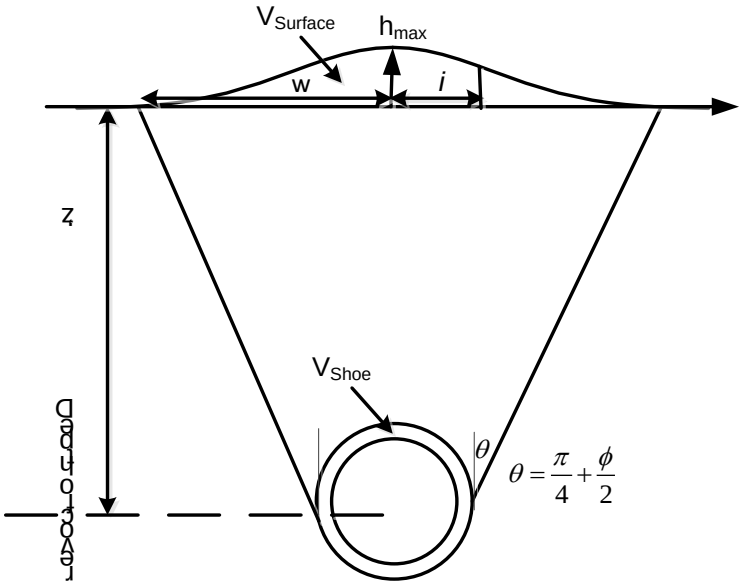

Figure 2.27: Idealized heave in transversal direction (*adopted from Bennett and Wallin 2010*).

2.6 CASE HISTORIES

2.6.1 Introduction

Pipe ramming has been successfully performed and adopted as a viable alternative for culvert installations. The information reviewed indicates that countries other than the United States, such as England and Germany, have used pipe ramming for a longer duration, and have performed more research and design development. The case histories reviewed for this report focused on projects completed in or around the United States. Projects using pipe ramming were evaluated by assessment of the following:

- Pipe hammer type, size, and energy;
- Culvert or pipe type and size;
- Cutting shoe used;
- Lubrication system;
- Soil type;
- Groundwater conditions; and,
- Pertinent data presented and conclusions determined.

In addition to providing an understanding of the equipment and operations necessary to perform a successful ramming installation, the case histories help to shed light on the engineering aspects of a pipe ramming operation including ground deformations, resistance to culvert penetration, efficacy of cutting shoes or lubrication, and efficiency over other trenchless or open-cut methods.

2.6.2 Overview of Reported Case Histories

Eleven case histories, reported from 2003 through 2009, were reviewed for this study and are summarized in Table 2.11. The case histories typically cited the selection of pipe ramming as

the trenchless technology of choice due to the presence of favorable soil conditions, schedule, limited surface disruption (i.e., traffic delays and surface deformations), and lower costs. In general, two case histories cited the use of hydraulic pipe hammers, whereas the remainder employed pneumatic hammers. Although the manufacturer of the hammers was not always reported, the type and size was usually given. The soils encountered ranged from boulders as large as 0.92 to 1.22 m (3 to 4 ft) (*Zubko 2003a*) to San Francisco Bay Mud (*Orton 2007b*) with both stable and unstable conditions. Ramming appeared to be more widely used in soils that are medium dense to very dense, although the lack of a front-heavy TBM is one advantage of pipe ramming in soft and weak cohesive soils. Lubrication was used for pipe ramming in clay deposits (*Najafi et al. 2004, Orton 2007b*). Open-ended ramming was selected for most applications due to either unstable soil conditions or the presence of boulders. The use of an open end also appears to be preferred for large diameter pipe installations, due to the reduced face resistance. Although it appears that pneumatic hammers are more common, hydraulic pipe hammers appear to be more efficient, cost effective, and powerful when the proposed culvert alignment is long, and the diameter is larger (*Zubko 2003a*). The benefits of a high rate of culvert installation and reduced support equipment are noted in many case histories.

2.6.3 Discussion of Selected Case Histories

2.6.3.1 Skykomish, WA (Schrank et al. 2009)

A utilidor was proposed to convey potentially contaminated groundwater beneath three active rail lines in Skykomish, Washington, to a Hydraulic Control and Containment System at a former fueling and storage station for the Burlington Northern-Santa Fe (BNSF) company. The project called for a 27 m (90 ft) long, 0.91 m (36 in) diameter steel casing to carry a gravity water line, a pressure water line, a compressed air line, a power conduit, and a signal line beneath the railways. Soil conditions consisted of 1.5 m (5 ft) thick fill containing loose to medium dense silty sand with a variable amount of organic matter and construction debris. Below the fill, the native soil consisted of sand, gravel, cobbles, and boulders with intermittent lenses of silt and clay. Although the depth of the water table was not explicitly stated, Schrank et al. (*2009*) report that the level was shallow, fluctuating seasonally with the adjacent Skykomish River.

The main concern of project engineers was the potential settlement or heave due to the pipe installation. Since the rail lines are a major artery for BNSF, detour of, or damage to the lines due to construction was ruled out. Other concerns were the presence of contaminants above the water table and unstable soil conditions. The potential for contaminated granular soils to mix with the water table was considered in the selection of the installation method. A pneumatic hammer was chosen to drive the pipe. To mitigate the potential for obstructions (e.g., construction debris, boulders), the leading pipe was fitted with a rock shoe to assist in the breaking of cobbles and boulders. The owner of the rail line required movements of the track to remain below 6 mm (0.25 in). The tracks were required to be surveyed every two hours, with measurements logged into a daily report for the railroad company and project engineers.

The installation advanced at an average rate of 0.3 m (1 ft) per 2.5 minutes. On the first day of installation the settlement reached 8 mm (0.3 in), exceeding the maximum

tolerance. With careful inspection of the settlement monitoring, the measurements were attributed to thermal expansion and contraction of the tracks. After the first day of installation, the settlement remained below 6 mm. Ramming continued and was completed with no major obstructions encountered or contamination of groundwater. After the evaluation of other trenchless methods, pipe ramming proved effective due the generation of little to no settlement and the ability to swallow spoils that potentially included boulders.

2.6.3.2 Whidbey Island, WA (Wetter et al. 2009)

The Saratoga Road Culvert Replacement project required the replacement of a damaged 0.46 m (18 in) concrete culvert beneath Saratoga Road on Whidbey Island, Washington. The length of the 1.37 m (54 in) diameter steel case was 51.8 m (170 ft), with the depth of cover for the proposed alignment ranging from 10.7 to 12.2 m (35 to 40 ft). The site characterization indicated 35 feet of embankment fill consisting of a 7.62 m (25 ft) thick layer of loose sand over 3.05 m (10 ft) thick layer of medium dense, silty sand. The soils below the fill materials were comprised of 2.7 m (9 ft) of extremely stiff; mottled, laminated silt over very dense sand. Perched groundwater was present at the interface of the silty sand fill and laminated silt. Reports also showed a possibility of old wood pilings from a historic bridge in the fill within the proposed alignment. The trenchless method selected by the contractor for the project was static pipe jacking and auger boring. After approximately 30 m (100 ft) of pipe jacking, soil and groundwater began to flow into the casing, resulting in the formation of a sinkhole on the shoulder of the Saratoga Road. The project was terminated, and the large casing abandoned.

Table 2.11: Summary of pipe ramming case histories.

Case No.	Reference	Location	Hammer Type and Size	Cutting Shoe and Lubrication	Culvert Size	Soils	Water table depth	Data/Findings
1	Schill (*2003*)	Aurora, IL	Pneumatic Grundoram Gigant; 254 mm (10 in) diameter	Specially designed shoe used, Size unknown, bentonite lubrication	305 mm (12 in) diameter; 1 @ 36.6 m (120 ft), 2 @ 19.8 m (65 ft)	glacial till with boulders	N/A	No data presented; duration of installation ranged from 30 to 60 min
2	Zubko (*2003a*)	Perham Creek, OR	Pneumatic 457 mm (18 in), Pneumatic 610 mm (24 in), Pneumatic 813 mm (32 in), and Hydraulic SCCI-280	External and internal cutting shoe, size unknown	3.66 m (12') diameter; 68.6 m (225')	Mixed soils including boulders	Near the ground surface, dewatering required for construction	Dynamic measurements available through ODOT, information to be developed
3	Zubko (*2003b*)	Gold Beach, OR	Hydraulic SCCI; size unknown	Unknown	3.05 m (10') diameter; 60.1 m (197')	Unknown	Near the ground surface, dewatering required for construction	Steered ramming, accomplished design alignment within 6 mm horizontal, 130 mm vertical
4	Najafi et al. (*2004*)	Columbia, MO	Pneumatic; size unknown	Bentonite used for lubrication, cutting shoe information unknown	607 mm (24 in) diameter; 9.5 mm (0.375 in) wall thickness; 30.5 m (100 ft)	Hard clay (CH)	N/A	No data presented; concluded no settlement issues on test survey points to date

Case No.	Reference	Location	Hammer Type and Size	Cutting Shoe and Lubrication	Culvert Size	Soils	Water table depth	Data/Findings
5	Jensen et al (*2007*)	Ramsey, MN	Grundoram Taurus pneumatic; size unknown	N/A	2 @ 1981 mm (78 in) diameter, 1 @ 2184 mm (86 in); 15.2 m (50 ft)	Loose to medium dense alluvium (SP-SM & SP)	2.13 m (7 ft) to 3.66 m (12 ft) below ground surface	Pre-construction settlement estimates and measurements presented; measurements less than predicted.
6	Orton (*2007a*)	Northern CA & NV	Pneumatic; 610 mm (24 in) diameter	N/A	1219 mm (48 in), 1524 mm (60 in)	Cobbles and boulders	N/A	No data presented
7	Orton (*2007b*)	San Francisco, CA	Pipe bursting equipment package, included a 610mm (24 in) Taurus Pipe Bursting tool with a 1066.8mm (42 in) Rear Expander , an 18-inch Goliath Ramming tool to push the column of pipe	Bentonite lubrication 500 gallon Grundomudd system to provide polymer for lubrication of the new pipe during bursting operations	914 mm (36 in) diameter HDPE pipe; 128 m (420 ft)	San Francisco Bay Mud (ML/CL - MH/CH)	High ground water conditions	No data presented
8	Goodman and Cluett (*2009*)	Rocky Mountain Region, AB, Canada	Hammerhead pnuematic, 610 mm (24 in) diameter	N/A	1067 mm (42 in) diameter; 30 @ 60 m (197 ft)	Cobbles	N/A	No data presented
9	Wetter et al (*2009*)	Whidbey Island, WA	Grundoram Koloss pneumatic, 350 mm (14 in) diameter	cutting shoe used, size unknown	762 mm (30 in) diameter; 14 mm (0.56 in) wall thickness; 21.3 m (170 ft)	Fill: Loose sand (SP) and medium dense silty fine sand (SM)	Unknown, level rose to invert during construction	No data presented; good description of ramming performance with two obstacle/obstruction

Case No.	Reference	Location	Hammer Type and Size	Cutting Shoe and Lubrication	Culvert Size	Soils	Water table depth	Data/Findings
10	Currey et al (*2009*)	Ajax, ON, Canada	Hammer Head pneumatic, 610 mm (24 in) diameter	Hardened steel, inward beveled cutting shoe	1050 mm (41.3 in); 15.7 mm (0.62 in) wall thickness; 60 m (197 ft)	Glacial till	N/A	No data presented
11	Schrank et al (*2009*)	Skykomish, WA	Pneumatic, size unknown	Rock cutting shoe used, size unknown	914 mm (36 in) diameter; 27.4 m (90 ft)	Alluvium: sand, gravel, cobbles , and boulders, w/ shallow discontinuous lenses of silt and clay	Near the ground surface	Settlements less than 6 mm (0.25 in) during installation.

The project was reassessed months following termination of the project. The two options included pipe ramming of the existing 1.37 m culvert and pipe ramming of a smaller, 0.76 m (30 in) steel pipe, determined to adequately carry the required flows following new hydraulic studies. Because the wall thickness of the larger pipe was 13 mm (0.5 in), the ability of the pipe to withstand the ramming forces required to remobilize the pipe months after the initial ground instability was uncertain. The decision was made to install the smaller culvert, fitted with a cutting shoe, through the existing larger culvert and ram the culvert the remaining 21.3 m (70 ft).

The new pipe was installed using a Grundoram Kolass manufactured by TT Technologies, with a percussive impact force rated to 4300 kN (nearly three times that anticipated to complete the installation). However, the initial rate of installation through the existing casing appeared abnormally slow; the low production rate appeared to be the result of vibration along the unsupported length of the smaller casing within the larger casing, where under normal conditions, the pipe would be supported along the entire circumference by soil. The vibrations were mitigated by placing the bucket of an excavator on the crown of the pipe. Forward advancement of the pipe subsequently increased to 25 mm/min (1 in/min) from the initial rate of less than 13 mm/min (0.5 in/min). Ramming was halted again by an unknown obstruction presumed to be the old wood pilings inside the fill area. Ramming failed to advance the pipe for over an hour until the pipe suddenly rotated 45 degrees. Thereafter the rate of advance increased up to 200 mm/min (8 in/min) until breakout. Examination of the spoil indicated numerous splintered wood fragments, and one large piece of wood 5.8 m (19 ft) long and 0.76 m (30 in) in diameter along with severed steel cables. Thus, pipe ramming was able to overcome potentially unstable soil conditions and significant obstructions.

2.7 SUMMARY OF LITERATURE REVIEW AND IDENTIFICATION OF KNOWLEDGE GAPS

This chapter reviewed the pertinent literature available regarding pipe ramming and, where applicable, related technologies. An overview of various trenchless technologies with focus on pipe ramming was addressed along with brief review of the open-cut method. The state of practice of pipe ramming technology was discussed by introducing the procedures and considerations for the pipe ramming technique. Different methods to estimate the governing mechanics associated with pipe ramming were described in the context of existing techniques that were developed for pipe jacking, and microtunneling. Methods to estimate the total soil resistance to ramming can be derived from traditional pipe jacking methods. The total soil resistance comprises the combination of the static and dynamic face and casing resistances. Empirical approaches for the prediction of ground deformations and ground vibrations were described in the context of tunneling and pipe bursting techniques. Finally, two case histories on pipe ramming installations reported in the literature were presented.

The review of the literature above shows that very little research has been performed in area of pipe ramming. The literature review identified the following knowledge gaps should be addressed to improve our understanding of pipe ramming installations:

- *Paucity of datasets.* It appears that there are very few case histories of pipe ramming installations where datasets associated with the governing mechanics are presented. No measurements of soil resistance to ramming and ground vibrations are documented other than those reported by Stuedlein and Meskele (*2012*). The deficiency of data sets related to soil resistance, driving stress, energy transfer, ground deformation, and ground vibration should be addressed since development of models to estimate these variables are predominantly dependent on actual installation databases.
- *There are no reliable methods to estimate ground deformation and ground vibrations for pipe ramming installations.* Methods currently exist to estimate ground deformation and ground vibration for tunneling and pile driving respectively. However, these methods have not been evaluated for suitability in pipe ramming applications. Thus existing methods should be verified and/or new methods should be developed based on actual installation databases.
- *There are no existing data published regarding the mechanics of dynamic pipe ramming installations, including the evaluation of the energy transfer to the pipe, the magnitude of compressive stresses, and the total soil resistance to ramming.* The dynamic response of rammed pipes can be evaluated using the basic theory of the pile driving dynamics, which is based on one-dimensional wave propagation theory.
- *There are no pipe ramming-specific models available for the estimation of the static soil resistance to ramming*. Methods currently exist to estimate face and casing resistance for pipe jacking and microtunneling, but these methods have not been evaluated for suitability in pipe ramming applications.
- *There is presently no existing framework for the evaluation of pipe drivability analyses for the assessment of project feasibility*. Ideally, a methodology should exist that allows owners, engineers, and contractors to select the optimal hammer for the installation of a given pipe in given subsurface conditions.

3 OBSERVATION SITES AND CASE HISTORIES

Field observations form the basis for the understanding of pipe ramming mechanics in this study. Performance data from five production installations (termed case histories) were collected to develop a database of pipe ramming behavior. In addition, a full scale experiment that included a subsurface investigation, laboratory testing, field instrumentation, and monitoring of performance was carried out to strengthen the database and address knowledge gaps. The details of field observations and data collected are presented in this chapter.

3.1 PRODUCTION INSTALLATIONS

3.1.1 Case 1: Pressurized water pipe Installation, Wildish Sand and Gravel Co. Site, Eugene, Oregon

Case 1 was developed at the Eugene, Oregon, quarry of the Wildish Sand and Gravel Co. in June 2010 (Figure 3.1). The site is characterized as a broad alluvial plain resulting from the continual filling of the Willamette valley lowlands with sediment from the flanking mountain ranges of Oregon Cascades (*O'Connor et al. 2001*). The Wildish Sand and Gravel Co. mines the high-grade alluvial deposits in the region to produce sand and gravel aggregates. The new pipe installation was required to upgrade the pressurized water supply used in the quarrying, crushing, and screening operations at the company's quarry. The pipe installation crossed below a two-tier embankment that supported an access road and powered conveyer belt used to transport aggregate (Figure 3.2). Pipe ramming was selected by the contractor for the pipe installation to avoid the loss of income resulting from the temporary closure of the road and disruption of the conveying operations.

The project called for the installation of an open-ended steel pipe of 610 mm diameter, 13 mm wall thickness, and 33.5 m in length. The installation was carried out using three pipe segments with lengths of 12.2 m, 9.1 m, and 12.2 m, driven respectively in three stages. The installation commenced with the placement of a leveled 0.3-m-thick compacted crushed rock bedding layer in the launching area on the west side of the embankment (Figure 3.2a). Due to the topography adjacent to the embankment, excavation of insertion or receiving pits was not required. Steel tracks approximately 20 m long and typically used with auger boring operations were placed on the leveled ground to help guide the hammer-pipe system and maintain the required grade and alignment during the installation (Figure 3.2a). In the first stage of installation, the 12.2 m pipe segment was driven with a welded cutting shoe at the leading edge.

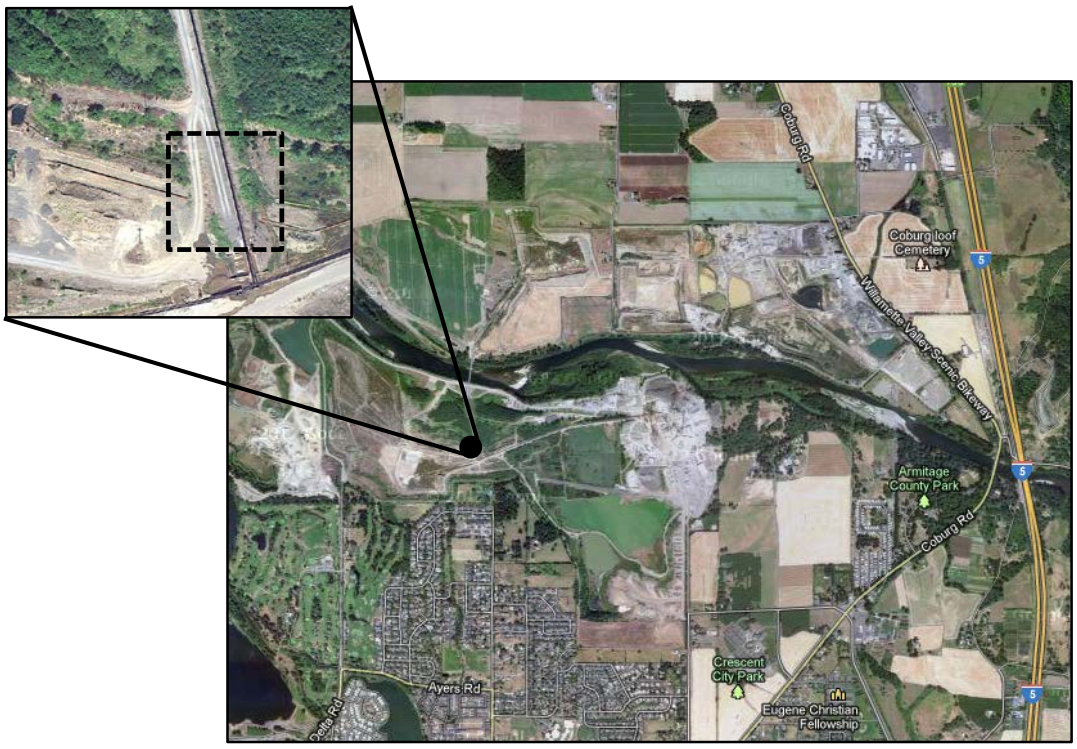

Figure 3.1: Location of the Case 1 project site (Source: USGS Earth Explorer).

The cutting shoe had an external diameter of 630 mm and internal diameter of 550 mm (Figure 3.2a). All but approximately 1.5 m of the initial pipe length was driven in a continuous operation; the remaining length of the first pipe was not installed in order to allow for welding of the next pipe segment (Figure 3.2c). The spoil accumulated within the pipe was removed using auger boring (Figure 3.2d) prior to welding the next segment. In the second and third stages, the 9.1 m and 12.2 m pipe segments were driven respectively to cross the embankment. The impact driving was carried out with a 400 mm pneumatic HammerHead hammer with an estimated rated energy of 6.4 kN-m and rate of blow of 231 strokes per minute. The hammer was fitted to the rear end of the pipe with collets that facilitate the connection and distribute the impact force of the hammer to the edge of the pipe casing. The pipe-collet-hammer system was held in place by tensioned chains hooked to eye pads welded on each segment of the pipe.

Figure 3.2: Photographs showing construction activities for the Case 1 pipe ramming project: (a) the first segment of the pipe with cutting shoe welded at the leading edge and situated steel auger boring tracks, (b) the ramming process under the embankment, (c) welding the second segment of the pipe, and (d) spoil removal using auger boring.

Subsequent to pipe installation, soil samples were retrieved for the purpose of laboratory testing: one sample at 4.6 m from the insertion point of the pipe during auger removal of spoils and the other at the exit point of the pipe on the other side of the embankment. Figure 3.3 provides the grain size distribution of the soil samples, and indicates that silty-sand (SM) comprises the embankment based on the Unified Soil Classification System (USCS) (*ASTM 2007*). A small percentage of gravel and clay (both less than seven percent) were observed in the samples tested. The in situ moisture content was determined to be 25 percent.

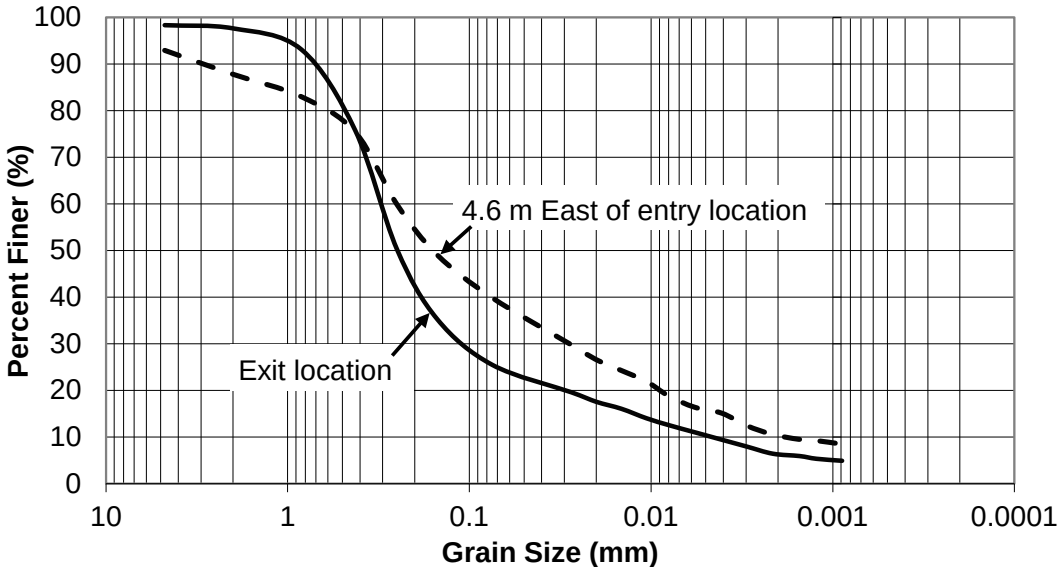

Figure 3.3: Grain size distribution of the soil sample taken from the project site.

Field instrumentation was installed to monitor the performance of the pipe and ground movement during installation. The instrumentation included ground deformation monitoring points (GDMPs) and dynamic strain gages and accelerometers to observe the pipe response to impact driving. The ground deformation was measured using a Leica DNA 10 digital level and bar-code invar rods. The measurement of vertical displacement had an accuracy and resolution of 1.5 mm/km and 0.1 mm, respectively. A total of 28 monitoring points were established along four cross sections (i.e., each cross section included seven GDMPs) transverse to the centerline axis of the advancing pipe for observing the ground deformation (Figure 3.4). At each cross section, one GDMP was located directly above the pipe, with three monitoring points offset on each side of the centerline at 0.75*D* (0.46 m), 1.5*D* (0.91 m) and 3*D* (1.83 m), where *D* equals the diameter of the pipe (Figure 3.4). A benchmark was established approximately 50 m from the nearest location of the pipe outside of anticipated area of influence from the ramming operation. Each day elevations were taken prior to the beginning of ramming (baseline survey) and subsequently after the commencement at a frequency that depended on the progress of the ramming. Measurements were generally performed every 10 m of installation.

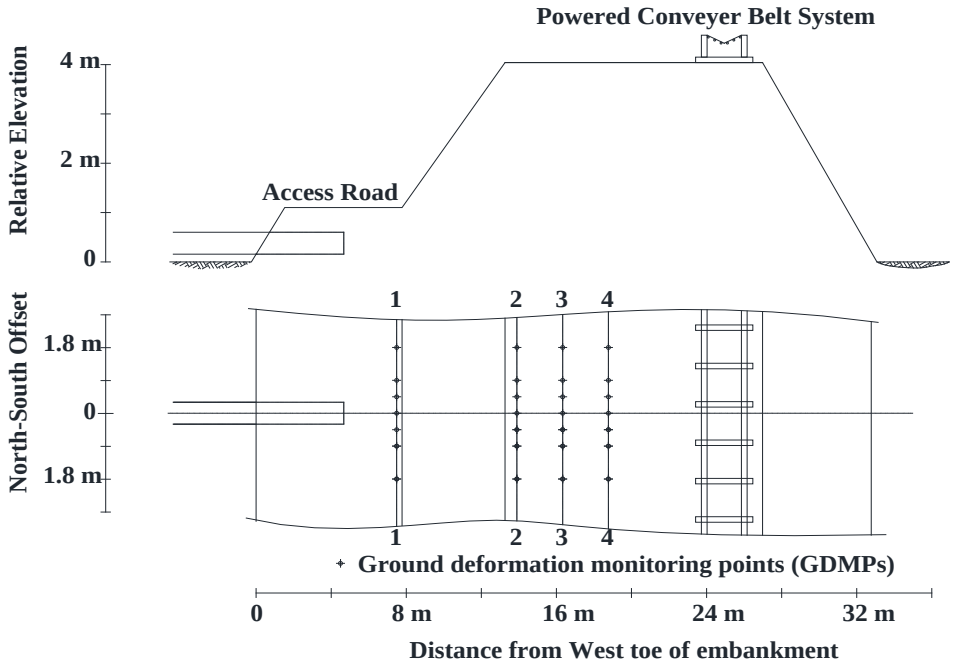

Figure 3.4: Profile and plan view of the access road and conveyer belt embankment and settlement monitoring points.

The computation of driving stress, energy transferred, and distribution of the soil resistances during impact driving are based on measurements of the forces and accelerations at the rear end of the pipe. The pile driving analyzer (PDA) is a widely used computerized system for dynamic load testing of piles during impact pile driving. It consists of high-frequency strain gauges and accelerometers (Figure 3.5) that are bolted on diametrically opposed sides of a pile to acquire the signals of dynamic strain and acceleration due to hammer impact (*Hannigan et al. 1997*). The strain and acceleration measurements are converted internally by the PDA to force and velocity time histories, respectively. The dynamic stress wave measurements were only observed for the second stage of the 9.1 m pipe segment installation. The strain gauges and piezoelectric accelerometers were mounted approximately 2*D* (1.22 m) from the rear end of the pipe segment (Figure 3.5), to allow for the observation of coherent stress waves, per ASTM (*2008*).

Figure 3.5: Photographs showing (a) pile driving analyzer (PDA), and (b) high frequency strain gage and accelerometer attached to the pipe.

3.1.2 Case 2: Corrugated Metal Pipe (CMP) replacement project under Highway 21 at Allan's Creek, Ontario

The Ministry of Transportation of Ontario (MTO) replaced the existing 2440 mm diameter corrugated metal pipe (CMP) culvert that transports Allan's Creek under Highway 21,north of Goderich, Ontario (Figure 3.6),due to collapse of the existing culvert. The project called for installation of a new 2440 mm diameter steel culvert with 25 mm wall thickness and 39 m in length parallel to the failing CMP culvert. The project was completed in July 2010. Realignment of the culvert centerline was requested due to the existence of abandoned concrete abutments that were constructed in the early 1900s at the crossings. However, Canadian Department of Ocean and Fisheries did not allow the realignment and the installation was accomplished by driving (i.e., ramming) the new pipe through the concrete structures. Another project requirement consisted of maintaining an adequate amount of stream flow to facilitate the migration of fish under the highway during construction. The flow requirement was met by placing two steel casings (yield strength of 248 MPa), with a 610 mm diameter steel pipe inserted in 1524 mm diameter pipe within the failing CMP culvert.

Figure 3.6 Location of the Case 2 project site (Source: USGS Earth Explorer).

The installation of the new culvert was carried out in four stages with installation of three 12 m long pipe segments and one 2.5 m pipe segment. The installation was started with excavation of a bore pit having a minimum length equal to the sum of the lengths of the ramming tool, the larger product pipe section and an additional 1.5 m of working space (*Holcomb 2012*). Then the launching area was prepared by the construction of a leveled crushed rock bedding layer. Steel tracks were placed on steel mats, in turn placed on the prepared ground surface to help guide the hammer-pipe system and maintain the required grade and alignment (Figure 3.7a). In the first stage of installation, the 12 m pipe segment was driven with a cutting shoe at the leading edge. The dimensions of the cutting shoe are provided in Figure 3.7b as described by J. Robinson (J. Robinson, personal communication, *2012*). The cutting shoe assisted in ramming through the four abandoned and buried concrete wing walls (*Holcomb 2012*). In the following three stages, the two 12 m and one 2.5 m pipe segments were driven, respectively, to cross the embankment. The impact driving was carried out with an 800 mm pneumatic Grundoram Apollo hammer with a rated energy of 40.5 kN-m and blow rate of 180 blows per minute (bpm). The hammer was fitted to the rear end of the pipe with tapered ram cone and cotter segments that facilitated the connection and distribute the impact force of the hammer to the edge of the pipe casing. The pipe-ram cone-hammer system was held in place by tensioned chains hooked to eye pads welded on each segment of the pipe.

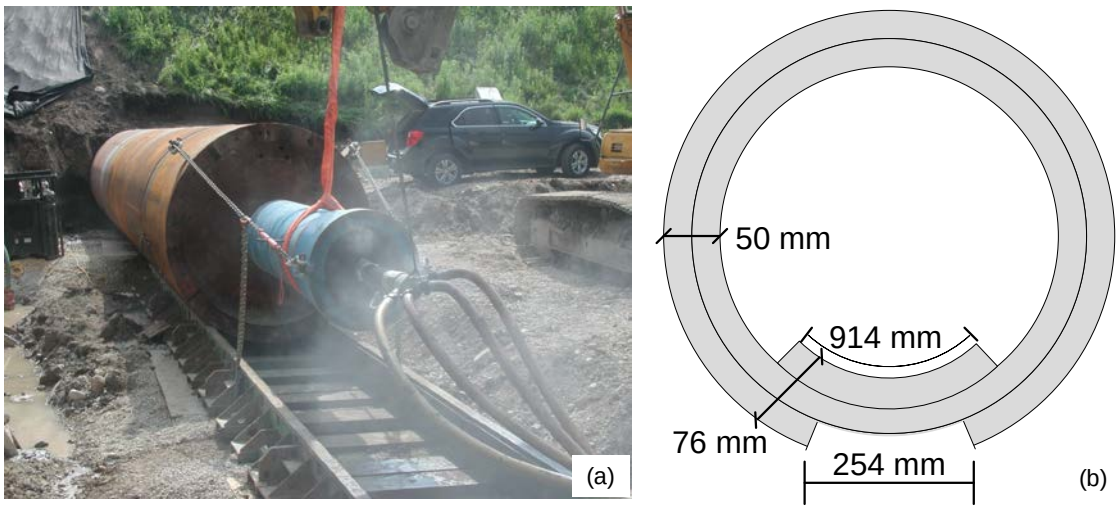

Figure 3.7 (a) Photograph showing installation of the new 2440 mm culvert parallel to the failing CMP culvert, and (b) geometry of the cutting shoe.

Prior to construction, a subsurface investigation of the project site was conducted by Golder Associates and included the drilling of four borings through the highway embankment (*Golder Associates 2010*). Figure 3.8 shows the location of the borings as well as the profiles of the embankment along the centerline of the culvert. Two boreholes were drilled in the shoulders through the existing embankment to depths of 11.1 m (B 302 and B 303); the other two borings were drilled near the west and east ends of the culvert to depths of 4.3 m. The boring logs are presented in Appendix A. Figure 3.8 presents the embankment cross-section, and indicates the variable nature of the embankment fill material, ranging from loose to medium dense sandy silt, silty sand, some sand and gravel, and stiff to very stiff clayey silt (*Golder Associates 2010*). The groundwater ranged in depth between 0.6 m below grade at B 301 and 6.7 m below grade of the embankment (B302 and B 303), just above the pipe invert.

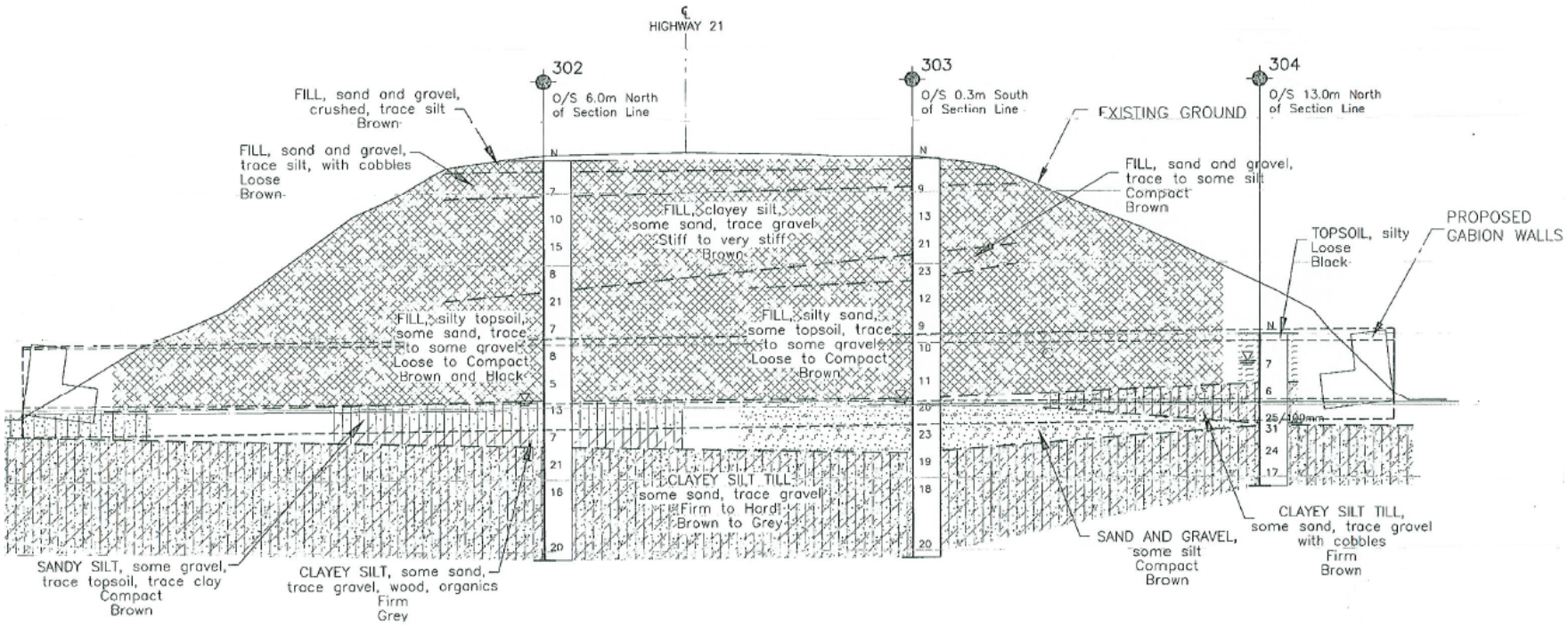

Figure 3.8 Profile along the centerline of the culvert showing location of borings (*Golder Associates 2010*).

The new culvert installation was instrumented to monitor overall performance of the steel casing during installation (Figure 3.9). The pile driving analyzer (PDA) system was hooked to twin accelerometers and stain gauges on each side of the springline of the pipe to measure the dynamic response of the pipe (Figure 3.9). The dynamic stress wave measurements were only observed for the second and third stage of the 12 m pipe segments installation. The strain gauges and piezoelectric accelerometers are usually mounted approximately at 2*D* from the rear end of the pipe segment; however, they were mounted approximately at 1*D* (2.4 m) due to the large diameter of the pipe and the relatively short installation segment lengths (Figure 3.9) so as to maximize the length of the penetration record.

Figure 3.9 Two pairs of accelerometers and strain gages mounted to the pipe.

3.1.3 Case 3: Culvert replacement project under Interstate Highway 84 at Perham Creek, Oregon

The Perham Creek culvert replacement project was commissioned by the Oregon Department of Transportation (ODOT) to replace a failing 1370 mm diameter culvert which conveyed Perham Creek underneath Interstate Highway 84 and railroad tracks adjacent to the highway, situated approximately 100 km east of Portland in the Columbia River Gorge (Figure 3.10 and Figure 3.11a). The failing culvert provided maintenance problems that resulted in the obstructed passage for salmon migrating to upstream spawning grounds. Therefore, a new steel culvert of 3660 mm diameter with wall thickness of 37.5 mm and length of 63 m was installed parallel to the failing culvert at Perham Creek under Interstate 84 and completed in November 2002. The installation of the new culvert was carried out in five stages with installation of four 13.6 m long pipe segments and one 8.5 m long pipe segment. The installation commenced with excavation of a launch pit on the south side of the Interstate 84. The sheet-pile supported excavation required stabilization of the base including a compacted granular blanket overlain by a concrete slab (Figure 3.11b), as well as dewatering to maintain a dry cut. To satisfy permit requirements, the dewatering of the streambed took place after the fish in the creek and pond area had been relocated. Then steel tracks were placed on the concrete slab to help guide the hammer-pipe system and maintain the required grade and alignment during the installation (Figure 3.11b).

During the installation of the pipe segments, the spoil accumulated within the pipe was removed on several occasions using auger boring prior to welding of the next segment.

Figure 3.10 Location of the Case 3 project site (Source: USGS Earth Explorer).

The Perham Creek culvert replacement project faced significant challenges due to difficult ground conditions consisting of large boulders (i.e. 900 to 1200 mm diameter) mixed with silts and sands (*Zubko 2003a*). The project team, finding effective refusal of the pipe at various penetration lengths, evaluated three pneumatic hammers and one hydraulic hammer to complete the driving below the active interstate highway embankment. The pneumatic hammers used include the 460 mm Grundoram Goliath with rated energy of 11.6 kN-m, the 610 mm Grundoram Taurus with rated energy of 18.6 kN-m, and the 800 mm Grundoram Apollo with rated energy of 40.5 kN-m (Figure 3.11c), each characterized with a blow rate of 180 bpm. The three pneumatic hammers encountered effective refusal after driving 8 m, 22.5 m and 16.5 m of culvert penetration, respectively. The hydraulic hammer used to complete the drive (i.e., about 7 m drive on Nov.9, 2002 and 11 m on Nov.16, 2002) was the 915 mm IHC S-280 hydraulic hammer (Figure 3.11d) with rated energy of 140 kN-m for horizontal driving, characterized with a blow rate of 45 bpm. The IHC S-280, fitted within a specially constructed cradle to allow the addition of a static thrust force, allowed the completion of the installation without difficulty. The hammers were fitted to the rear end of the pipe with tapered adapters that provided a reduced diameter and allowed transfer of the impact energy to the pipe casing. The hydraulic hammer-pipe system was held together using a winch and a cable where the winch pulls the hammer forward after each blow during the impact driving; approximately 1100 kN of tensile force was achieved in the winch cable, providing an equal component of compressive force on the connection.

The performance of the culvert was monitored during installation through the use of pile driving analyzer (PDA) system which was connected to dynamic strain gages and accelerometers bolted on diametrically opposed sides of the pipe springline. The dynamic stress wave measurements were observed only during the installation of the second, fourth and fifth culvert segments over penetration lengths of 14 m to 27 m and 41 m to 63 m. The strain gauges and piezoelectric accelerometers were mounted approximately 2.4 m from the rear end of the pipe segment due to space limitations.

Figure 3.11 Photos showing activities related to Perham Creek culvert replacement project: (a) pipe ramming operation under Interstate 84, (b) launch pit set-up, (c) 800 mm pneumatic Grundoram Apollo hammer (*J.W. Fowler, personal communication, 2012*), and (d) 915 mm hydraulic IHC S-280 hammer (*ODOT 2010*).

3.1.4 Case 4: Ramsey Town Center Storm water Conveyance Installation, Ramsey, Minnesota (*Jensen et al. 2007*)

Ramsey Town Center is a large commercial and residential development in Ramsey, Minnesota (Figure 3.12). The town required additional storm water conveyances to increase drainage capacity. One 1520 mm and twin 1370 mm diameter storm water pipes that pass under active Burlington Northern Santa Fe (BNSF) railroad tracks were installed in March 2006 to improve the storm water capacity (*Jensen et al. 2007*). The 1520 mm and twin 1370 mm pipes were installed through steel casings with diameters of 2180 mm and 1980 mm, respectively. All of the pipes were installed in three 15.2 m long segments by means of the pipe ramming technique. The depth of cover ranged from 2.1 m to 3.1 m. A cutting shoe was welded to each casing to reinforce the casing section at the face and facilitate face penetration. The casings for the twin storm water pipes were installed 4.3 m from one another (*Jensen et al. 2007*). The installation of casings began within shored insertion and receiving pits.

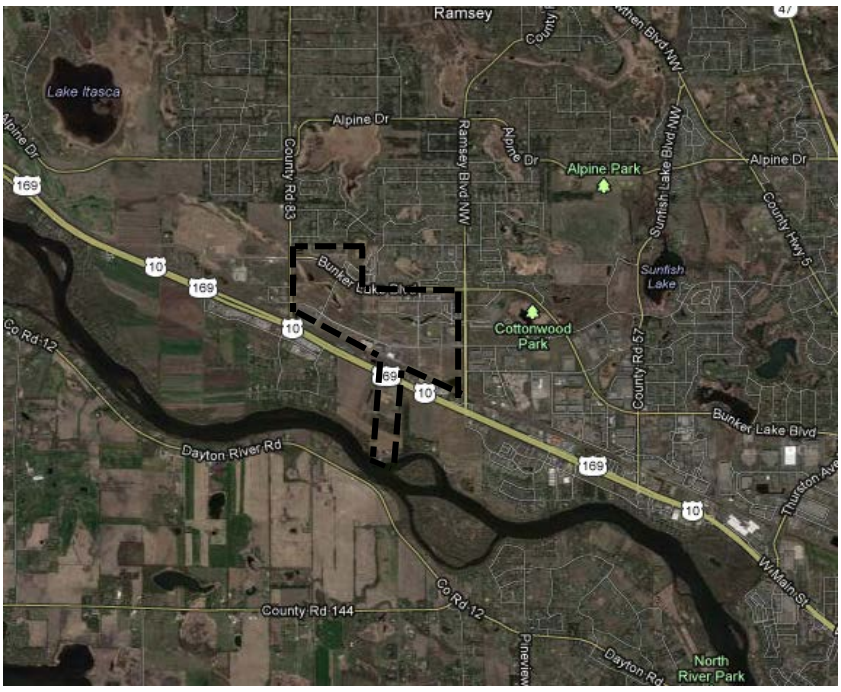

Figure 3.12 Location of the Case 4 project site (Source: USGS Earth Explorer).

The project utilized a 610 mm pneumatic Grundoram Taurus hammer with a rated energy of 18.6 kN-m and rate of blow of 180 bpm. The hammer was fitted to the rear end of the pipe with collets, and the pipe-collet-hammer system was held in place by tensioned chains hooked to eye pads welded on the pipe. Spoils were generally removed from the casings at the end of the drive after the entire casing length was in place.

A subsurface investigation was conducted to explore the site; four borings and one hand-auger boring were drilled to support the project planning. Figure 3.13 shows the location of the borings relative to the location of the pipes. The subsurface investigation indicated topsoil from the ground surface to depths of 0.5 –1.4 m below ground surface, underlain by alluvium. The topsoil was composed of organic, silty sand (OL-SM), and the alluvium layer consisted of poorly graded sand with silt (SP-SM) and poorly graded sand (SP). Fill material was observed directly under the railroad tracks. A cross section of the subsurface along the 2180 mm casing is provided in Figure 3.14. The standard penetration tests (SPT) yielded blow counts ranging from 2 to 17, and indicated relative densities ranging from very loose to medium dense for the alluvium layer through which the casings were driven. The groundwater table at the time of drilling was noted to range from 2.1 and 3.7 m below ground surface.

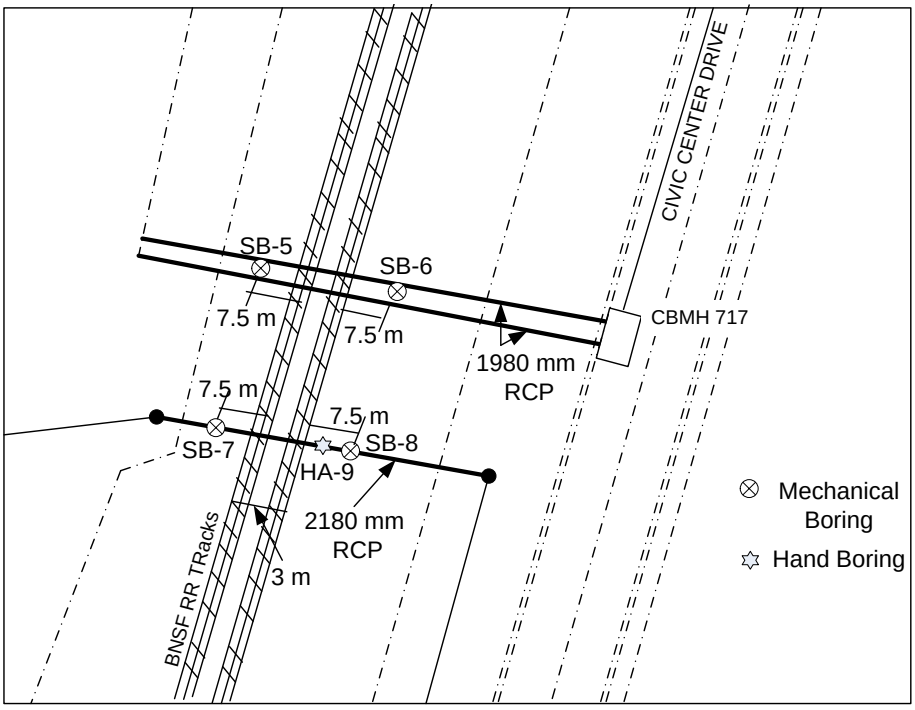

Figure 3.13 Boring location relative to the casing crossings (*adapted from Jensen et al. 2007*).

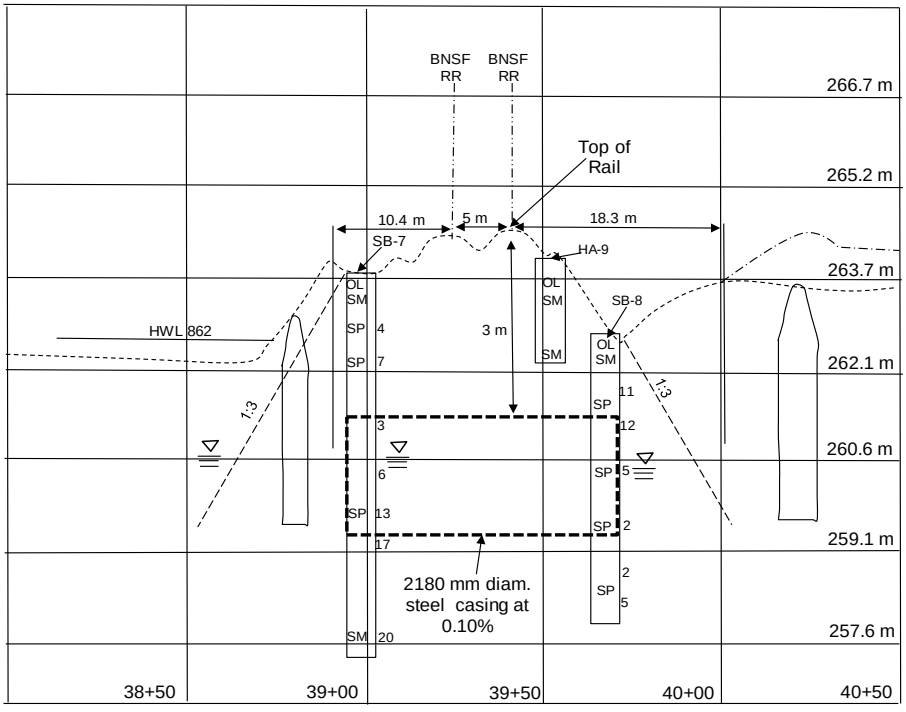

Figure 3.14: Cross section of the boring along the 2180 mm casing (*adapted from Jensen et al. 2007*).

Due to the sensitivity of the railroad tracks to ground movements, real time monitoring of settlement and heave along the railway was required to monitor potential for damage to railroad tracks. The BNSF Utility Accommodation Policy required that any vertical track movements greater than 6.5 mm must be immediately reported to the BNSF rail road master. However, the BNSF increased their threshold of acceptable settlement to 25 mm after a discussion with project team, and reached an agreement of real time update of the magnitude of settlement during pipe ramming to BNSF personnel (*Jensen et al. 2007*). The real-time ground deformations monitoring was performed by means of an automated system consisting of a Leica TCA 1103 theodolite and 74 mini-prisms. The theodolite had an accuracy of angle measurement of 3 seconds and an infrared distance measurement accuracy of 2 mm. It was installed on a storage container adjacent to and north of the railroad tracks and recorded a reading of all prisms every 30 minutes (*Jensen et al. 2007*). The ground deformation monitoring points (GDMPs) (Figure 3.15) consisted of 25 prisms on each railroad track, 7 prisms on the railroad embankment to the south of the tracks towards the ramming pits, 7 prisms on each of the north and south sheet pile walls and 3 reference prisms outside of the construction zone (Figure 3.15).

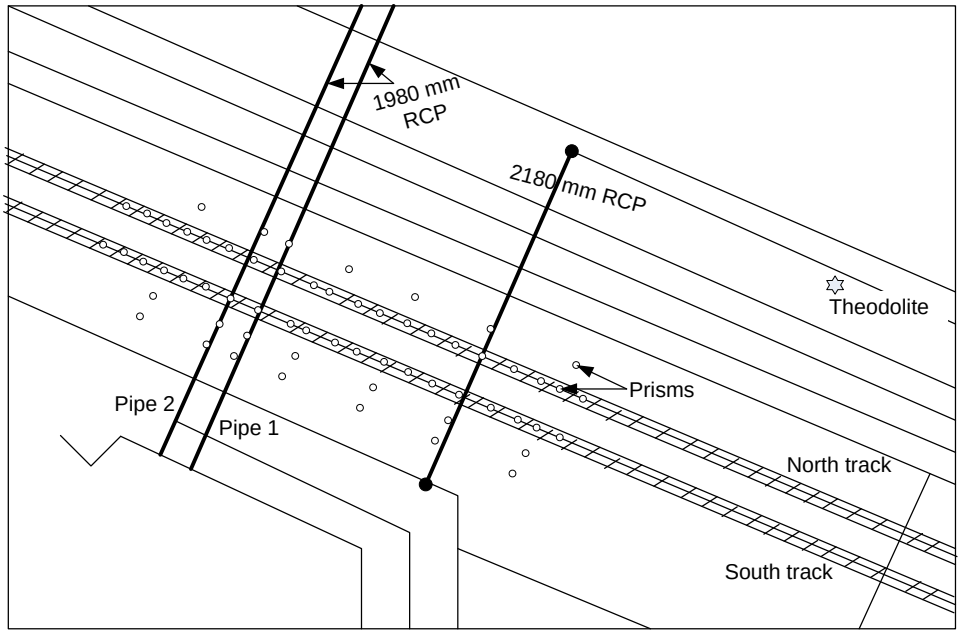

Figure 3.15: Ground deformation monitoring point layout plan (*adapted from Jensen et al. 2007*).

3.1.5 Case 5: Water main Installation under US Highway 50, Rancho Cordova, California

The water main installation project under US Highway 50 in Rancho Cordova, California, was carried out to connect existing pipelines servicing groundwater extraction wells and treatment systems. The design team selected pipe ramming for the installation of the service casing and completed the project in September 2010. The project required the installation of a 250 mm diameter ductile iron water main crossing US Highway 50 (US 50) encased within a 760 mm diameter steel casing characterized with a 16 mm wall thickness. The pipeline alignment extended 66 m from South White Rock Road to the intersection of Mills Park Drive and North White Rock Road across US 50 (Figure 3.16).

Figure 3.16: Location of the Case 5 project site (Source: USGS Earth Explorer).

The installation of the casing began with the excavation of an insertion pit and receiving pit in the Boyd Channel (south of US 50) and on the edge of Caltrans right-of-way towards Mills Park Drive (north of US 50), respectively. Steel tracks were placed on the leveled ground in the insertion pit to help guide the hammer-pipe system and maintain the required grade and alignment during the installation (Figure 3.17). The California Department of Transportation (Caltrans) construction permit requires monitoring pipelines (e.g., grade and alignment) every 9 m of the penetrated length. The installation was carried out in eleven stages using eleven 6 m long pipe segments driven in each stage. The spoil accumulated within the pipe was removed every 12 m of length using auger boring. The depth of cover above the casing crown was about 2 m near the launch pit, 2.5 m beneath the center of the highway median, and 2.2 m near the receiving pit. The project utilized a 355 mm pneumatic Grundoram Koloss hammer with a rated energy of 6.8 kN-m and a blow rate of 220 bpm. The hammer was fitted to the rear end of the pipe through a hammer adaptor which was welded to the pipe and which facilitated the connection and distribute the impact force of the hammer to the pipe casing (Figure 3.17). The pipe-adaptor-hammer system was held in place by tensioned chains hooked to eye pads welded on each segment of the pipe.

Figure 3.17: Pipe ramming in progress for 760 mm casing installation (*Bennett Trenchless 2010a*).

A subsurface investigation was conducted by Kleinfelder, Inc. Three borings were drilled to depths ranging from 8 to 15 m below the ground surface to evaluate the subsurface conditions (Figure 3.18). The borings were performed using a truck-mounted drill rig equipped with a sonic core sampling system. The system comprised of a 114 mm diameter core barrel inside 152 mm diameter casings 6 m in length. The core barrel was retrieved at nominal 2 to 3m intervals providing continuous soil sampling. This allowed a detailed logging of the entire soil stratigraphy, as demonstrated on the logs of borings (provided in Appendix B) along with photographs of each core. In general, the ground conditions at the crossing consisted 0 to 2 m of clayey sand, underlain by 6.5 to 10 m of coarse-grained soils (i.e. sand, gravel, and cobbles with little fines) followed by finer-grained silt, clay, and silty sand to the depths explored. The borings indicated that pipe passed through clayey gravel, silty gravel, and poorly graded gravel with varying amounts of sand and cobbles (Figure 3.18). The borings also indicated that groundwater was not encountered during the drilling.

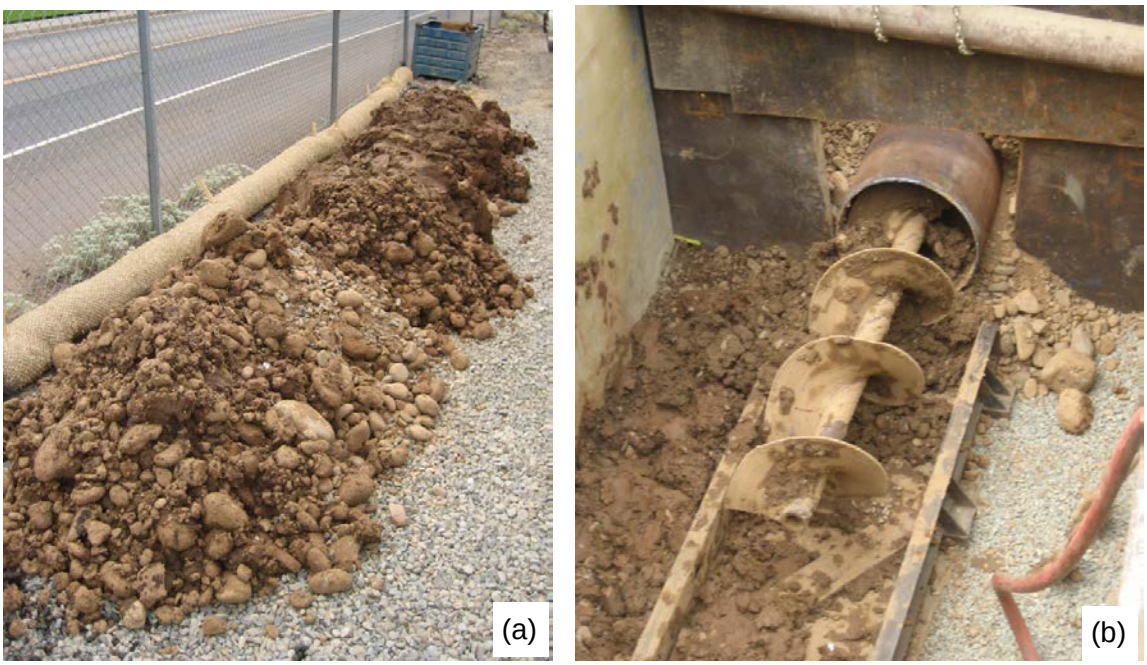

Figure 3.18: Spoil obtained from inside of the pipe: (a) spoils from 0 to 3 m penetration in foreground and from 3 to 6 m in background, and (b) augers approximately 8 m into the casing (*Bennett Trenchless 2010b*).

Ground movements were monitored in real-time during the pipe installation as Caltrans was concerned about the impact of ground deformations on the busy highway. The ground deformation was measured using a Trimble S6 Robotic Total Station characterized with an angular accuracy of 2 seconds and a distance measurement accuracy of 2 mm. Twenty-five monitoring points were established along five sections transverse to the centerline axis of the pipe and an additional eight GDMPs along the centerline of the pipe (Figure 3.19).

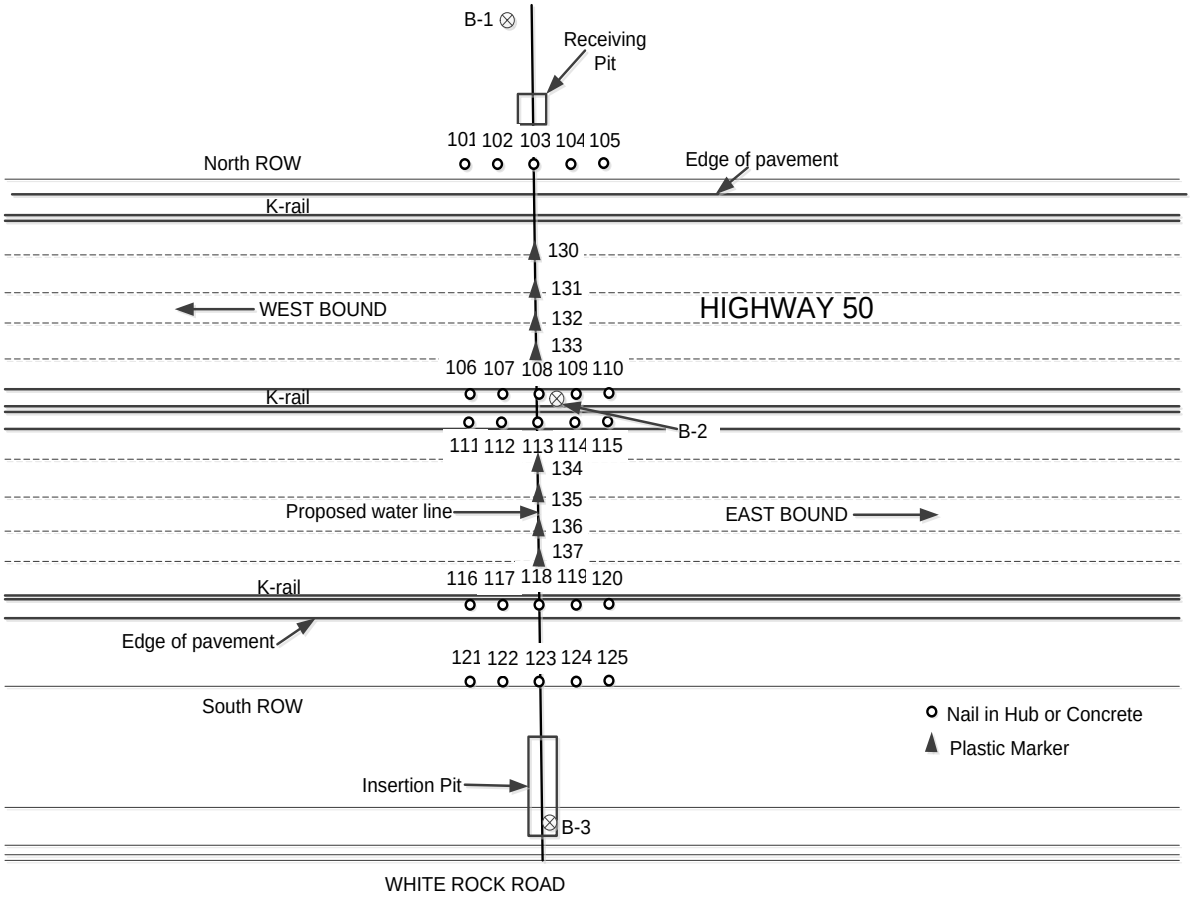

Figure 3.19: Location of ground deformation monitoring points (GDMPs) (*adapted from Stantec 2010*).

3.1.6 Full-scale Pipe Ramming Experiment at Emery & Sons, Inc., Yard in Salem, Oregon (Case 6)

3.1.6.1 Background

A full-scale field experiment on pipe ramming was carried out in August 2010 by the authors under the auspices of the Oregon Department of Transportation (ODOT) and with the assistance of the Oregon and Southwest Washington Chapter of the National Utility Contractor's Association. The main objective of the experiment was to collect performance data under a controlled condition to increase understanding of the mechanics of pipe ramming. The field experiment was carried out at the yard of Emery and Sons, Inc., near Salem, Oregon (Figure 3.20). The experiment involved installation of a 1070 mm diameter open-ended steel casing (yield strength 622 MPa) approximately 35 m in length and with a wall thickness of 12.5 mm.

Figure 3.20: Location of the Case 6 project site (Source: USGS Earth Explorer).

3.1.6.2 Site Investigation and Laboratory testing

Subsurface explorations were performed to evaluate site stratigraphy using standard penetration tests (SPTs) and cone penetration tests (CPTs). Eight hollow stem auger borings, designated as B-1A through B-4A and B-1B through B-4B, and two CPT soundings (P-3B and P-4B) were advanced (Figure 3.21) to assess the consistency of subsurface materials and obtain disturbed samples (i.e. split-spoon samples) for laboratory testing. The auger borings were performed to depths ranging from 1.8 to 5 m below the existing grade. The sampler was driven into the ground by a drop hammer weighing 68 kg falling 76 cm (Figure 3.22a) and terminated in very dense sandy gravel. In general the drilling operations were slow and difficult due to the presence of gravels and large cobbles. The soil samples recovered from the sampler during the boring were visually classified in the field and representative portions of the samples were preserved in sealed jars for laboratory testing.

The CPT soundings were performed by pushing a 36 mm diameter cone probe into the ground to depths of 1.9 m for P-3B and 2.6 m for P-4B. The probe was advanced downward at a constant velocity of 2 cm/s using hydraulic actuators (Figure 3.22b). The dense, gravels and cobbles at the site forced termination of the CPTs at relatively shallow depths.

In general, the soil stratigraphy was found to vary from medium to very dense, silty, sandy gravel with cobbles based on the SPT and CPT testing. The open trenchcut along the pipe after driving also indicated a layer silty sandy gravel for the upper 2 m depth and

silty sandy gravel with many cobbles below 2 m depth (Figure 3.23). The details of the boring logs and analysis of the CPT test results are attached in the Appendix C. The groundwater table was observed at a depth of 2.6 m below the surface of the ground in all the borings.

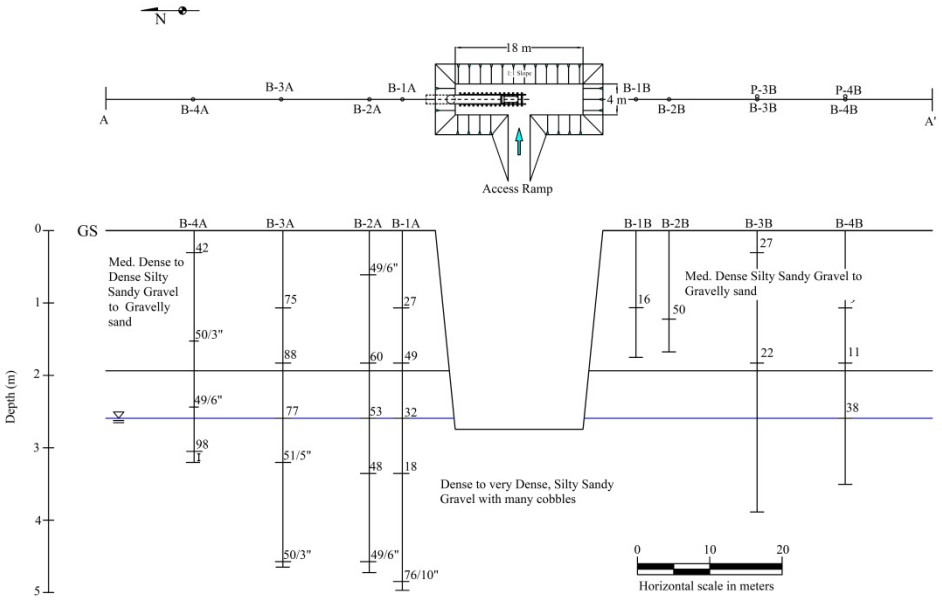

Figure 3.21: Exploration plan and cross-section of subsurface for Case 6.

Figure 3.22: In-situ testing at the site including (a) Standard Penetration Testing (SPT) , and (b) Cone Penetration Testing (CPT).

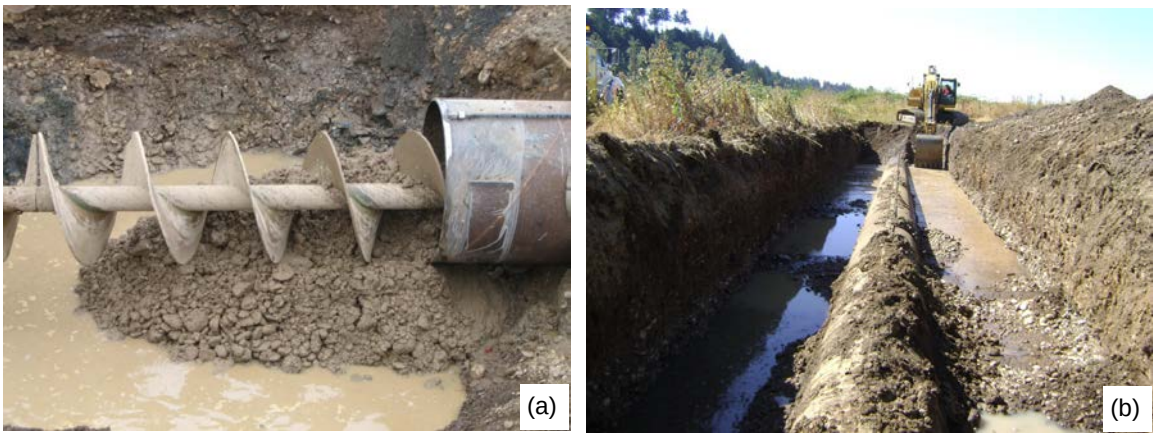

Figure 3.23: Representative photographs indicating soil stratigraphy: (a) soil augured out of the pipe, and (b) soil exposed along the pipe following installation.

Laboratory tests were carried out to characterize the engineering properties of the soil at the experimental site. The laboratory testing of soils ranged from a simple moisture content determination to sophisticated triaxial strength testing. Moisture contents were determined for all samples obtained from the auger borings, and provided average moisture contents of 18 and 36 percent for depth above and below 2.5 m respectively. A representative grain size distribution of samples taken from the site is presented in Figure 3.24, and confirms the sandy gravel soils with cobbles that were encountered in the auger borings and launch pit construction. The presence of cobbles and large gravels provides difficultly for the evaluation of the shear strength of the samples. Therefore, a parallel gradation modeling technique, originally developed by Lowe (*1964*), was employed to create the design grain size distribution for the triaxial strength tests. The parallel gradation model assumes that a smaller grain-size distribution model of the soil, composed of the same material as the in-situ material, can be used for triaxial testing at a scaled down grain-size if the model material's grain size is parallel to the in-situ material. Remolded specimens at the scaled down gradation were generated from samples retrieved from the experimental site by compacting the soil to a targeted maximum dry unit weight of 19.25 kN/m3. The triaxial testing was conducted under different confining pressures corresponding to the confining stresses at the pipe crown, springline, and invert, of the pipe and equaled 15 kPa, 30 kPa and 60 kPa, respectively. Figure 3.25 presents the results of the Consolidated- Drained (CD) triaxial tests. The principal stress difference curves show that the linear stress-strain response part of the curve becomes stiffer as confining pressure increases. The peak principal stress difference increases with increasing confining pressure. The volumetric strain graph demonstrates that the specimen first slightly compresses and then dilates for all the confining pressures considered, which were representative of the relative density in the field. The Mohr-Coulomb failure envelopes imply that the peak and residual angle of internal friction are 480 and 440 respectively.

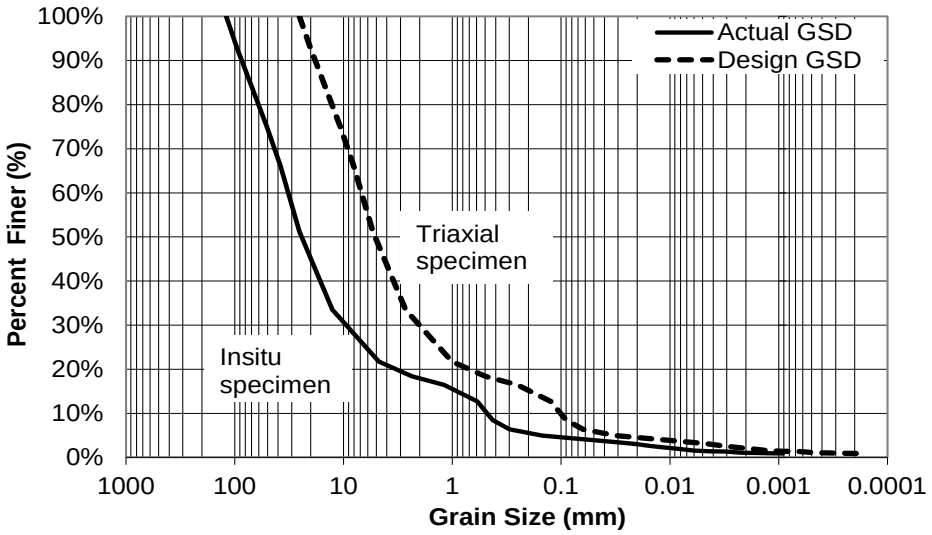

Figure 3.24: Grain size distribution (GSD) curve for a soil sample taken from experimental site.

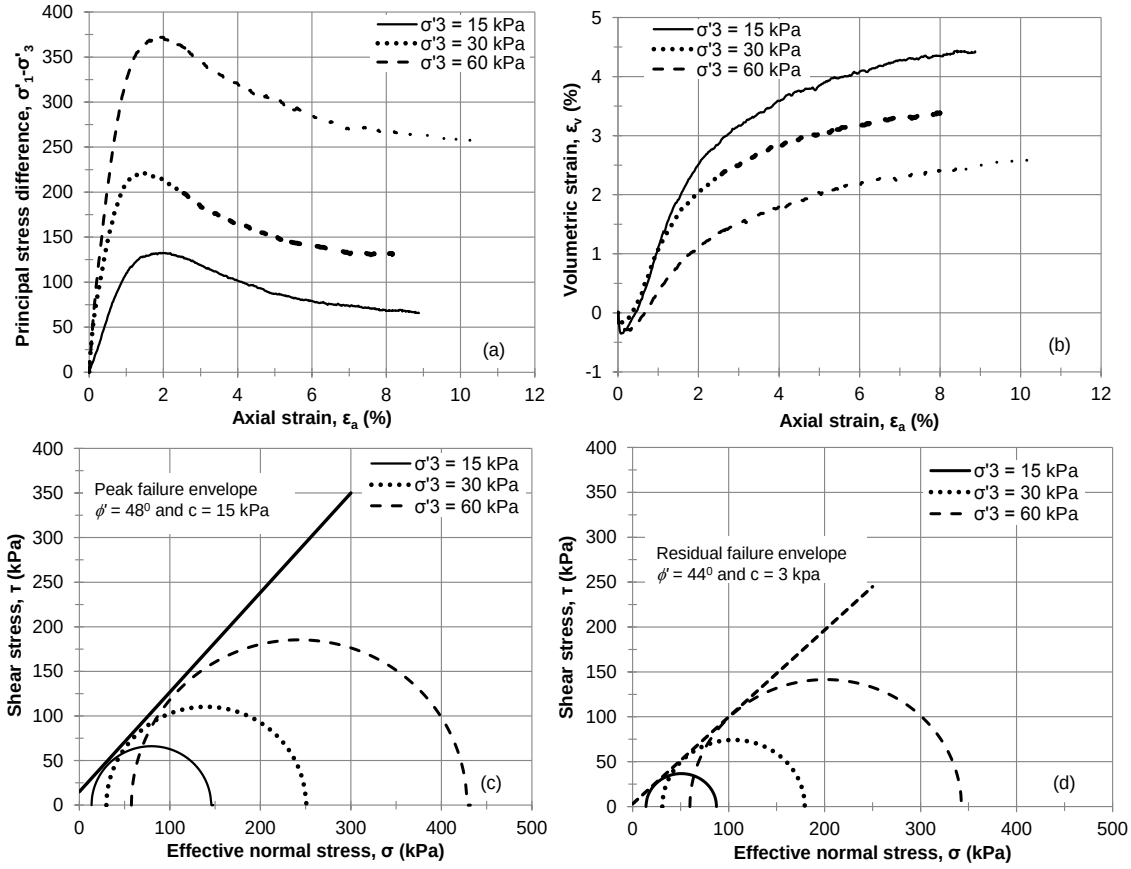

Figure 3.25: Triaxial test results for Case 6 (a) principal stress difference versus axial strain (b) volumetric strain versus axial strain (c) Peak Mohr-Coulomb failure envelopes (d) Residual Mohr-Coulomb failure envelopes.

3.1.6.3 Test Pipe and Instrumentation

The experimental pipe ramming installation employed six segments of open-ended steel pipe, each approximately 6 m long, with diameter of 1070 mm and wall thickness of 12.5

mm. The pipe was instrumented with resistance-type strain gages at 11 sections, where each section included four pairs of gages in the longitudinal direction, for the purpose of monitoring static soil resistance. One gage pair was fitted to the top of the pipe, one pair to the base of the pipe and the other two pairs along each of the springlines (Figure 3.26). Thus, eighty-eight strain gages were mounted on the pipe for monitoring the soil resistance. Additionally, temperature gages were mounted at the mid-length of each pipe segment to monitor changes in strain due to temperature.

The installation of strain gages began with cleaning of the mill surface on the pipe over an area larger than the intended strain measuring point. The cleaning process consisted of grinding the surface with a coarse sand belt, smoothing the surface with fine sand belt grinder to remove asperities that impair bonding, and apply solvents to clean the prepared surface. The surface was then roughened to produce an ideal bonding surface. Then the strain gage was glued to the surface of the pipe with extreme care and covered with a high temperature self-adhesive tape. Figure 3.27 shows the strain gage instrumentation process with the strain gage shown on the right hand bottom corner of the picture.

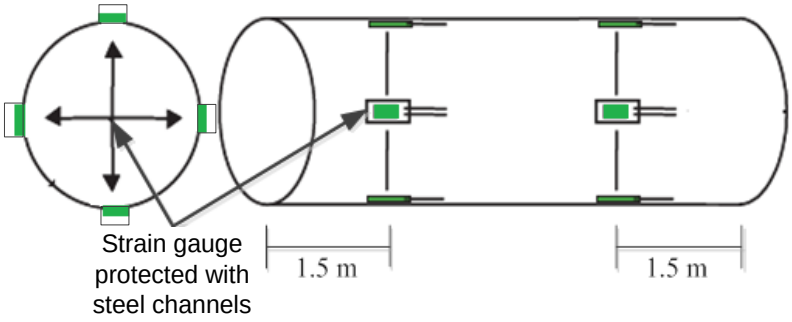

Figure 3.26: Location of the strain gages on each pipe segment.

Figure 3.27: Pipe instrumentation with strain gages; note, pairs of gages were installed to provide redundancy.

3.1.6.4 Experimental Set up

The experimental set up commenced with hauling the instrumented pipe to the site and excavation of the launching pit (Figure 3.28). The floor of the pit had dimensions of 18 m by 4 m and was 2.75 m deep. The excavation was sloped at 1H: 1V. Dewatering of the pit was performed throughout the experiment to avoid flooding of the working area and to facilitate welding of pipe segments, as the pit was excavated below the ground water table (Figure 3.28c). The pit was stabilized by laying a leveled gravel bed and placing steel sheets (Figure 3.28d) to form a stable working surface. Steel tracks (Figure 3.28d) were placed on the steel sheets to guide the pipe–hammer setup and were subsequently used for removing spoils with an auger boring machine.

Figure 3.28: Photos showing site preparation activities for the field experiment: (a) transportation of the instrumented pipe the experiment site, (b) excavation of the insertion pit, (c) dewatering the insertion pit, and (d) steel tracks on the leveled gravel bed and steel sheets.

The installation of the pipe was carried out in six stages. In the first stage of installation, a T1 steel cutting shoe of 1085 mm in diameter and 38 mm in thickness was welded to the leading edge of the first 6 m long pipe segment. The pipe and hammer were assembled on the steel tracks (Figure 3.29). Almost 4.5 m of the initial length of the pipe segment was installed, allowing a stick-out of 1.5 m for welding of the next pipe segment. A similar approach was practiced during the installation of all pipe segments. The spoil accumulated within the pipe was removed using auger boring (Figure 3.29c) once during the installation process prior to welding the third pipe segment. Two

hammer types were used on the project: a 400 mm pneumatic HammerHead hammer, with an estimated rated energy of 6.4 kN-m and blow rate of 231 bpm, used during installation of the first five pipe segments, and a 610 mm Grundoram Taurus hammer, with rated energy of 18.6 kN-m and blow rate of 180 bpm used to install the last segment. The hammers were fitted to the rear end of the pipe segments with the driving system and held in place by tensioned chains hooked to eye pads welded on each segment of the pipe. The hammer-pipe connections consisted of pipe ram collars and collets for the HammerHead hammer and an inverted pipe cone and ram cone for the Grundoram Taurus hammer.

During the experiment, a lubricant was applied during installation of the fourth and fifth pipe segments to observe the effect of lubrication on the installation. A MICRO-GEL™ bentonite product was mixed with water in a high-shear mixer (Figure 3.29d) and injected into the face and over-cut area between the pipe and the excavated bore by a small diameter steel conduit installed on the pipe. The performance of the bentonite slurries was further improved with addition of synthetic polymers and additives such as MTA-1(Acrylic copolymer) and UNI-DRILL® (liquid viscosifier and fluid loss control agent). Lubricants are characterized by their viscosity; a Marsh Funnel (*ASTM 2004*) was used in the experiment to measure the qualitative viscosity (Figure 3.29d). The viscosity was measured indirectly as the time required for a given volume of lubricant to flow out of the Marsh funnel. The target viscosity is dependent on the soil type and generally ranges 55 to 65 seconds for sandy soil, 40 to 45 seconds for cohesive soil (*Boyce et al. 2011*).

Figure 3.29: Photographs showing experiment activities: (a) welding of the T1 steel cutting shoe to the first pipe segment, (b) pipe ramming in progress, (c) spoil removal using auger boring, and (d) bentonite mixing and field testing of viscosity.

3.1.6.5 Field Instrumentation

Field monitoring of pipe ramming induced ground movements are a relatively common practice since intolerable magnitudes of deformation could cause loss of service to adjacent buried utilities, structure foundations, or roadway pavements. Unfortunately, the monitoring of ground vibration does not appear commonplace, as no pipe-ramming induced ground vibrations have been reported in the literature to-date. In the field experiment, both ground movement and vibrations were observed in order to observe the ground response to the pipe impact driving. Vertical ground deformations were measured using a Leica DNA 10 digital level and bar-code invar rods. The measurement of vertical displacement had an accuracy and resolution of 1.5 mm/km and 0.1 mm, respectively. A total of 42 GDMPs were established along six cross sections transverse to the centerline axis of the advancing pipe (Figure 3.31). At each cross section, one GDMP was located directly above the pipe, with three GDMPs on each side of the centerline at offsets of 0.5*D* (0.53 m), 1.5*D* (1.6 m) and 3*D* (3.2 m), where *D* equals the diameter of the pipe (Figure 3.31). A benchmark was established approximately 30 m from the insertion pit outside of the anticipated area of influence. Measurements were taken each day prior to the beginning of ramming and after completion of installation of each segment.

The ground vibration was measured using a Minimate Plus seismograph (Figure 3.30a) designed for vibration and blast monitoring. The device has a capability of measuring vibration up to 254 mm/s with an accuracy of 0.5 mm/s using a standard triaxial geophone. A total of 12 vibration monitoring points were established along three cross sections (i.e. each cross section with four monitoring points) transverse to the centerline axis of the advancing pipe (Figure 3.32). At each cross section, one monitoring point was located directly above the pipe, with three monitoring points on right hand side of the centerline at offsets of *D* (1.1 m), 3*D* (3.2 m) and 5*D* (5.3 m), where *D* equals the diameter of the pipe (Figure 3.22). The vibration measurements were taken each day by moving the seismograph from one monitoring point to the other and recording the vibration wave forms for approximately 30 seconds at each monitoring point during the pipe driving. A heavy sand bag was placed over the geophone to ensure satisfactory coupling to the ground and minimize vibration measurement error.

The performance of the pipe installation was also monitored through the use of pile driving analyzer (PDA) (*ASTM 2008*) (Figure 3.30 b and c). The PDA stress wave measurements were performed on all pipe segments by mounting strain gauges and piezoelectric accelerometers on diametrically opposed sides of the pipe springline at approximately 1.5 m from the rear end of the pipe segment (Figure 3.30c). The measurements consist of force and velocity time histories for each hammer blow, which are subsequently analyzed using wave mechanics (see Chapter 6 for additional information).

Figure 3.30: Photos showing field instrumentation: (a) Minimate Plus seismograph with standard geophone and a sandbag (b) Pile Driving Analyzer (PDA), and (c) high frequency strain gauges and accelerometers attached to the pipe.

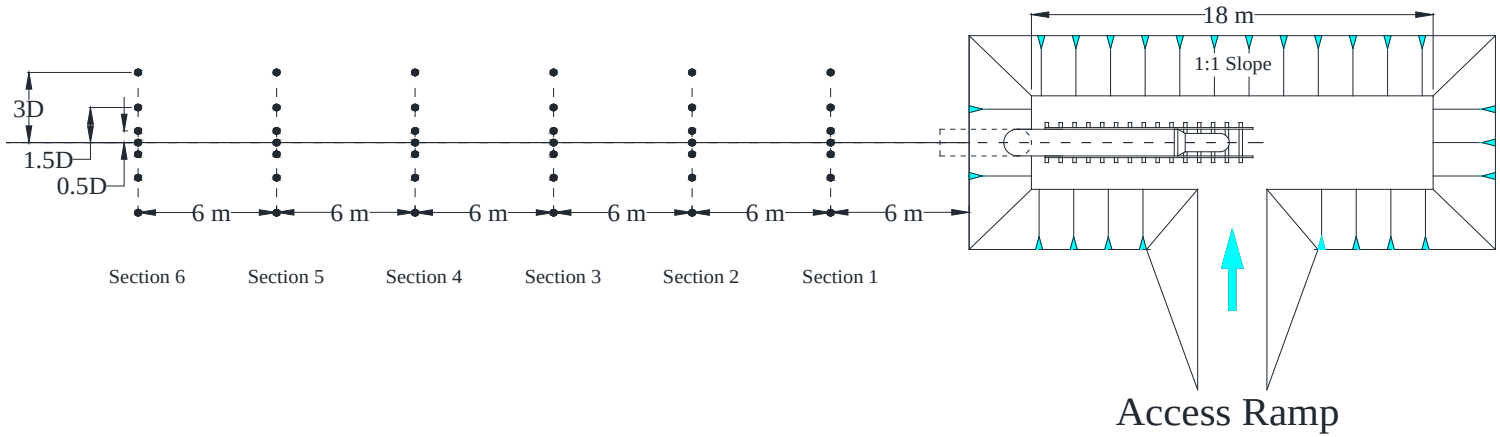

Figure 3.31: Location of the ground deformation monitoring points.

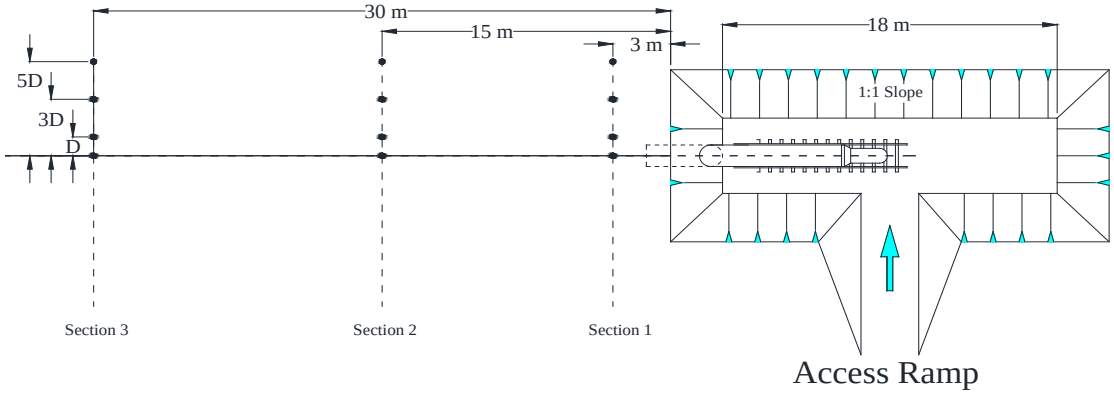

Figure 3.32: Location of ground vibration monitoring points.

3.2 SUMMARY

Evaluation and development of design models necessitates the generation of a database of actual performance measurements. Field observations are used herein to form the basis for such a database. We used database to understand the mechanics associated with pipe ramming installations, ranging from vertical ground movements, ground vibrations, and installation performance. This chapter presented the details of five production pipe ramming installations and a full-scale field experiment that form the basis of this study, including the subsurface conditions, pipes, hammers, instrumentation, and performance measurements. Table 3.1 summarizes the case histories along with the associated hammer and pipe properties. Subsequent sections of this report will describe the evaluation and development of models and methodologies that aim to address the gaps in knowledge identified in Chapter 2 in the context of the data described in this chapter.

Table 3.1: Summary of case histories

Project description	Pipe Diameter (mm)	Pipe Thickness (mm)	Pipe Length (m)	Ram Type	Rated Energy (kN-m)	Ram Size (mm)	Blow per min
Case 1: Pressurized water pipe Installation, Wildish Sand and Gravel Co. Site, Eugene, Oregon	610	13	33.5	HammerHead	6.4*	400	231
Case 2: Corrugated Metal Pipe (CMP) replacement project under Highway 21 at Allan's Creek, Ontario	2440	25	39	Grundoram Apollo	40.5	800	180
Case 3: Culvert replacement project under Interstate Highway 84 at Perham Creek, Oregon	3660	38	63	Grundoram Goliath Grundoram Taurus Grundoram Apollo IHC S-280	11.6 18.6 40.5 142.4	460 610 800 915	180 180 180 45
Case 4: Ramsey Town Center Storm water Conveyance Installation, Ramsey, Minnesota (Jensen et al. 2007)	2180 and twin 1980	—	45	Grundoram Taurus	18.6	610	180
Case 5: Water main Installation under US Highway 50, Rancho Cordova, California	760	16	66	Grundoram Koloss	6.8	355	220
Case 6: Full-scale Pipe Ramming Experiment at Emery & Sons, Inc., yard in Salem, Oregon	1060	12	35	HammerHead and Grundoram Taurus	6.4* 18.6	400 610	231 180

4 ANALYSIS OF SETTLEMENT

Vertical ground movements observed from three production installations (Cases 1, 4 and 5) and a full-scale field experiment (Case 6) are discussed in this chapter. The settlement measurements were observed using digital levels and total stations. The measurements and empirical model predictions of the ground deformations are compared to examine the applicability of the models. The accuracy and variability of the empirical models are evaluated using the bias, Λ, defined as the ratio of the observed and calculated ground movement (i.e., Λ = observed settlement / calculated settlement). An unbiased or accurate calculation produces a bias equal to unity. A bias greater than unity indicates an under-estimation of the model. A bias less than unity indicates an over-estimation of the calculated value. Sensitivity analyses were performed to identify the effect of various model parameters used in the empirical settlement prediction models on the estimated vertical ground movements. Refer to Chapter 3 for details regarding the locations of monitoring points and instruments used to observe movements for each project case study.

The main source of settlement in pipe ramming applications is generally considered to result from the collapse of the overcut (see Section 2.5). The overcut is created as result of a combination of the excavation of material and subsequent compaction of the non-excavated material by the cutting shoe, which is welded on to the leading edge of the pipe. Therefore, a portion or all of the volume of the overcut annulus can be considered in the analysis of settlement assuming that no volume change occurs in the soil mass (i.e. no dilation or contraction; note that this assumption may not be appropriate in granular soils where local vibrations can cause volume change, typically in the form of contraction). In general, the entire overcut is considered to contribute to settlement in the analysis for cases where lubrication is not forced into the overcut during driving (*Bennett 1998*). If lubricant or another material is injected into the overcut during driving, only part of the overcut volume should be adopted in the analysis of settlement (*Bennett 1998*). In case of volume change, dilation of the soil mass can lead to the less settlement whereas contraction of the soil mass (i.e. densification) results in settlements greater than that corresponding to the volume of overcut (*Bennett 1998*). Additionally, soil arching mobilized by the generation of the overcut can occur and prevent the soil from completely collapsing onto the pipe; in these instances, it is common to assume that approximately half of the overcut volume contributes to settlement (*Bennett and Wallin 2010*). In light of the possible settlement mechanisms, two cases of the overcut volume were considered for the analysis of settlement for the case histories: full collapse of the overcut, and partial collapse of the overcut (half-volume contribution). The settlement at each cross section was evaluated using the three empirical settlement prediction methods described in Section 2.5 (*i.e. O'Reilly and New 1982, Mair and Taylor 1997, and Cording and Hansmire 1975*). Heave estimates were based on the Bennett and Wallin (*2010*) approach described in Section 2.5.

4.1 CASE 1: PRESSURIZED WATER PIPE INSTALLATION, WILDISH SAND AND GRAVEL CO. SITE, EUGENE, OREGON

The ground deformation monitoring points (GDMPs) for Case 1 are shown in Figure 3.2, along with the plan and cross-section of the embankment. The GDMPs are established along four cross sections with each cross section having seven monitoring points. At each cross section, one monitoring point was located directly above the pipe, with three monitoring points on each side of the centerline at offsets of 0.75*D* (0.46 m), 1.5*D* (0.91 m) and 3*D* (1.83 m) where *D* equals the diameter of the pipe. The pipe installation was carried out underneath a two-tier embankment that supported an access road and powered conveyer (Figure 3.2). The depth of cover above the centerline of the pipe was 1 m for the access road crossing (i.e. where Section 1 is located), whereas the depth of cover equaled 3.75 m for the embankment that supported the conveyer belt. The soil comprising the embankment was characterized as a dense silty sand with an assumed peak friction angle, $\phi' = 42°$. The overcut, defined as the annular space between the cutting shoe and the pipe, defined as difference between the radius of the cutting shoe and pipe (equal to 315 mm and 305 mm, respectively) was 10 mm thick.

Figure 4.1 and Figure 4.2 present the vertical ground movement measured transverse to the advancing pipe at the top of the ground surface of the embankment along with the calculated settlement. At Section 1 (Figure 4.1), the magnitudes of settlement were observed to range from 1 to 8 mm. The comparison of the measured and calculated settlement at Section 1 shows that none of the empirical methods considered adequately capture the observed settlement for either overcut scenario considered. The error in the settlement models can be attributed to the small depth of cover under the embankment of the access road.

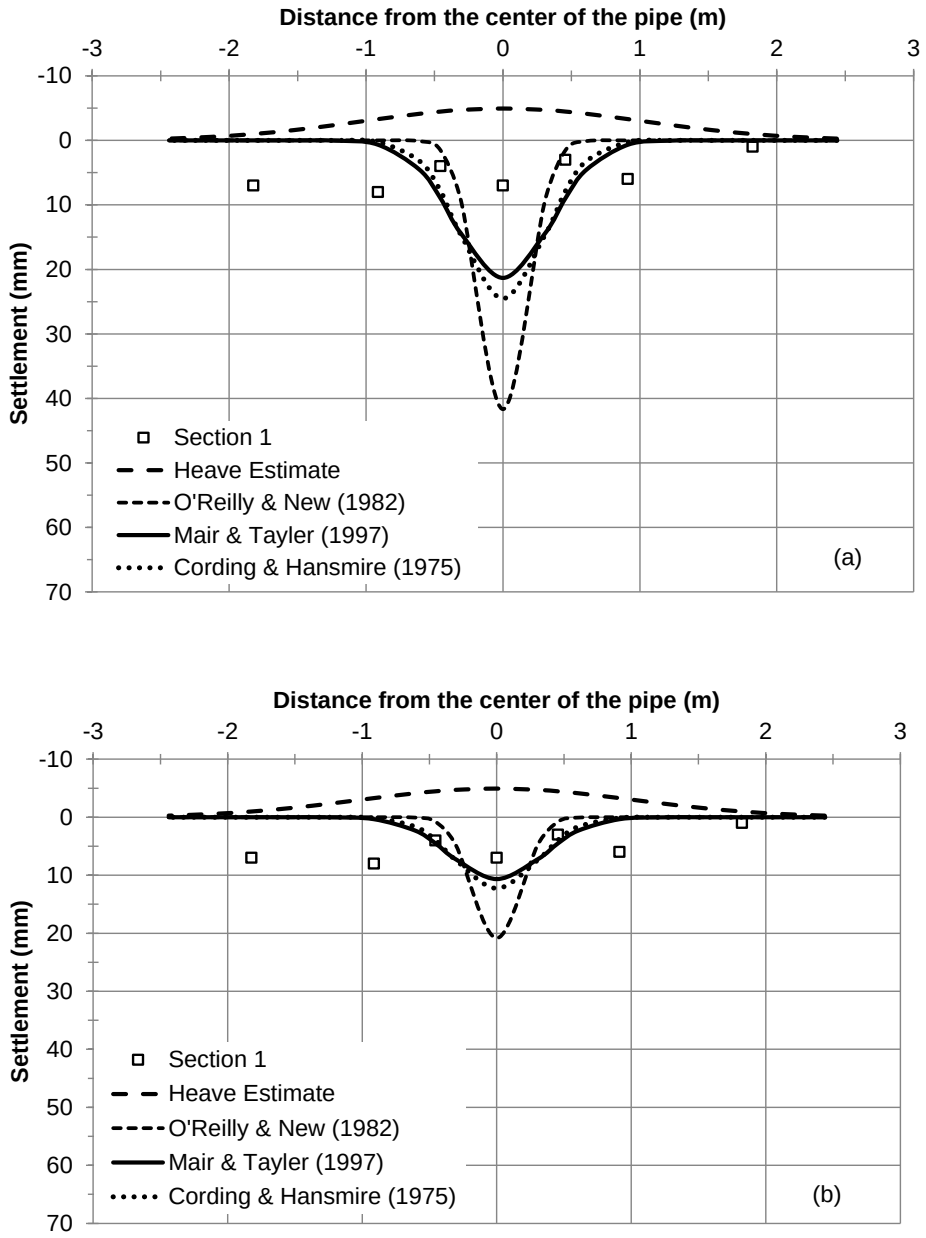

Figure 4.1: Observed and calculated ground movement profiles transverse to the advancing pipe for Case 1, at Section 1, considering (a) entire overcut volume, and (b) half of the overcut volume.

Figure 4.2 presents the monitoring results for Sections 2, 3 and 4. At Section 2, which lies along the crest of the embankment, the observed settlements were greater than those at Sections 3 and 4, the latter of which can be assumed to represent level ground conditions. This is attributed in part to the amplification of ramming-induced vibrations associated with slope crests (*Brennan and Madabhushi 2009*). Note that heave was observed at Section 4. In general, the maximum observed settlement and heave were approximately 14 and 6 mm, respectively, indicating that total magnitude of settlement is small to negligible (on the order of half an inch or less). Approximately 90 percent of all settlement observations were smaller than the 10 mm thick annulus generated by the cutting shoe overcut. The comparison of empirical model calculations and observed settlements at Sections 2, 3 and 4 appeared to capture the observation close to the

center of the pipe considering the entire volume overcut; however, measurements at distances greater than 1 m on either side of the center of the pipe indicate that settlements can be generated at distances farther than those suggested by the empirical models. The half overcut volume consideration led to overall underestimation of the settlements for all the three models employed. On the other hand, the heave model appears to capture the small number of observed heave data points fairly well.

Figure 4.3 compares the vertical ground deformation measurements at the centerline and centerline offset distances of 0.75*D* (0.46 m), 1.5*D* (0.91 m) and 3*D* (1.83 m) to the maximum (centerline) settlement calculated. The plot indicates over-estimation of the calculated settlement at Section 1 and 4 for entire overcut volume consideration; however, the models did slightly under-estimate settlement at Section 2 for reasons mentioned earlier. Thus, the calculation of centerline settlement using the empirical models appears to adequately capture the maximum observed pipe-ramming induced settlement. In the case where only half of the overcut volume was considered to contribute to settlement, underestimation of the calculated settlement was generally observed except for Section 1.

The accuracy of the empirical models can be assessed using the bias as discussed in the beginning of this section and as shown in Figure 4.4. Many sample biases of the three empirical models are greater than one, indicating an under-estimation of the settlement. For the case where the entire overcut volume has been considered, these instances have resulted from settlement observations at distances greater than 1 m on either side of the center of the pipe. On the other hand, some of the bias values are observed to be less than one, indicating an over-estimation of settlement. The over-estimated settlements are primarily due to the settlement observations close to the center of the pipe.

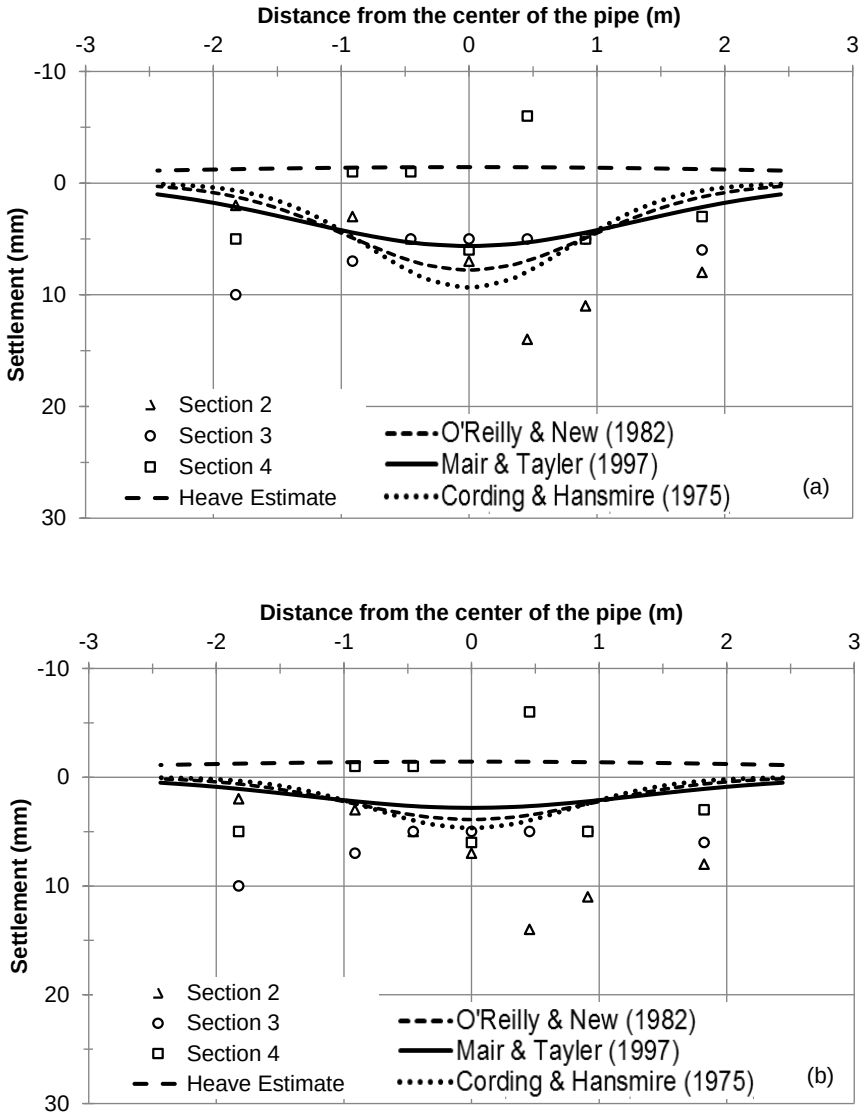

Figure 4.2: Observed and calculated ground movement profiles transverse to the advancing pipe for Case 1, at Sections 2,3 and 4, considering (a) entire overcut volume, and (b) half of the overcut volume.

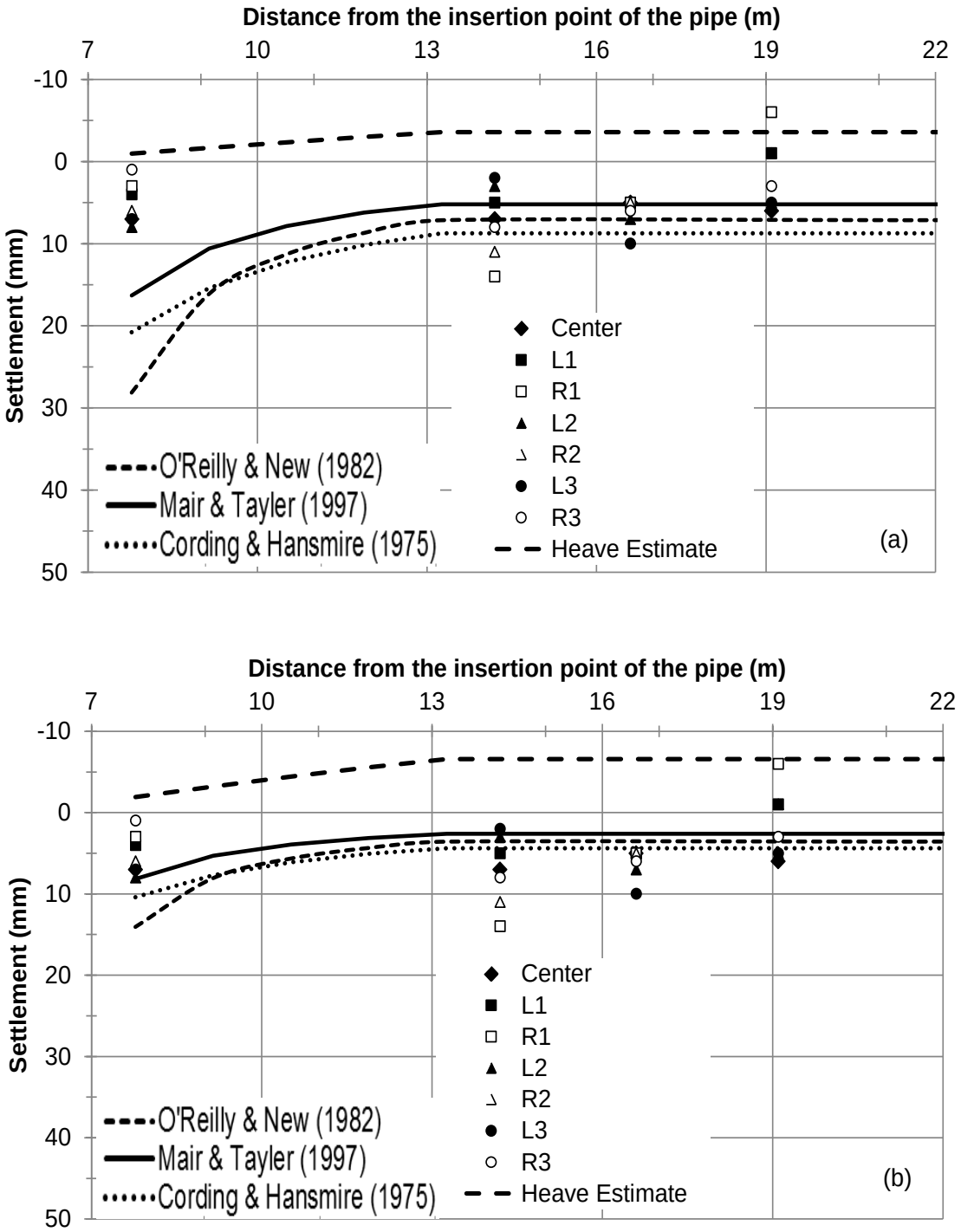

Figure 4.3: Case 1 observed vertical ground movements and calculated settlement profiles. The vertical ground movement calculations represent the centerline of the pipe in the longitudinal direction considering (a) entire overcut volume, and (b) half-overcut volume. The settlement measurements were observed along the center and offset distances of 0.75*D*, 1.5*D* and 3*D* (e.g., L1 = offset left 0.75*D*, R2 = offset right 1.5*D*).

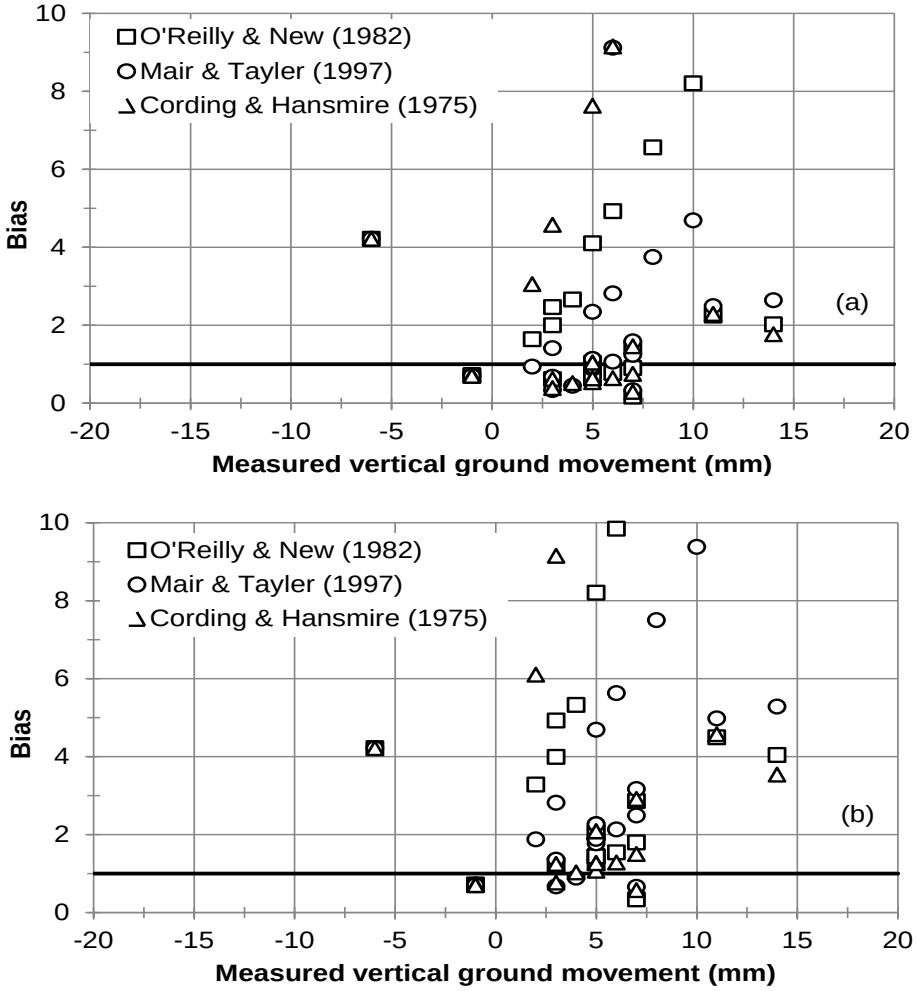

Figure 4.4: Sample biases for vertical ground deformation estimates for Case 1 considering (a) entire overcut volume, and (b) half of the overcut volume.

4.2 CASE 4: RAMSEY TOWN CENTER STORM WATER CONVEYANCE INSTALLATION, RAMSEY, MINNESOTA (*JENSEN ET AL. 2007*)

The storm water conveyance installation project for the Town Center of the City of Ramsey, Minnesota, was performed under an active railway embankment sensitive to settlement. Real-time settlement monitoring was carried out using 74 mini-prisms (i.e. ground deformation monitoring points) established along and parallel to the edges of railway (Figure 3.16) during the installation of the three casings under railroad tracks. Jensen et al. (*2007*) reported measurements for 22 of the mini-prisms located in the immediate vicinity of the casing installations. The total settlements observed during pipe ramming and their relative locations are provided in Table 4.1 and Table 4.2. The embankments under the railroad tracks are characterized by a silty sand topsoil underlain by alluvium layer of poorly graded sand with silt with an angle of internal friction $\phi' = 34°$ estimated using correlations to SPT N (*Wolff 1989, and Schmertmann 1975*). The depth of cover above the centerline of the casings was approximately 3.7 m (Figure 3.14). During the ramming process, the cutting shoe created an

overcut of 12.5 mm. Lubrication lines were welded to the casing, however, lubrication wasn't applied to the pipe during the drive (*D. Poduska, personal communication, 2012*). Similar to Case 1, two cases of overcut volume were considered for the purposes of making settlement estimates.

The settlements for each casing were computed using the three empirical settlement prediction models described in Section 2.5. However, to model the settlement for the twin casing installations, a modified inverted normal probability distribution curve was used, and is given by:

$$S_z(y) = S_{\max} \cdot [e^{-\frac{y^2}{2i^2}} + e^{-\frac{(y-d)^2}{2i^2}}] \quad \textbf{(4.1)}$$

where d equals the separation distance between the centerlines of the pipes. For Case 4, the casings were separated by 4.3 m (center-to-center).

Figure 4.5 and Figure 4.6 present the measured and computed settlement profiles in the direction transverse to the advancing pipe (i.e. along the north and south rail tracks) for the 2180 mm and twin1980 mm casings, respectively. The magnitudes of measured settlement ranged from 0 to 17 mm, indicating that the threshold of maximum acceptable settlement of 25 mm specified for the project was not exceeded. The measured and calculated settlements for both Case 4 sites exhibit fairly good agreement close to the center of the pipe for the half overcut volume case; however, the models resulted in a slight under-estimation at distances further from the center of the pipes. On the other hand, when the entire overcut volume was considered fairly good agreement between the measured and computed settlement resulted at distances further from the center of the pipes, and an over-estimates of settlement resulted near the center of the pipe. The sample biases are plotted in Figure 4.7, and lie near unity for many of the measured settlements for both entire and half overcut volume cases.

Table 4.1: Measured total settlements for the Case 4, 2180 mm pipe installation.

North track		South track	
Distance from the center of the pipe (m)	**Settlement (mm)**	**Distance from the center of the pipe (m)**	**Settlement (mm)**
6	1	6	2
4	1	1	14
2	8	-1	15
0	10	-3	8
-2	6	-5	1
-4	1		

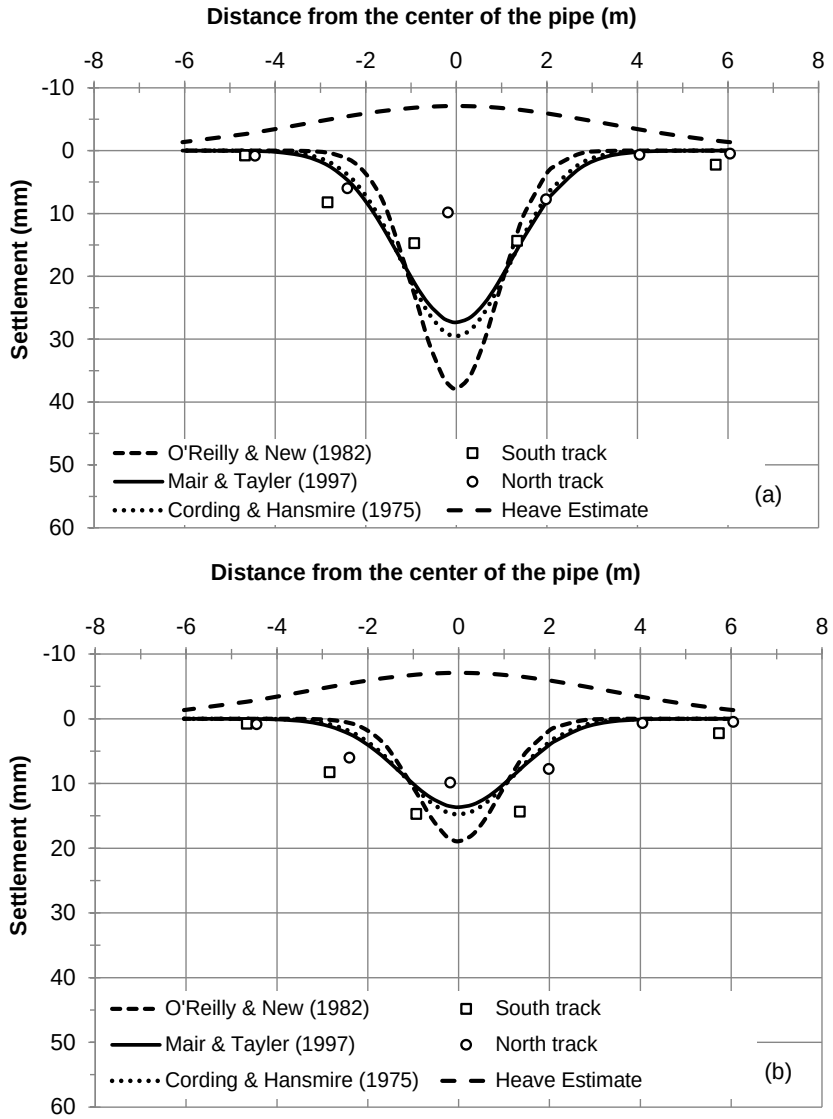

Figure 4.5: Observed and calculated ground movement profiles transverse to the advancing 2180 mm diameter pipe for Case 4, considering (a) entire overcut volume, and (b) half of the overcut volume.

Table 4.2: Measured total settlements for the Case 4, 1980 mm twin pipe installation.

North track		South track	
Distance from the center of the pipe 1 (m)	**Settlement (mm)**	**Distance from the center of the pipe 1(m)**	**Settlement (mm)**
-1	2	-3	2
1	8	-1	12
3	9	1	17
5	3	3	13
7	0	6	10
--	--	8	3

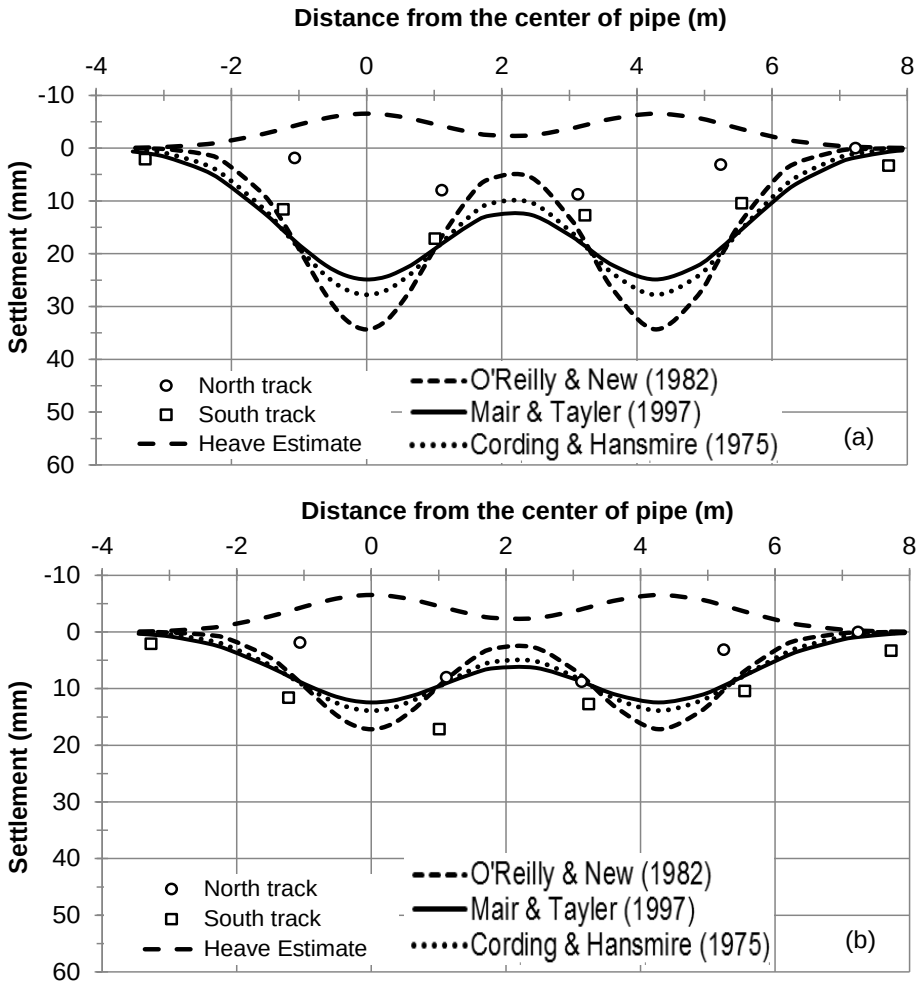

Figure 4.6: Observed and calculated ground movement profiles transverse to the advancing twin 1980 mm diameter pipes for Case 4, considering (a) entire overcut volume, and (b) half of the overcut volume.

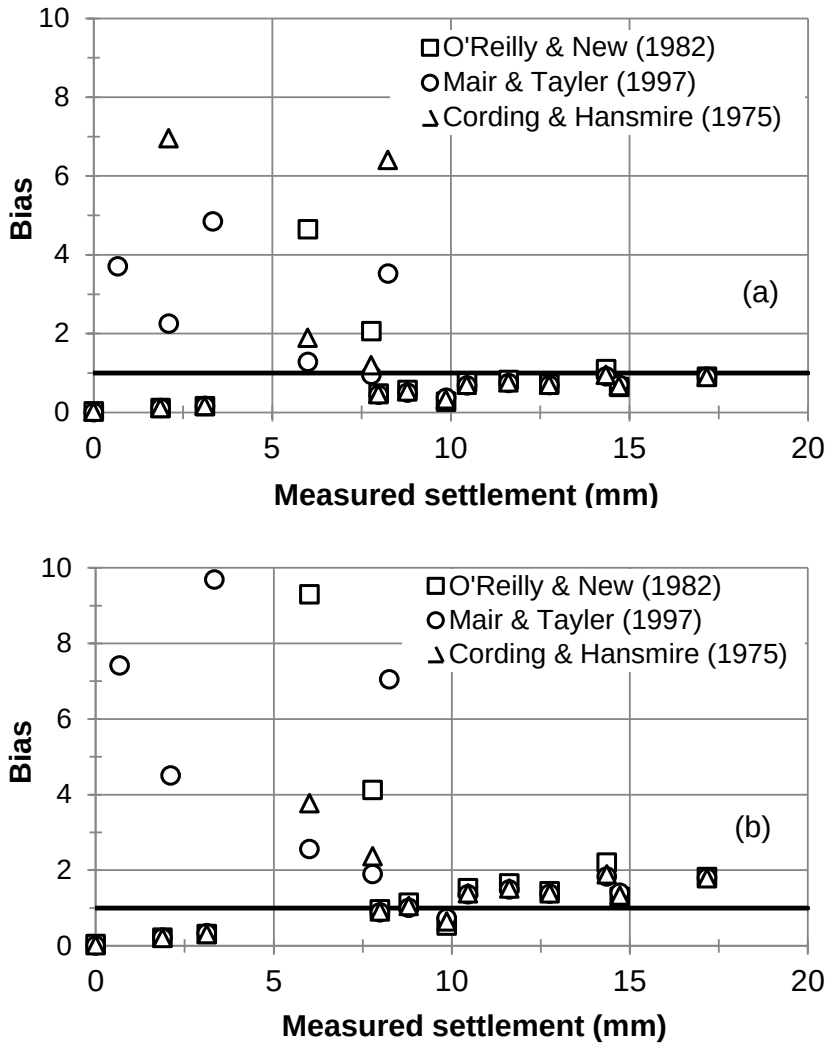

Figure 4.7: Sample biases for vertical ground deformation estimates for Case 4 considering (a) entire overcut volume, and (b) half of the overcut volume.

4.3 CASE 5: WATER MAIN INSTALLATION UNDER US HIGHWAY 50, RANCHO CORDOVA, CALIFORNIA

The City of Rancho Cordova executed a water main construction project that was required to cross below the ten-lane US Highway 50. Due to the impact to traffic, the risk of settlement-related damage during installation of the 760 mm diameter pipe was intolerable. The project team specified field instrumentation to monitor the potential for vertical ground movement along longitudinal direction of the pipe and at five cross sections in the transverse direction to the pipe. Figure 3.19 shows the location of the ground monitoring points relative to the location of insertion and receiving pit. The maximum measured settlement at each monitoring point is summarized in Table 4.3 and Table 4.4.

The roadway embankment under US 50 was characterized by poorly graded gravel with varying amounts of sand and cobbles (Figure 3.18) with an estimated angle of internal friction $\phi' = 36°$ (*Bennett and Wallin 2010*). The depth of cover above the center of the casing varied from 2.4 m

near the insertion pit, to 2.9 m beneath the center of the median, to 2.6 m near the reception pit (Figure 3.19). A 7 mm thick of overcut was assumed to be created by the cutting shoe based on photographs of the pipe provided by Bennett (*D. Bennett, personal communication, 2012*). Again, settlement comparisons were made using the two overcut volume cases.

Table 4.3: Measured total settlements for at cross sections in the transversal direction for 760 mm casing installation.

	GDMP Designation	Distance from the center of pipe (m)	Settlement (mm)
Northern ROW	101	3.0	2
	102	1.5	2
	103	0	3
	104	1.5	2
	105	3.0	3
West Bound 50 Median	106	3.0	1
	107	1.5	1
	108	0	1
	109	1.5	1
	110	3.0	2
East Bound 50 Median	111	3.0	2
	112	1.5	1
	113	0	1
	114	1.5	1
	115	3.0	2
Southern K-Rail	116	3.0	2
	117	1.5	3
	118	0	2
	119	1.5	2
	120	3.0	1
Southern ROW	121	3.0	3
	122	1.5	7
	123	0	8
	124	1.5	4
	125	3.0	3

Table 4.4: Measured total settlements by the reflectors along the centerline in the longitudinal direction.

GDMP Designation	130	131	132	133	134	135	136	137
Distance from the insertion pit (m)	54	50	46	42	31	27	23	19
Settlement (mm)	2	2	1	0	2	3	0	2

The accuracy of the three empirical settlement models was evaluated by comparing the settlement calculated to that observed on US 50. Figures 4.8 to 4.11 compare the measured settlements and model calculations in the transverse and longitudinal directions. The largest settlement was measured at the Southern ROW and Southern K-Rail, which could be attributed to the shallow depth of cover as compared to the Northern ROW and the center of the median.

In general, the measured settlements are smaller than 5 mm, except near the Southern ROW. For radial distances greater than 2 m from the centerline of the pipe, the calculated settlement under-estimated the measured settlement when half of the overcut volume was assumed to contribute to settlement. However, good agreement between the model calculations and measurements were observed at the center and radial distances less than 2 m (i.e. 1.3*D* to 2.6*D*). When the entire overcut volume is assumed to contribute to settlement, the computed settlement overestimated the actual settlement near the pipe centerline and improved with increasing distance away from the centerline.

Monitoring points were placed along the centerline to provide additional resolution for the observed settlement profile directly below the pipe (Figure 3.19). Figure 4.11 shows the vertical ground deformations measured along and parallel to the pipe centerline and at 2*D* and 4*D* in comparison to the calculated centerline settlement. All of the observed settlements were less than the calculated maximum settlements for both cases of overcut volume considered. The effect of the depth of cover is clearly shown in the Figure 4.11, with larger settlements corresponding to the smallest depth of cover.

Figure 4.12 presents the sample biases for each of the settlement estimation methods. Sample biases that lie between zero and unity indicate an over-estimate of settlement and correspond to observations near the center of the pipe. Those sample biases that are greater than unity represent an under-estimate of the actual settlement magnitude and correspond to measurements away from the center of the pipe.

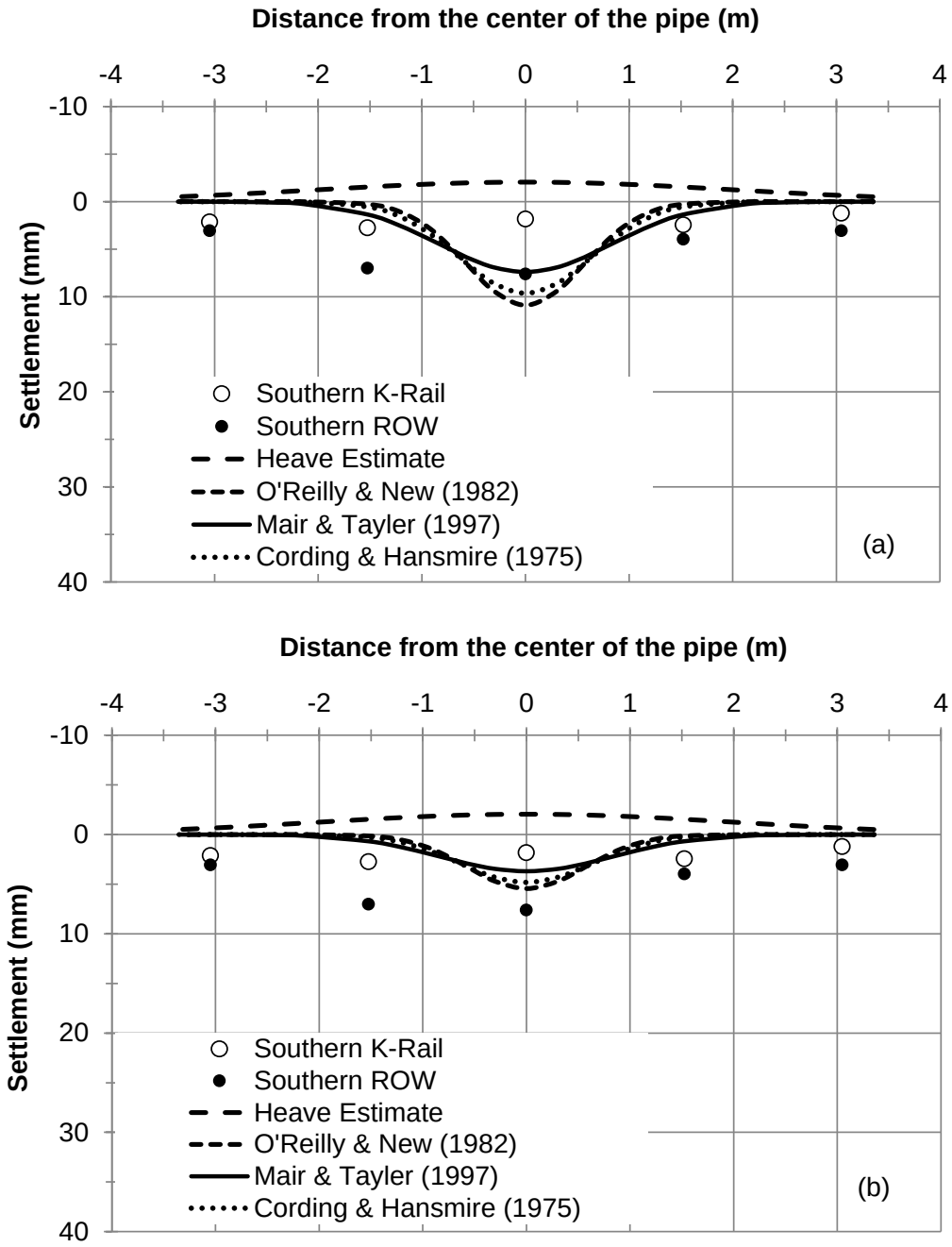

Figure 4.8: Observed and calculated ground movement profiles transverse to the advancing pipe for Case 5, at Southern ROW and Southern K-Rail, considering (a) entire overcut volume, and (b) half of the overcut volume.

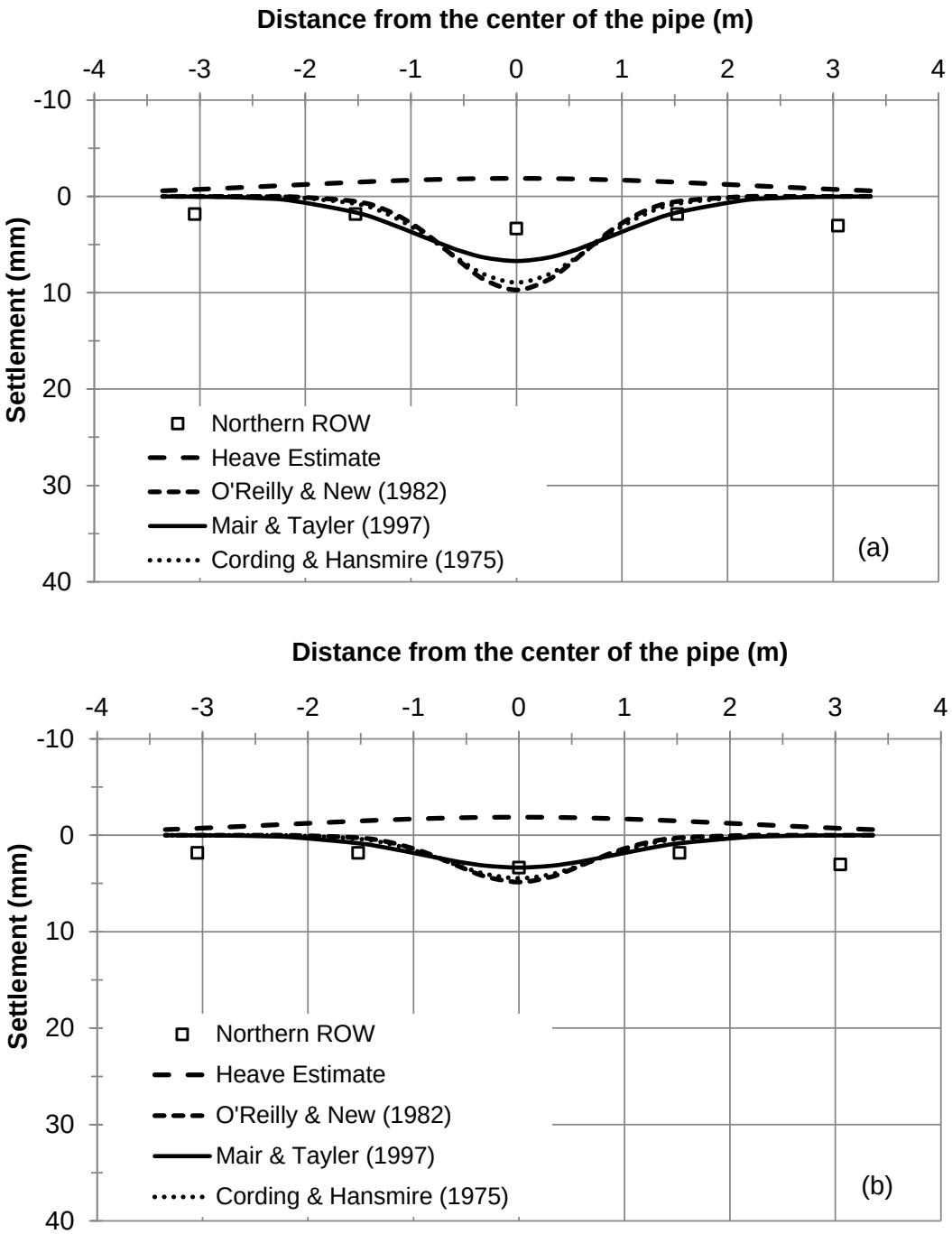

Figure 4.9: Observed and calculated ground movement profiles transverse to the advancing pipe for Case 5, at Northern ROW, considering (a) entire overcut volume, and (b) half of the overcut volume.

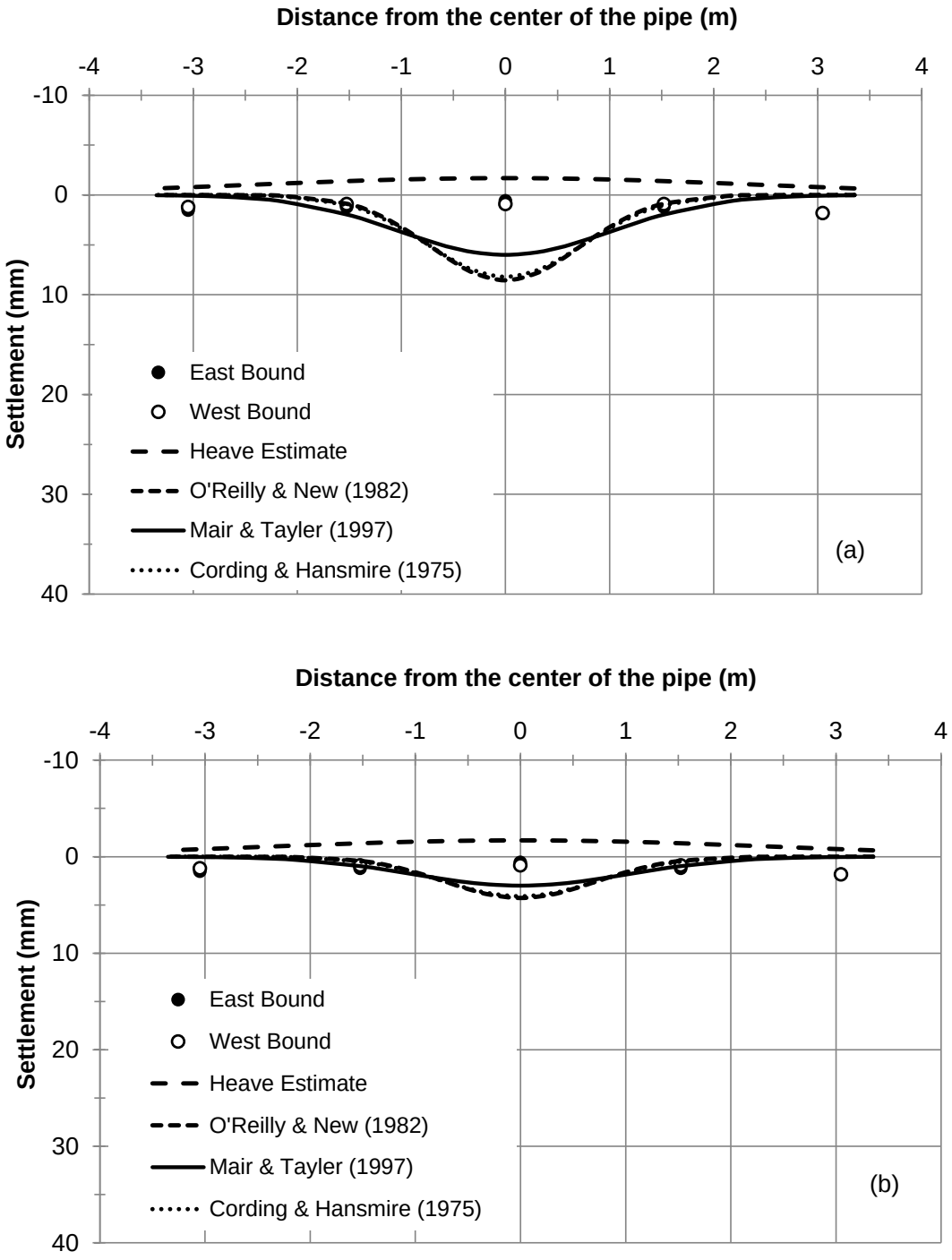

Figure 4.10: Observed and calculated ground movement profiles transverse to the advancing pipe for Case 5, at East and West Bound, considering (a) entire overcut volume, and (b) half of the overcut volume.

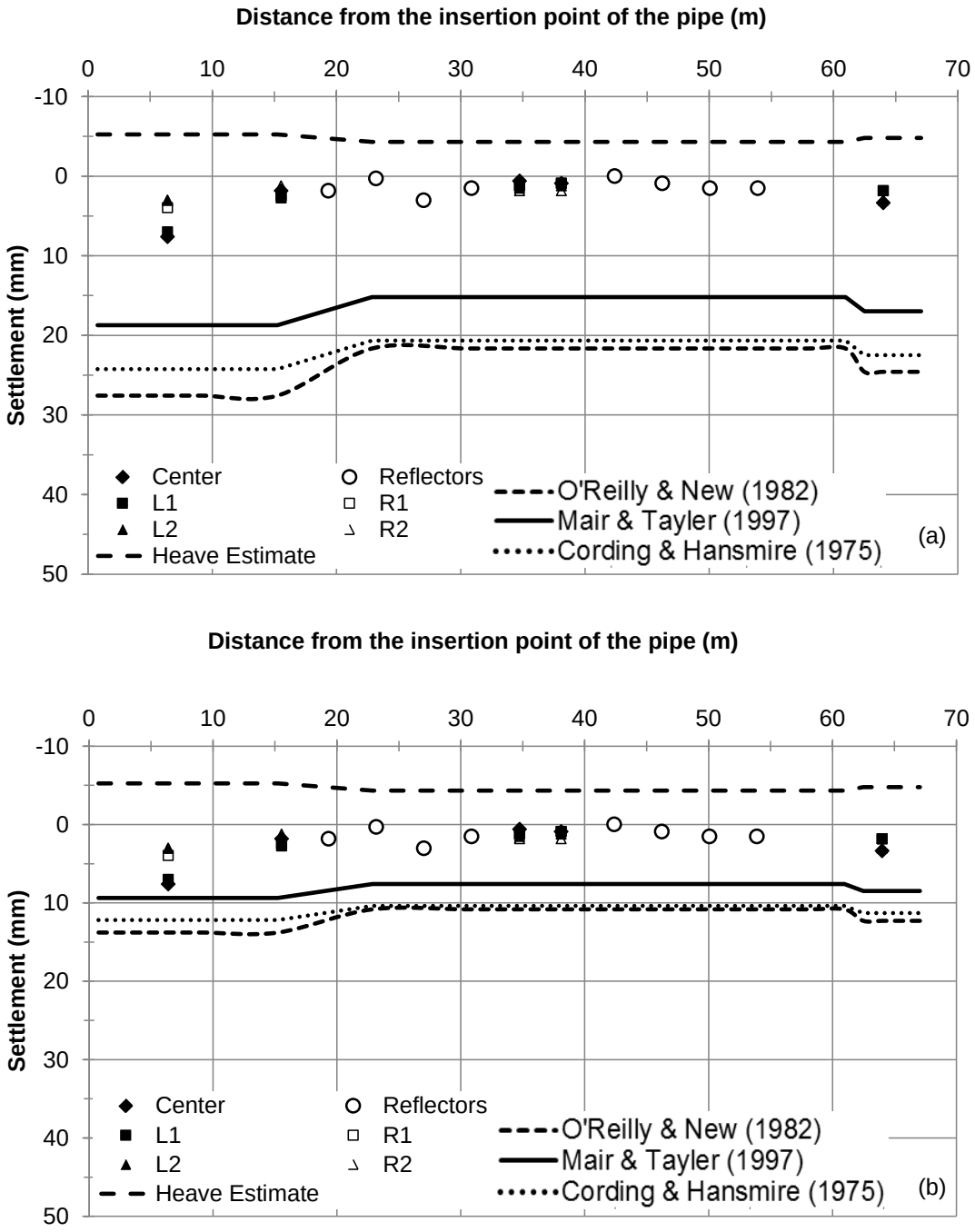

Figure 4.11: Case 5 observed vertical ground movements and calculated settlement profiles. The vertical ground movement calculations represent the centerline of the pipe in the longitudinal direction considering (a) entire overcut volume, and (b) half-overcut volume. The settlement measurements were observed along the center and offset distances of 2*D* and 4*D* (e.g., L1 = offset left 2*D*, R2 = offset right 4*D*).

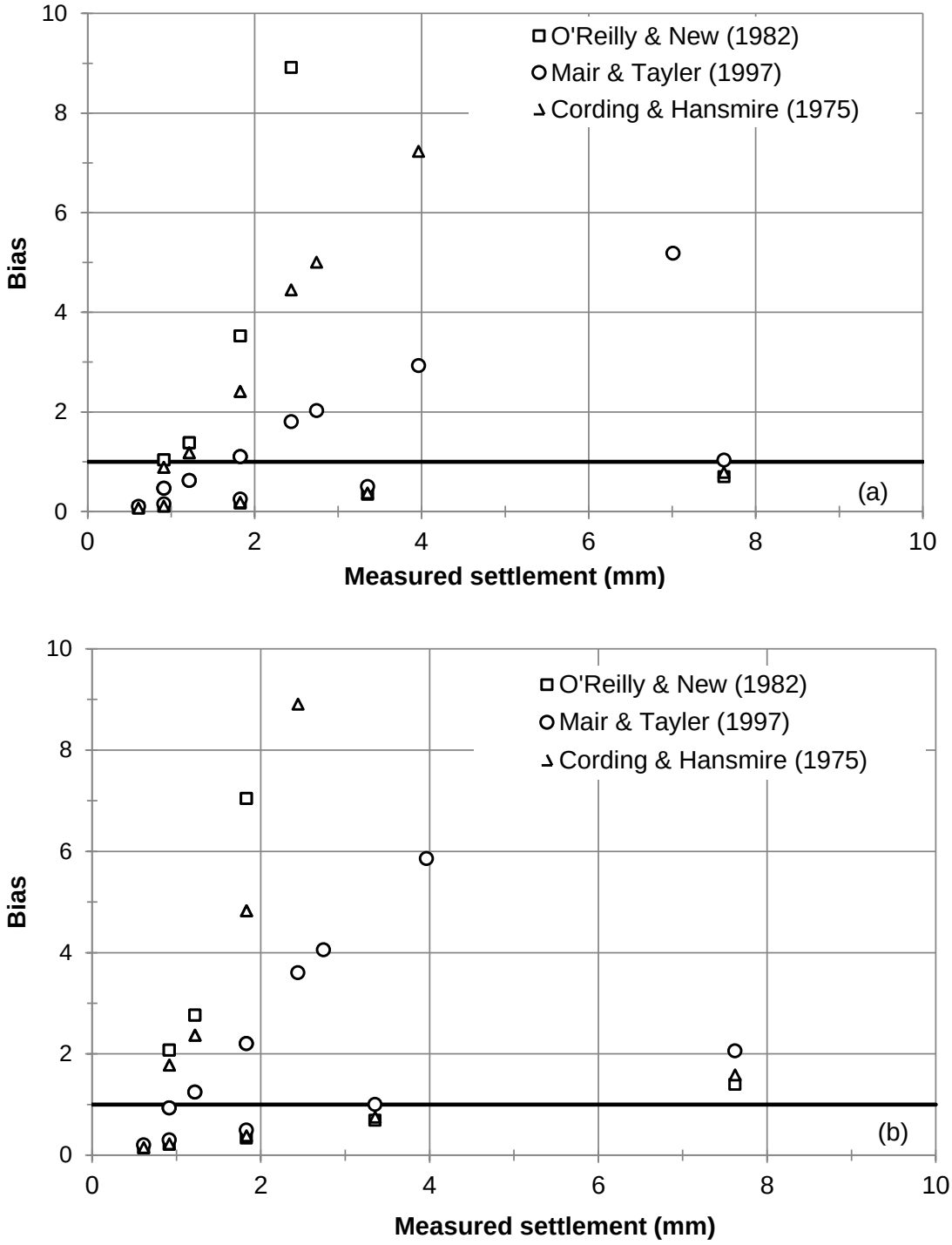

Figure 4.12: Sample biases for vertical ground deformation estimates for Case 5 considering (a) entire overcut volume, and (b) half of the overcut volume.

4.4 CASE 6: FULL-SCALE PIPE RAMMING EXPERIMENT AT EMERY & SONS SITE NEAR SALEM, OREGON

The locations of the GDMPs at the Case 6 experimental project were established along six cross sections with each cross section having seven monitoring points, as discussed in Section 3.6 (Figure 3.31). At each cross section, one monitoring point was located directly above the pipe and three monitoring points were established on each side of the centerline at offset distances of 0.5*D* (0.53 m), 1.5*D* (1.6 m) and 3*D* (3.2 m), where *D* equals the diameter of the pipe (Figure 3.31). The subsurface conditions at the site were characterized as dense silty sandy gravel with a significant number of cobbles (Section 3.6.2), and $\phi' = 48°$ as obtained from laboratory triaxial testing. The depth of cover above the centerline of the pipe was 1.7 m. The overcut created by the cutting shoe during installation was 10 mm; lubrication was applied for part of the installation as described in Section 3.6.4. Similar to the previous cases, settlement estimates were calculated assuming partial and full collapse of the overcut.

Figure 4.13 presents the vertical ground movement observed transverse to the advancing pipe and the computed settlement profiles. In general the measured settlements are less than or equal to 5 mm for the majority of GDMPs, although ground heave in the range of 1 to 3 mm was also observed. Note, the accuracy of the settlement measurements was 1.5 mm, such that much of the observed movement falls within the possible measurement error. Comparison of the model estimates and measured settlements at the different cross-sections demonstrate a greater degree over-estimation close to the center of the pipe and slight under-estimation at radial distances greater than 1 m (1D), similar to the previous three cases. Figure 4.14 shows the vertical ground deformation measurements along and parallel to centerline of the pipe, and the maximum centerline model profiles in the longitudinal direction. The settlements are found to be over-estimated along all cross sections. Figure 4.15 presents an alternate view of the model over-estimates, with most sample biases falling below unity.

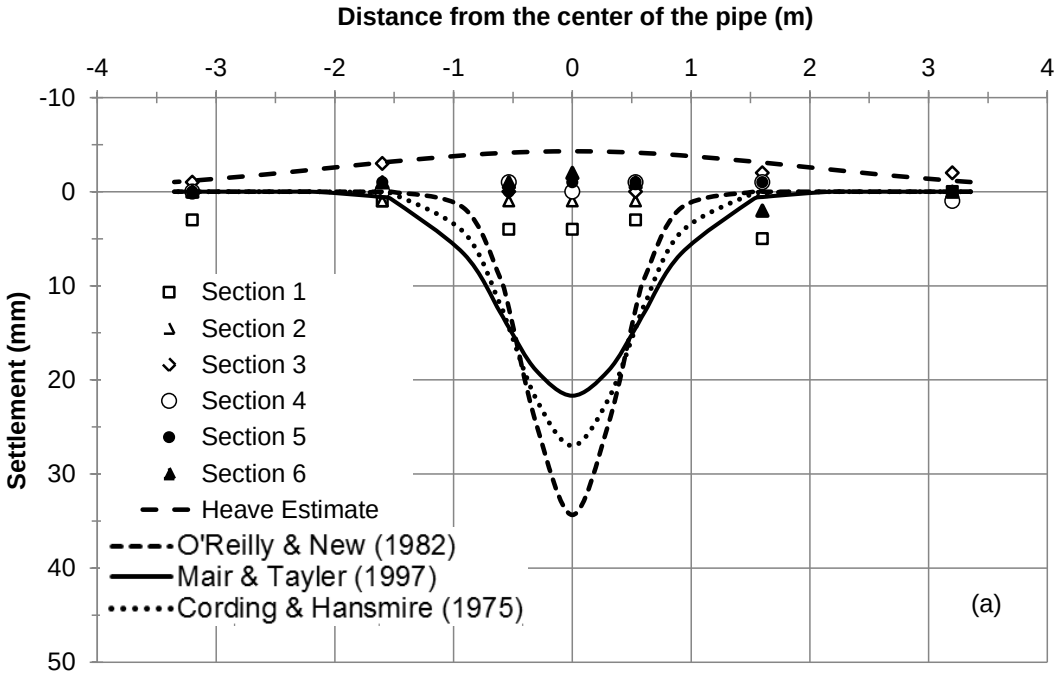

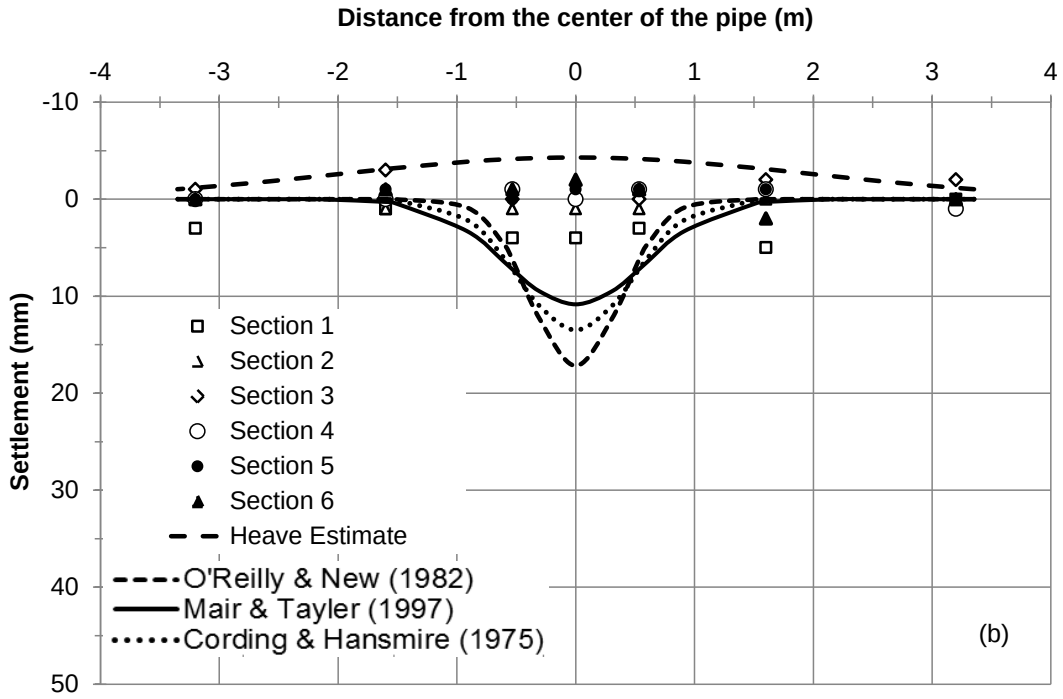

Figure 4.13: Observed and calculated ground movement profiles transverse to the advancing pipe for Case 6, considering (a) entire overcut volume, and (b) half of the overcut volume.

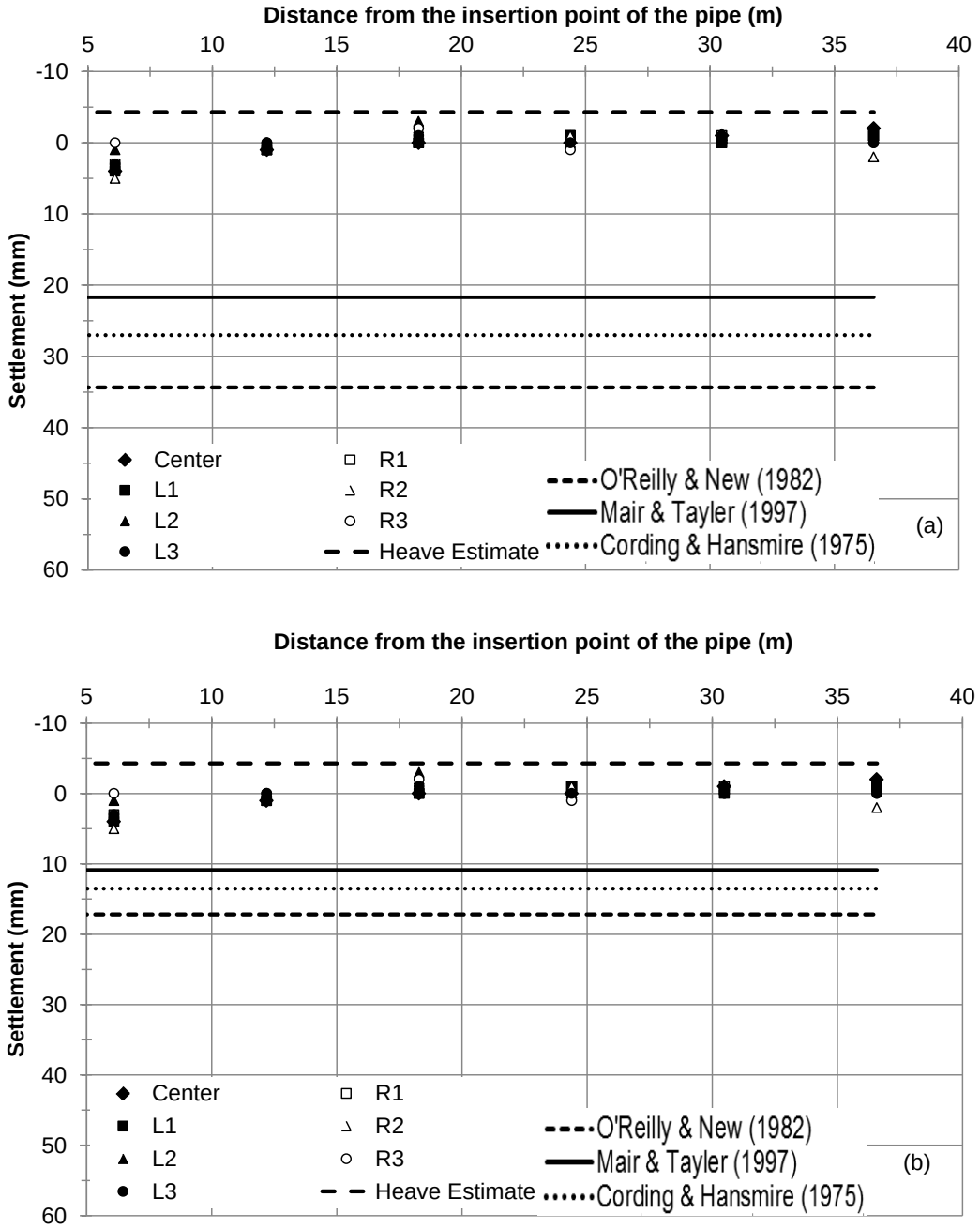

Figure 4.14: Case 6 observed vertical ground movements and calculated settlement profiles. The vertical ground movement calculations represent the centerline of the pipe in the longitudinal direction considering (a) entire overcut volume, and (b) half-overcut volume. The settlement measurements were observed along the center and offset distances of 0.5*D*, 1.5*D* and 3*D* (e.g., L1 = offset left 0.5*D*, R2 = offset right 1.5*D*).

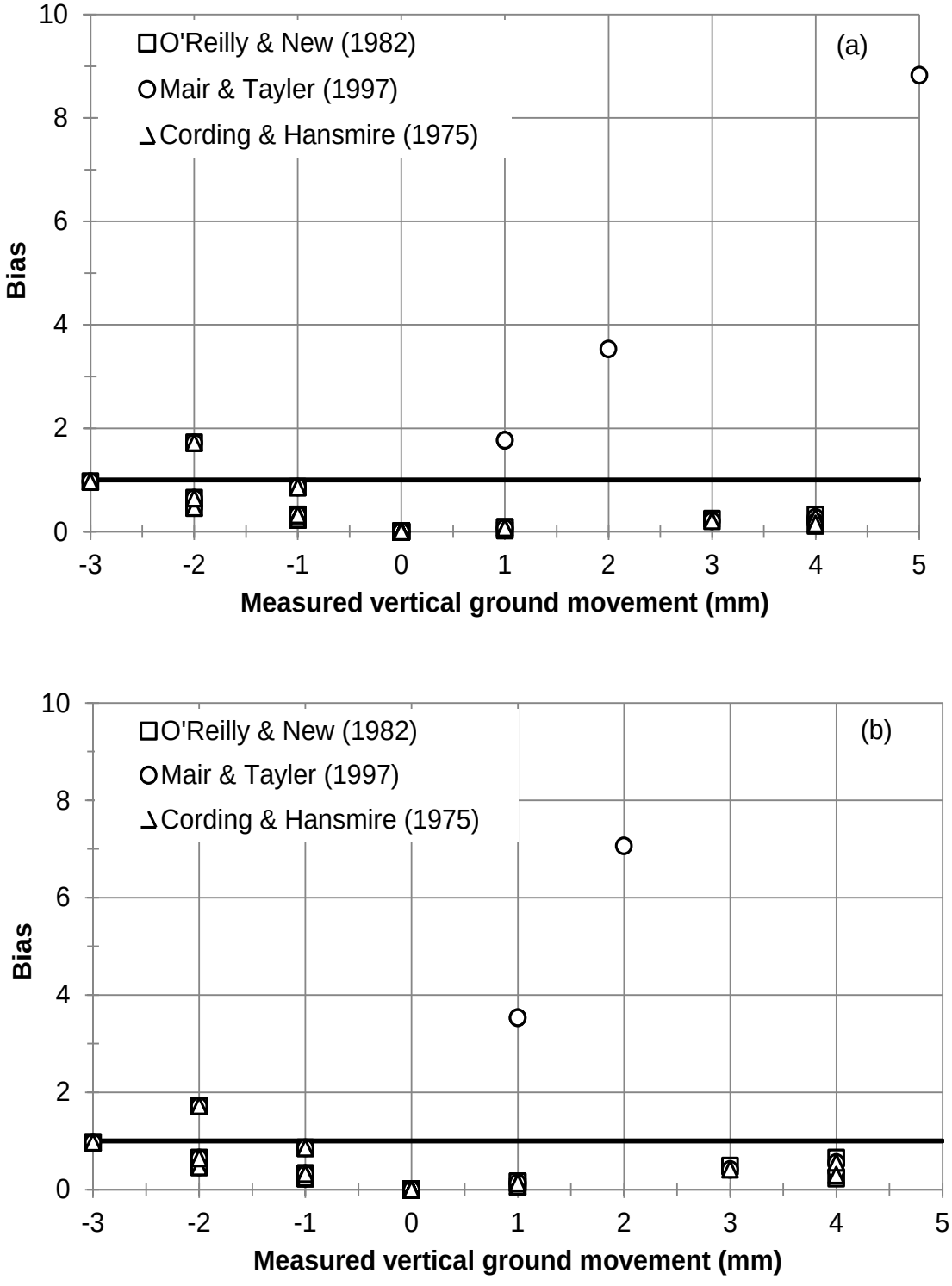

Figure 4.15: Sample biases for vertical ground deformation estimates for Case 6 considering (a) entire overcut volume, and (b) half of the overcut volume.

4.5 EVALUATION AND DEVELOPMENT OF SETTLEMENT MODELS

4.5.1 Global Accuracy of Selected Settlement Models

The observed production installations and the full-scale field experiment analyzed in this section generally correspond to pipes driven in granular soils. Therefore, the settlement measurements were compiled into a single dataset and compared to the empirical inverted normal probability distribution-based models to examine the overall or global performance of the models. It is noted that approximately 97 percent of all settlement observations were smaller than 10 mm indicating the total magnitude of settlement induced by pipe ramming to be very small or negligible.

Figure 4.16 presents the total vertical ground movement observations and corresponding estimates for the O'Reilly and New (*1982*), Mair and Taylor (*1997*), and Cording and Hansmire (*1975*) empirical models and considering either the entire overcut volume or half of the overcut volume. The solid line represents a one-to-one line between the observations and model estimates, whereas the dashed line represents one standard deviation of the model residuals (i.e., errors) added or subtracted from the one-to-one line. Most of the measured settlements fall within one standard deviation of the residuals for both collapse volumes considered. The bounds indirectly indicate the level of uncertainty associated with model estimates; the narrower bound indicates better global model accuracy whereas wider bounds indicate poor global accuracy. In general it appears that assuming that arching develops above the pipe and that only half of the overcut volume contributes to the observed settlement provides a more accurate and less variable estimate of vertical ground movement. All three methods produce relatively smaller standard deviations in the model errors as compared to the assumption of full collapse of the overcut. In general, the Mair and Taylor (*1997*) model provided the least global model error, followed by Cording and Hansmire (*1975*) and O'Reilly and New (*1982*), as shown in Figure 4.16.

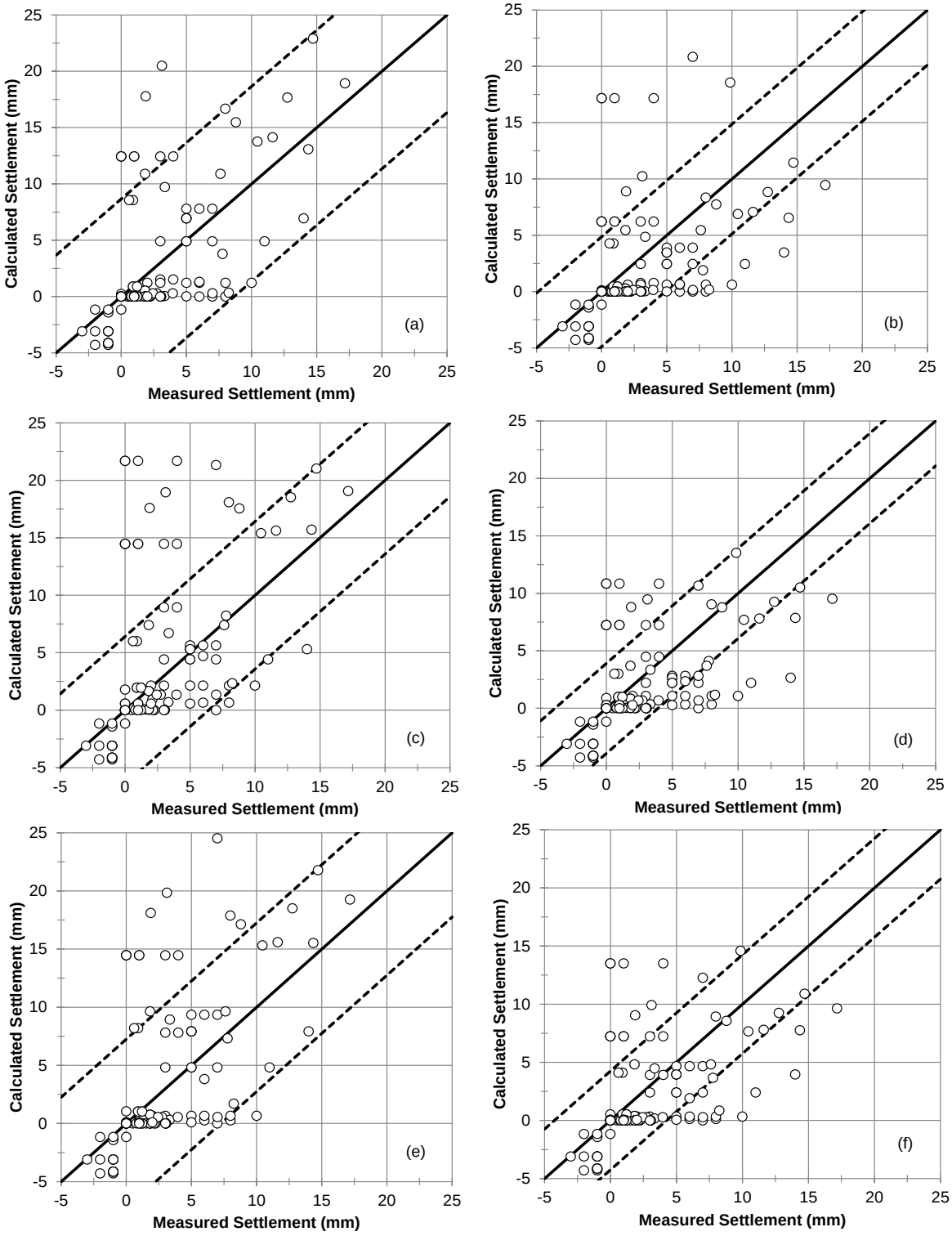

Figure 4.16: Settlement observation and model estimations based on O'Reilly and New (*1982*) considering (a) entire overcut volume and (b) half overcut volume; Mair and Taylor (*1997*) considering (c) entire overcut volume and (d) half overcut volume; Cording and Hansmire (*1975*) considering (e) entire overcut volume and (f) half overcut volume.

4.5.2 Development of a Pipe Ramming-specific Settlement Model

The settlement models analyzed were based on the inverted normal probability distribution curve approaches originally proposed by Schmidt (*1969*) and Peck (*1969*). In general the comparison of the measured settlement and model estimates reveal an overestimate of the settlement close to the center of the pipe and underestimate of settlement at radial distances away from the center of the pipe. Therefore, the settlement computations based on an inverted normal probability distribution model may not be provide a satisfactory estimate of the settlement induced by pipe ramming in granular soils. The Gaussian curve (i.e., normal distribution) was also noted to provide a poor settlement estimate for tunneling by Celestino et al. (*2000*), Vorster et al. (*2005*), and Marshall et al. (*2010*).

Based on these findings, a different model curve may be required to generate a better estimate of the vertical settlement induced by pipe ramming in granular soils. A three parameter, hyperbolic model, commonly used to represent the stiffness degradation of soil and rock (i.e. shear-modulus reduction curve) subjected to seismically-induced cyclic ground motions (*Stokoe et al. 1999*), was adopted and modified for settlement analysis induced by pipe ramming. The model has been evaluated for the purpose of modeling settlement in tunneling (*Celestino et al. 2000*) and yields satisfactory estimates. The formulation of the hyperbolic model is given by (*Celestino et al. 2000*):

$$S_z(y) = S_{\max}\left(1+\left(\frac{y}{a}\right)^b\right)^{-1} \qquad \textbf{(4.2)}$$

where S_{max} = the maximum settlement at the center, and is given by:

$$S_{\max} = \frac{V_s \cdot b \cdot \sin\left(\frac{\pi}{b}\right)}{2\pi a} \qquad \textbf{(4.3)}$$

and a and b = parameters related to the width and the shape of the settlement trough respectively. The maximum settlement S_{max} can be obtained by equating the total volume of settlement trough and the ground loss due to the over-cut, V_s:

$$V_s = \frac{\pi}{4}\left[D_c^2 - D^2\right] = \int_{-\infty}^{\infty} S_z(y)\, dy = \left(\frac{2\pi a}{b \cdot \sin\left(\frac{\pi}{b}\right)}\right) \cdot S_{\max} \qquad \textbf{(4.4)}$$

where V_s = volume of soil loss per unit of length, D_c = external diameter of the cutting shoe or excavated bore, and D = external diameter of the pipe. The parameter a and b are expected to vary with depth of cover, pipe size, soil type and soil property (e.g. density, consistency). Identification of a and b can be based on nonlinear least-squares curve fitting approximation. For pipe ramming induced settlement, the parameter which controls the width of the settlement

trough can be related to the dimensionless depth z/D (where z is the depth of the pipe to center of the pipe and D is the pipe diameter) using a linear equation given by:

$$\frac{a}{D} = m\left(\frac{z}{D}\right) + n \qquad \textbf{(4.5)}$$

where m and n are constants. The parameter b governs the shape of the curve and should be greater than unity. Ordinary least squares optimization provided parameters values of m = 0.8, n = 0.4 and b = 5 for the pipe ramming installations in medium dense to dense granular soils (e.g., Case 1, 4, 5, and 6). This approximation renders a slightly conservative estimate of the settlement, with about 60 percent of the settlement estimates slightly higher than the measurement.

Figure 4.17 presents the vertical settlement estimates of the proposed model for all previously discussed case histories (Case 1, Case 4, Case 5, and Case 6) and the comparisons with settlement observation in the transversal direction to the advancing pipe. Unlike the inverted normal probability distribution models, the proposed model provided a good match of the model estimates and settlement measurements both at the center and at radial distances from the center of the pipe. The bias plot on Figure 4.18 also reinforces the goodness of fit of the proposed model estimates to the observations.

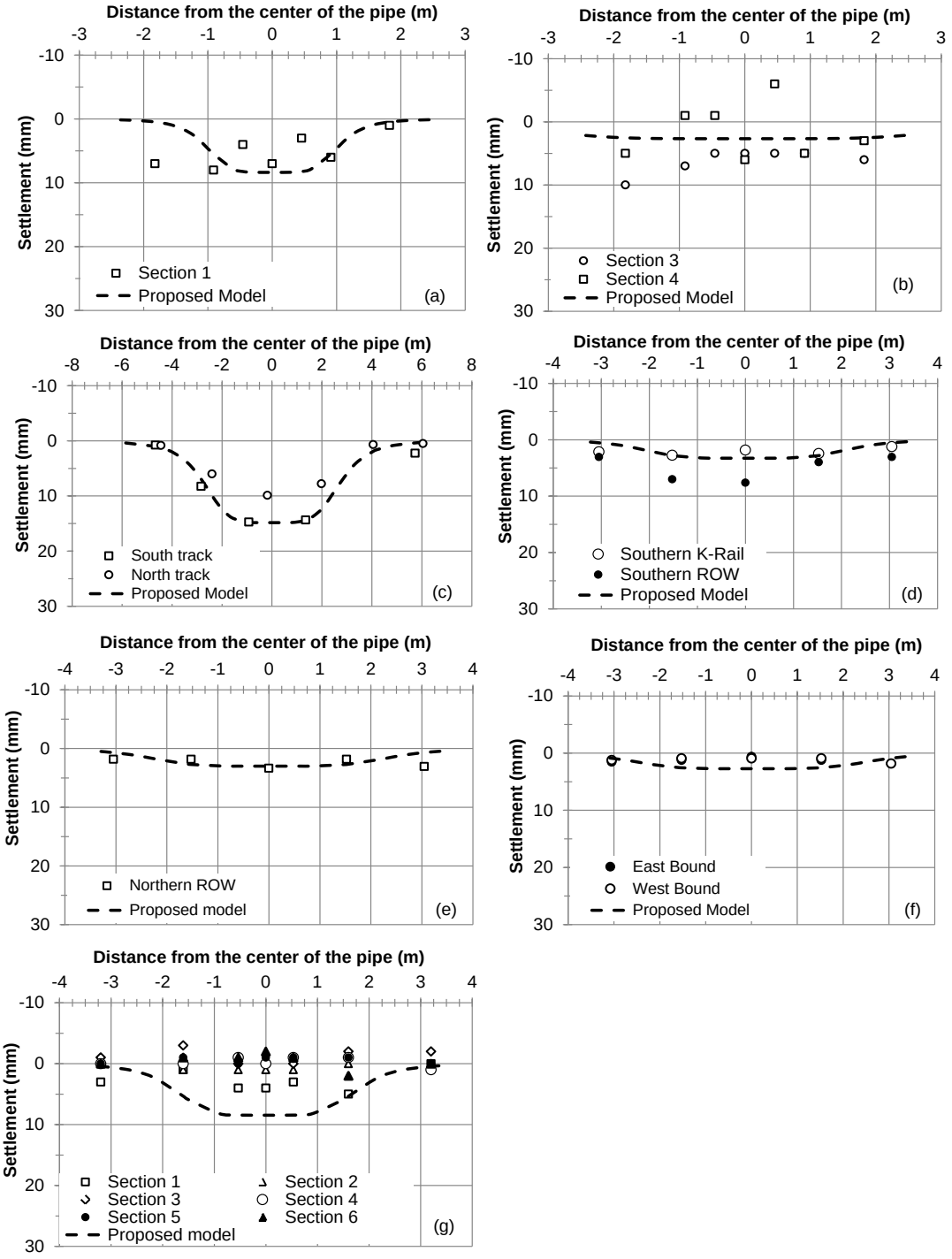

Figure 4.17: Settlement observation and proposed model estimates at (a) Section 1 for Case 1 (b) Section 2, 3 and 4 for Case 1 (c) South and North track for Case 4 (d) Southern K-Rail and ROW for Case 5(e) Northern ROW for Case 5 (f) East- and West bound lanes for Case 5, and (g) Sections 1 through 6 for Case 6.

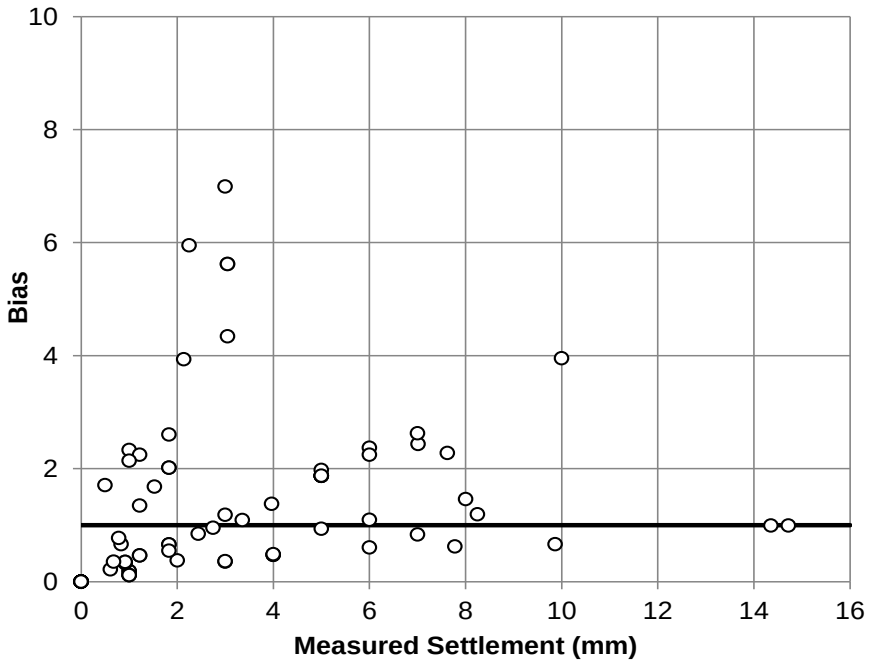

Figure 4.18: Proposed model biases for the entire database.

4.5.3 Parametric Analysis of Proposed Settlement Model

The effect of the new hyperbolic settlement model parameters on the calculated settlement was investigated by performing a sensitivity analysis. The model parameters investigated included the depth of cover above the crown of the pipe (*h*), the diameter of the pipe (*D*), and the overcut thickness (*OC*). The model parameters were varied one at a time over the range of values anticipated with a pipe ramming project, with baseline values of h = 5 m, D = 600 mm, and OC = 10 mm. Figure 4.19 presents the results of the parametric analysis, and shows the significance of the overcut thickness (*OC*) on the settlement estimate. The settlement magnitudes are moderately sensitive to the depth of cover and the diameter of the pipe. The model estimates that the magnitude of settlement increases rapidly with depths of cover less than 4 m.

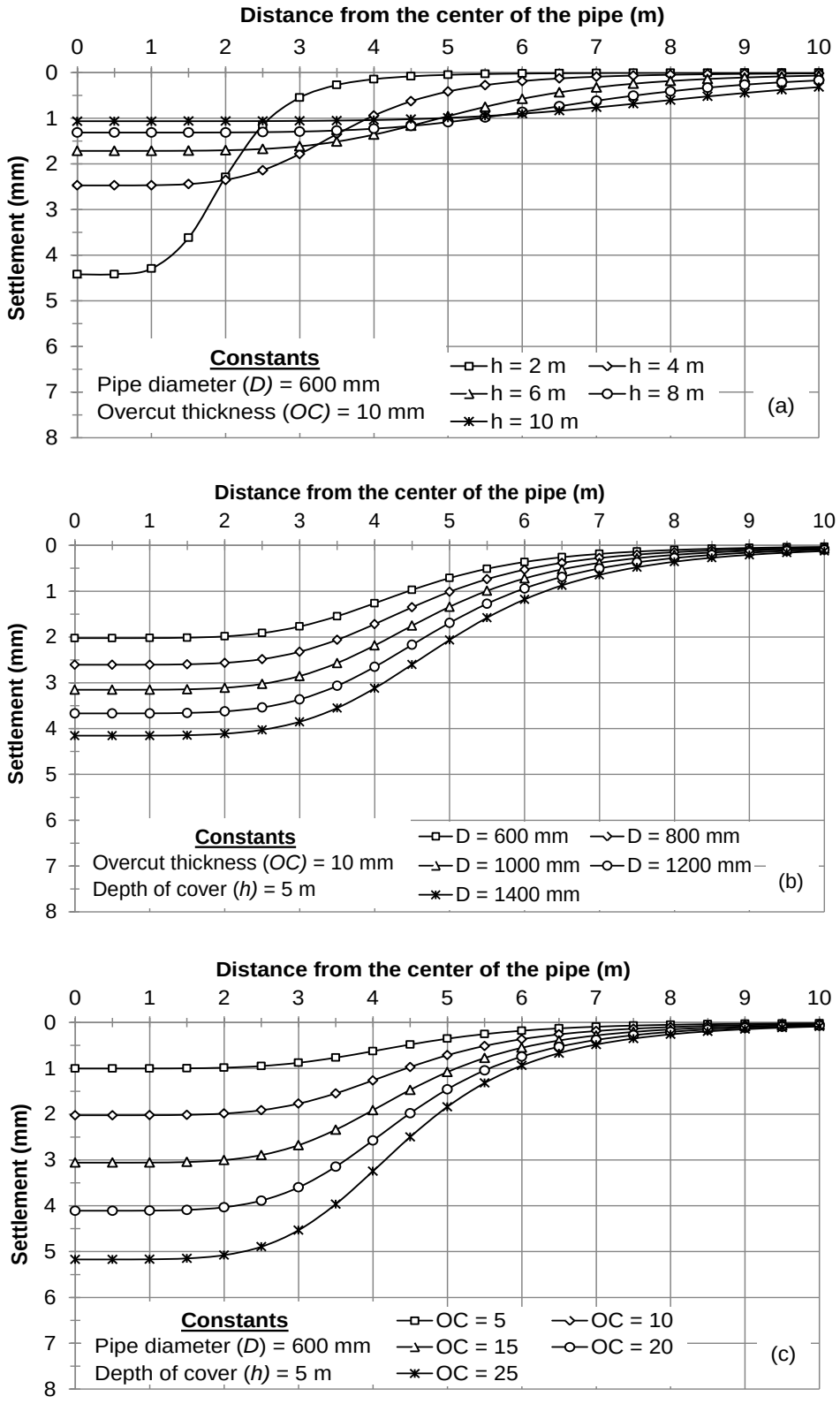

Figure 4.19: Parametric analysis of settlement prediction by varying (a) depth of cover above the crown of the pipe (b) diameter of the pipe, and (c) diameter of the cutting shoe.

4.5.4 Estimation of Settlement Based on In-situ tests

The magnitude of the settlement induced by pipe ramming should be sensitive to the relative density of the soil. However, ascertaining the relative density of granular soils directly is rarely feasible due to the difficulties associated with recovering undisturbed samples from borings, particularly in clean sands, gravels, and larger particles. In-situ tests, such as the standard penetration test (SPT) and the cone penetration test (CPT) (*Meyerhof 1965, Schmertmann et al. 1970, and Berardi et al. 1991*) have been used to correlate to geotechnical performance metrics to circumvent sampling problems. The settlement induced by pipe ramming may also be estimated from in-situ tests by developing a correlation between the maximum settlement and SPT blow count. In this study, a nonlinear regression model was developed based on maximum settlements observed from Case 4 (i.e. North and south track for 2180 mm casing) and Case 6 (i.e. Section 1 to 6), and SPT blow counts above the crown of the pipe from the borings adjacent to the pipe alignments. Figure 4.20 presents the regression model representing the relationship between the maximum settlement and SPT blow counts, which is given by:

$$S_{max} = -6.7 \ln(N) + 26 \qquad \textbf{(4.6)}$$

with a coefficient of determination, $R^2 = 0.90$. The dashed line represents one standard deviation of the residuals (i.e., errors) added or subtracted to the model estimates. The model indicates a good fit to the available data. Because there are few data (n = 8), this model should be used with caution and updated as new data become available.

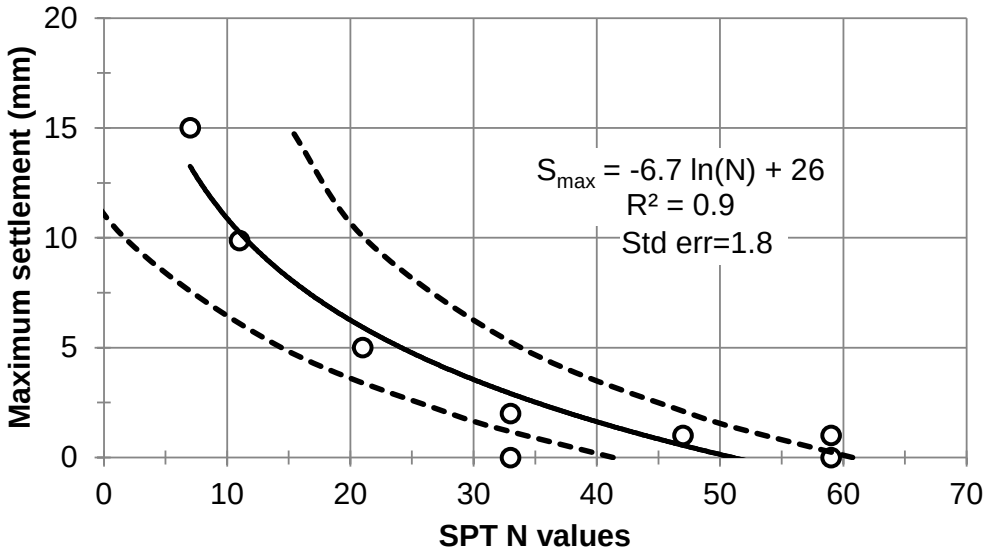

Figure 4.20: Regression model for the estimate of maximum settlement based on SPT *N* blow counts.

4.6 SUMMARY

The analysis of settlement possible due to pipe ramming installations is critical for installations in urban areas or in proximity to structures or buried utilities. Confirming anecdotal data, the case histories evaluated indicated that approximately 97 percent of all settlements were smaller than 10 mm; this indicates that the total magnitude of settlement induced by pipe ramming is generally small, and may be negligible. However, because the data evaluated herein did include settlements larger than 10 mm, it remains important to evaluate the magnitude of settlement possible with pipe ramming.

Settlements induced by pipe ramming are primarily assumed to be caused by the collapse of the overcut due to soil loosening; however, it is possible that vibration-induced contraction of the granular materials contributes to settlement as well. Because of soil arching, it is likely that the settlement resulting from ramming is due to a portion of the overcut volume collapse, rather than its entirety. Based on the likely soil arching phenomena, the settlement analysis presented herein investigated cases of annular space collapse around pipe: the case of collapse of the entire overcut volume, and the case of collapse of half of the overcut volume. The estimate of settlements were evaluated using the inverted normal probability distribution approach for tunneling and pipe jacking, including methods by O'Reilly and New (*1982*) and Cording and Hansmire (*1975*) and Mair and Taylor (*1997*). Generally, these methods seem to over-estimate the observed settlements close to the center of the pipe and under-estimate at radial distances on either side from the center of the pipes when collapse of the entire overcut volume was assumed to occur. On the other hand, these models produced an improved estimate of the measured settlements close to the center of the pipe when collapse of half of the overcut volume was assumed, although substantial under-estimate of settlements were calculated at radial distances far from the center of the pipe.

In order to improve the estimate of ramming-induced settlement, a three parameter hyperbolic settlement model was developed using the settlement database collected as part of this study (Equation 4.2). The parameters of the hyperbolic model were determined using ordinary least-squares optimization to produce an improved estimate of the observed settlement both at the center and at further radial distances from the center of the pipe. A sensitivity analysis was performed on the proposed settlement model to examine the relative effect of the model parameters. It was found that the model estimate is highly sensitivity to changing the overcut (OC) volume, and moderately sensitive to the depth of cover above the crown of the pipe and diameter of the pipe. An in-situ-based model was developed using SPT N in order to relate the expected maximum settlement associated with pipe ramming to the relative density of the granular soils above the pipe alignment (Equation 4.6). The regression model demonstrated a good fit to the relatively scarce data, with coefficient of determination equal to 0.90. Additional data will be required to improve the reliability of the model given the relatively small number of settlement cases available. Although vibration-induced contraction was not directly accounted for in the new settlement models, the effect of vibration on the resulting settlement was indirectly accounted for through the empirical data fitting approach.

5 ANALYSIS OF GROUND VIBRATIONS

The impact blow delivered to a pipe from the pipe ramming hammer results in a stress wave that travels down the pipe, which in turn is partially transferred to the surrounding soil. The dynamic stresses provide ground vibrations that can result in serious adverse effects on adjacent structures and nearby utilities if sufficient distance from the pipe is not maintained. The potential danger includes differential settlements, densification in dry granular soils and liquefaction in loose saturated granular soils. Thus, the planning for pipe ramming installations should include a quantitative estimate of the vibration levels that existing structures or utilities may encounter. The ground vibration monitoring points and observation protocols that form the basis of this section were discussed in Section 3.6. In this section, the ground vibrations caused by pipe ramming observed as part of Case 6, the full scale field experiment, are presented and analyzed.

5.1 GROUND VIBRATION IN THE TIME DOMAIN

Observations of ground vibration were made using the Minimate Plus seismograph. This instrument has two modes operation: the histogram mode and the waveform mode. The histogram mode is usually used for long term monitoring and samples data continuously at a preselected sample rate, storing only the maximum amplitude over the measurement interval. This mode of operation significantly reduces the data stored and enables longer recording durations. On the other hand, the waveform mode records vibration traces for short periods of time (i.e. less than 10 sec) when the vibration level exceeds a pre-set trigger level. The geophone measures the particle velocity in three orthogonal directions: transverse, vertical, and longitudinal (Figure 5.1). The transverse ground vibrations agitate particles in a side to side motion whereas the vertical and longitudinal stirs the particles in up and down and in a forward and back motion, respectively. The sign conventions for each of the orthogonal particle velocities are provided in Figure 5.1. However, for practical purposes, it is customary to combine the measured velocities in a peak vector sum (*PVS*), given by:

$$PVS = \sqrt{v_{Long}^2 + v_{Tran}^2 + v_{Vert}^2} \qquad \textbf{(5.1)}$$

where v_{Long} = longitudinal, v_{Tran} = transversal, and v_{Vert} = vertical ground vibrations.

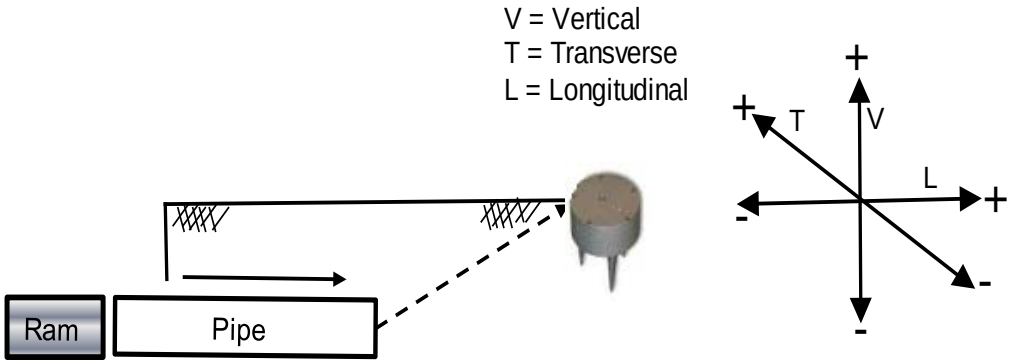

Figure 5.1: Sign convention of the ground vibration in orthogonal directions.

Two series of vibration data were selected from the Case 6 database and presented in Figures 5.2 to 5.5 to demonstrate the variation of particle velocity in the time domain and to visualize the motion of particles within the propagating wave. The time series were obtained with a sampling rate of 1024 samples per second. The first time series was taken at Section 2 directly above the center of the pipe at an instant when the face of the pipe was at a hypocentral distance of 2.7 m from the geophone (see Figure 3.32). The 400 mm HammerHead hammer was driving the pipe when this data was recorded. Figure 5.2 depicts the particle velocities in the three orthogonal directions recorded over 5 seconds. The transverse velocity magnitudes were observed to be smaller than the longitudinal and vertical velocities, which can be expected given the location of the pipe and its movement towards the instrument. The longitudinal and vertical velocities share similar magnitudes. The particle motions in Figure 5.3 show a combination of largely well-defined and slightly irregular patterns of particle excitation with a mainly vertical motion in the transversal plane and somewhat ellipsoidal-like motion in the longitudinal plane. An ellipsoidal motion in the direction of the wave propagation is considered a distinctive pattern of Rayleigh waves (*Kramer 1996*). Thus Rayleigh waves likely form the dominating wave type for particle motions in Figure 5.3.

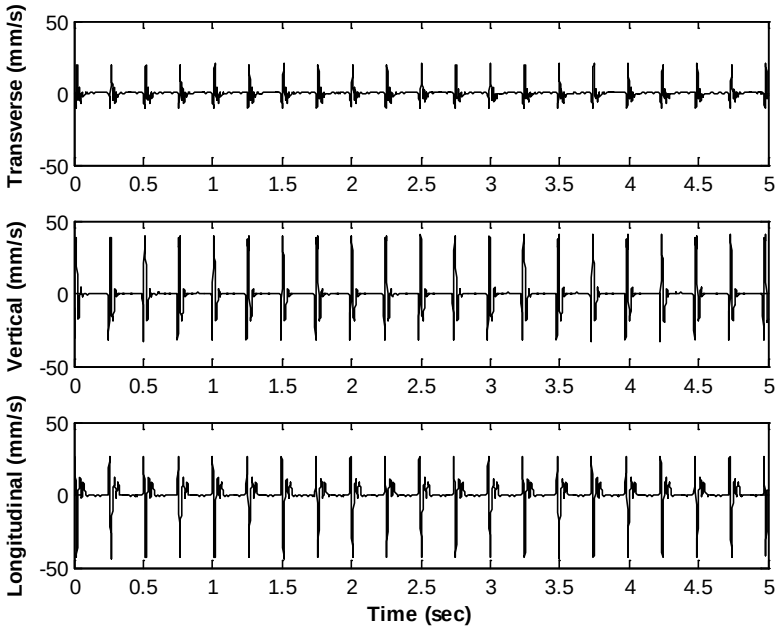

Figure 5.2: Transverse, vertical and longitudinal particle velocity at Section 2 directly above the center of the pipe.

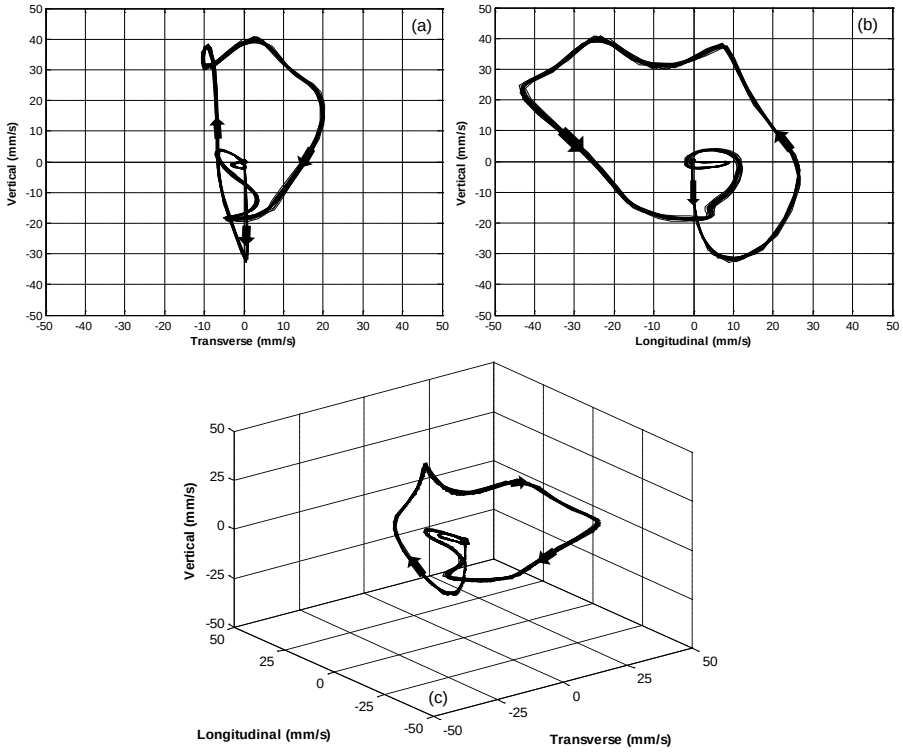

Figure 5.3: Particle motion at Section 2 directly above the center of the pipe (a) transverse versus vertical particle motion (b) longitudinal versus vertical particle motion, and (c) three dimensional particle motion.

The second time series was observed directly above the center of the third pipe segment during installation of the sixth pipe segment, with the 610 mm Grundoram Taurus hammer. In this instance, the face of the pipe was at a hypo-central distance of 2.3 m from the geophone. The particle velocities in orthogonal directions recorded over 5 sec are shown in Figure 5.4. The plot shows larger vibration magnitudes in the vertical as compared to transverse and longitudinal directions. The particle motions plots presented in Figure 5.5 show an irregular movement of the particles which might be a potential influence of the interaction of body waves and surface waves (*Liden 2012*).

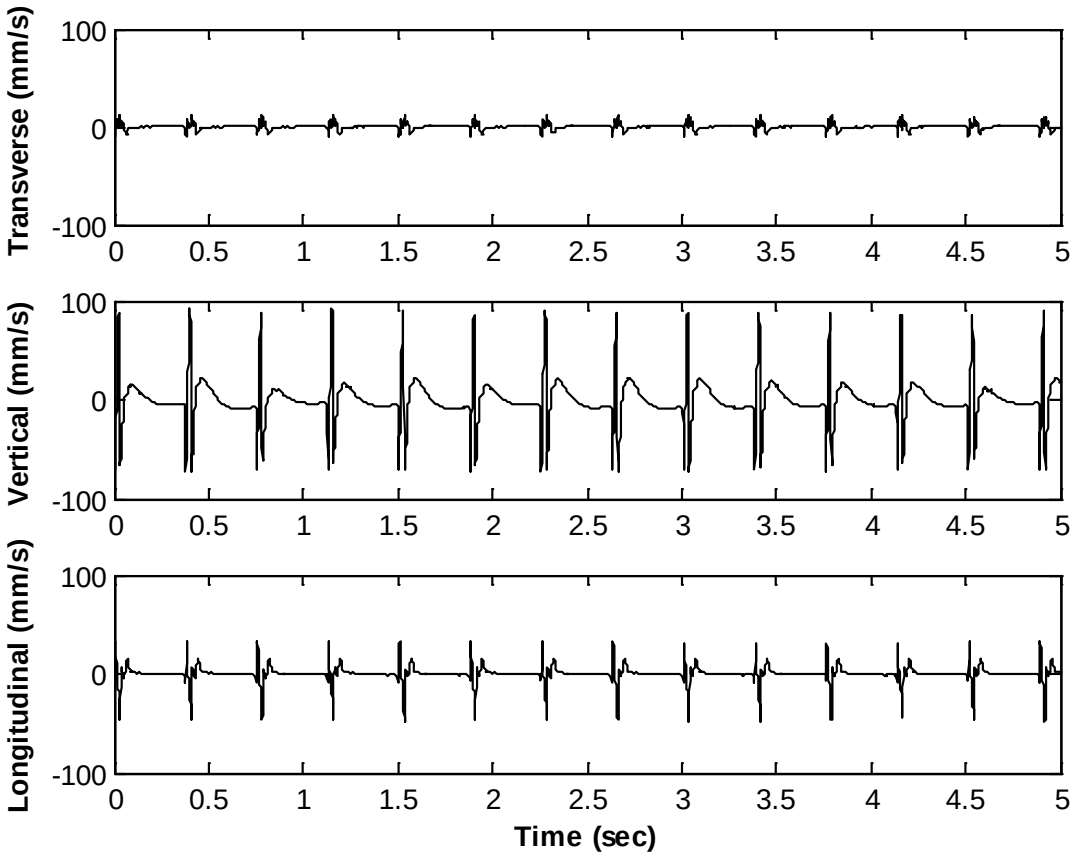

Figure 5.4: Transversal, vertical, and longitudinal particle velocity at Section 3 directly above the center of the pipe.

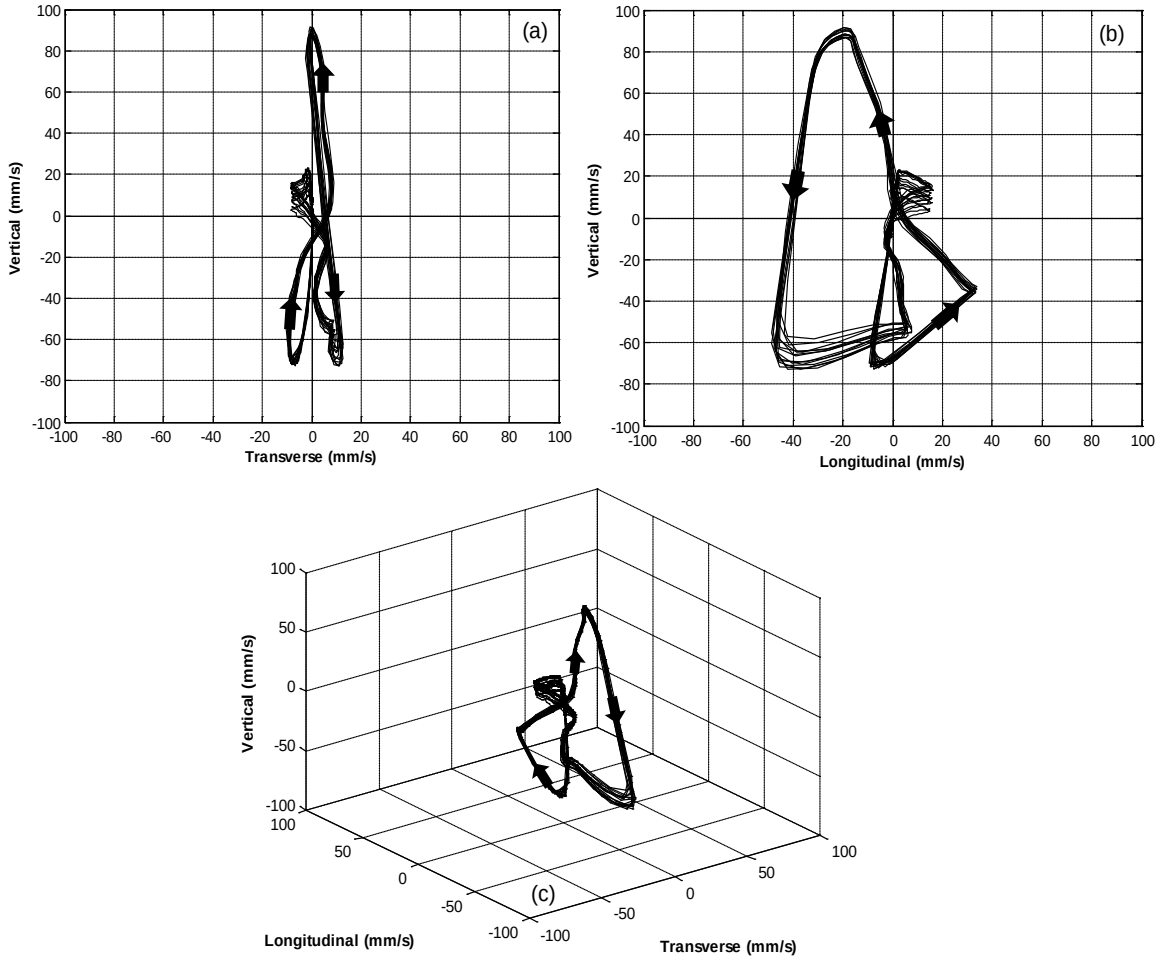

Figure 5.5: Particle motion at Section 3 directly above the center of the pipe (a) transverse versus vertical particle motion, (b) longitudinal versus vertical particle motion, and (c) three dimensional particle motion.

5.2 GROUND VIBRATIONS IN THE FREQUENCY DOMAIN

Traditionally, the assessment of ground vibrations is based on two basic parameters: the peak particle velocity and the frequency at which it occurs. The hammer impact during pipe ramming can force the ground to vibrate in certain frequencies. If the ground vibration frequencies coincide or include the characteristic frequency (i.e. natural frequency) of an existing structure, resonance may develop and cause damage to the structure. Thus it is important to include the frequency content of the vibration when establishing "red flag" or "shut down" criteria to prevent structural damage. The pipe ramming-induced vibration consists of a wide range of amplitudes and frequencies, largely ranging from 1 to 100 mm/sec and 20 to 100 Hz, respectively. For comparison, the US Bureau of Mines (USBM) set the limits on vibration to structural damage at 50 mm/sec peak particle velocity for up to 3 Hz and at 0.1g acceleration to 100 Hz (*Woods 1997*).

The peak particle velocities and frequencies observed were analyzed and compared to the safe vibration criteria established by Office of Surface Mining (OSM) and US Bureau of Mines (USBM) for indirect assessment of vibration effects on existing structures (see Section 2.4). The safe limit criteria indicate more sensitivity of structures to low frequency vibration where a lower

magnitude of permissible particle velocity is established. Two cases of vibration propagation were considered in the analysis of vibrations measured for Case 6: forward propagation and lateral propagation. The forward propagation of vibration is considered to emanate from the face of the pipe and propagates ahead of the advancing pipe (i.e. point A relative to the pipe on Figure 5.6). Lateral propagation of vibration is emitted from the side of the pipe casing transmits energy outward (i.e. point B relative to the pipe on Figure 5.6). The forward propagation frequency and vibration relationships are presented on Figure 5.7 and Figure 5.8 for the HammerHead and Taurus rams respectively. Both of the vibration plots demonstrate the effect of distance from the source (e.g. the face of the leading edge of the pipe for forward propagation) on the attenuation of vibrations. The vibration levels are significant, up to 100 mm/sec, for some observations at small source-to-site distances (e.g. 1 to 3 m), whereas all vibrations observed further than 3 m fall below the OSM and USBM safe vibration criteria thresholds. Thus, forward vibrations generated using pipe ramming may cause damage when the proposed alignment passes within 3 m of existing structures or buried utilities for the pipe ramming hammers (i.e., the energy) investigated. However, we note that some forward propagation measurements within 3 m did not exceed the OSM and USBM thresholds. Efforts to mitigate vibration amplitudes may need to be developed when proposed alignments run near existing structures, and the observations indicate the need for establishing a vibration monitoring plan in these instances. For lateral propagation, the observed vibrations fell far below the established OSM and USBM safe vibration criteria lines as demonstrated on Figure 5.9, indicating little potential for danger to existing structures once the leading edge of the pipe has passed a critical point of interest.

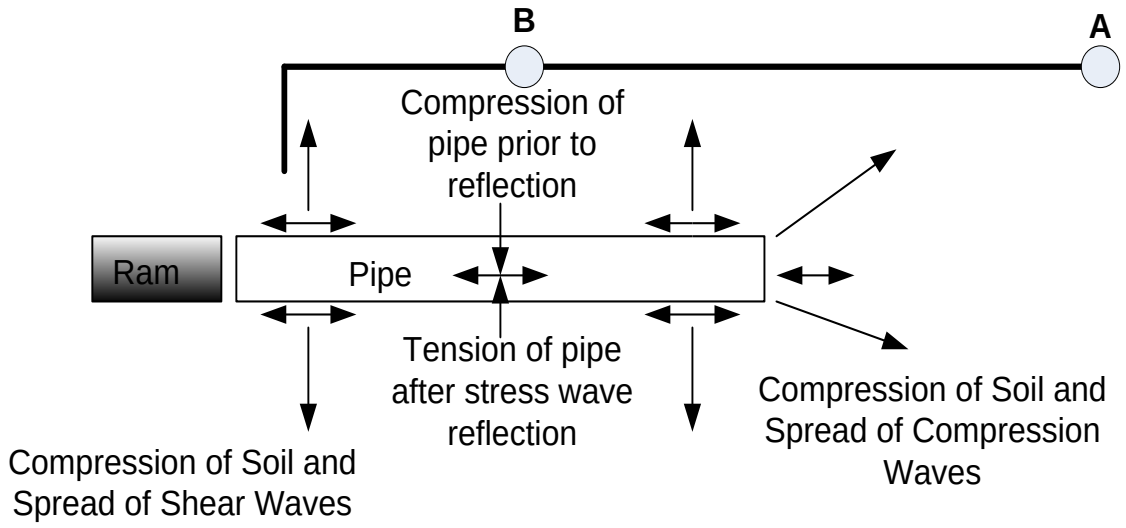

Figure 5.6: Schematic showing vibration propagation induced by pipe ramming.

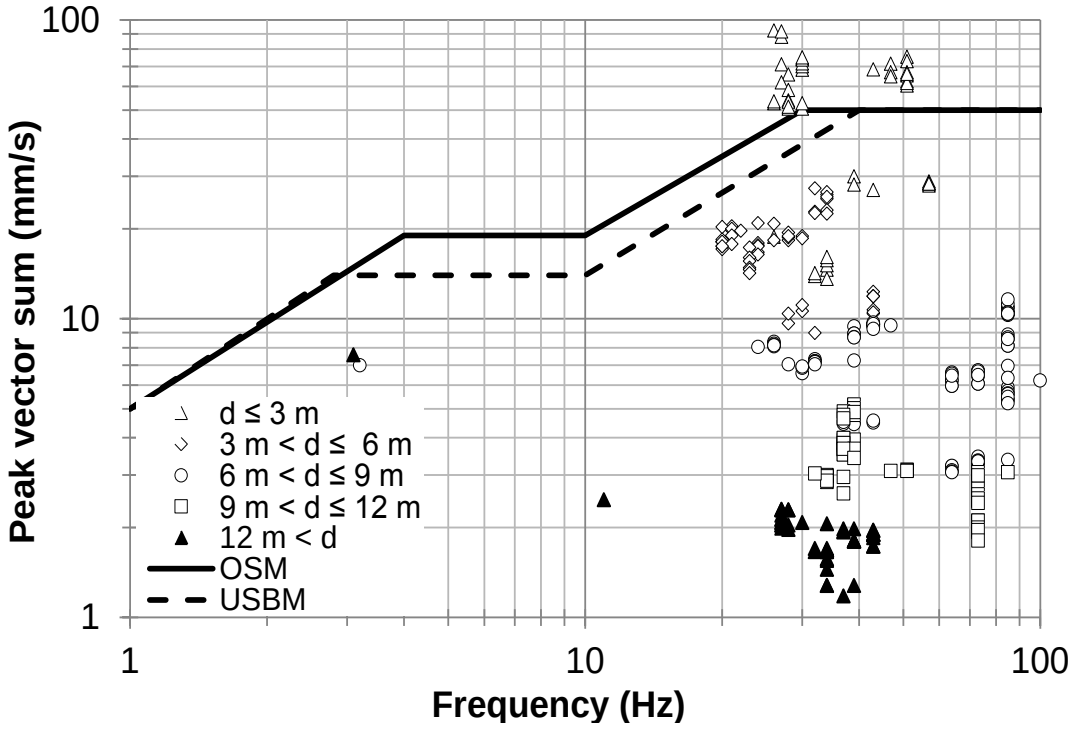

Figure 5.7: Peak vector sum velocities versus dominant frequency of Forward propagating vibration using the 400 mm HammerHead hammer.

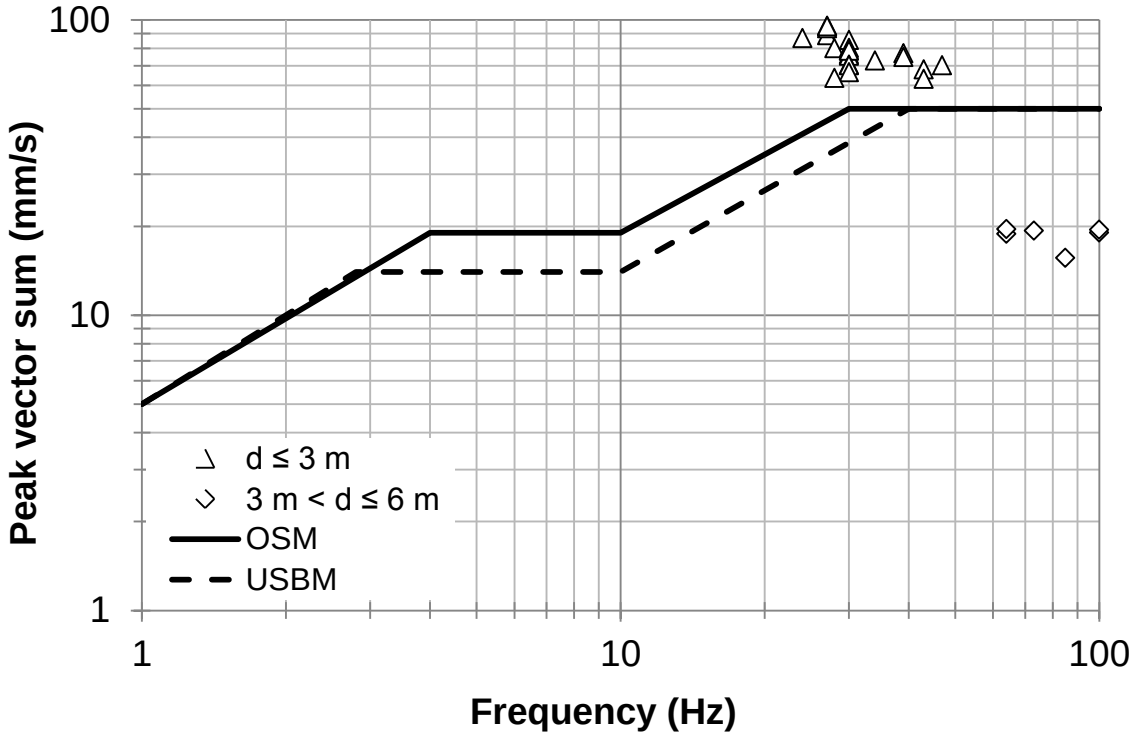

Figure 5.8: Peak vector sum velocities versus dominant frequency of Forward propagating vibration using the 610 mm Grundoram Taurus hammer.

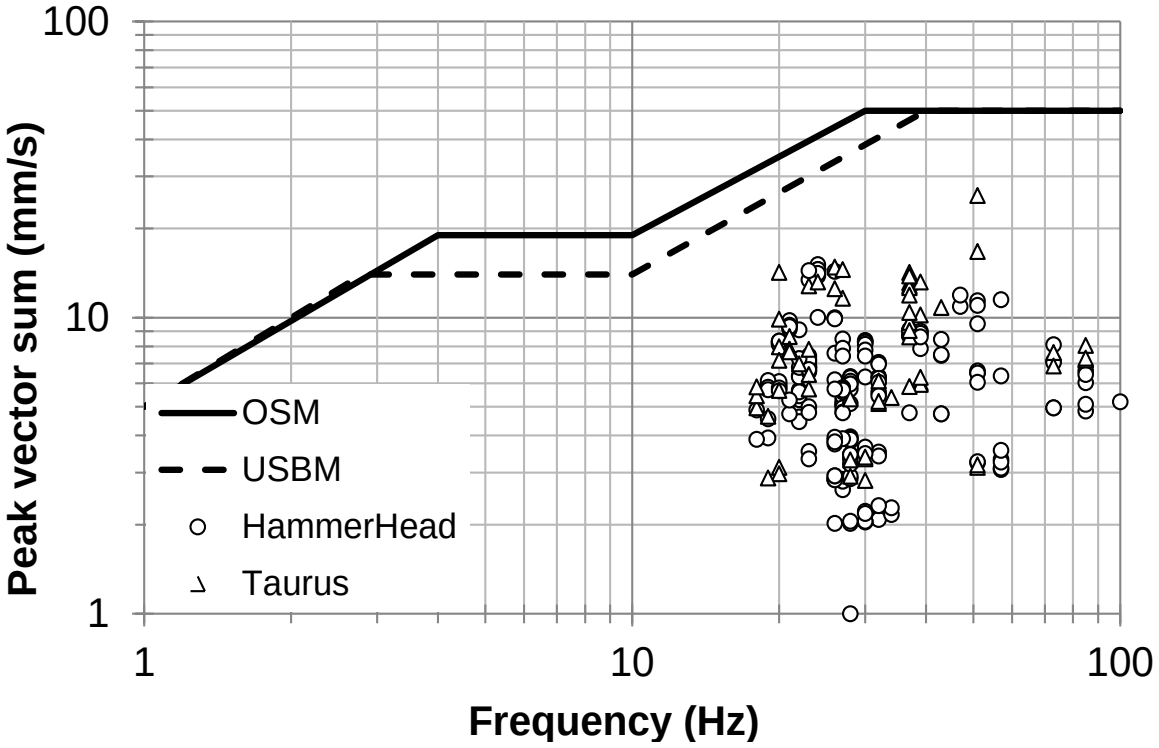

Figure 5.9: Peak vector sum velocities versus dominant frequency of lateral propagating vibration.

5.3 ATTENUATION OF PIPE RAMMING-INDUCED VIBRATIONS

Based on the observations made for Case 6, the estimation of likely ground vibrations can be critical for the case of forward propagation. Pipe ramming-induced vibrations generally attenuate with distance from the energy source (i.e. the face of the leading edge of the pipe). The decay of the ground vibrations with distance can be attributed to two damping components, geometric (i.e., radiation) and material (i.e., hysteretic) damping. Geometric damping occurs as a result of energy distribution over an increasingly larger surface area or volume that leads to diminishing amplitude of the vibration (i.e., energy density reduction with radial distance). Material damping is attributed to energy reduction due to strain energy dissipation of soil particles resulting from hysteresis. Thus, the geometric damping mainly depends on the type and location of the vibration source while the material damping is a function of ground properties.

An empirical power law approach proposed by Wiss (*1981*) was adopted for modeling the attenuation of ground vibration for Case 6. The Wiss (*1981*) model requires the magnitude of the energy of the hammer transferred to the pipe, WE, and the radial (or hypocentral) distance between the source of energy and location of interest (e.g., geophone location), r. Historically, the Wiss (*1981*) model and subsequent derivative works have not been sensitive to the geotechnical properties of the subsurface (see Section 2.4). The model uses a scaled-distance propagation equation to predict peak vector sum (*PVS*) velocity, *v*, of the form:

$$v = K_d \left[\frac{r}{\sqrt{E}} \right]^{-n} \qquad \textbf{(5.2)}$$

where K_d = intercept value of vibration amplitude at "scaled-distance" $r/\sqrt{E} = 1$ and n = the attenuation rate. The parameters of the Wiss (*1981*) model (i.e., K_d and n) were obtained through least squares regression by fitting the best power law to the peak vector sum vibrations as a function of scaled-distance (i.e. distance normalized by the square root of energy). The regression optimization were performed for three different scenarios: (1) forward propagation and source of energy at the face of the pipe (i.e., energy transferred to face of the pipe), (2) forward propagation and source of energy at the rear end the pipe (i.e., energy transferred to rear end of the pipe), and (3) lateral propagation and source of energy at the rear end of the pipe.

As described above, two scenarios of forward propagation were investigated. Scenario1 assumed that the energy at the face of the pipe can be estimated; however, the estimation of the face energy is not a trivial exercise, and requires a detailed drivability analysis. Therefore, Scenario 2 in which the energy applied to the end of the pipe is used, and can be estimated if the hammer and the hammer-pipe energy transfer efficiency is known or can be estimated, was investigated. Hammer-pipe energy transfer efficiency is described in detail in Section 7.4. Scenario 1 (Figure 5.10a) yielded K_d = 237 and n = 1.65 while Scenario 2 (Figure 5.10b) provided K_d = 97 and n = 1.34 for the vibration dataset collected for Case 6. The third scenario investigated, lateral vibration propagation (Figure 5.10c), yielded K_d = 19 and n = 0.5. The solid lines in Figure 5.10 represent the best fit model and the dashed line represents the bounds of one standard deviation of the model residuals. An assessment of the model accuracy is illustrated in Figure 5.11 for each of the scenarios; the mean bias and coefficient of variation in bias is equal to 1.1 and 50 percent for Scenario 1, 0.86 and 50 percent for Scenario 2, and 1.0 and 53 percent for Scenario 3.

Figure 5.12 shows the vibration contour and surface map generated based on the calibrated Wiss (*1981*) model for the forward propagation using the energy transferred at the rear end of the pipe. The map shows the birds-eye view of the vibration levels with the face of the pipe assumed to be located at the zero point on the ordinate. The arrows indicate the direction of the pipe progression. The vibration magnitudes are large close to the face of the pipe and reduce dramatically at radial distances away from the face of the pipe.

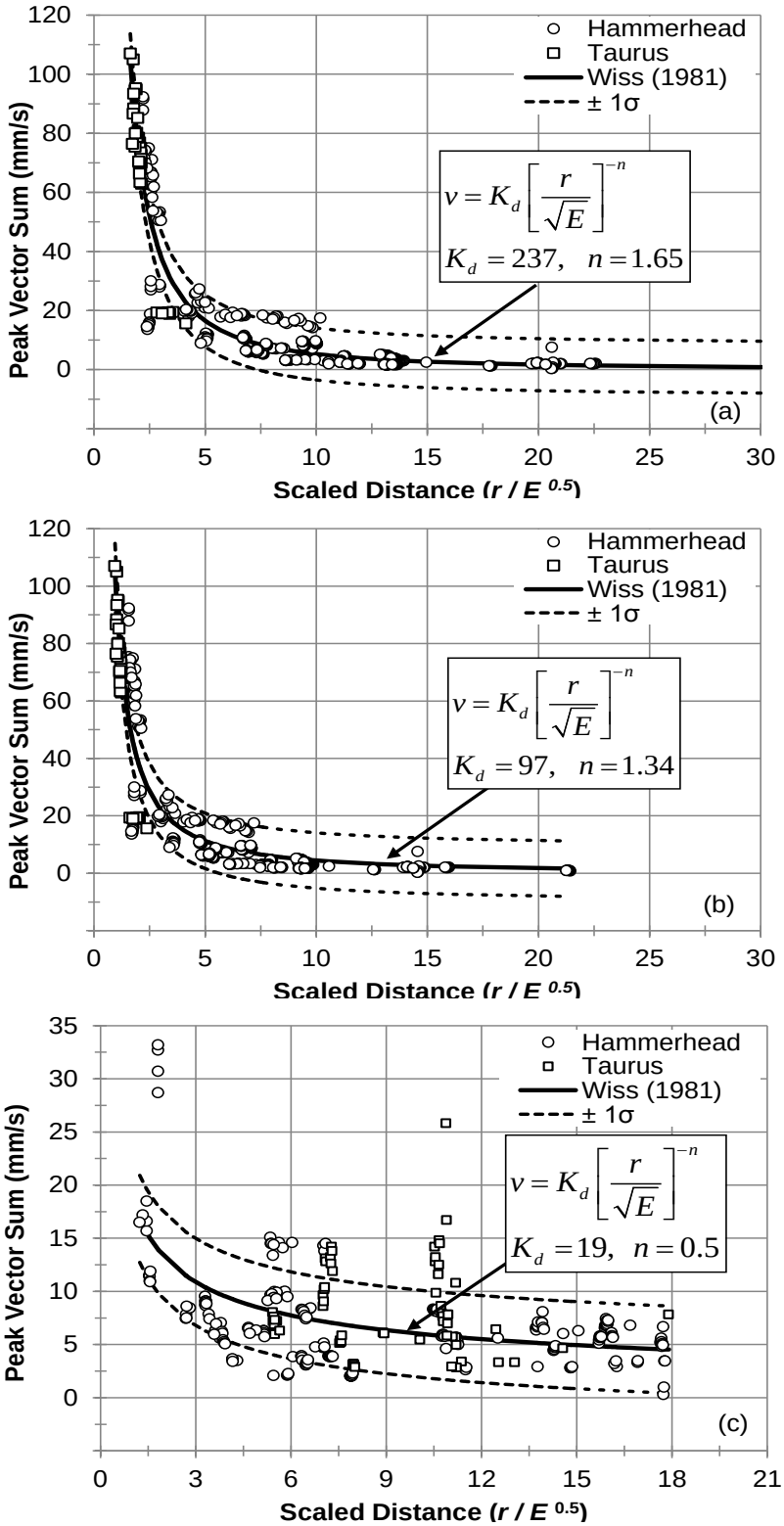

Figure 5.10: Observed vibrations versus scaled distance and calibration of attenuation model based on the Case 6 vibration observations: (a) Scenario 1, forward propagation and source of energy at the face of the pipe, (b) Scenario 2, forward propagation and source of energy at the rear end the pipe, (c) Scenario 3, lateral propagation and source of energy at the rear end of the pipe.

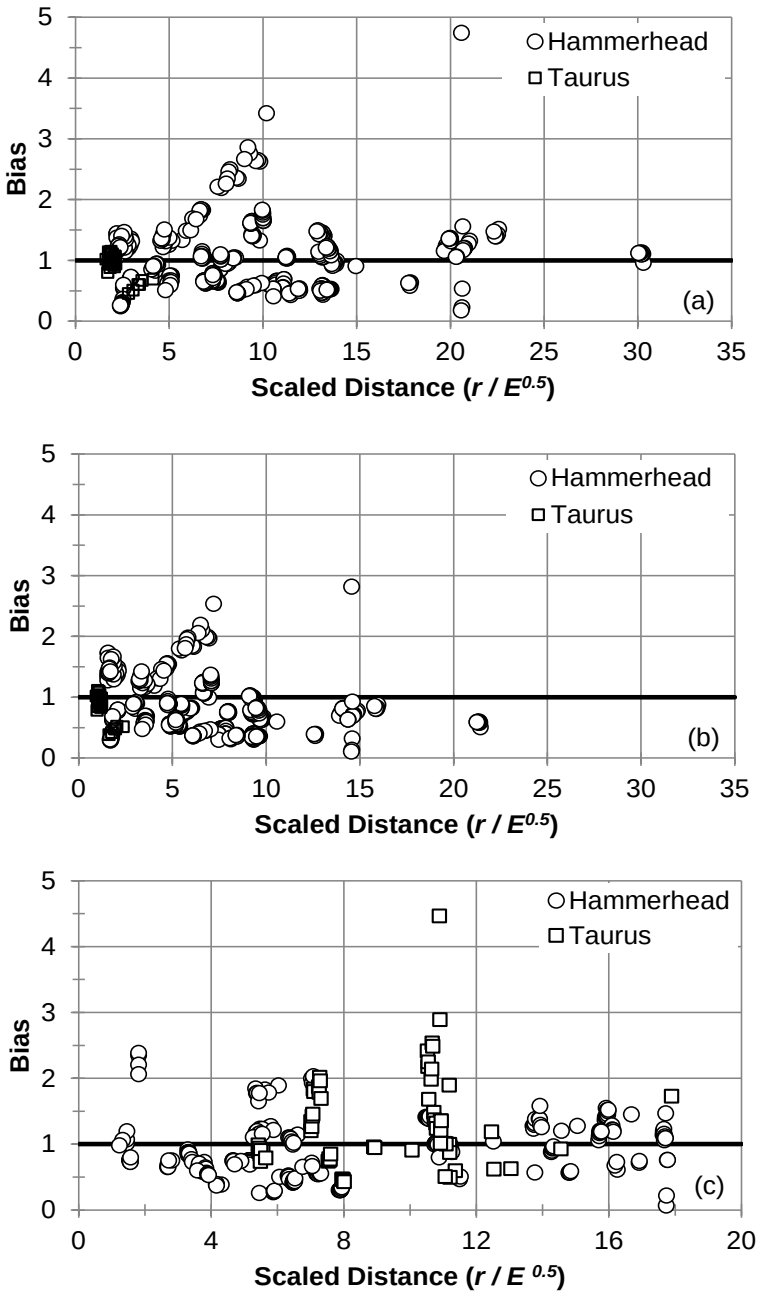

Figure 5.11: Distribution of sample bias with scaled distance for the vibration attenuation model (a) Scenario 1, forward propagation and source of energy at the face of the pipe, (b) Scenario 2, forward propagation and source of energy at the rear end the pipe, (c) Scenario 3, lateral propagation and source of energy at the rear end of the pipe.

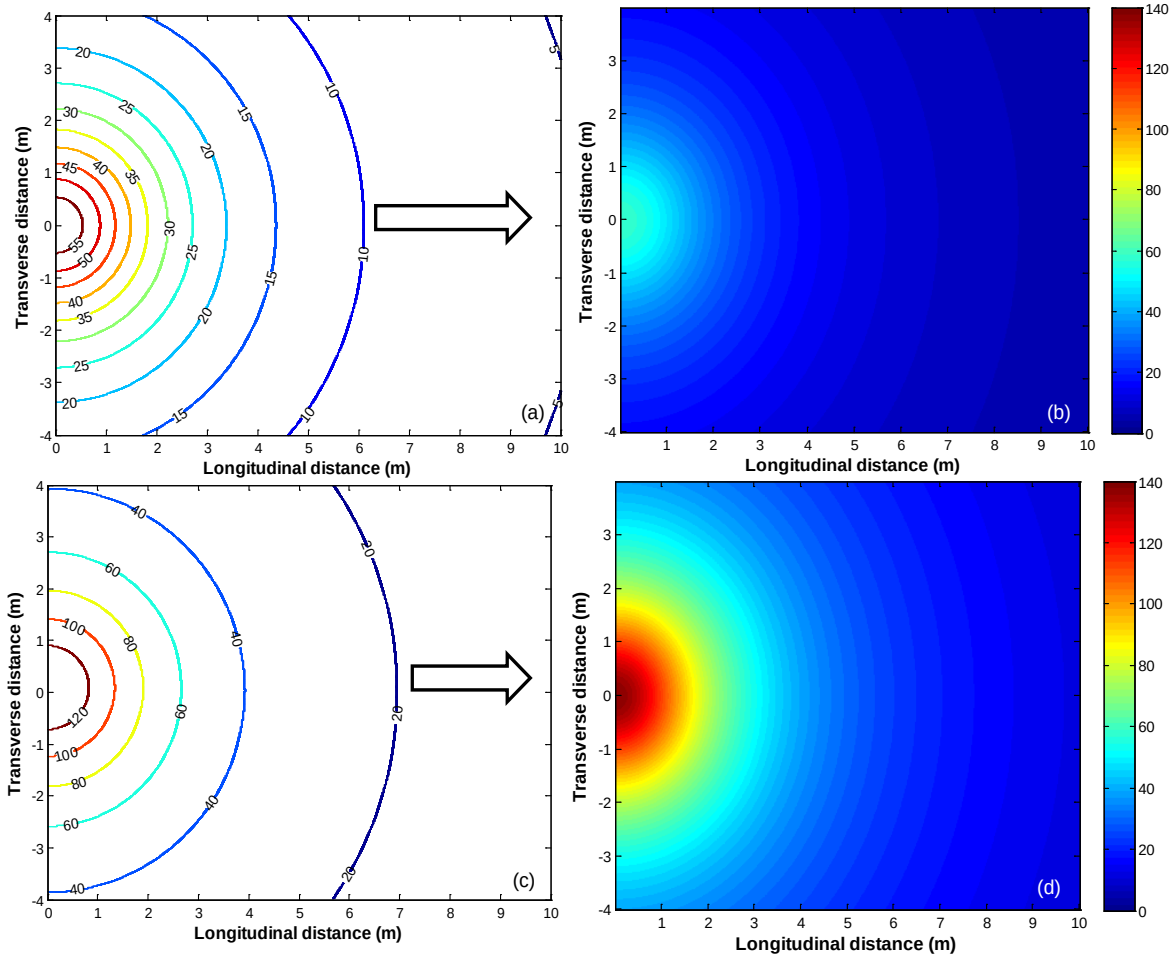

Figure 5.12: Vibration contour and surface maps in mm/s: (a) and (b) for HammerHead hammer; (c) and (d) for Grundoram Taurus hammer.

5.4 SUMMARY

The ground vibrations generated using pipe ramming were observed in the experimental ramming installation (Case 6). Measurements indicated that significant magnitudes of peak particle velocity are possible, indicating that vibration can pose a hazard to adjacent structures, especially in urban areas. Pipe ramming induced ground vibration can cause aesthetic and structural damage to buildings, disturbance to nearby people, and densification and settlement in sandy soils. This chapter focused on the characterization of measured vibrations with respect to magnitude and frequency content, and adaptation of an existing vibration-attenuation model for pipe ramming-induced vibrations.

The ground vibrations observed for Case 6 were compared against simple approaches for evaluating the safe magnitude and frequency content (e.g., the OSM and USBM safe vibration criteria). Because of noticeably different behavior, forward and lateral vibration propagation was analyzed separately. Forward vibrations are larger than lateral vibrations, and may pose a hazard to existing structures or buried utilities, whereas lateral vibrations are smaller, but attenuate more slowly with radial distance. The attenuation of vibration was modeled using the simple empirical approach proposed by Wiss (*1981*), which requires an estimate of energy of the hammer and the distance between the pipe and the point of interest. Calibration of the model was performed using least squares regression by fitting the model to the vibrations as a function of scaled distance. The calibrated model provides reasonable estimates of vibrations for hammer energies and sites with similar characteristics to that of Case 6 (e.g., granular soils). Additional research should be performed to determine vibration model parameters for other hammer types, energies, and soil conditions.

6 ANALYSIS OF PIPE RAMMING DYNAMICS

6.1 INTRODUCTION

Pipe ramming forces a horizontal or near horizontal pipe to penetrate the ground using a series of short duration hammer impacts. The dynamic force delivered by the hammer at the rear end of the pipe results in a compressive stress wave that travels down the casing to the pipe face transferring a portion of the energy along the way due to frictional soil resistance. Upon reaching the face of the pipe, the stress wave is reflected and returns back along the pipe as a tensile or compressive stress wave depending on the soil reaction at the face of the pipe. Generally, the dynamic response of pipes during pipe ramming is quite similar to that of pile driving. Therefore, the dynamic analysis of pipe ramming can be based on the one-dimensional wave propagation analysis used with pile driving.

6.2 WAVE PROPAGATION ANALYSIS

6.2.1 Basics of Stress Wave Equation

Consider a linearly elastic pipe of uniform cross section which is struck at the rear end by a hammer. The hammer impact creates a pulse or a compression wave that travels down the pipe to the face of the pipe. Given the distance x along the pipe from the rear end, Newton's second law can be applied to an infinitesimal element of the pipe as shown in Figure 6.1. The sum of the forces on the infinitesimal element due to the compressive wave and external soil resistance force can be equated to the product of the elemental mass and the resultant acceleration of the cross section, as given by (Holloway, *1975*):

$$\left[\left(\sigma_x + \frac{\partial \sigma_x}{\partial x}dx\right) - \sigma_x\right] \cdot A + R(x) = \left(\rho \cdot A \cdot dx\right)\frac{\partial^2 u}{\partial t^2} \qquad \textbf{(6.1)}$$

where σ_x = stress at a distance x along the pipe, A = cross sectional area, $R(x)$ = the soil resistance as function of x, ρ = mass density and u = the displacement in x-direction.

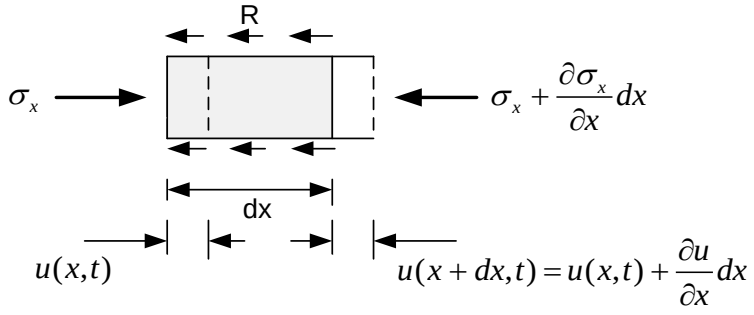

Figure 6.1: Infinitesimal pipe element subjected to a compressive wave.

Assuming a linear relationship between stress and strain, Hooke's law for the pipe material yields:

$$\sigma_x = E \cdot \varepsilon_x = E \frac{\partial u}{\partial x} \quad \textbf{(6.2)}$$

where E = Young's modulus and ε_x = strain at a distance x along the pipe. Combining Equation 6.1 and 6.2 for isotropic and homogeneous condition, the formulation can simplify to the form:

$$c^2 \frac{\partial^2 u}{\partial x^2} + \frac{R(x)}{\rho A dx} = \frac{\partial^2 u}{\partial t^2} \quad \textbf{(6.3)}$$

where c = the velocity of wave propagation and given by:

$$c = \sqrt{\frac{E}{\rho}} \quad \textbf{(6.4)}$$

and is commonly equal to 5155 m/sec for steel.

The solution of the partial differential equation above can be determined provided that the initial conditions and physical boundary conditions are stated (*Holloway 1975*). The initial conditions are generally specified by the displacement, velocity, and resistance distribution at a known instant of time. The boundary conditions can be established with the appropriate deformation response at the rear end or face of the pipe. Assuming no external resistances, Equation 6.3 can further simplify to common form of the one dimensional wave equation, given by:

$$c^2 \frac{\partial^2 u}{\partial x^2} = \frac{\partial^2 u}{\partial t^2} \quad \textbf{(6.5)}$$

In general, the solution of the one dimensional wave equation can be achieved through an analytical method of characteristics or numerical methods (i.e. finite difference method (FDM) and finite element method (FEM)). The numerical solutions are typically preferred to analytical solutions due to their simplification of the complex impact driving problem (*Holloway 1975*). The FDM approach approximates the solution to wave equation by discretizing the pipe into small segments and subdividing the time into small increments. An approximation to the second partial differential of displacement with respect to location on the pipe can be obtained by taking the finite difference of the first order partial differential equations (i.e. the forward and backward difference) and dividing by Δx (*Holloway 1975*):

$$\frac{\partial^2 u}{\partial x^2} \approx \frac{u_{i+1,t} - 2u_{i,t} + u_{i-1,t}}{\Delta x^2} \quad \textbf{(6.6)}$$

where i = pile element and t = time interval. Similarly, the second partial derivative of displacement with respect to time can be approximated by:

$$\frac{\partial^2 u}{\partial t^2} \approx \frac{u_{i,t+1} - 2u_{i,t} + u_{i,t-1}}{\Delta t^2} \quad \textbf{(6.7)}$$

Substituting Equation 6.6 and 6.7 in to Equation 6.5 (and assuming $R(x) = 0$), and rearranging the terms, the FDM-based solution of the wave equation is obtained and given by:

$$u_{i,t+1} \approx M \cdot u_{i+1,t} + 2 \cdot (1 - M) \cdot u_{i,t} + M \cdot u_{i-1,t} - u_{i,t-1} \quad \textbf{(6.8)}$$

where $M = c^2 \cdot \Delta t^2 / \Delta x^2$, a dimensionless parameter that insures the numerical stability of the finite-difference solution. The stability of the numerical scheme is achieved by constraining $M \leq 1$.

6.2.2 Smith's Idealization of Wave Equation

Analysis of impact driving with simplified numerical solution of the one-dimensional (1-D) wave equation is attributed to Smith (*1960*). Previously, impact analyses were accomplished using dynamic pile driving formulas which were based on rigid body mechanics (Lee et al., *1988*). Smith (*1960*) proposed the solution of wave propagation in an elastic pile using a finite difference scheme by idealizing the actual continuous pile as a series of discretized lumped masses connected by massless linear springs with the soil resistance acting on each discrete mass. In addition, dashpots were added in parallel with the springs to account the internal material damping in the pipe. The mobilized soil resistance consists of an elasto-plastic static component represented by the spring and slider, and the dynamic component by the dashpot (i.e., damper) where the resistance is assumed to be proportional to the pile velocity. A typical representation of the Smith hammer-pipe-soil system for pipe ramming is shown in Figure 6.2.

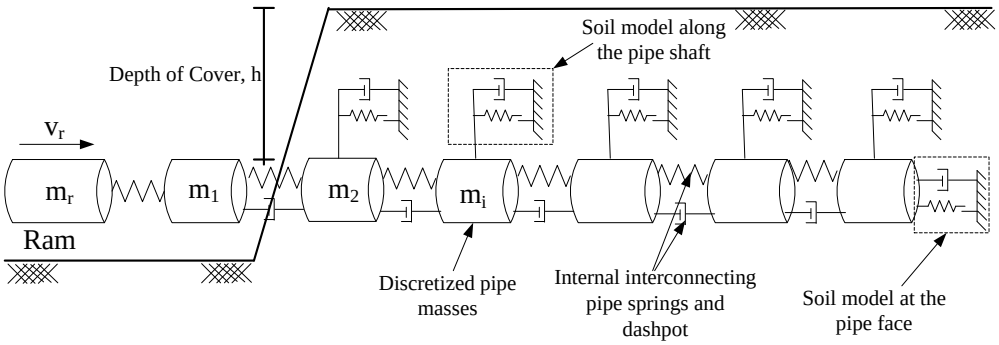

Figure 6.2: Smith's pipe discretization for pipe ramming and soil resistance model.

Smith (*1960*) applied the basic equations of motion to the discrete masses separated by linear springs and dashpots to derive the difference equations. Each discrete mass of the pipe can be represented by m_i, with linear spring constants, $S_{p,i}$ and dashpot damping constants $c_{p,i}$. With this notation, the velocity of the i^{th} mass at any time t can be given by:

$$v_{i,t} = v_{i,t-1} + a_{i,t} \cdot \Delta t \quad \textbf{(6.9)}$$

where the acceleration ($a_{i,t}$) of each mass is given by:

$$a_{i,t} = \frac{F_{i-1,t} - F_{i,t} - R_{i,t}}{m_i} \quad \textbf{(6.10)}$$

In this equation $R_{i,t}$ represents the total soil resistance (static and dynamic) mobilized along the casing and at the face of the pipe, and $F_{i,t}$ represents the force in spring and dashpot below the i^{th} mass which is given by:

$$F_{i,t} = S_{p,i} \cdot \left(u_{i,t} - u_{i+1,t}\right) + cp_i \cdot \left(v_{i,t-1} - v_{i+1,t-1}\right) \quad \textbf{(6.11)}$$

The viscous damping constant of the dashpots between the pipe segments can be determined as a fraction of the critical damping coefficient of Single Degree of Freedom (SDOF) systems (*Goble and Rausche 1981*). Thus the dashpot damping constant can be obtained as the product of the damping ratio (ζ) and critical damping coefficient (c_{cr}) which is given by:

$$cp_i = \zeta \cdot c_{cr} = \zeta \cdot 2\sqrt{S_{p,i} \cdot m_i} = \zeta \cdot 2 \cdot \frac{EA}{c} \quad \textbf{(6.12)}$$

The displacement of the i^{th} mass at time t is computed by considering the displacement at a previous time step (i.e., $t - 1$) and the previous velocity:

$$u_{i,t} = u_{i,t-1} + v_{i,t-1} \cdot \Delta t \quad \textbf{(6.13)}$$

The accuracy of Smith's discrete-element solution depends on the time increment, Δt, selected. The stability of Smith's discrete-mass solution can achieved by limiting Δt to be less than the critical time required for the pulse(i.e. created by the hammer) to travel down a pipe element. The critical value of the time interval for each pipe element can be obtained by:

$$\Delta t_{crit} \leq \sqrt{\frac{m_i}{S_{p,i}}} = \frac{\Delta L}{c} \quad \textbf{(6.14)}$$

where Δt_{crit} = the critical time and ΔL = length of the discrete masses. Approximately 1 m long segments are generally adapted for discretizing the length of the pipe. Smith (*1960*) recommends using one-half of the critical time to prevent instabilities arising from factors such as inelastic springs, materials of different densities and elastic moduli (*Samson et al. 1963*).

6.2.3 Modeling Soil Resistance

Smith (*1960*) modeled the soil resistance using a Kelvin–Voigt-type rheological model shown in Figure 6.3 in which the resistance is represented with a system of series of springs and sliders connected in parallel with a dashpot. The soil resistance includes a long-term static component and a short-term dynamic component to represent the damping of the soil. The static soil resistance (face and casing) is represented by a linear elasto-plastic model where the spring has a limiting resistance beyond which plastic yielding occurs. Thus, the static case indicates that the

soil compresses elastically for a certain distance and fails plastically with constant soil resistance. The maximum elastic displacement of the soil is termed the "quake", Q, and this quantity must be specified for the face, Q_f, and the casing Q_c. For any hammer blow that results in displacement greater than the quake, the pipe movement continues but is resisted by a constant value of soil resistance (i.e., displacement results from plastic deformation). The plastic deformation results in an irreversible compression of the soil at the face and a permanent relative slip along the casing, and is termed "permanent set". The dynamic component of the soil resistance (face and casing) is assumed to be linearly proportional to the instantaneous velocity of the pipe through the dashpot coefficient, C. Smith (*1960*) defined the dashpot coefficient as the product of static soil resistance and a damping parameter (i.e. Smith face damping, J_f, and Smith casing damping, J_c). The total soil resistance (i.e. sum of static and dynamic) model for both the face and casing resistances considering the quake and damping is given by:

$$R = k \cdot u + C \cdot v = \frac{R_u}{Q} \cdot u \cdot \left(1 + J \cdot v\right) \qquad for\ u < Q \qquad \textbf{(6.15)}$$

$$R = R_u + C \cdot v = R_u \cdot \left(1 + J \cdot v\right) \qquad for\ u \geq Q \qquad \textbf{(6.16)}$$

where R_u represents the ultimate static resistance equaling the sum of the face, R_{fu}, and casing, R_{su}, resistance (i.e. $R_u = R_{fu} + R_{su}$). The soil quake, Q, and damping constant, J, are not standard soil parameters; rather, they are empirical constants which are usually determined from back-analysis of impact driving records.

The generalized spring stiffness of static soil resistance (face and casing) is given by:

$$S = \frac{R}{Q} \qquad \textbf{(6.17)}$$

where $S = S_f$ for the spring stiffness associated with the face resistance and $S = S_c$ for the spring stiffness associated with the casing resistance. If the deformation of the pipe exceeds the quake of the soil, then the resistance transitions from an elastic (i.e., spring) deformation-based resistance to failure of the soil, with activation of the slider and soil resistance equal to the ultimate static soil resistance. The dynamic soil resistance is a function of the pipe velocity and the soil damping available. The dynamic soil resistance is typically modeled as a linear function of velocity, where the slope of the linear relationship is given by:

$$C = J \cdot R_u \qquad \textbf{(6.18)}$$

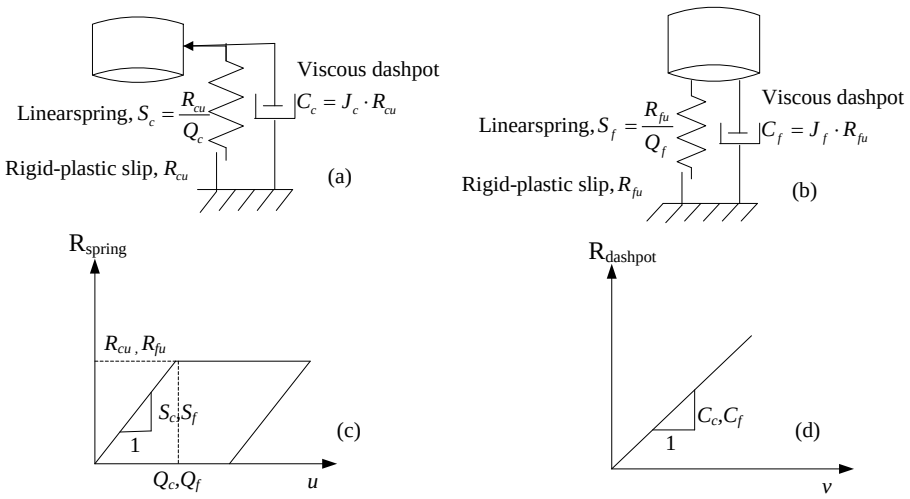

Figure 6.3: Smith's soil resistance models (a) casing resistance model (b) face resistance model (c) linear elastic perfectly plastic load-displacement relationship for static soil resistance, and (d) load-velocity relationship for dynamic soil resistance.

The Smith model remains a widely popular model that accounts for elastic ground deformation, ultimate static soil resistance and viscous damping; however, the model suffers a number of theoretical limitations (e.g. disconnect between the model parameters and basic soil properties). Samson et al. (*1963*), Lowery et al. (*1969*), Rausche et al. (*1972*), Goble and Rausche (*1976*), Randolph and Simons (*1986*), Lee et al. (*1988*), and others have suggested improvements that address limitations in the Smith model. Researchers at the Texas Transport Institute (TTI) and Texas A&M University considered a soil damping model that accounts for the nonlinearity of the damping force with the pile velocity (*Hirsch et al. 1976*). The soil resistance model in the TTI program is given by (*Coyle and Gibson 1970*):

$$R = R_L \left(1 + J \cdot v^N\right) \tag{6.19}$$

where J = the damping coefficient which has units in (s/m)N. and N = an exponent less than unity to reflect the nonlinearity of the damping force with velocity.

Goble and Rausche (*1976*) suggested another development in the soil model, where they assumed that the static soil resistance could be uncoupled from the viscous (dynamic) soil resistance. Their model is given by:

$$R_t = R_u + J \cdot Z \cdot v \tag{6.20}$$

where J = dimensionless Case damping coefficient and Z = the impedance of the pile defined by EA/c where E = the elastic modulus of the pile, A = cross sectional area of the pipe, and c = wave speed propagation.

6.2.4 One-Dimensional Wave Equation Models

During the last half century, a number of wave equation models have been developed and employed successfully in dynamic analysis of pile foundations. In the following section a

review of one of the commonly used and commercially available wave equation analysis programs, the Wave Equation Analysis of Piles (WEAP) is provided. In addition, a development and implementation of basic wave analysis program based on Smith's discrete-element solution will be discussed with the intent of simulating and analyzing the propagation of stress waves in pipe ramming.

6.2.4.1 Wave Equation Analysis of Piles (WEAP)

The software Wave Equation Analysis of Piles (WEAP) is the most widely used wave equation program for dynamic analysis of piles in the United States and was developed by Goble and Rausche (*1976*). The latest version of the program is known as GRLWEAP ® (GRL Wave Equation Analysis for Piles), and is used by many agencies such as the US Army Corps of Engineers, Federal Highway Administration, and various state departments of transportation for the analysis of pile driving (*Hannigan et al. 2006*). The program allows the prediction of driving stresses, modeling of hammer performance, and the prediction of the relationship between pile bearing capacity and net set per blow (i.e., net pile penetration per blow). The model can be used for the purpose of investigating a potential hammer to evaluate its effectiveness and economy for a given pile and soil condition. An analysis of drivability can be performed to determine if the pile (or in this case, the pipe) will be overstressed during driving (or ramming) or if refusal would occur before achieving the desired penetration.

WEAP's numerical procedure is based on a Smith-type lumped mass representation of the pile and hammer model with a Newmark predictor-corrector type solution (*GRLWEAP 2010*). The "predictor" part of the algorithm obtains an approximate solution at time step while the "corrector" portion corrects the solution iteratively until the desired level of convergence is satisfied (e.g., user specified maximum time). Figure 6.4 shows the set of equations and the flow chart followed in the numerical solution. Initially, the acceleration of each pile segment is assumed to be equal to the gravitational acceleration of the hammer. The velocity and displacement of each lumped mass can be predicted via simple equations of motion based on the assumed acceleration. The spring forces are computed by multiplying the spring stiffness and relative displacement of two consecutive pile segments, and the dashpot forces are obtained by multiplying pile damping factors and relative velocities of two consecutive pile segments. Then, the acceleration of the pile segments are revised based on Newton's second law and external resistance forces (i.e., velocity and displacement values are corrected by integration). Thereafter, the velocities and displacements of the pile segments are corrected and all the forces are recalculated. The computation is iterated until the convergence criterion is achieved, which consists of equilibrium of velocities (i.e. convergence of the newly computed and previously predicted velocities). The permanent set is subsequently obtained as the difference between the maximum toe displacement and the average toe quake. The inverse of the permanent set per blow is the penetration rate (i.e., blow count) which is usually expressed in blows per meter.

The newest release of GRLWEAP® (*GRLWEAP 2010*) enabled the analysis of impact driving in horizontal and near horizontal directions. However, very little experience exists in employing the program to model horizontal or near horizontal pipe driving. Due

to the program formulation, the static capacity analysis tools used to create the soil profiles for pile resistance are not supported (i.e., enabled) during the horizontal driving option.

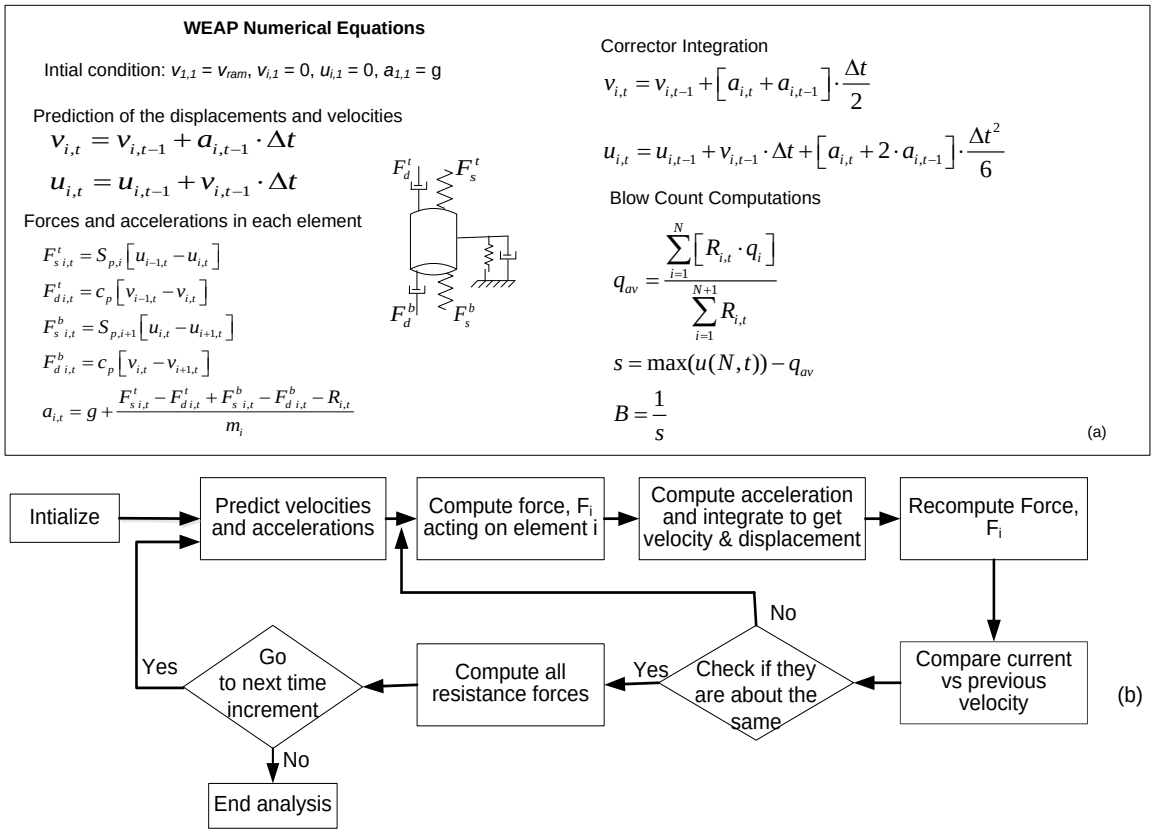

Figure 6.4: WEAP numerical procedure and integration (a) List of Numerical Equations and (b) Flow chart for the Predictor-Corrector analysis (*adapted from GRLWEAP ® 2010*).

6.2.4.2 Wave Analysis Program based on Smith's Difference Equations

Smith's idealization of the wave equation for pile driving forms the basis for many of the wave analysis programs. In this report, Smith's approach was implemented in the MATLAB® platform to be used for the planning and evaluation of pipe ramming installations (referred to as the Wave Equation Analysis for Pipe Ramming Installations, WEAPRI). The program (see Appendix D) has the capability to predict driving stresses, and the relationship between static soil resistance and the net set per blow (or blow count) during pipe ramming. The Matlab script of the program is attached in Appendix D.

The analysis of the wave equation starts with the ram mass impacting the rear end of the pipe with a velocity v_{ram}. The impact velocity, which is the function of the energy of the hammer, can be derived from kinematic energy consideration which is given by:

$$v_{ram} = \sqrt{\frac{2 \cdot e \cdot E_{rated}}{m_{ram}}} \qquad \textbf{(6.21)}$$

where E_{rated} = rated energy of the hammer, m_{ram} = mass of the ram, and e = is the energy transfer efficiency that accounts for energy losses inside the hammer system and the assembly placed between the hammer and the pipe. The pipe is discretized into lumped masses connected by linear springs and dashpots (Figure 6.2). The discrete pipe masses for each of the pipe elements are given by:

$$m_i = \rho \cdot \Delta L_i \cdot A \tag{6.22}$$

where ρ = density of the pipe material, A = cross sectional area, and ΔL_i = the length of pipe segment i. The pipe discretization can be generally based on the length of pipe embedded and the soil profile. The stiffness of the springs connecting the pipe segments is given by:

$$S_{p,i} = \frac{E \cdot A}{0.5(\Delta L_i + \Delta L_{i-1})} \tag{6.23}$$

The spring in between the ram and the rear end of the pipe must represent both the stiffness of the ram and the first pipe segment, which can be described by (*Loukidis et al. 2008*):

$$S_{p,i} = \frac{\left(\frac{EA}{0.5\Delta L}\right)_{pipe}\left(\frac{EA}{L}\right)_{ram}}{\left(\frac{EA}{0.5\Delta L}\right)_{pipe} + \left(\frac{EA}{L}\right)_{ram}} \tag{6.24}$$

Figure 6.5 presents a flowchart that illustrates the numerical procedure followed in the WEAPRI program. First, the velocity associated with an impact blow to be modeled is applied at time $t = 0$. Then, the displacements are computed, followed by the calculation of spring forces between the discrete masses of the pipe and the soil resistances acting on the discrete masses. Then the accelerations of the masses are determined and new velocities are derived. WEAPRI uses an explicit algorithm, such that all of the solution variables at time t are solved for t and are then used together to solve the solution variables at time step t+1. In contrast WEAP uses a predictor–corrector approach. This procedure is executed in a repetitive manner for successive time intervals until the stopping criterion is met. The stopping criterion is achieved when all of the mass velocities are less than zero and pipe face is no longer penetrating soil (i.e. the pipe has penetrated the soil to some maximum value and started rebounding backward) as recommended by Smith (*1960*). Another common stopping criterion is set by the specification of the maximum number of solution iterations; however, it is possible that the analysis could be stopped prior to completing all of the necessary calculations, particularly in case of long pipes (*Choe and Juvkam-Wold 2002*). Therefore, WEAPRI sets the stopping criterion based on the mass velocities.

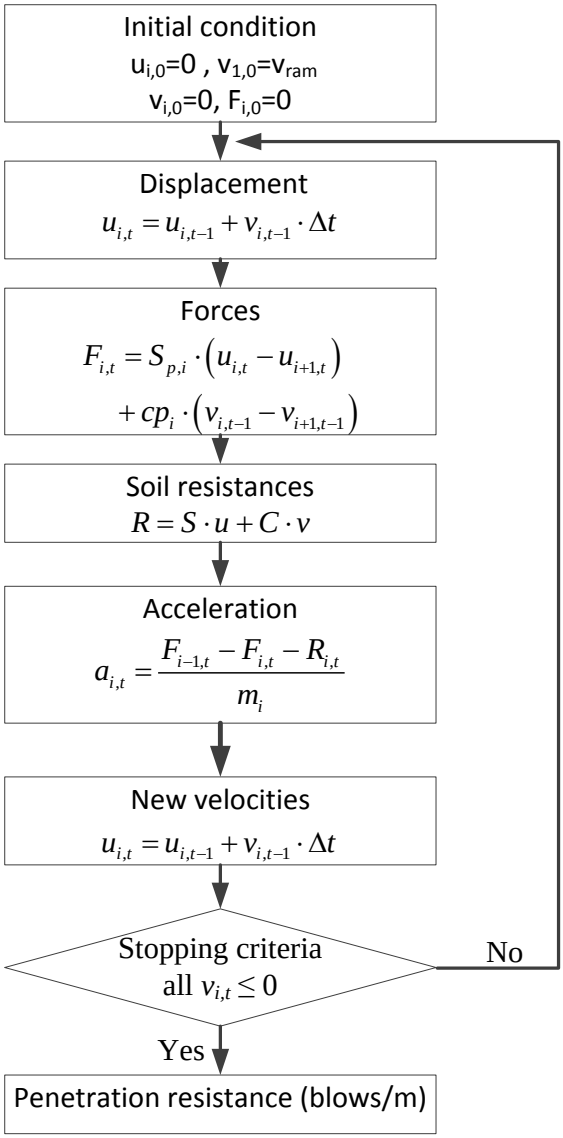

Figure 6.5: Numerical analysis procedures for WEAPRI.

Generally the wave propagation analysis requires the specification of various model inputs, including the pipe properties (diameter, length, wall thickness, modulus, and mass density), soil properties (face and casing static soil resistance, quake, and damping), and hammer properties (rated energy, energy transfer efficiency). The wave propagation analysis results in a prediction of penetration rate (i.e., blow count) measured in blows per foot or blows per meter. Additionally, the output from the wave analysis includes driving stresses induced in the pipe, maximum energy transferred to the pipe, and force and velocity traces as a function of time at the rear end of the pipe.

6.3 ANALYSIS OF STRESS WAVE OBSERVATIONS

6.3.1 Theoretical Background

The dynamic response of a pipe during impact driving can be studied using wave propagation models and stress wave measurements obtained during pipe driving. Pipe monitoring is carried out with high-frequency sampling strain gauges and accelerometers that are attached to the pipe at a distance of one to two diameters from the rear end of the pipe. This practice is incorporated into standard specifications for deep foundation monitoring by the American Society of Testing and Materials specification D 4945 (*ASTM 2008*). Force, *F*, and velocity traces of each hammer blow are digitally recorded and stored in the Pile Driving Analyzer (PDA) for real-time monitoring and post-processing and analysis. The stress wave measurements (velocity and force traces) can be used to qualitatively evaluate the soil response. To assist in real-time monitoring, the PDA typically plots both the force and velocity records on the same scale by converting the velocity to an equivalent force (F^*) using:

$$F^* = \frac{E \cdot A}{c} v = Z \cdot v \qquad \textbf{(6.25)}$$

where Z = the impedance of the pile. The time required for the force or velocity wave to travel down the pipe to the pipe face and back to the rear end of the pipe is given by $2L/c$. The traces F and F^* initially overlap and develop a peak response simultaneously; however, the traces separate post-peak due to the activation of soil resistance along the pipe. The separation of the F and F^* traces between the time of impact and the time $2L/c$ corresponds to the shaft or casing soil resistance, whereas this difference at time $2L/c$ represent the face resistance. Figure 6.6 illustrates the force and velocity traces for different soil resistance conditions (*Hannigan 1990*): Figure 6.6a shows a slight separation of the traces over the range of time $t = 0$ and $t = 2L/c$ and abrupt increase and decrease in velocity and force records, respectively, at $t = 2L/c$. This indicates the minimal existence of casing and face soil resistances. Figure 6.6b also indicates minimal separation between the force and velocity traces in the range of time $t = 0$ and $t = 2L/c$; however, there is a large increase in the force and decrease in the velocity records occur at t = 2L/c. This indicates minimal casing resistance and high face soil resistance. Figure 6.6c, on the other hand, shows a large separation of the force and velocity traces over the time range of t = 0 and t = 2L/c, and indicates high casing resistance.

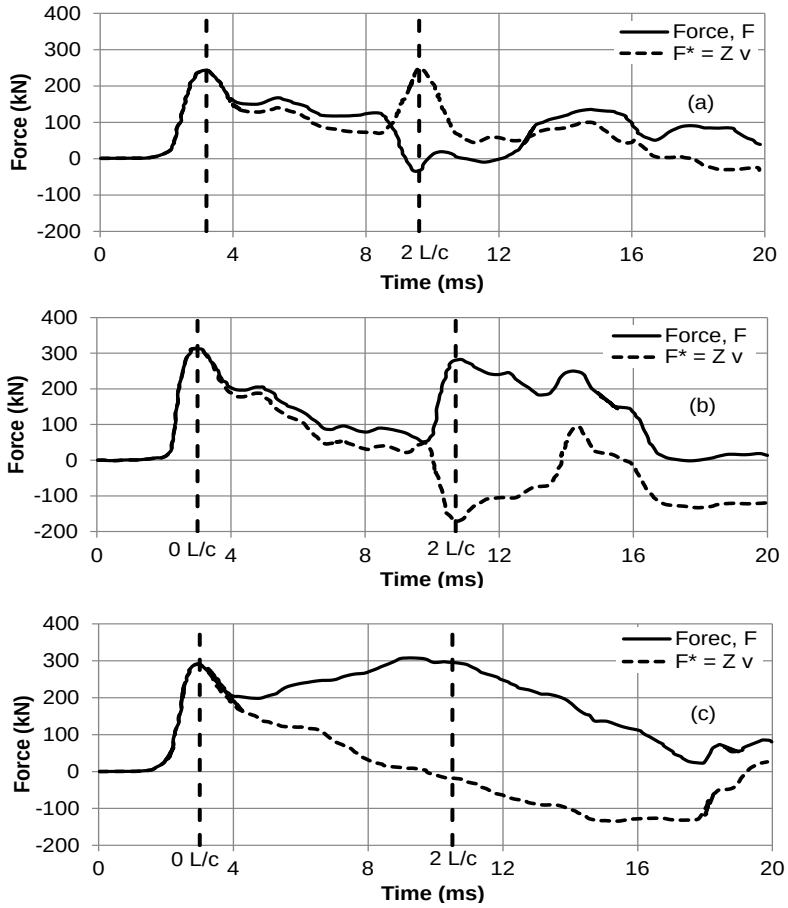

Figure 6.6: Typical force and velocity traces for (a) minimal casing and face resistance condition, (b) significant face resistance conditions, and (c) significant casing resistance condition (*after Hannigan 1990*).

The need for the prediction of the soil resistance, energy transferred, and the driving stress during each hammer blow has resulted in the development of a simple closed-form solution of the wave equation that can be used in real-time (i.e., without computationally expensive numerical analyses). The Case Method (*Goble et al. 1975* and *Rausche et al. 1985*) is one of the popular closed form solutions of the wave equation for the evaluation of the various quantities associated with driving based on the dynamic measurements of force and velocity signals. The method incorporates the static and dynamic driving resistance and assumes that the soil resistance is concentrated at the toe of the pile (or in this case, the face of the pipe). The total soil resistance (i.e. static and dynamic) acting on the pipe during driving is given by (*Goble et al. 1975*):

$$R_t = \frac{F(t_1)+F(t_2)}{2} + \frac{Z\cdot\left[v(t_1)-v(t_2)\right]}{2} \qquad \textbf{(6.26)}$$

where F = force measured at the gauge location; v = velocity measured at the gauge location, t_1 = time of initial impact, t_2 = time of reflection of initial impact from pile toe = t_1 + 2L/c, Z = the impedance (Z = EA/c) and where L = length of pipe below the gauge location.

The dynamic portion of the driving resistance is determined based on an assumed dimensionless damping factor and approximated as a linear function of the damping factor multiplied by the toe velocity (*Goble et al. 1975*):

$$R_d = J \cdot Z \cdot v_{toe} \qquad \textbf{(6.27)}$$

where J = Case damping factor near the pile toe and v_{toe} = toe velocity. The Case damping factor has a significant effect on the magnitude of the soil resistance predicted by the Case Method, and the selection of its value is an important task. For recommendations on typical ranges, see Goble et al. (*1975*). The static soil resistance is simply the difference between the total and dynamic resistance, which is given by (*Rausche et al. 1985*):

$$R_s = R_t - R_d = (1-J)\left[\frac{F(t_1)+Z\cdot v(t_1)}{2}\right]+(1+J)\left[\frac{F(t_2)-Z\cdot v(t_2)}{2}\right] \qquad \textbf{(6.28)}$$

Because pipes are not required to carry the significant axial loads that piles are designed to carry, the main concern for pipe ramming installations rests with drivability of the pipe. Thus, the main task for pipe drivability is to determine the total soil resistance (static and dynamic, R_t). In general, the Case Method offers an approximate estimate of the soil resistance, useful for real-time monitoring in known soil stratigraphies, and a more reliable estimate of the soil resistance requires a rigorous analysis of the force and velocity records through a signal matching process. Signal matching, as it pertains to this report, is described below.

The stress developed in the pipe during impact driving can be attributed to compressive, tensile, and flexural forces. However, the compressive stress is usually the most important component due to the nature of the impact (compression) and the presence of soil resistance. The PDA computes the maximum compression stress at the rear end of the pipe by dividing the maximum measured force with cross sectional area of the pipe for each hammer blow. The maximum compressive stress developed in the pipe should not exceed the limiting design strength of the pipe (i.e., the yield stress) to prevent damage. The maximum allowable compressive stresses should generally be limited to 90 percent of the nominal yield stress of the steel pipe (i.e. f_y = 241 MPa) based on recommendations for pile driving operations (*Hannigan et al. 2006*). The estimate of the compressive stress, σ_c , can also be estimated using the axial wave propagation equation for uniform elastic bar subjected to impact by a rigid body, given by (*Stuedlein and Meskele 2012*):

$$\sigma_c = \frac{E}{c}\cdot v_p \qquad \textbf{(6.29)}$$

where v_p = pipe particle velocity upon impact. Equation 6.29 provides a conservative upper bound stress estimate if the velocity of the pipe is set equal to the velocity of the ram; however, Fellenius (*2011*) noted that v_p can be derived from the hammer (or ram) velocity immediately before impact, v_r:

$$v_p = \frac{v_r}{1 + Z_p / Z_r} = \frac{v_r}{1 + A_p / A_r} \quad \textbf{(6.30)}$$

where Z_p and Z_r = impedance of the pipe and ram, respectively, and A_p and A_r = the cross-section area of the pipe and ram (i.e. encased piston), respectively. The impedance, Z, of a pipe is a function of its modulus of elasticity, cross sectional area, and wave propagation velocity ($Z = EA/c$). The ratio of impedance reduces to the ratio of their area if the pipe and hammer are made of the same material as is the case for pipe ramming.

The energy transfer from the hammer to the pipe can be computed for each impact by integrating the product of force and velocity signals with respect to time, which is given by (*Goble et al. 1980*):

$$E_{transfer}(t) = \int_0^t F(t) \cdot v(t) dt \quad \textbf{(6.31)}$$

The maximum energy transferred to the pipe for each hammer strike can be obtained by taking the maximum value of $E_{transfer}$ for the force and velocity traces and interval of time considered. This allows an evaluation of the performance of the driving system (i.e., the hammer, the pipe and their connection).

6.3.2 Case Method Analysis of Field Observations

The Case Method of analysis was carried out for three production installations (Case 1, Case 2 and Case 3) and the full scale field experiment (Case 6), which are described in Chapter 3. The Case method computations provides the driving stress, energy transferred, and total soil resistance during impact driving in real-time based on the PDA force and velocity measurements at the rear end of the pipe. Figure 6.7 shows the maximum transferred energy, induced compressive stresses, and total soil resistance observed during the Case 1 installation. The analysis was carried out for the second 9.1 m pipe segment over the penetration length of 11.7 to 20.4 m (Section 3.1). The dynamic pipe material properties required to evaluate driving stresses includes the elastic modulus, E = 210 GPa, material density, ρ = 7881 kg/m3, wave speed, c = 5155 m/s and nominal pile impedance, Z = 964 kN sec/m. The energy transfer profile (Figure 6.7a) decreases with penetration length, decreasing to approximately 17 percent of the estimated rated HammerHead hammer energy (i.e. 6.4 kN-m) at a penetration length of 19.5 m. The compressive stress profile (Figure 6.7b) indicates a relatively constant average stress of 60 MPa for most of the penetration length, which is significantly smaller than the allowable compressive stress in the pipe (i.e. 241 MPa). The total soil resistance plotted in Figure 6.7c shows an increasing trend over the length of the pipe due to the increasing casing area available to generate frictional resistance. However, a relatively high soil resistance was observed initially, which could have resulted from the loss of soil arching over the interval of welding of the second pipe segment before the resumption of driving.

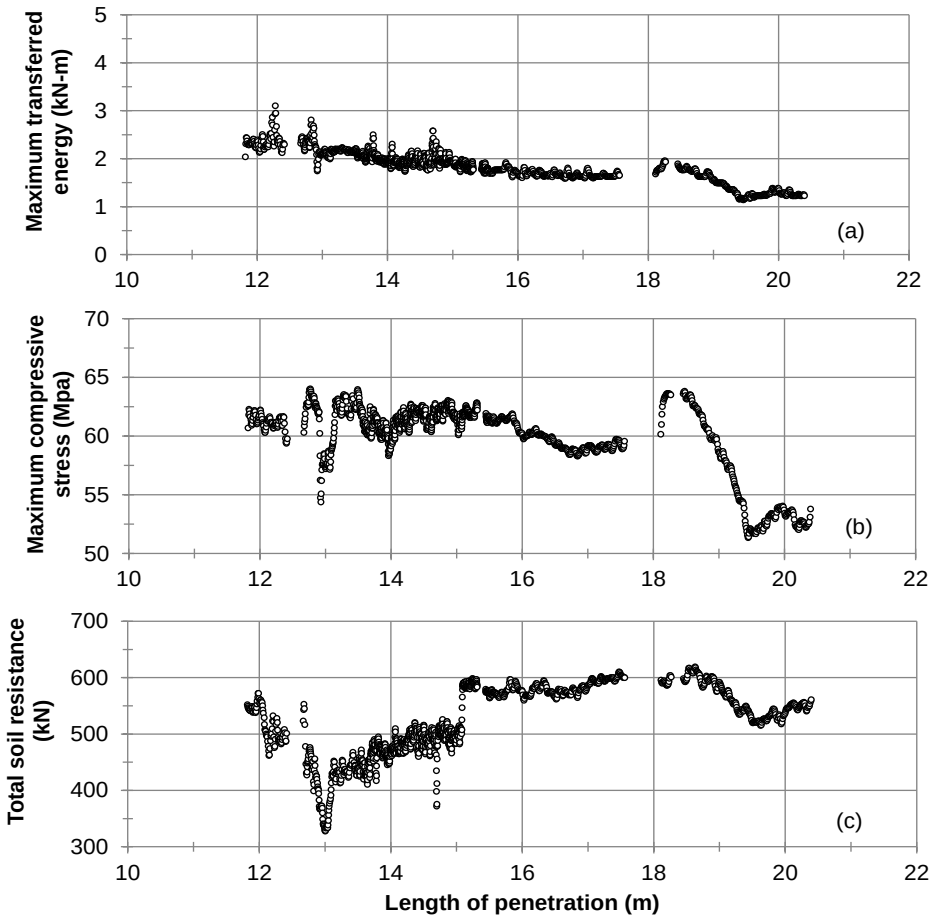

Figure 6.7: Case Method results indicating pipe performance for Case 1: (a) maximum transferred energy (b) maximum induced compressive stress in the pipe, and (c) total (static and dynamic) soil resistance.

Figure 6.8 presents the maximum transferred energy, compressive stresses, and total soil resistance observed during the Case 2 installation. The analysis was carried out for the second and third pipe segment installations (each 12 m in length, Section 3.2). The energy transfer profile (Figure 6.8a) shows an increasing trend over a penetration length of 8 m to 20 m; which is attributed to the consistent tightening of the restraining chains that ensure connection of the hammer to the pipe during the initial portion of the drive. The average energy transferred is equal to approximately 40 and 50 percent of the rated Grundoram Apollo energy (i.e., 40.5 kN-m) for the second and third pipe segment installations respectively. The maximum compressive stress profile (Figure 6.8b) shows a somewhat similar trend to that of the maximum energy transfer profile with an average

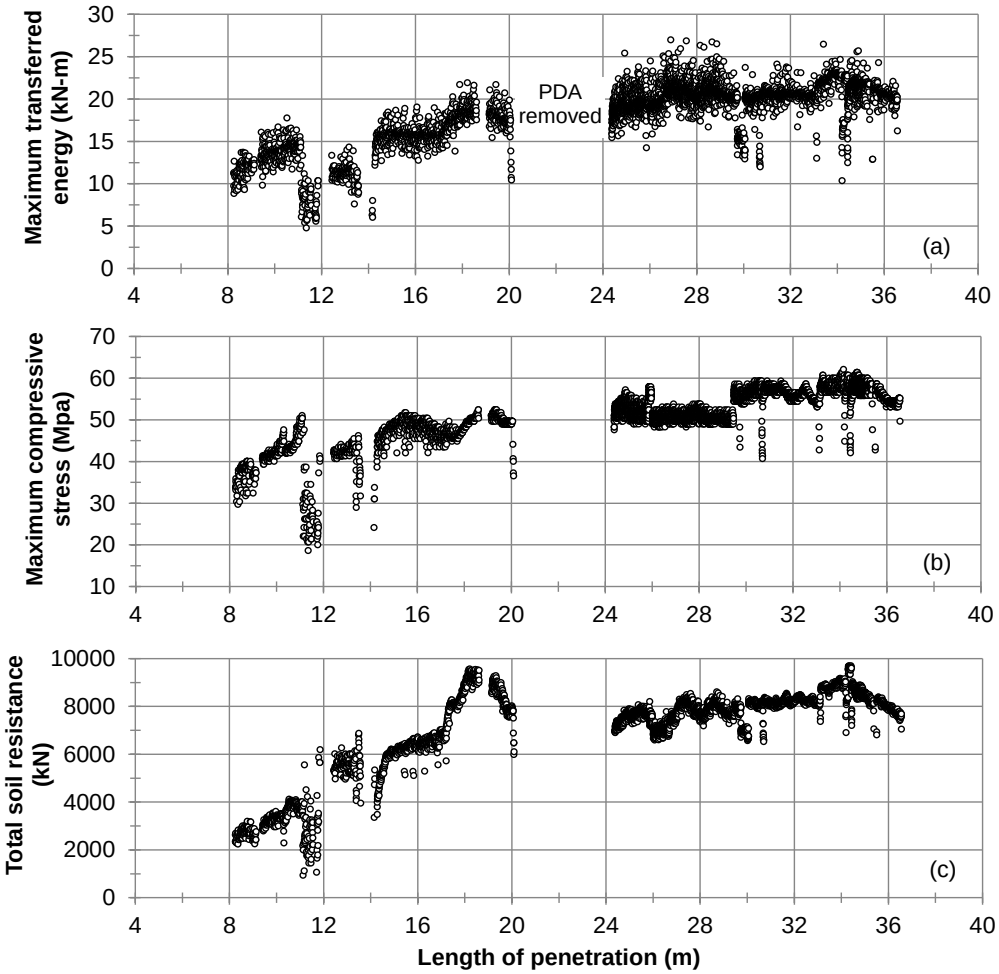

Figure 6.8: Case Method results indicating pipe performance for Case 2: (a) maximum transferred energy (b) maximum induced compressive stress in the pipe and (c) total (static and dynamic) soil resistance.

value of 45 MP and 55 MPa over the second and third pipe segment, respectively. These values are considerably smaller than the allowable compressive stress for the pipe. The total soil resistance profile (Figure 6.8c) increases over the second length of the pipe and at a somewhat constant trend (i.e. approximately 8,000 kN) for the third segment of the pipe. The increasing trend of the total soil resistance can be attributed to one or more of the following reasons: (1) an increasing depth of cover above the crown of the pipe associated with the highway embankment resulting in a corresponding increase in the overburden pressure (Figure 3.8), (2) the increase in the strength of the embankment fill material along the length of the pipe (Figure 3.8), and (3) an increasing casing area available to generate frictional resistance. In addition, the concrete walls resulted in higher face resistances at length of penetration around 34 m which contributed to a higher total soil resistance.

The Case Method results for the Case 3 installation are presented in Figure 6.9. The analysis was carried out for a portion of the fourth pipe segment driven by an IHC S-280 hammer. The IHC S-280 hammer and the pipe were held together using a winch and a cable that applied a tensile force of approximately 1,100 kN, providing an equal component of compressive force on the connection. The IHC S-280 hammer has a nominal maximum rated energy of 280 kN-m for

vertical impact driving; however, for horizontal driving, it can provide a nominal maximum rated energy of 142 kN-m. The energy transfer profile (Figure 6.9a) shows a constant energy transfer of 60 kN-m over a penetration length of 47 m to 49 m, and 75 kN-m over a penetration length of 49 m to 52 m. The compressive stress profile (Figure 6.9b) also tracks the general trend of the energy transfer, and exhibits an average of 55 MPa over a penetration length of 47 m to 49 m, and 65 MPa over a penetration length of 49 m to 52 m, which is significantly smaller than the allowable compressive stress (i.e., 241 MPa). The total soil resistance profile (Figure 6.9c) indicates a somewhat constant resistance of 20,000 kN for the observed penetration length.

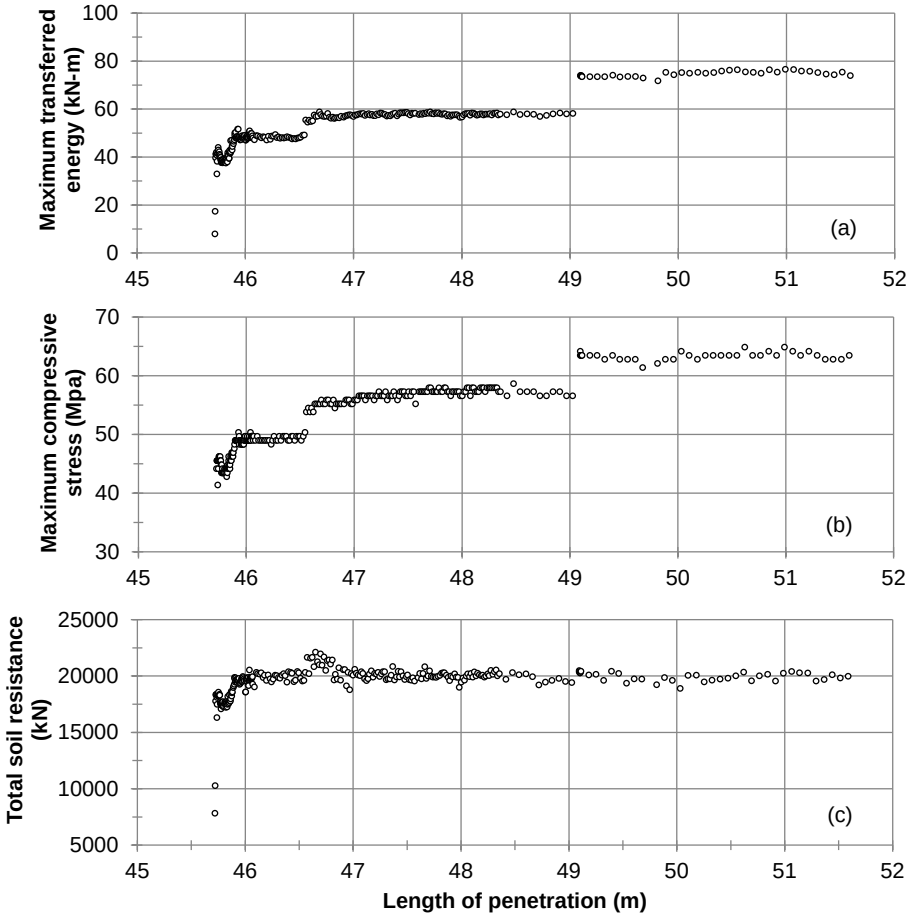

Figure 6.9: Case Method results indicating pipe performance for Case 3: (a) maximum transferred energy (b) maximum induced compressive stress in the pipe, and (c) total (static and dynamic) soil resistance.

Figure 6.10 presents the Case Method analyses for the six, 6 m long pipe segments of the Case 6 pipe installation. The details of the experimental setup are provided in Section 3.6.4. The 400 mm HammerHead hammer was used to drive the first five pipe segments; the 610 mm Grundoram Taurus was used for the sixth and last pipe segment. The Grundoram Taurus hammer was supported vertically by straps tied to an excavator, and was restrained horizontally with tensioned chains. The energy transfer profile (Figure 6.10a) shows a relatively constant transfer of energy for the first five segments, which is attributed to the careful monitoring and adjustment of the tensioned chains during the ramming. The overall increase in transferred energy shown for the sixth segment is indicative of the greater energy associated with the Taurus hammer. However, the energy transfer is significantly more variable, due to issues associated with the

hammer-pipe connection, as described below (Section 7.4). The compressive stress profile (Figure 6.10b) followed the general trend of the maximum energy transfer, and indicates an average of approximately 40 MPa for the first five segments. For the last pipe segment, the overall compressive stress increased from 40 MPa to 80 MPa over a penetration length of 29.2 m to 32.2 m, with a subsequent drop and relatively constant compressive stress of 60 MPa was observed over the rest of the penetration length. At approximate penetration lengths of 29.5 m, 30.1 m and 30.7 m significant drops in compressive stress as well as energy transfer were observed, corresponding to instances where excavator boom could not keep the hammer level and aligned with the pipe.

The soil resistance profile (Figure 6.10c) displays an increasing trend over the first pipe segment. Towards the end of the first segment (i.e., at a penetration length of approximately 4.5 m), the resistance was relatively high due to the soil plug that had filled the pipe and was reacting against the collet and back-plate hammer connection. For the second pipe segment, comparatively larger resistances were observed compared to the first segment due to the increase in casing area available to generate casing resistances. However, the total soil resistance decreased with greater penetration due to the decrease in the dynamic soil resistance associated with the reduction in energy transfer and slower pipe velocities. A reduction in the resistance was also observed for the third pipe segment due to the removal of the soil before the commencement of driving. For the fourth and fifth pipe segments, the profile illustrates a lower resistance on average which is attributed to the use of lubrication during driving. The soil resistance showed a rise around a penetration length 25 m (i.e., halfway through the driving of the fifth pipe segment) due to the bleeding and loss of the lubrication around the annulus, likely due to damage of the buried lubricant conduit. Figure 6.11 shows the rapid flow of lubricant from the top of the pipe at this point in the drive. However, at the beginning of the fourth and fifth pipe segments, the initial soil resistance to ramming was relatively high; this is likely due to the loss of soil arching over the pipe during the time between the previous drive and the completion of welding and resumption of driving. The delay was equal to 89 and 8 hours for the fourth and fifth pipe, respectively. As ramming continued, soil resistance decreased as the soil arch above the pipe was re-established and as lubricant was pumped into the overcut. Finally, the soil resistance observed for the last pipe segment was higher in comparison to the other pipe segments due to the use of a hammer with a larger rated energy, which induces higher viscous or dynamic resistance to ramming due to the higher pipe velocities.

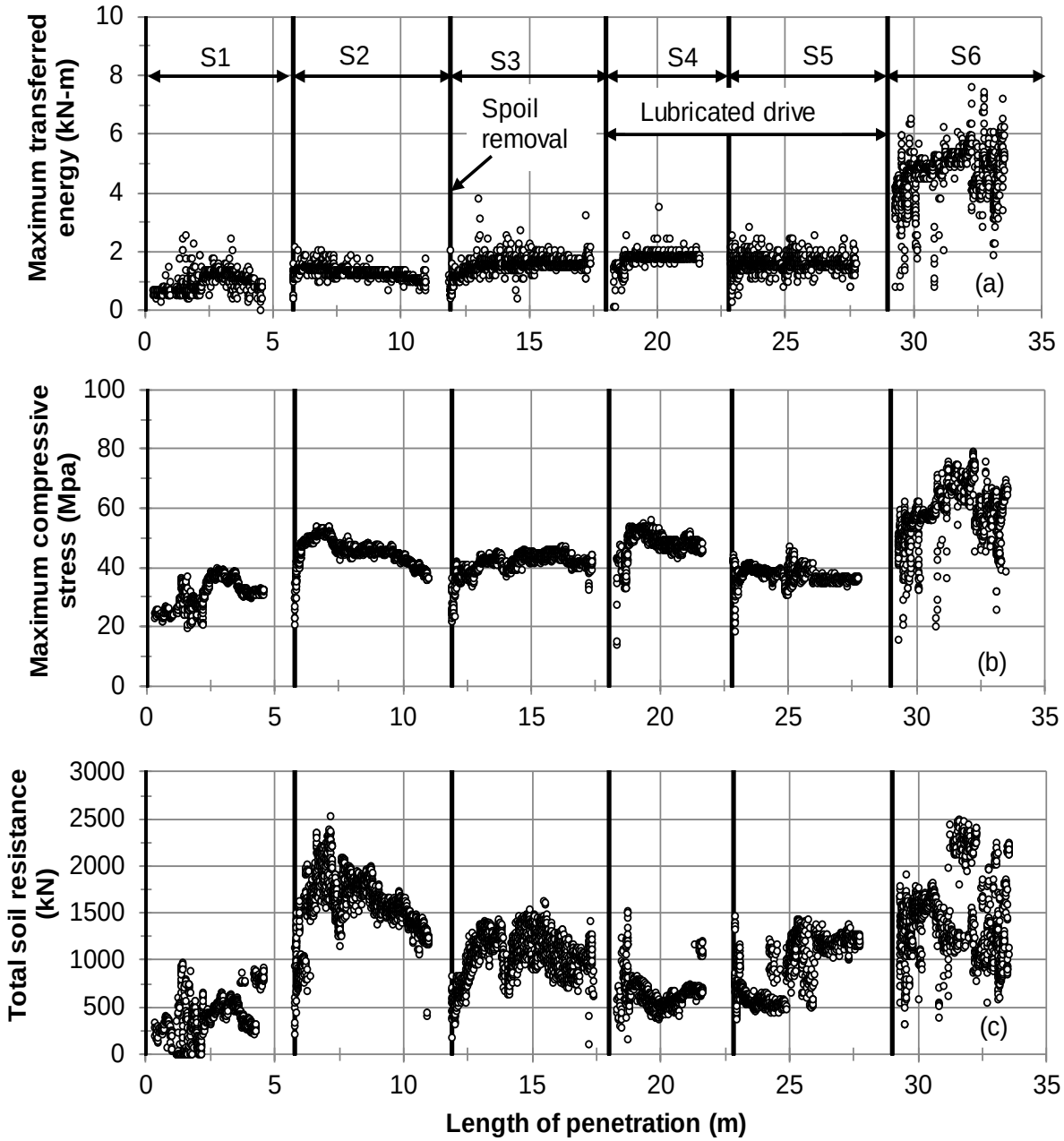

Figure 6.10: Case Method results indicating pipe performance for Case 6: (a) maximum transferred energy (b) maximum induced compressive stress in the pipe, and (c) total (static and dynamic) soil resistance.

Figure 6.11: Photo showing the bleeding loss of the lubricant due to the likely damage of the lubricant hose close to the insertion of the pipe.

The values of the maximum energy transferred for the four case histories (Cases 1 through 3 and Case 6) are summarized in Table 6.1. The mean and coefficient of variation (COV, equal to the standard deviation divided by the mean) of the maximum energy transferred ranged from 1.4 kN-m to 53.6 kN-m and 14 to 20 percent, respectively. Hammer-pipe energy transfer efficiency is analyzed in greater detail in Section 7.4. The compressive stresses of Cases 1 through 3, and Case 6 are summarized in Table 6.2. The mean and COV of the compressive stresses ranged from 40 MPa to 60 MPa and 0.05 to 0.15 respectively. In other words, the mean of the compressive stresses ranged from 9 to 24 percent of the yield stress and indicates the likely use of excessive wall thicknesses for each of the case histories.

Table 6.1: Statistical summary of Case Method derived maximum energy transfer.

Project description	Ram Type	Rated Energy (kN-m)	Max. Energy Transferred (kN-m)	
			μ = Mean	COV
Case 1	HammerHead	6.4	1.9	0.19
Case 2	Grundoram Apollo	40.5	17.5	0.14
Case 3	IHC S-280	142	53.6	0.20
Case 6	HammerHead	6.4	1.4	0.16
Case 6	Grundoram Taurus	18.6	4.7	0.17

Table 6.2: Statistical summary of Case Method derived compressive stress.

Project description	Ram Type	Rated Energy (kN-m)	Pipe diameter (mm)	Pipe wall thickness (mm)	Max. Compressive Stress (MPa)		
					μ = Mean	COV	Percent of yield stress
Case 1	HammerHead	6.4	610	12.5	60.3	0.05	24
Case 2	Grundoram Apollo	40.5	2440	25	49	0.09	20
Case 3	IHC S-280	142	3660	38	53	0.12	21*
Case 6	HammerHead	6.4	1060	12	40.9	0.09	7
Case 6	Grundoram Taurus	18.6	1060	12	58	0.15	9

* Estimated yield stress

6.4 BACK-ANALYSIS OF SOIL RESISTANCE TO RAMMING

6.4.1 Theoretical Background

Soil resistance parameters such as the ultimate static face and casing resistance, the face and casing quake, and the face and casing damping are commonly back-calculated using signal matching. The signal matching process consists of the simulation of the stress wave signals that are measured at the rear end of the pipe during driving using the Smith (*1960*) model. The signal matching process involves the optimization of the set of soil resistance parameters that minimizes the difference between the simulated and measured force and velocity records. The modeling starts with imposing either the measured force or the measured velocity signal as the loading boundary condition at the rear end on the pipe and the initial assumed soil resistance parameters. Then, the simulation of either the force or velocity signal follows, with gradual variation of the soil resistance parameters in an iterative process until the difference between the measured and simulated velocity or force traces meets an acceptable match criterion. An objective function to be minimized in the signal matching process can be described by (*Balthaus 1988*):

$$D = \int_0^t \left| F_m - F_s \right| \cdot dt \qquad \textbf{(6.32)}$$

where F_m = measured force and F_s = simulated force. Figure 6.12 demonstrates a general framework of the numerical stress wave matching procedure.

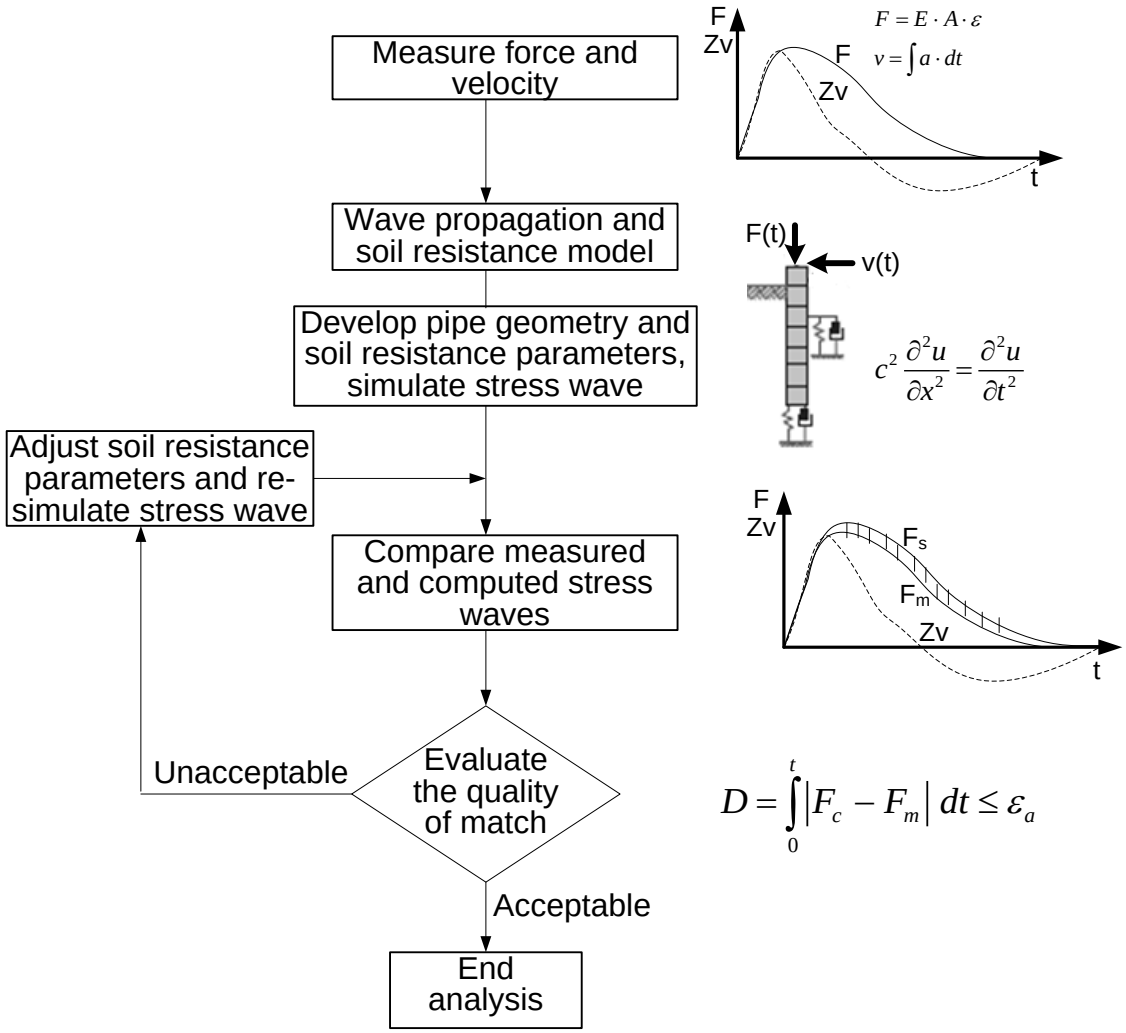

Figure 6.12: General procedure for numerical simulation of measured stress wave signals (*adapted from Balthaus 1988*).

The Case Pile Wave Analysis Program (CAPWAP) (*Rausche et al. 1972*) is a widely used signal matching program where the matching is done iteratively by varying the soil resistance parameters such as static face and casing resistance, face and casing quake, and face and casing damping. The program generates a representation of a pile (or in this case, a pipe) as a series of pile segments and models the soil resistance by the use of elastic-plastic springs and dashpots, similar to the Smith model described earlier. The matching processes starts by introducing a reasonable estimate of soil parameters in the model. In the early stage of development, CAPWAP used force matching or velocity matching based on minimization of the target function (Equation 6.32). However, the current CAPWAP program matches the upward travelling wave trace with the downward traveling wave trace, the latter of which is forced on the rear end of the pipe model and represents the loading boundary condition. The stress wave-up (*UW*) and wave-down (*DW*) traces can be represented by:

$$UW(t) = \frac{F(t) - v(t) \cdot Z}{2} \qquad \textbf{(6.33)}$$

$$DW(t) = \frac{F(t) + v(t) \cdot z}{2} \tag{6.34}$$

where $F(t)$ = force time history, and $v(t)$ = velocity time history. The program computes the upward traveling wave and compares the computed and measured records. The soil parameters are adjusted and simulations are iterated until an acceptable match is computed (e.g., Figure 6.13). CAPWAP employs an objective function that is based on the sum of the absolute difference between the measured and computed upward wave traces normalized by the sum of the absolute measured upward stress wave trace. This function is defined as the match quality number and is minimized during the signal matching process and is given by (*Rausche et al. 2010*):

$$MQN = \frac{\sum_{t_1}^{t_n} \left| UW_m - UW_c \right|}{\sum_{t_1}^{t_n} \left| UW_m \right|} \tag{6.35}$$

the subscripts *m* and *c* represents the measured and computed upward traveling waves.

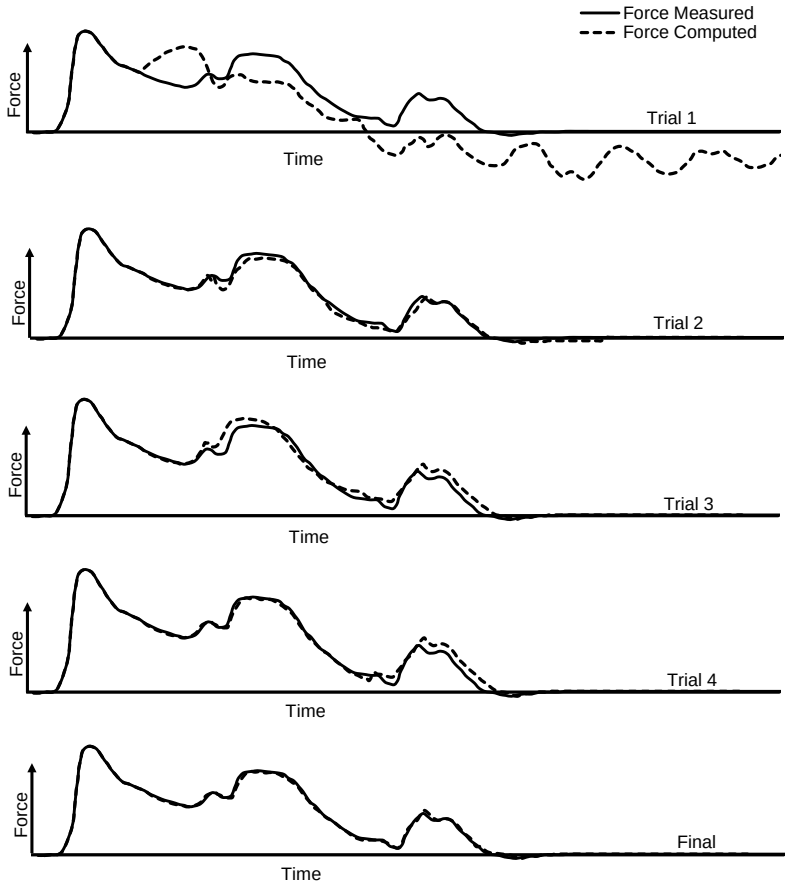

Figure 6.13: CAPWAP Iteration for the signal matching process (*adapted from Hannigan et al. 2006*).

6.4.2 CAPWAP Analysis of Field Observations

The CAPWAP analysis was carried out for three production installations (Case 1 through 3) and the full scale field experiment (Case 6), which were previously discussed. The CAPWAP analysis provided a refined estimate of static face and casing resistance, face and casing quakes, and face and casing damping coefficients. The CAPWAP analysis is performed on an individual hammer blow at a desired length of penetration. Twenty-four hammer blows from the four case histories were selected for CAPWAP analysis and the results are described below.

Two hammer blows were assessed for Case 1. The CAPWAP analyses for these two blows indicates a moderate increase in total static resistance with increasing penetration length due to an increase in the area of casing resistances with penetration (Figure 6.14). The static face resistance remains constant over the length observed, because the height of overburden was relatively constant for the length of the pipe monitored. The face and casing quake values were found to vary between 2 and 3 mm. The Smith face damping coefficients varied narrowly between 2.5 and 3 sec/m and were independent of static soil resistance. Similarly the Smith casing damping coefficients ranged between 2.3 and 2.6 sec/m. On the other hand, the Case damping coefficients increased with static soil resistance for both of the hammer blows analyzed, and ranged from approximately 0.20 to 0.55.

Figure 6.15 illustrates the CAPWAP results of Case 2 where ramming of a culvert encountered abandoned and buried concrete wing-walls. Four hammer blows were analyzed for Case 2. The static soil resistances were observed to show an increasing trend over the penetration length of the pipe due to an increase in the area of casing resistances, an increase in overburden pressure with penetration (over the first 20 m), and increase in soil strength with penetration (see Figure 3.8). The spikes in total resistance to ramming during penetration of the concrete wing walls was verified with the CAPWAP-based static resistance, as noted at a length of approximately 34 m. The increase in static soil resistance to ramming in proximity to the concrete wingwall was evident both in casing resistance (though a significant contribution of the increase in strength in the embankment soils must be acknowledged) and the face resistance. Most of the face and casing quake values were found to vary between 2 and 3 mm. The Smith face damping coefficients were observed to be independent of the static soil resistance and ranged between 2 and 4.3 sec/m. Similarly, the Smith casing damping coefficients were observed to vary between 1.5 and 2.7 sec/m. The Case damping coefficients for the face and casing showed an increasing trend over the range of static soil resistance encountered.

Four hammer blows were evaluated using CAPWAP analysis for Case 3, in which the pipe was rammed through abundant cobbles and large boulders. The CAPWAP results are presented in Figure 6.16, and show an increase in the static soil resistance due to an increase in the area of casing resistance along the length of penetration. The static face resistances were observed to be constant due to relatively invariant overburden pressure and soil conditions encountered throughout the length of penetration. The face and casing quake values were found to vary between 0.5 and 2 mm independent of the magnitude of the static soil resistance. The Smith face damping coefficients were observed to vary between 1.4 and 4 sec/m, whereas the Smith Casing damping coefficients were found to fluctuate in the narrow range of 3.5 and 4 sec/m. The casing Case damping coefficients exhibited an increase with the static soil resistance over the range of

0.4 and 1.5, whereas the face Case damping coefficient appeared to be relatively constant with a value of approximately 0.1, independent of the static soil resistance.

Figure 6.17 presents the fourteen hammer blows selected for CAPWAP analysis for the full-scale experimental test (Case 6) described in Section 3.6.4 and Section 6.3.2. The static resistances showed a slightly increasing trend with length of penetration for the first four pipe segments due to a mild increase in both the face and casing resistances. The spoil accumulated in the first two pipe segments was removed before welding the third pipe segment which is likely the cause for lower soil resistances on the third pipe segment. Also, the lubrication applied during installation of the fourth pipe segment appeared to have a significant impact of lessening the soil resistance (described in Section 7.2). On the fifth pipe segment, the static soil resistances were found to moderately increase due to loss of lubrication because of damage to the lubricant conduit. The static soil resistance showed further increase on the last segment of the pipe due to the increase in casing resistance and the termination of the use of lubrication. The face and casing quake values were found to vary in a narrow range of 1.8 and 2.6 mm independent of the static soil resistances. The Smith face damping coefficient was found to vary between 1 and 3 sec/m while the Smith casing damping coefficient was in the range of 0.5 and 2 sec/m, independent of the static soil resistances. The Case damping coefficients for both the face and casing showed increasing trends with the static soil resistance over a range of 0.02 and 0.45.

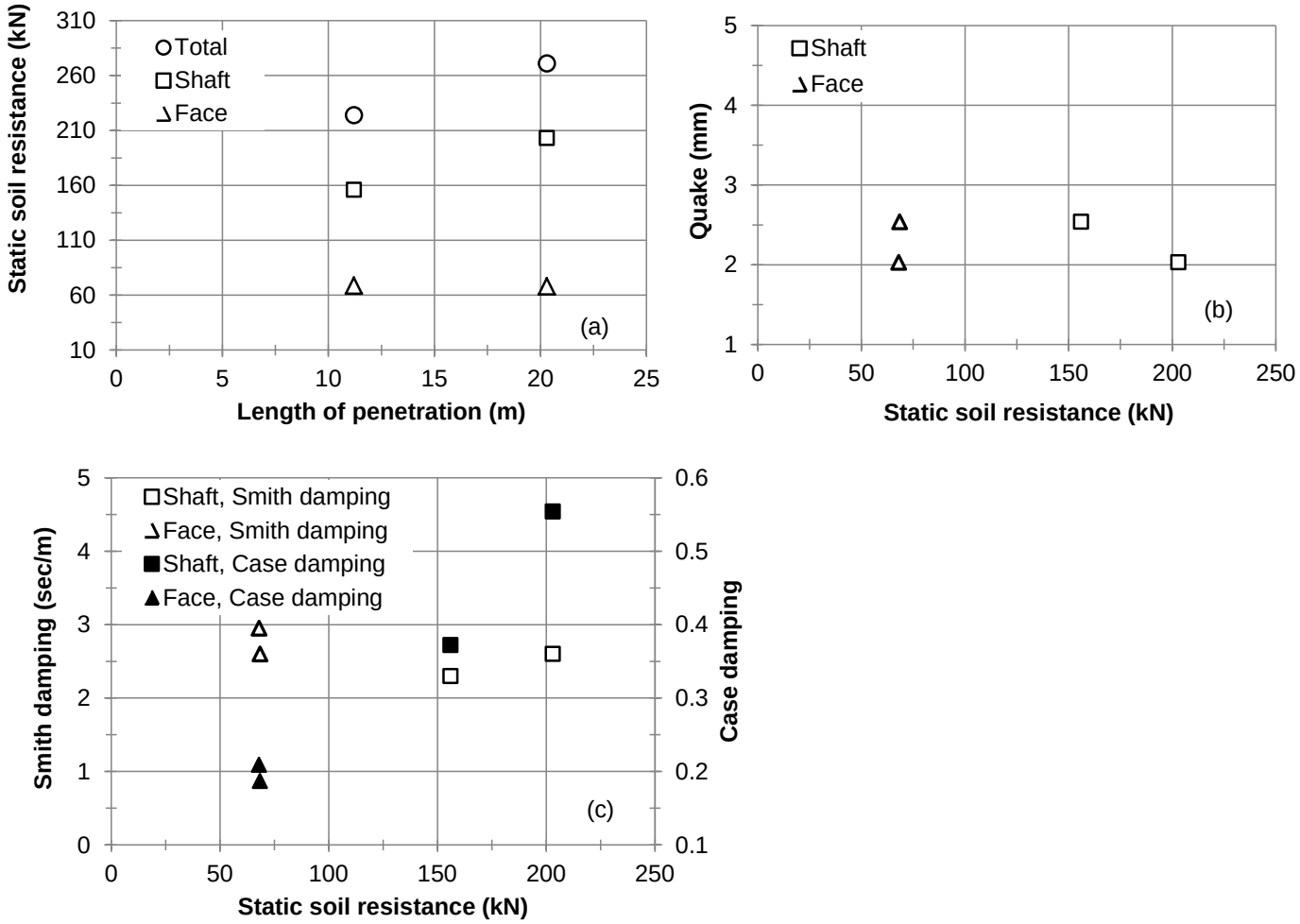

Figure 6.14: CAPWAP results for the Case 1 installation: (a) static soil resistance, (b) quake values, and (c) Smith and Case damping constants.

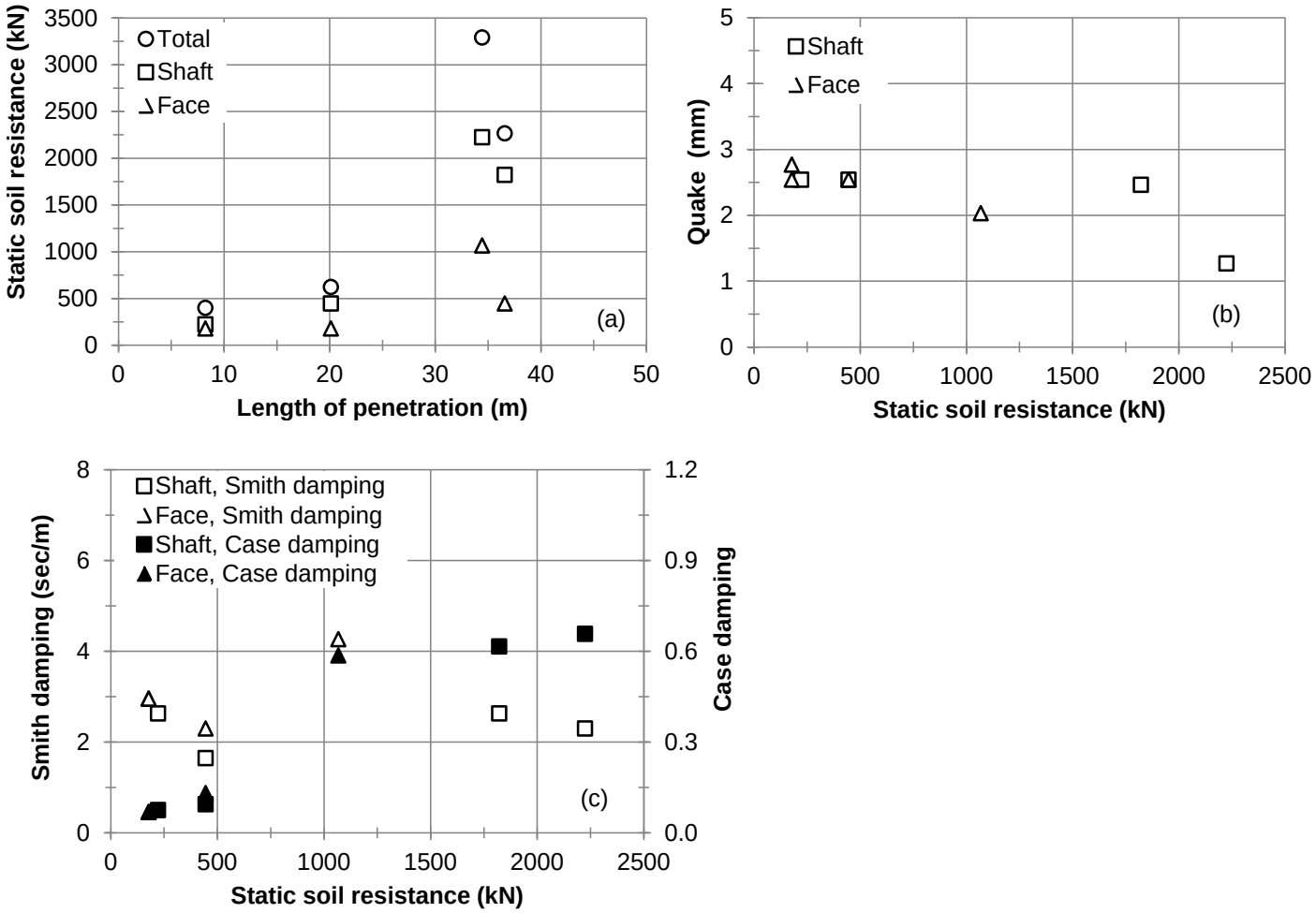

Figure 6.15: CAPWAP results for the Case 2 installation: (a) static soil resistance, (b) quake values, and (c) Smith and Case damping constants.

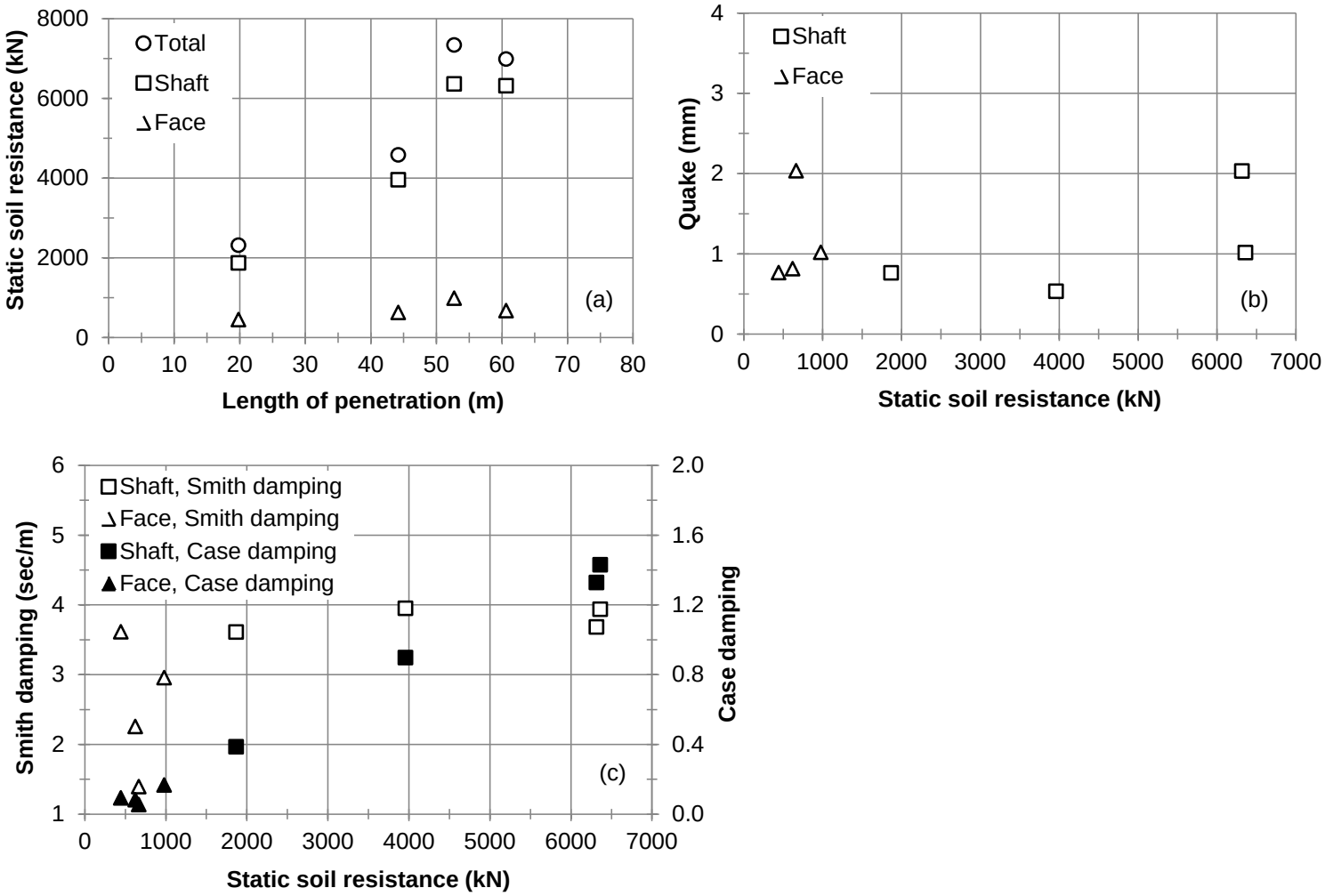

Figure 6.16: CAPWAP results for the Case 3 installation: (a) static soil resistance, (b) quake values, and (c) Smith and Case damping constants.

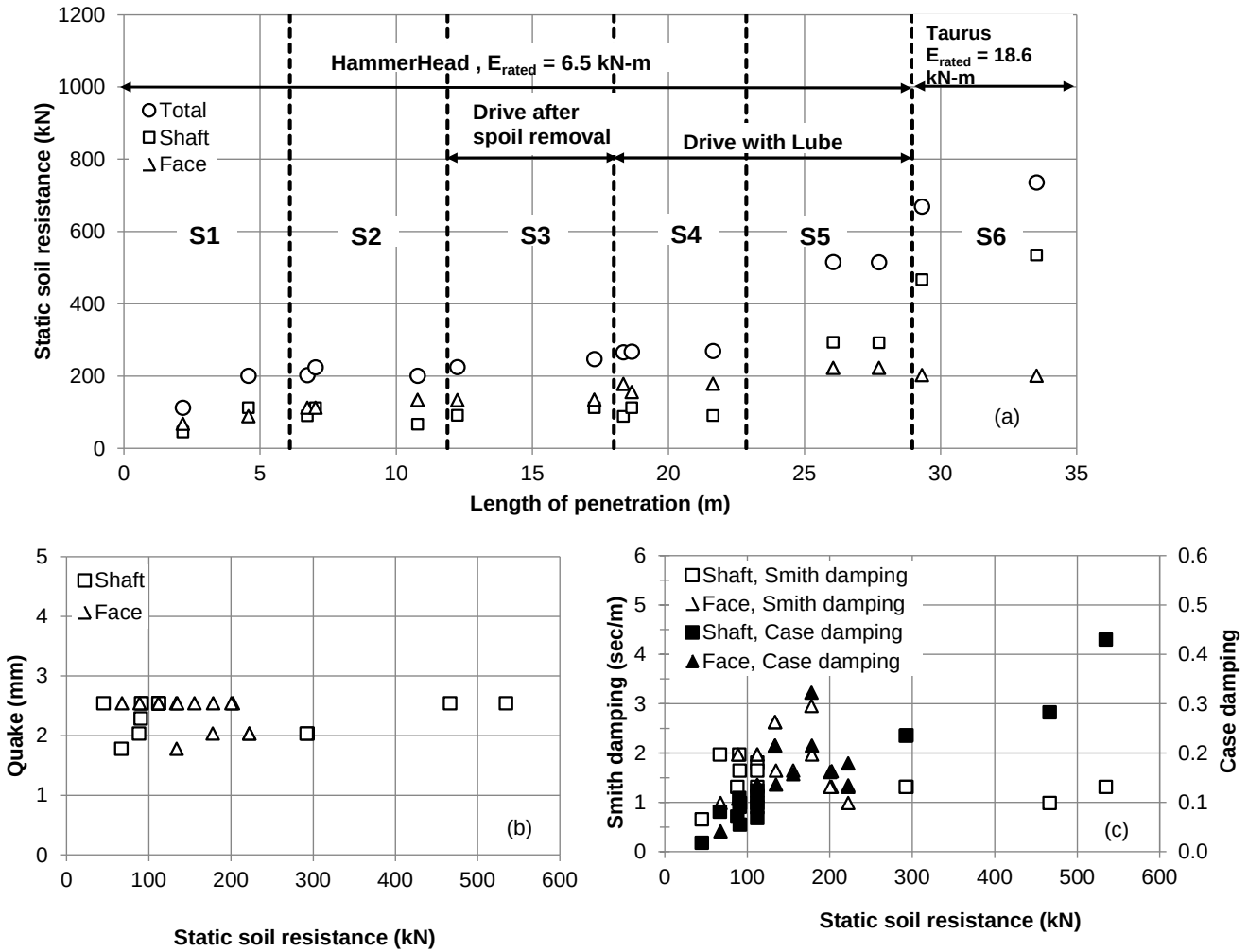

Figure 6.17: CAPWAP results for the Case 6 installation: (a) static soil resistance, (b) quake values, and (c) Smith and Case damping constants.

6.4.3 Comparison of CAPWAP, Case Method, and Traditional Jacking Methods

In practice, those planning pipe ramming projects will need to make a priori estimates of drivability; that is, they will likely not have site-specific measurements of the pertinent soil resistance parameters. Additionally, no experience regarding the performance of methods to predict the soil resistance to ramming has been reported prior to Meskele and Stuedlein (*2011*) and Stuedlein and Meskele (*2012*). Therefore, a comparison of the soil resistance derived from CAPWAP analyses, the Case Method, and the traditional static pipe jacking methods is provided for the case histories in this report. This comparison indicates the accuracy of existing methods, and makes the case for the development of a new method, as necessary. First, the Case Method and CAPWAP results are compared to evaluate the relative accuracy of the real-time Case Method PDA monitoring. Next a comparison is made between the CAPWAP and pipe jacking method resistances to evaluate the accuracy of a priori estimates of soil resistance to ramming using existing methods.

Figure 6.18 provides the comparison of total (static and dynamic) and static CAPWAP and Case Method resistances for Case1, 2, and 6. Case 3 is not included in the comparisons due to lack of Case Method data for Case 3. The static soil resistance for the Case Method incorporated the damping constant, J_c = 0.8, inferred from the author's experience with pile-driving operations in granular soils. Because a CAPWAP analysis provides the static resistance to ramming, the total (static and dynamic) CAPWAP-based soil resistance was computed using linear viscous damping and given by:

$$R_t = R_{fu}\left(1 + J_f \cdot v_f\right) + R_{cu}\left(1 + J_c \cdot v_{p,avg}\right) \quad \textbf{(6.36)}$$

where R_{fu} and R_{cu} represents the ultimate static face and casing resistance, v_f = velocity at the face of the pipe, $v_{p,avg}$ = average velocity over the length of the pipe, J_f = Smith face damping, and J_c = Smith shaft damping. Figure 6.18a indicates that the static soil resistances obtained using the CAPWAP and Case Method analyses are relatively similar for Case 1. Figure 6.18a also indicates that the total soil resistance to ramming estimated using CAPWAP analyses and an assumed viscous damping model is twice that of the Case Method analyses. Considerable scatter is noted for the remaining case histories in the comparisons for Case 2 and Case 6 shown in Figure 6.18b, 6.18c, and 6.18d. In general, the CAPWAP-based total soil resistance to ramming was underestimated by the Case Method values, whereas the static soil resistance to ramming was generally overestimated by the Case Method (e.g., Figure 6.18c and Figure 6.18d). However, it is important to note that the Case Method soil resistance estimates are sensitive to assumed Case damping factor, J_c, and does not allow the decomposition of source resistances.

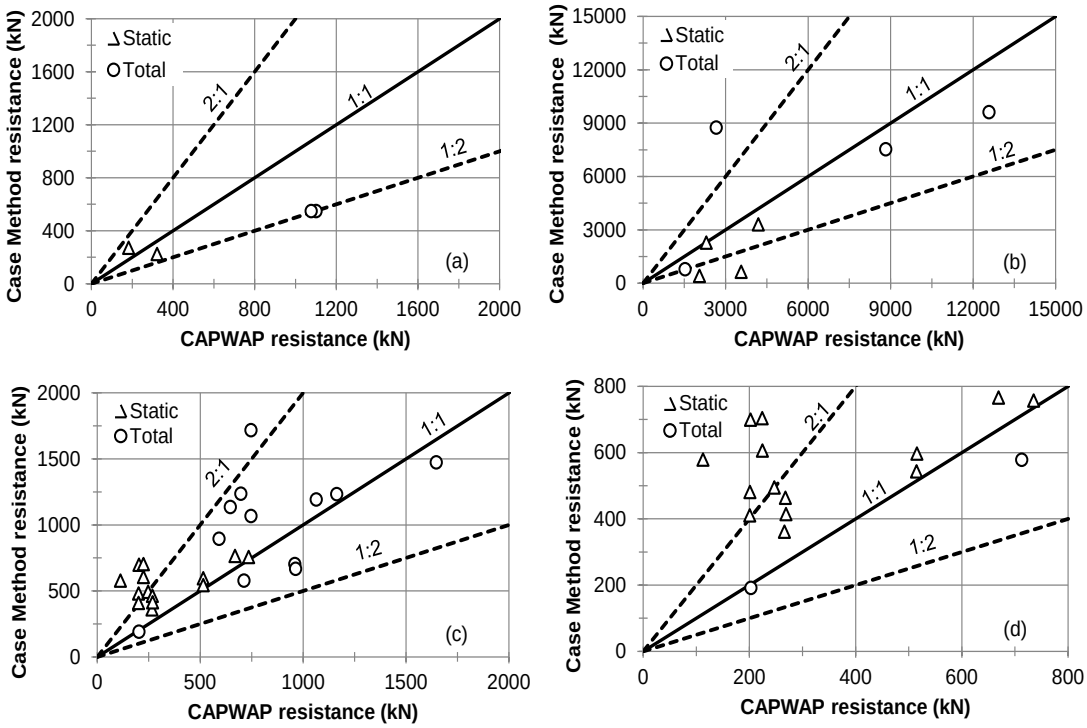

Figure 6.18: CAPWAP and Case Method soil resistance comparisons for (a) Case 1, (b) Case 2, (c) Case 6, and (d) expanded view of Case 6 resistances.

The accuracy of static soil resistance predictions using traditional pipe jacking methods was evaluated using the CAPWAP-based static soil resistance. The jacking methods, described in Section 2.3 and summarized by Stuedlein and Meskele (*2012*), provide the static soil resistance equal to the sum of the face resistance and casing resistance. The face resistance is calculated using an empirical approach proposed by Weber and Hurtz (*1981*), whereas the casing resistance was calculated using the ATV (*1990*), PJA (*Milligan and Norris 1994*), Staheli (*2006*), and Terzaghi (*1943*) methods. The geometric and soil parameters used for the jacking method calculations are summarized in Table 6.3.

Table 6.3: Parameters employed in static soil resistance calculations.

Project description	Pipe dimensions		Cutting Shoe dimensions		Depth of cover (m), h	Peak friction angle, ϕ_p	Residual friction angle, ϕ_r
	D (mm)	t (mm)	D_c (mm)	t_c (mm)			
Case 1	610	12. 5	630	38	3.6, 4.1	42	33
Case 2	2440	25	2490	50	3.1, 5.0	34,36,39	31,32,33
Case 3	3660	38	3710	90	3.4	42	33
Case 6	1060	12	1090	38	1.2	48	44

The peak friction angle was adopted for face resistance calculations, whereas the peak and residual (i.e., critical state) friction angles were investigated for the casing resistance calculations. The residual friction angle is probably most appropriate for casing resistance, due to the high localized shear strains that develop along interface with the pipe during ramming. The residual friction angles were determined using the linear regressions proposed by Bolton (*1986*), which is a function of peak friction angle and relative density of the soil, and given by:

$$\phi_p = \phi_r + 3I_R \quad \textbf{(6.37)}$$

for triaxial conditions where I_R represents the relative dilatancy index. The dilatancy index is related to the relative density and effective confining stress through:

$$I_R = D_r\left(Q - \ln\frac{100\sigma'_m}{P_a}\right) - R \quad \textbf{(6.38)}$$

where D_r = relative density , σ'_m = mean effective stress at peak strength, P_a = reference stress (i.e., atmospheric pressure, 100 kPa), Q and R = fitting parameters (i.e. Q = 10 and R = 1). For preliminary calculations, the mean effective stress can be approximated as twice the vertical effective stress (i.e., assume at rest condition with K_0 = 1). The relative density of the soil was estimated using the SPT *N* correlation described by Kulhawy and Mayne (*1990*) (i.e. Table 2.9 of the EPRI manual). For example, the average SPT *N* values for Case 2 were observed to be 8, 15, and 17 at borings 302, 303, and 304 respectively (Figure 3.8). The peak friction angles were estimated using correlations to SPT *N* (Wolff, *1989*; Schmertmann, *1975*; and Meyerhof, *1956*) and found to be 34°, 36°, and 39° corresponding to the average SPT *N* values at borings 302, 303, and 304 respectively. The residual friction angles were computed based on the equations 6.37 and 6.38 and produced 31°, 32°, and 33°.

Comparison of the CAPWAP and jacking method soil resistances are presented in Figures 6.19 through 6.23. The comparison of face resistance estimated using the Weber and Hurtz (*1981*) model indicates a significant over-estimation of the CAPWAP-based face resistance for all of the case histories considered since the empirical model is mainly developed for jacking loads associated with microtunneling. The estimates of face resistances for Case 1 (Figure 6.19a) were about six times the CAPWAP-based face resistance, whereas the model estimates for Case 2 (Figure 6.20a) were up to four times higher than the CAPWAP-based face resistances. The estimates of face resistance for Case 3 (Figure 6.21a) and Case 6 (Figure 6.22a) greatly over-estimated the CAPWAP-based face resistance. For instance, CAPWAP face resistance for Case 6 varied over the range of 60 to 200 kN while the corresponding estimate was equal to 750 kN for entire length (i.e., the depth of cover remained constant).

The casing resistance estimates were computed considering both the peak and residual friction angles, but produced similar estimates of casing resistance for all of the cases considered (i.e., Case 1, through 3 and 6). For instance, the casing resistance model estimates based on peak and residual friction angles are presented for Case 1 on Figure 6.19b and Figure 6.19c, respectively. Comparison of the two figures indicates that the model estimates of the casing resistances are almost identical for all the jacking methods considered. The ATVA and PJA method produced similar estimates to one another and overestimated the casing resistances in most cases (Figure 6.20b, Figure 6.21b, and Figure 6.22b). The Staheli (*2006*) method gave rise to lower estimates and underestimated the casing resistances for more than half of the model estimates considering all the case histories (Figure 6.19b, Figure 6.20b, and Figure 6.22b). On the other hand, Terzaghi (*1943*) estimates were observed to moderately overestimate the casing resistances in most cases (Figure 6.20b, Figure 6.21b, and Figure 6.22b). The difference in the jacking methods mainly emerged from difference in the assumption of the lateral earth pressure

coefficient, wall friction angle in the vertical shear plane and trap door width of the vertical shear plane.

Figure 6.23 presents the CAPWAP and pipe jacking method estimates of casing resistance for each of the pipe segments in Case 6. The casing resistance estimated using the Terzaghi, ATVA, and PJA methods produce reasonably good agreement to the CAPWAP-based casing resistances for the first two segments. However, these methods produced substantially over-estimated casing resistances for the subsequent three pipe segments. The lack of accuracy may have resulted from the specific experimental variables that were investigated during this experimental installation: the third pipe segment was driven after the spoil was removed (using auger boring, see Section 3.6.4 for details), whereas lubrication was used during the fourth and fifth pipe segments. The spoil removal reduces the total weight of the pipe which in turn lessens the casing resistance and enhances the rate of penetration of the pipe. The application of the lubricant also reduces the casing resistance by reducing the friction along the outer surface of the pipe. The Terzaghi method under-estimated the casing resistance for the sixth pipe segment, whereas the ATVA and PJA methods resulted in moderate over-estimates of casing resistance. On average, the Staheli method produced smaller estimates of casing resistance for all of the pipe segments.

Considerable scatter in all estimates of static soil resistance to pipe ramming is observed in the measured data, suggesting that significant improvement in our understanding of the mechanics of soil-pipe interaction is needed. Section 7 of this report makes a first attempt at a pipe ramming-specific soil resistance methodology.

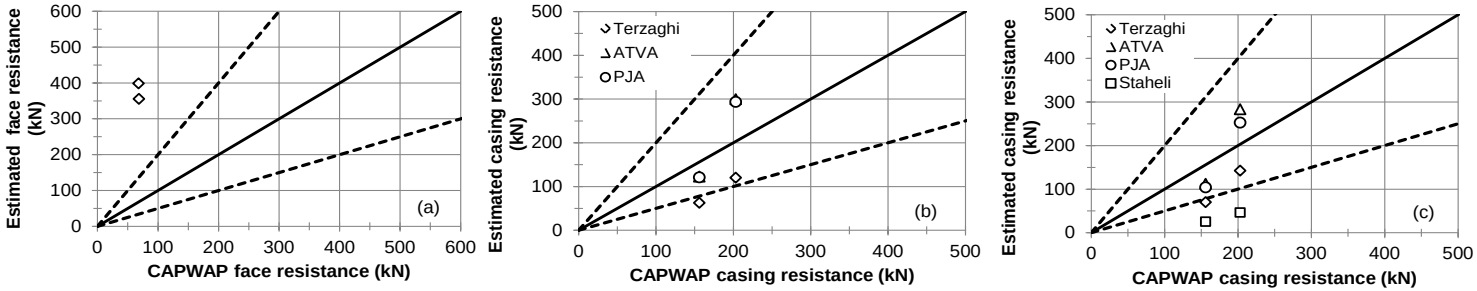

Figure 6.19: Comparison of CAPWAP and jacking method soil resistance for Case 1 (a) face resistance (b) casing resistance using peak angle of friction, and (c) casing resistance using residual state angle of friction. Note: Staheli Method uses only residual angle of friction.

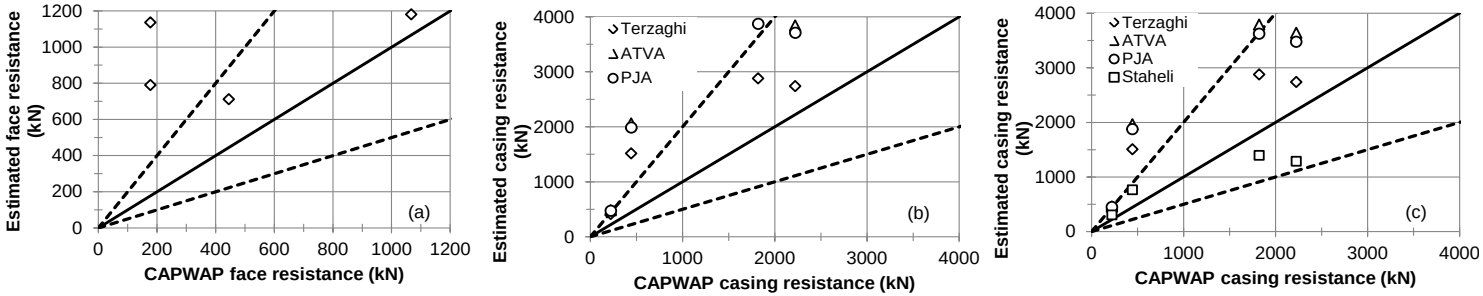

Figure 6.20: Comparison of CAPWAP and jacking method soil resistance for Case 2 (a) face resistance (b) casing resistance using peak angle of friction, and (c) casing resistance using residual state angle of friction. Note: Staheli Method uses only residual angle of friction.

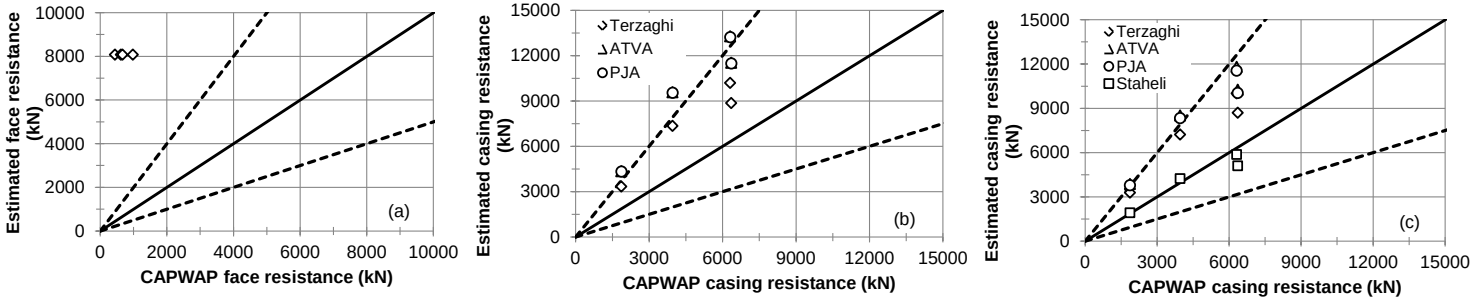

Figure 6.21: CAPWAP and jacking method soil resistance comparisons for Case 3 (a) face resistance (b) casing resistance using peak angle of friction, and (c) casing resistance using residual state angle of friction. Note: Staheli Method uses only residual angle of friction.

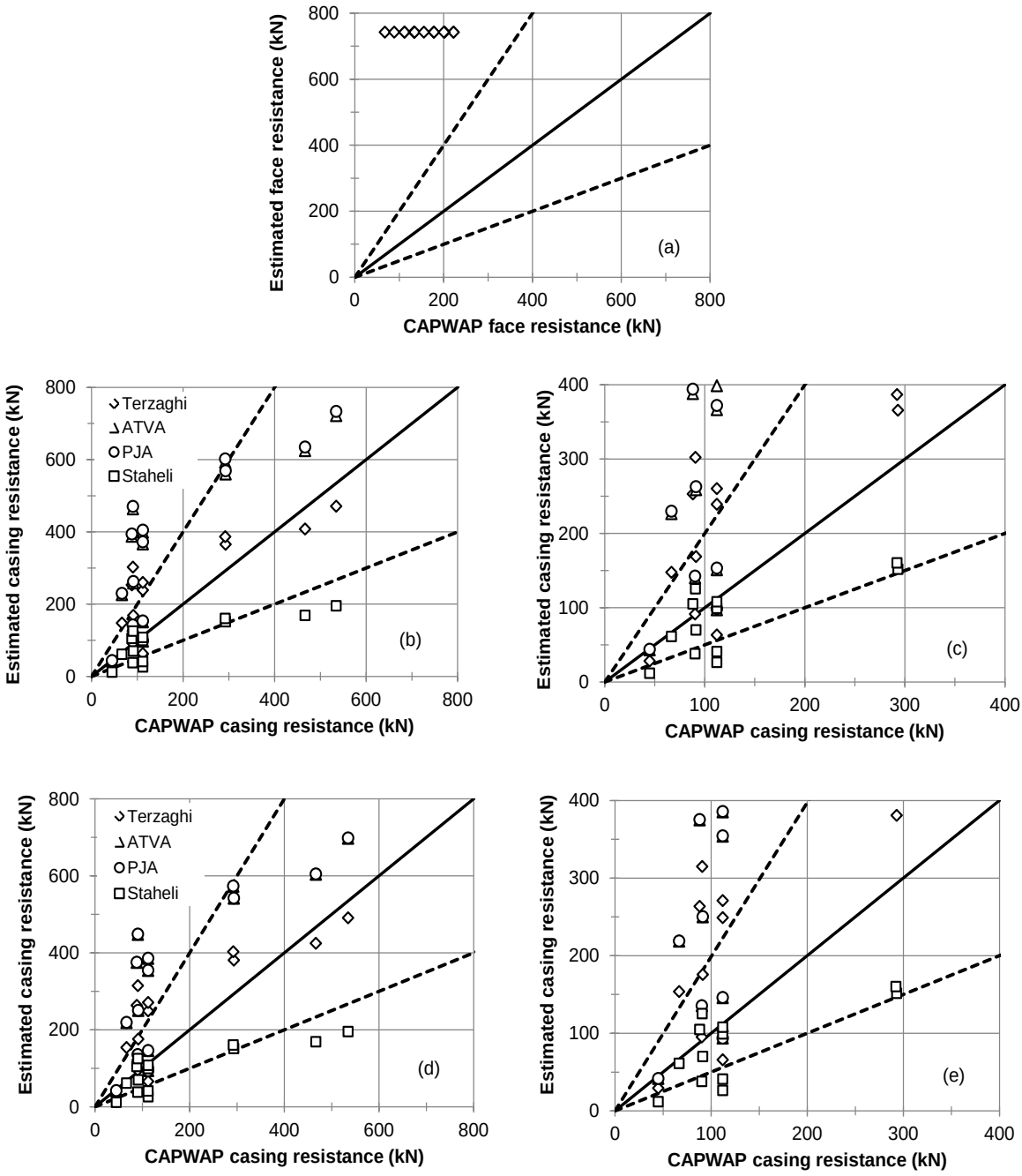

Figure 6.22: CAPWAP-based and jacking method soil resistance comparisons for Case 6: (a) face resistance, (b) casing resistance using peak angle of friction, (c) expanded view of casing resistance using peak angle of friction, (d) casing resistance using of the residual friction angle, and (e) expanded view of casing resistance using the residual angle of friction.

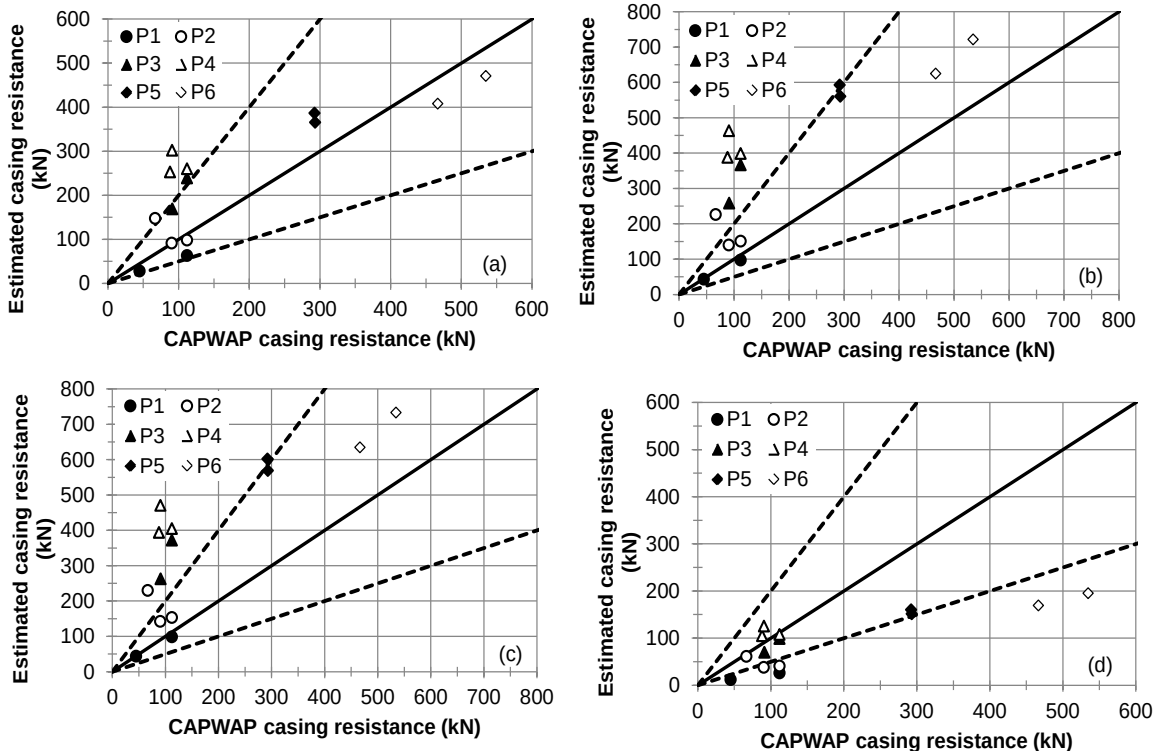

Figure 6.23: CAPWAP-based and jacking method soil resistance comparisons for each Case 6 pipe segment: (a) Terzaghi (*1943*) method, (b) ATVA method, (c) PJA method, and (d) Staheli (*2006*) method.

6.5 SUMMARY

The first step towards providing a framework for the estimation of pipe drivability is to understand the mechanisms of the soil resistance to ramming. By providing an estimate of the static and dynamic component of soil resistance, wave equation analyses can be performed to optimize the hammer energy required to install the pipe without damage. This section provided an overview of the basic theory of wave propagation analysis commonly applied to the testing of pile foundations. The background of two wave equation models, the Wave Equation Analysis of Piles (WEAP) and Wave Equation Analysis of Pipes for Ramming Installations (WEAPRI) were discussed. These two programs, based on Smith's discrete-element solution simulate and analyze stress wave propagation in pipe ramming. The critical soil parameters required to perform a satisfactory drivability study include the static soil resistance, quake, damping and hammer-pipe energy transfer efficiency, and this chapter presented a first and comprehensive assessment of these parameters for pipe ramming applications.

First, real-time measurements made with the Pile Driving Analyzer, such as the soil resistance, energy transferred, and the driving stresses and based on the Case Method were presented for Cases 1 through 3 and Case 6. The maximum compressive stresses for all the case histories were found to be considerably smaller than the allowable compressive stress of the pipe, indicating that significant economy could be realized by evaluating driving stresses with drivability studies. The maximum energy transfer was found to depend on the type of hammer the hammer alignment, and the degree of tension on restraining chains; additional analyses on energy are addressed in Chapter 7. The total soil resistances were noticed to generally exhibit an increase with penetration length due to an increasing depth of cover above the crown of the pipe, an

increasing soil strength with length of penetration (for Case 2),and (3) an increasing casing area available to generate frictional resistance.

An accurate estimate of the soil resistance can be obtained through rigorous numerical analysis of the wave equation and signal matching of the observed and simulated stress-waves. The Case Pile Wave Analysis Program (CAPWAP) was used to analyze the instrumented case histories (i.e., Case 1 through 3, and Case 6). The CAPWAP-based static resistance generally confirmed the Case method PDA data, but provided more refined estimates, as well as providing other critical dynamic soil parameters such as the Smith face and casing damping coefficients, Case damping coefficients, and soil quakes for the face and casing. These dynamic parameters form the basis for the proposed drivability methodology for rammed pipes as described in the next section.

This section concludes with a comparison of the soil resistance derived from CAPWAP analyses, the Case Method, and the traditional static pipe jacking methods. In general, the CAPWAP-based static soil resistance to ramming was largely over-estimated by the Case Method, due to the necessary selection of a single value for viscous damping. The Weber and Hurtz (*1981*) method was selected for the evaluation of face resistance, whereas estimates of the casing resistance were modeled using the ATV (*1990*), PJA (*Milligan and Norris 1994*), Staheli (*2006*), and Terzaghi (*1943*) methods. The Weber and Hurtz (*1981*) model yielded an estimate of face resistance that is significantly higher than the CAPWAP-based face resistance for all of the case histories. The comparison of the observed and calculated casing resistance resulted in an over-estimate of the CAPWAP-based casing resistance by the ATV and PJA methods. The Staheli (*2006*) method provided an under-estimate of casing resistance, whereas the Terzaghi (*1943*) method appeared to provide the most accurate estimate. Nonetheless, considerable scatter in all of the static soil resistance estimates was noted, and the development of pipe ramming-specific methods appears warranted

7 DRIVABILITY ANALYSIS OF PIPE RAMMING INSTALLATIONS

7.1 INTRODUCTION

Planning of pipe ramming installations requires the assessment of the constructability of the required length, diameter, and thickness of pipe with a given hammer and the evaluation of the likelihood of damage to the pipe due to excessive driving stress. The principles of stress wave theory and stress wave measurements, routinely used in drivability analyses for pile foundations, can be used for the evaluation of pipe ramming installations despite the difference in driving systems, orientation of the pipe, hammer energy, and impact frequency. The current practice of drivability analysis often starts with an evaluation of site specific soil conditions and estimate of the soil resistance to ramming against the forced penetration of the pipe. Then, a one-dimensional wave equation analysis (e.g., Chapter 6) is employed to evaluate if a particular hammer and pipe combination can overcome the estimated soil resistances. This analysis can be used to select an optimal hammer that can drive the pipe safely and efficiently. The engineering framework proposed in Chapter 1, which integrates the energy transfer efficiency of the hammers, soil resistance and dynamic soil parameters of the pipe ramming installations, has been adopted in the analysis to simulate the dynamic response of the pipe.

In this section, the basis for conducting a drivability analysis for pipe ramming installations is presented. First, new static soil resistance models that are empirically calibrated to the observed production installations (Case 1 through 3) and the full-scale field experiment (Case 6) is presented. Then, dynamic soil parameters required for drivability analyses are summarized. The hammer-pipe energy efficiency is characterized for common hammer-pipe connections, indicating the significance of good connection practices on the actual amount of energy delivered to the pipe. A sensitivity analysis is performed to identify critical wave equation model parameters, and then drivability analyses are performed for the observed case histories, with emphasis on model parameter selection. The section concludes with specific recommendations for performing drivability studies for pipe ramming installations.

7.2 DEVELOPMENT OF A PIPE RAMMING-SPECIFIC STATIC SOIL RESISTANCE MODEL

Drivability analyses of pipes using the wave equation establish the relationship between the static soil resistance and the dynamic pipe penetration resistance at the time of driving. As described in Chapter 6, the wave equation model represents the total soil resistance, consisting of both the static and dynamic components, by a series of springs and dashpots, where the former represents the static soil resistance and the latter represents the dynamic resistance (and is proportional to static resistance). Thus, determination of the static soil resistance to ramming is critical for drivability analyses. The back-calculated static soil resistance to ramming was evaluated using the traditional quasi-static pipe jacking models in Chapter 6. In general, the quasi-static pipe jacking models over-estimated the face resistance, and produced highly variable and biased estimates of casing resistance when evaluated with the ATVA, PJA, Terzaghi (*1943*),

and Staheli (*2006*) methods. Therefore, the calculation of static soil resistance based on traditional pipe jacking models does not be provide a satisfactory estimate of the static soil resistances to ramming in the granular soils evaluated herein. The development of pipe-ramming specific static resistance models for granular soils is therefore warranted.

7.2.1 Face Soil Resistance Model

The face resistance during ramming can be considered proportional to the effective overburden pressure at the face of the pipe, similar to the toe bearing resistance of a deep foundation. Thus, the unit face resistance, r_f, or the ratio of the total static face resistance and corresponding projected cross-sectional area of the cutting shoe can be given by:

$$r_f = \lambda \cdot \sigma'_v \qquad \textbf{(7.1)}$$

where λ is a coefficient of unit face resistance given as a function of the effective soil angle of internal friction, ϕ', and σ'_v is effective overburden pressure considering the depth of cover above the center of the pipe (i.e., the springline). The coefficient of unit face resistance is assumed to vary exponentially with the tangent of the internal angle of friction, given by:

$$\lambda = a \cdot e^{b \cdot \tan\phi'} \qquad \textbf{(7.2)}$$

similar to typical toe bearing capacity factors for pile foundations, where *a* and *b* are constants that govern the shape of the curve. Ordinary least squares optimization resulted in parameter values of a = 0.011 and b = 7.22 for the pipe ramming installations observed (coinciding with medium dense to dense granular soils) based on Cases 1 through 3 and 6. Figure 7.1 depicts the variation of the back-calculated coefficient of unit face resistance as a function of friction angle for the case histories. Figure 7.2 presents the comparisons of the CAPWAP unit face resistances and estimates of the proposed unit face resistance model after calibrating the proposed model. Two of the CAPWAP analyses for Case 2 (i.e. S3 #7673 and S3 #9324) were excluded from the plots, as they represent hammer blows through buried concrete wing-walls, and are not representative of typical subsurface conditions. The CAPWAP unit face resistances were obtained by taking the ratio of the face resistances and corresponding projected cross-sectional area of the cutting shoe. The solid line represents a one-to-one line between the CAPWAP and model estimates, whereas the upper dashed line represent two-to-one line and lower one represent a one-to-two line. Most of the model estimates were found to fall within these bounds. The total static face resistance is computed as the product of projected cross-sectional area of the leading edge (typically the cutting shoe, the pipe area is appropriate in the absence of a cutting shoe), A_f, and the unit face resistance, r_f, given by:

$$R_f = r_f \cdot A_f \qquad \textbf{(7.3)}$$

The comparison of the CAPWAP and model estimate of unit face resistance illustrate that the face resistance model calculations under-estimate the CAPWAP observation for Case 1, Case 2 and part of Case 6. On the other hand, the model was observed to over-estimate the CAPWAP observation for a portion of the data of Case 3 and 6. In general, most of the unit face resistance data were found to lie between the 1:2 and 2:1 bounds. If desired, a sensitivity analysis on the effect of the estimated face resistance can be performed during the planning stages of a pipe

ramming installation by varying the calculated face resistance by 50 and 200 percent to reflect the possible bounds of the unit face resistance model.

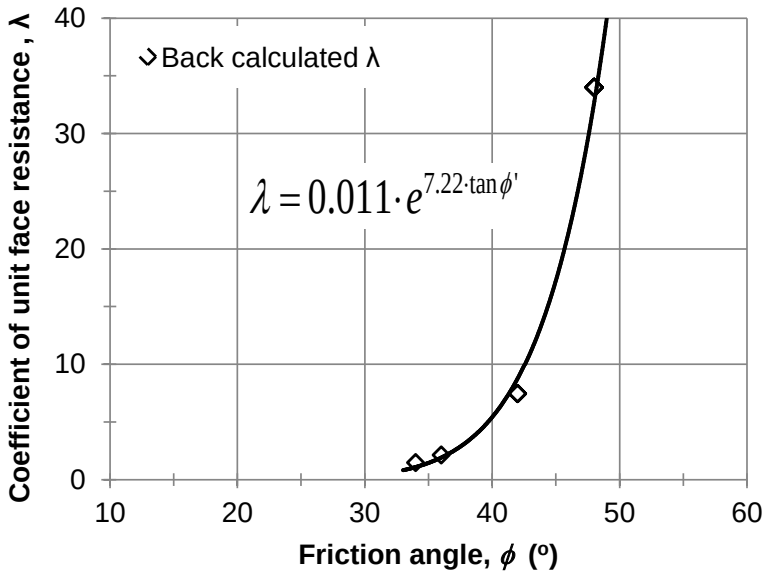

Figure 7.1: Variation of coefficient of unit face resistance with soil friction angle for the case histories.

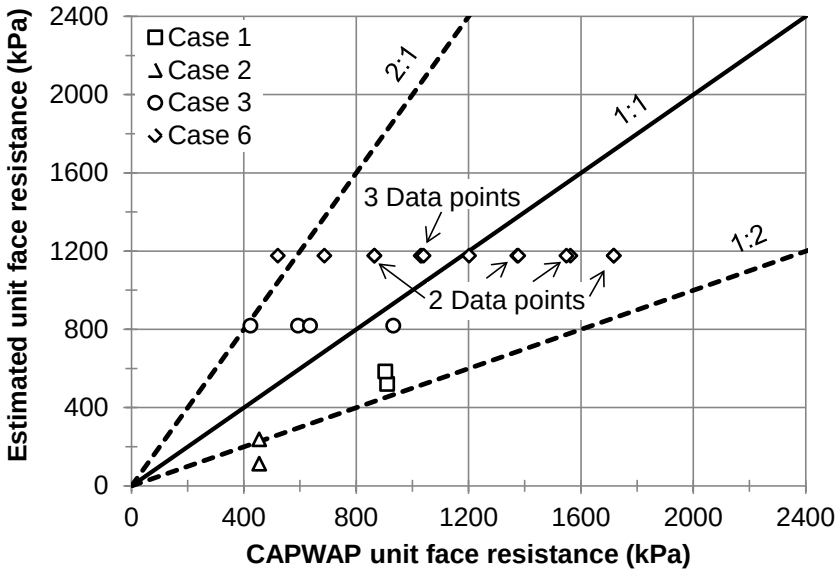

Figure 7.2: Comparison of CAPWAP and proposed model unit face resistances for the case histories. Note, many CAPWAP-based resistances coincide on this plot; the number of coincidental data is indicated.

7.2.2 Casing Soil Resistance Model

The casing soil resistance, R_c, along the length of the casing accounts for the majority of the force required to install a pipe or culvert. The ground around the pipe can be assumed to be in full contact with the entire surface area of the pipe during the installation. Thus, the casing resistance can be obtained as a function of the coefficient of friction between the pipe and the soil, and the normal stress around the periphery of pipe. The unit casing resistance, r_c, along the embedded length of the pipe can be given by:

$$r_c = \frac{R_c}{A_c} = \frac{\mu \cdot 2 \cdot \int_o^L \int_0^\pi \sigma'_n \frac{D}{2} d\theta dL}{\pi D \int_0^L dL} \quad \textbf{(7.4)}$$

where R_c = total static casing resistance, A_c = contact area along the length of the pipe, μ = the coefficient of soil-pipe friction which varies as a function of the interface friction angle, σ'_n = the normal stress acting on the pipe, L = embedded length of the pipe, and D = diameter of the pipe. The normal stress acting radially on the pipe can be estimated by considering the vertical and horizontal stresses in the immediate vicinity of the pipe (see Section 2.3.2). The horizontal stress acting at springline axis of the pipe can be obtained by:

$$\sigma'_h = K_h \left(\sigma'_v + 0.5\gamma' D \right) \quad \textbf{(7.5)}$$

where K_h = the horizontal pressure coefficient. The vertical stress at the top of a pipe can be estimated based on Terzaghi's (*1943*) trapdoor model, which is broadly discussed in Section 2.3.2. The vertical stress above the crown of the pipe is given by (*Terzaghi 1943*):

$$\sigma'_v = k \cdot \gamma' \cdot h \quad \textbf{(7.6)}$$

where k = the stress reduction factor assumed to account for the loosening of the ground around the pipe and given by:

$$k = \frac{1 - e^{-2K\frac{h}{b}\tan\delta}}{2K\frac{h}{b}\tan\delta} \quad \textbf{(7.7)}$$

where h = height of cover above the pipe crown, γ' = unit weight of the soil, K = lateral coefficient of the soil pressure above the pipe crown, b = the trap width that influence the soil above the pipe, and δ = wall friction angle in the vertical shear plane. The width of the trap door (i.e. ideal silo width) controls the location of the limiting shear surface of the soil. A sliding wedge, oriented at angle of $\alpha = 45 - \phi'/2$, is assumed to form at the sides of the pipe (Figure 7.3) due to loosening of the soil. Thus, the failure surface has an inclined surface at the sides of the pipe which become a vertical shear surface above the crown of the pipe (Figure 7.3).

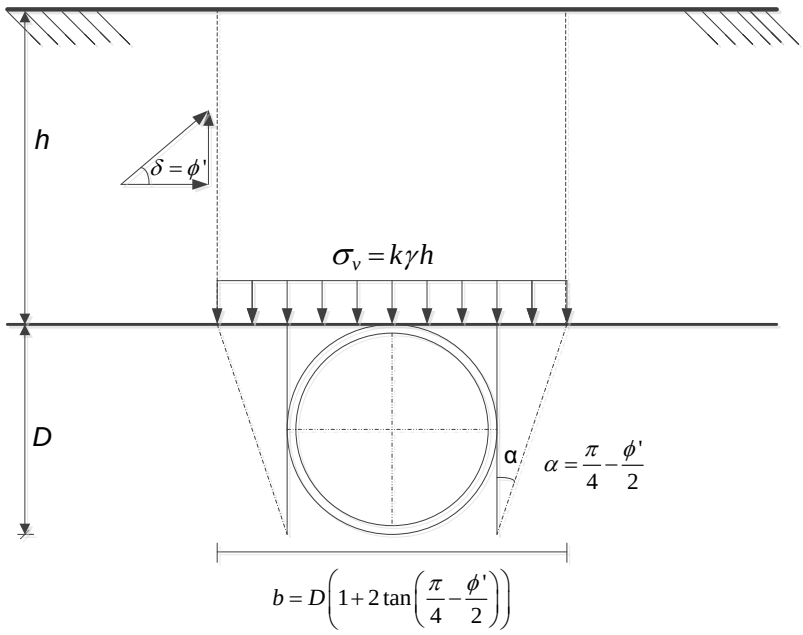

Figure 7.3: Assumed shear surfaces for pipe ramming installations.

The trap door width can be established from the geometry of the assumed failure surface, and is given by (*Terzaghi 1943*):

$$b = D \cdot \left(1 + 2 \cdot \tan\left(\frac{\pi}{4} - \frac{\phi'}{2}\right)\right) \quad \textbf{(7.8)}$$

The wall friction angle, δ, in the vertical shear plane is determined from the shear displacement in the soil (*Stein 2005*). The amount of shear displacement mainly depends on the state of stress in the soil. In pipe ramming, the angle of internal friction was assumed to equal the wall friction for soil-to-soil shear (i.e., $\delta = \phi'$). The lateral coefficient of the soil pressure above the crown of the pipe can be approximated by Rankine's active earth pressure coefficient, which is defined as (*Rankine 1857*):

$$K = K_a = \tan^2\left(\frac{\pi}{4} - \frac{\phi'}{2}\right) \quad \textbf{(7.9)}$$

At the same time, the lateral coefficient of the soil pressure below the crown of the pipe can be estimated by Jaky's approximation of the coefficient of earth pressure at rest for granular soil, which is given by (*Jaky 1944*):

$$K_h = K_o = 1 - \sin\phi' \quad \textbf{(7.10)}$$

The coefficient of friction between the soil and the pipe can be determined from the soil-pipe interface friction angle. To account for the soil-pipe interface behavior of the steel casings observed in this study, an interface friction reduction constant, *n*, is used to calculate the soil-pipe coefficient of friction:

$$\mu = n \cdot \tan\phi' \qquad \textbf{(7.11)}$$

The constant, *n*, can be determined through ordinary least squares optimization of the difference between the model estimates and CAPWAP observations. The least squares optimization of error of the model resulted in a value of $n = 0.19$ for the observed pipe ramming installations (performed in medium dense to dense granular soils) excluding the unit casing resistances that represent the pipe lubrication (i.e., pipe segment 4 and 5 of Case 6). The least squares optimization for the unit casing resistances with lubrication led to a value of $n = 0.14$, which is smaller than the previous n value. The *n* constant correspond to coefficient of friction factors that ranged from 0.11 to 0.19 for the case without lubrication, and from 0.08 to 0.14 for the cases with lubrication, assuming a range in friction angle of 30 and 45 degrees. The NAVFAC (*1986*) manual recommends coefficient of friction factors that ranges from 0.25 to 0.4 for steel-soil interfaces and granular soils. Thus, the interface friction reduction constants for both cases (i.e., with and without lubrication) are observed to provide a coefficient of friction factor less than the values recommended by NAVFAC (*1986*). This is likely due to the high state of shear strain along the soil-pipe interface, resulting in constant-volume shearing and corresponding residual or constant-volume friction angles.

Figure 7.4 presents the comparisons of the CAPWAP unit casing resistances and estimates of the proposed unit casing resistance model for the case without (Figure 7.4a) and with (Figure7.4b) lubrication. The model yielded good estimates of the unit casing resistances for Case 1, Case 3 and Case 6, and resulted in a slight over-estimation of unit casing resistances for Case 2 (Figure 7.4a).

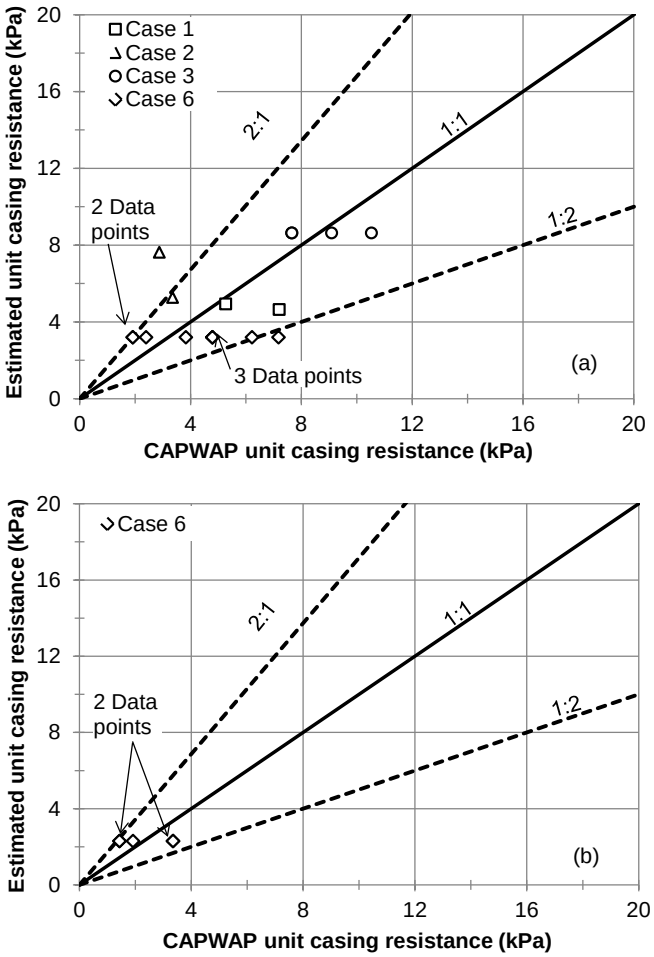

Figure 7.4: Comparison of CAPWAP and proposed model unit casing resistances for the observed case histories considering (a) data without lubrication (b) data with lubrication. Note, many CAPWAP-based resistances coincide on this plot; the number of coincidental data is indicated.

7.2.3 Global Performance of New Total Static Soil Resistance Model

The total static soil resistance is the sum of the face resistance and casing resistance. The face resistance can be computed as a product of the unit face resistance and the projected cross-sectional area of the cutting shoe (Equation 7.3) whereas the casing resistance is calculated as a product of the unit casing resistance and the contact area along the length of the pipe (Equation 7.4, rearranged). In order to assess the proposed unit resistance models, the total static soil resistance was estimated using the proposed face and casing resistance models discussed above and compared to that measured. Figure 7.5 compares the estimated total static soil resistance and the CAPWAP-based observations. The comparisons demonstrated that the combination of the proposed face and casing resistance models yielded good estimates of the total static soil resistances for all of the case histories.

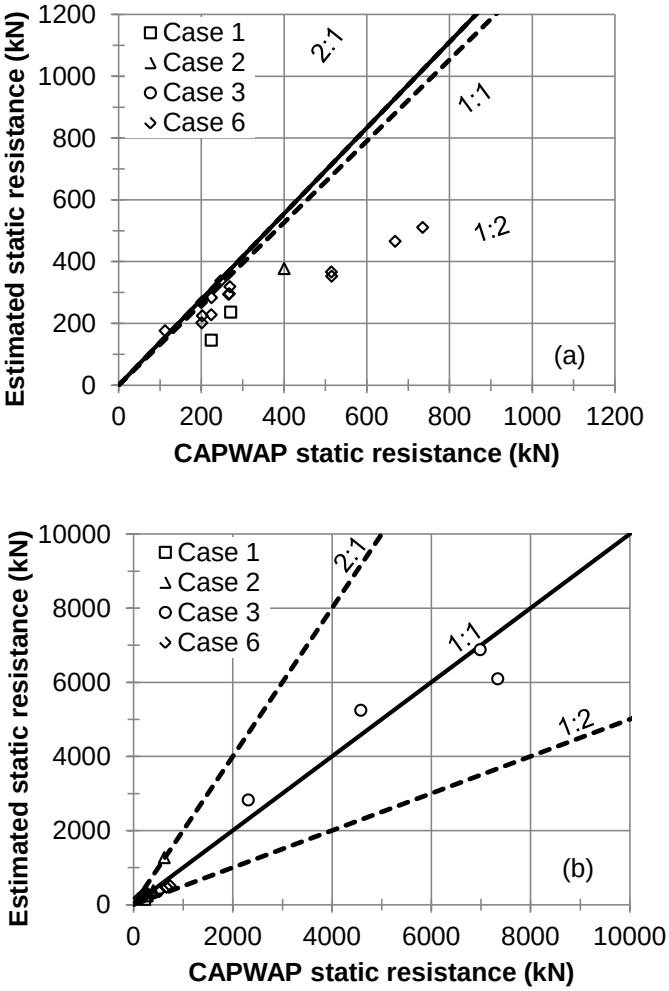

Figure 7.5: Comparison of CAPWAP and proposed model total static soil resistance (a) expanded view showing Case 1, 2 and 6, and (b) full range of resistance showing all of the case histories.

7.3 DYNAMIC SOIL MODEL PARAMETERS (QUAKE AND DAMPING)

Analysis of wave propagation requires the use of dynamic soil parameter in addition to the pipe and hammer data. Selection of dynamic soil parameters, such as the quake and damping, is a necessary step for the modeling of the dynamic response of the pipe during driving. Smith's soil model, discussed broadly in Section 6.2.3, characterizes the soil resistance as a function of soil quake and damping for the face and casing resistance. These parameters can be obtained from back-calculation based on the pipe driving records using CAPWAP. Similarly, soil damping could be back-calculated using the Case soil model (*Goble and Rausche 1976*), in which the analysis yields a dimensionless constant referred as Case damping factor. The CASE- and CAPWAP-derived dynamic soil parameters for each of the case histories are summarized in, Table 7.1 along with the CAPWAP-derived static soil resistances.

Table 7.1: Summary of static and dynamic soil parameters from the CAPWAP and CASE analyses.

Case histories	Segment and blow number	Length of embedment (m)	Static Soil Resistance (kN)			Soil quake (mm)		Smith damping (s/m)		Case damping	
			Face	Shaft	Total	Face	Shaft	Face	Shaft	Face	Shaft
Case 1	S2 #42	11.9	69	156	224	2.54	2.54	2.60	2.30	0.19	0.37
	S2 #3304	20.3	68	203	271	2.03	2.03	2.95	2.60	0.21	0.55
Case 2	S2 #14	8.2	178	222	400	2.77	2.54	2.95	2.62	0.07	0.08
	S2 #1885	20.1	178	445	623	2.54	2.54	2.95	1.64	0.07	0.09
	S3 #7673	34.4	1068	2224	3292	2.03	1.27	4.27	2.30	0.59	0.66
	S3 #9324	36.6	445	1822	2267	2.54	2.46	2.30	2.62	0.13	0.62
Case 3	S2 #1291	19.8	445	1868	2313	0.76	0.76	3.61	3.61	0.09	0.39
	S4 #10	44.2	623	3959	4582	0.81	0.53	2.25	3.95	0.08	0.90
	S5 #4	52.7	979	6361	7340	1.02	1.02	2.95	3.94	0.17	1.43
	S5 #3676	60.7	667	6317	6984	2.03	2.03	1.39	3.68	0.05	1.33
Case 6	S1 #406	2.2	68	45	113	2.54	2.54	0.98	0.66	0.04	0.02
	S1 #1154	4.6	89	112	201	2.54	2.54	1.97	1.80	0.11	0.12
	S2 #512	6.7	112	90	202	2.54	2.29	1.97	1.97	0.14	0.11
	S2 #607	7.0	112	112	224	2.54	2.54	1.97	1.64	0.14	0.11
	S2 #2387	10.8	134	67	201	1.78	1.78	2.62	1.97	0.22	0.08
	S3 #200	12.3	133	91	225	2.54	2.54	2.62	0.98	0.22	0.06
	S3 #1991	17.3	135	112	247	2.54	2.54	1.64	0.98	0.14	0.07
	S4 #8	18.3	178	88	266	2.03	2.03	2.95	1.31	0.32	0.07
	S4 #63	18.7	156	112	268	2.54	2.54	1.64	1.31	0.16	0.09
	S4 #1282	21.6	178	91	269	2.54	2.54	1.97	1.64	0.22	0.09
	S5 #3067	26.1	222	293	516	2.03	2.03	0.98	1.31	0.13	0.24
	S5 #4815	27.7	222	292	515	2.03	2.03	1.31	1.31	0.18	0.24
	S6 #40	29.3	202	467	669	2.54	2.54	1.31	0.98	0.16	0.28
	S6 #2404	33.5	201	535	735	2.54	2.54	1.31	1.31	0.16	0.43

Figure 7.6 and Figure 7.7 present the variation of face and casing quake and damping values, respectively, for the case histories as a function of the normalized face and casing resistance (i.e., ratio of face or casing resistance by the total static soil resistance). Two of the CAPWAP analyses for Case 2 (i.e. S3 #7673 and S3 #9324) were excluded from the plots as they represent hammer blows through buried concrete wing-walls. Additionally, because the pipe for Case 3 was installed in large cobbles and boulders, ground conditions that are difficult to quantify with respect to strength parameters, the CAPWAP analyses for Case 3 were also omitted.

Most of the face and casing quake values were found to equal approximately 2.5 mm, although some of the quake values were equal to approximately 2 mm. Additionally, it was noted that the face and casing quake values remained relatively constant, regardless of the normalized resistance (i.e., the proportion of resistance). On the other hand, face and casing damping coefficients derived using the Smith model were observed to vary between 1 and 3 sec/m, and were also independent of the normalized face and casing resistance. The Case casing damping coefficients were found to increase moderately with increases in the normalized casing resistance, however, no significant trend was observed for the Case face damping coefficients. This study employed the Smith model, and therefore the Smith damping coefficients were used in the drivability analyses described below.

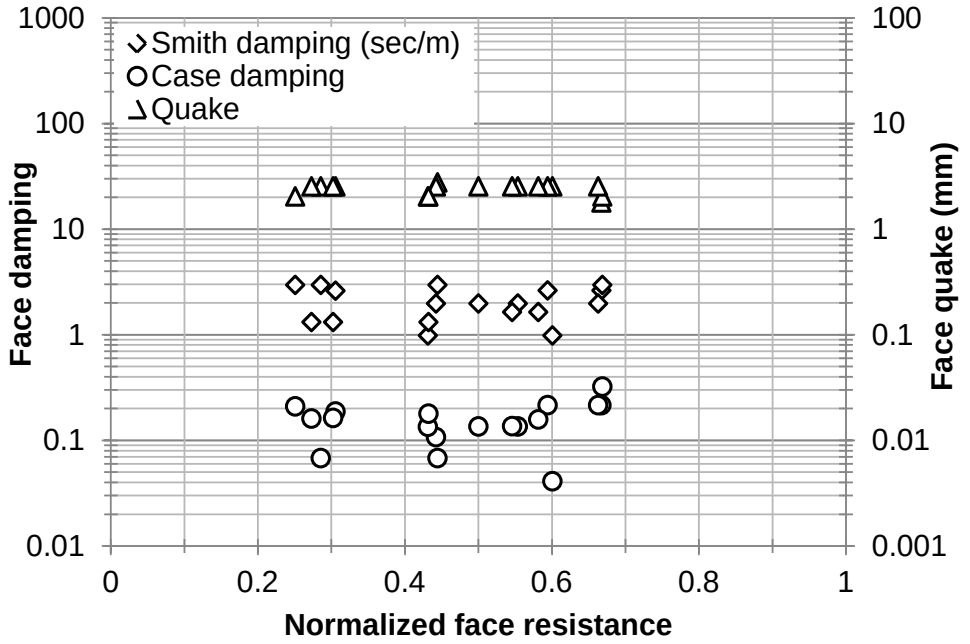

Figure 7.6: Normalized face resistances versus back-calculated dynamic soil parameters.

In general, the soil quake and Smith damping coefficients ranged from 1.8 to 2.8 mm and 1 to 3 sec/m respectively for the face resistances, and ranged from 1.8 to 2.5 mm and 0.7 to 2.6 sec/m respectively for casing resistances. The statistical summary of the soil parameters for the case histories are provided on Table 7.2. As noted in Table 7.2, the uncertainty in soil quake is rather low, with a COV ranging from 11 to 12 percent, whereas the uncertainty in the Smith damping coefficients is relatively higher, with a COV of 35 percent.

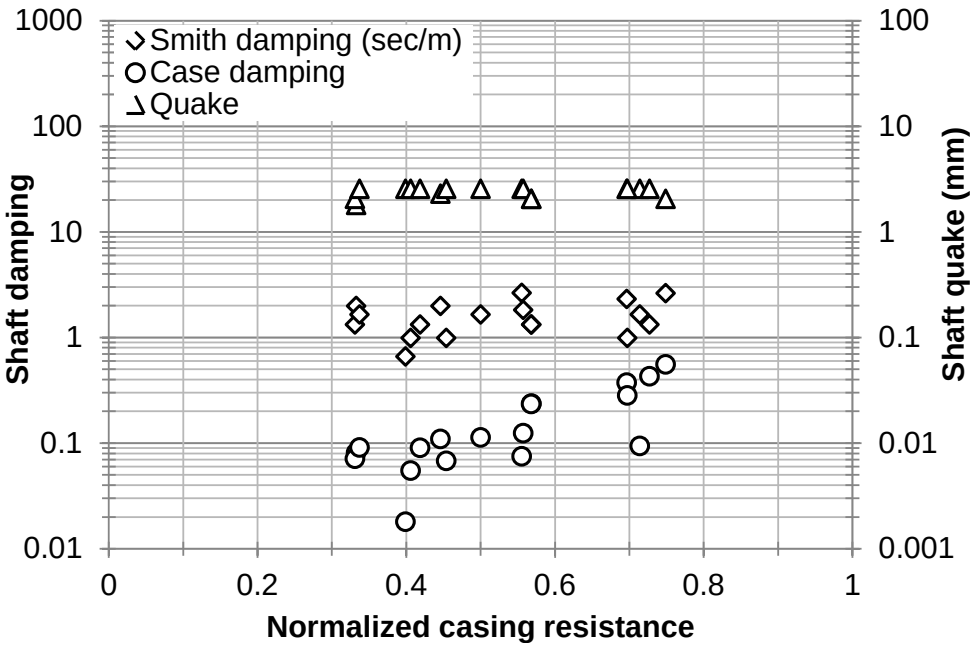

Figure 7.7: Normalized casing resistances versus back-calculated dynamic soil parameters.

Table 7.2: Statistical summary of dynamic soil parameters (quake and damping) excluding Case 3.

Statistical Summary	Soil Quake (mm)		Smith Damping Coefficient (sec/m)	
	Face	Casing	Face	Casing
Minimum	1.8	1.8	1	0.7
Maximum	2.8	2.5	3	2.6
Mean	2.4	2.4	2	1.6
COV	0.12	0.11	0.35	0.35

Figure 7.8 depicts the back-calculated soil stiffness as the function of static soil resistance. The soil stiffness is calculated as the ratio of the static soil resistance and the soil quake obtained from the CAPWAP analysis, and represents an assumed linear elastic stiffness. The line on the plot illustrates a fitted regression model representing the relationship between the soil stiffness (K) and static soil resistance (R) for both the face and casing resistance, which is given by:

$$S = 0.41 \cdot R \tag{7.12}$$

with a coefficient of determination, $R^2 = 0.97$. The inverse of the slope of the regression line, which is equal to 2.4 mm, indicates the average face and casing quake for the case histories.

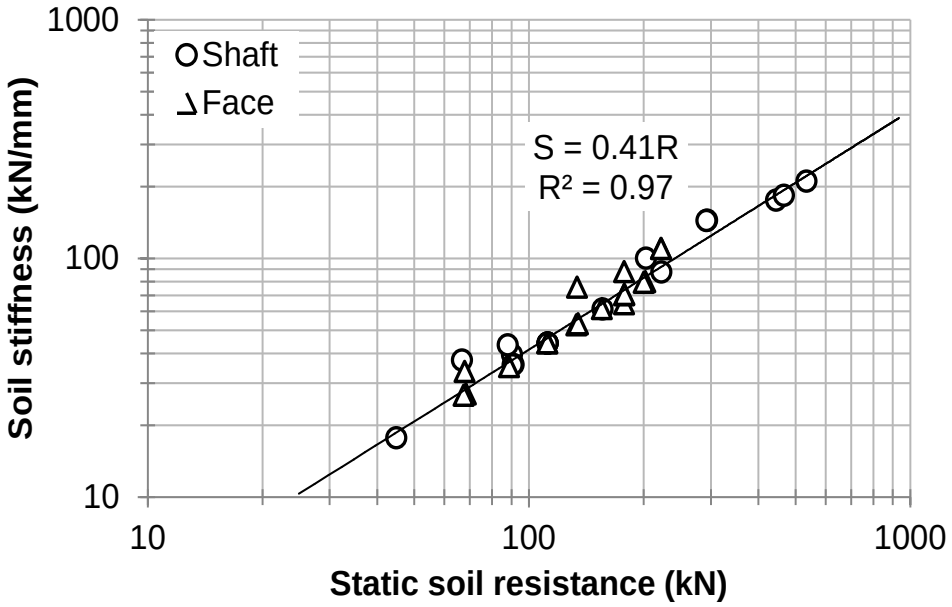

Figure 7.8: Back calculated soil stiffness for the case histories.

7.4 PIPE RAMMING HAMMER–PIPE ENERGY TRANSFER EFFICIENCY

The amount of energy transfer from the hammer to the casing is a critical consideration for assessing of the constructability of the required length and diameter of pipe with a given hammer (i.e. pneumatic and hydraulic hammers). Since the transfer of energy from the hammer to the

pipe is imperfect, characterizing the actual energy propelling the pipe is an essential step in the evaluation of the drivability and rate of penetration of the pipe. The amount of energy and frequency of impact of a hammer can be varied during driving by changing the air or fluid pressure supplied to the hammer and the rate at which it flows within the hammer casing. Generally speaking, contractors elect to operate hammers at medium high to maximal operational levels, with adjustments made to limit the pipe recoil that develops in response to restitution and elastic rebound of the pipe. The transfer of energy from the hammer to the pipe depends mainly on the type of connection between the hammer and the pipe and the force used to maintain the integrity of the connection (e.g., tension in the restraining chains), however internal hammer losses such as friction and heat are likely to contribute inefficiencies. Commonly used hammer-pipe connections that can join the hammer to the pipe are depicted on Figure 7.9. Collets (Figure 7.9a) and ram cones (Figure 7.9f) can be used solely or along with pipe ram collars (Figure 7.9b) and pipe reducing cones or adapters (Figure 7.9c), respectively. Cotter segments can be applied around a pipe cone edge (Figure 7.9d) or pipe edge (Figure 7.9e) to avoid flaring of the wall of the steel pipe and evenly distribute the energy transfer to the pipe. The entire system (e.g., a pipe-collet-hammer connection) is held in place by tensioned chains hooked to eye pads welded on the rear end of the pipe or cables tensioned with a motorized winch.

The hammer types and hammer-pipe connections employed on the observed projects are summarized on Table 7.3.

Table 7.3: Hammers and type of connections used for the case histories.

Project description	Ram Type	Ram Size (mm)	Rated Energy (kN-m)	Blow per min.	Pipe size (mm)	Pipe thickness (mm)	Type of connection
Case 1	HammerHead	400	6.4*	231	610	13	Collets
Case 2	Grundoram Apollo	800	40.5	180	2440	25.4	Ram cone and cotter segments
Case 3	IHC S-280	915	142	45	3650	37.5	Ram helmet and inverted pipe cone
Case 6	HammerHead	400	6.4	231	1070	12.5	Collets with pipe ram collars
	Grundoram Taurus	610	18.6	180	1070	12.5	Ram cone, cotter segments and inverted pipe cone

* Estimated rated energy

Figure 7.9: Hammer-pipe connections (a) collets showing moderate wear or damage (b) pipe ram collar and collets, the latter showing significant wear (c) pipe reducing cone/adapter, and (d) cotter segments (e) ram cone and cotter segments, and (f) ram cone.

The impact of the hammer-pipe connection on the energy transfer efficiency is presented on Figures 7.10 through 7.14. The same HammerHead hammer was employed for Case 1 and Case 6 with pipe sizes of 610 mm and 1070 mm, respectively. The difference in pipe sizes led to the usage of different hammer-pipe connections (compare Figure 7.10 and Figure 7.11). For Case 1, 610 mm diameter collets (comprising three steel segments) with moderate wear were used to couple the hammer to the pipe, whereas for Case 6, a 1070 mm diameter pipe collar was used in conjunctions with the 610 mm collets to join the hammer and the pipe. During ramming in Case 6, the collets suffered additional wear (see Figure 7.9). The energy transfer has a two-step pathway for Case 1 and a three-step pathway for Case 6. There is a greater potential for energy inefficiency in Case 6 because there are a larger number of frictional interfaces in the pipe-hammer connection, and more opportunity for the dissipation of energy in friction. Additionally, wear on the connection can impact the efficiency of energy transfer. The measurements of energy shown in Figure 7.10 and Figure 7.11 confirm the expected outcome: Case 1 exhibited an average energy transfer efficiency of 30 percent, whereas for Case 6, an average efficiency of 23 percent was observed. Additional statistics, such as the COV representing the sample distributions determined through fitting of Gaussian (i.e., normal) distributions are shown in Figure 7.10b and Figure 7.11b.

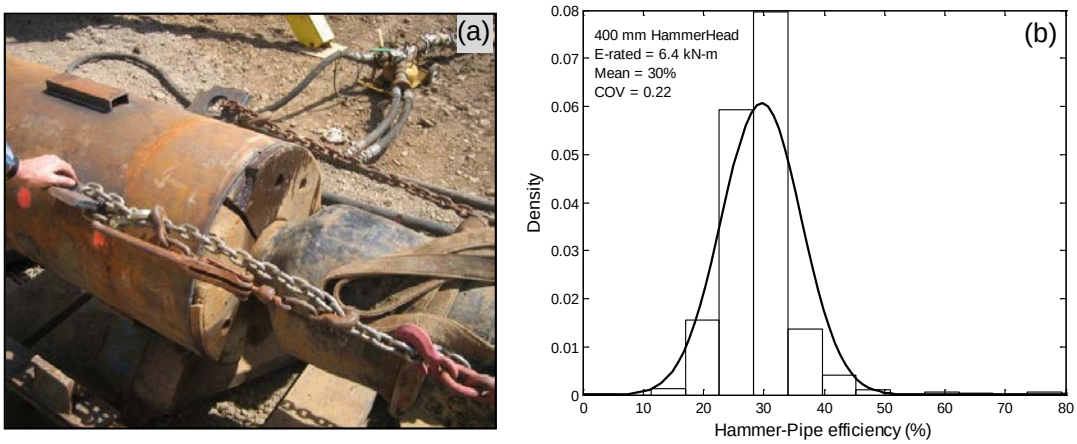

Figure 7.10: Hammer–pipe connection for Case 1: (a) the 400 mm diameter HammerHead hammer, and (b) observed hammer–pipe energy transfer efficiency distribution.

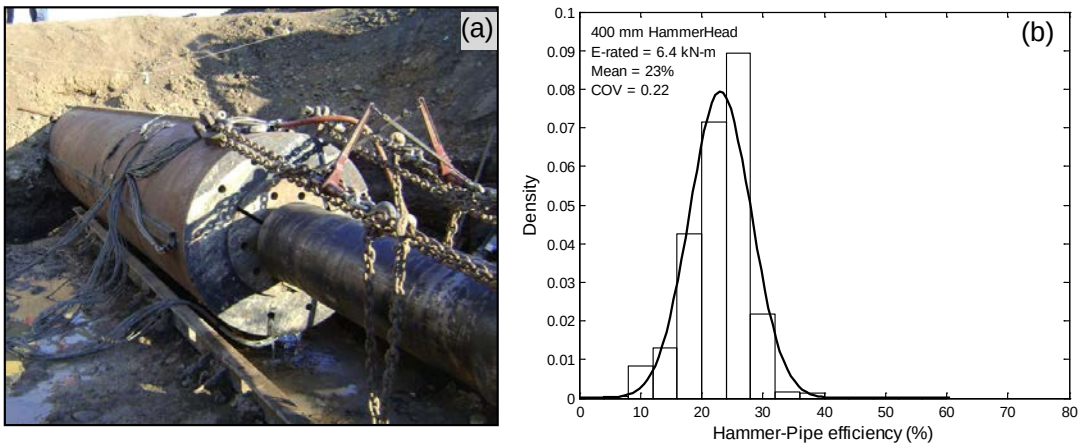

Figure 7.11: Hammer–pipe connection for Case 6. (a) a 400 mm diameter HammerHead hammer (b) observed hammer–pipe energy transfer efficiency distribution.

For the 800 mm Grundoram Apollo hammer, which was utilized on Case 2, the hammer-pipe connection consisted of two ram cones (1800 mm and 780 mm diameter tapered ram cones that mated to one another) and cotter segments, comprising a four-step pathway of energy transfer: hammer-ram cone-ram cone-cotter segments-pipe (Figure 7.12). Unlike the collets, the ram cone is made of a single solid piece of metal that enhances the efficiency of the energy transfer. The sample statistics of energy transfer efficiency indicate a more efficient transfer of energy with mean value of 46 percent and COV of 0.19 (Figure 7.12b).

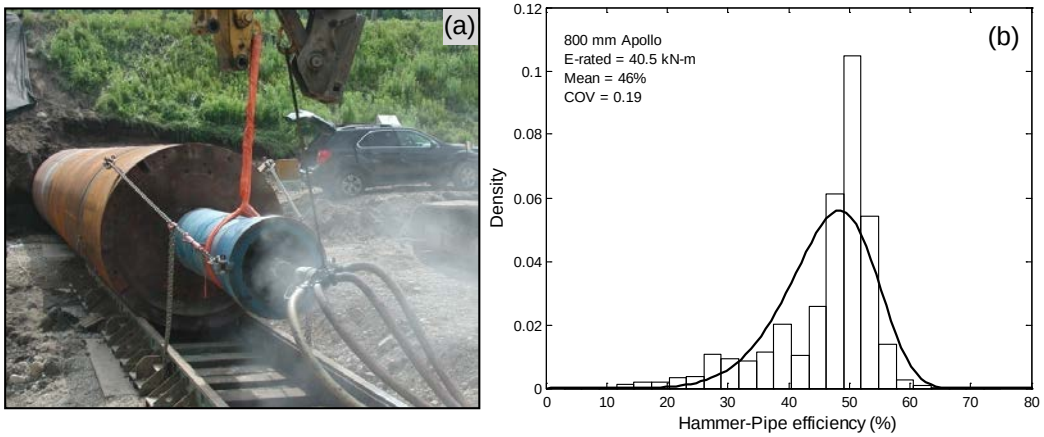

Figure 7.12: Hammer–pipe connection for Case 2. (a) a 800 mm diameter Grundoram Apollo hammer (b) observed hammer–pipe energy transfer efficiency distribution.

The IHC double-acting Hydrohammer S-280 was utilized to drive a 3650 mm culvert for Case 3 with a helmet and inverted pipe cone that comprised the hammer-pipe connection (Figure 7.13). The hammer-pipe system was held together using a winch and a cable where the winch pulls the hammer forward after each blow during the impact driving; approximately 1100 kN of tensile force was achieved in the winch cable, providing an equal component of compressive force on the connection. The energy flow followed a three-step pathway for energy transfer: hammer-helmet-pipe cone-pipe. The mean efficiency for this case was 50 percent with a COV of 0.1, representing a narrow dispersion of efficiency around the mean. Clearly, a motorized winch that provided a compressive thrust improved the transfer of energy.

A second hammer, the 610 mm Grundoram Taurus, was evaluated during Case 6. The connection consisted of a pipe cone and ram cone with tensioned chains (Figure 7.14). Cotter segments were used to protect the edges of the pipe cone and transfer impact energy. This connection provided a four-step pathway of energy transfer: hammer-ram cone-cotter segments-pipe cone-pipe (Figure 7.14). The average energy transfer efficiency observed was 25 percent with a COV of 0.17. This relatively low transfer efficiency was largely due to the connection inefficiencies between the hammer and the pipe, perhaps associated with the use of cotter segments between the ram cone and pipe cone. Additionally, the use of a boom-supported hammer (instead of a hammer cradle) likely contributed to a lower average energy transfer.

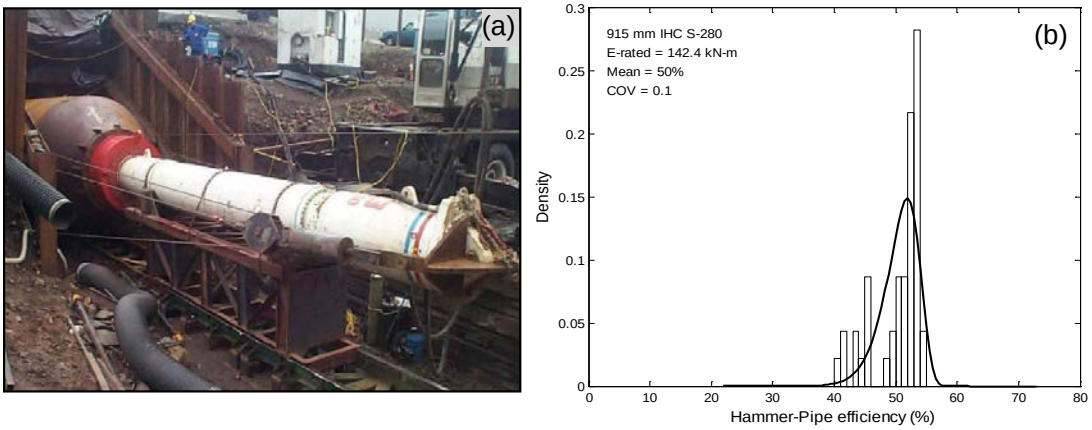

Figure 7.13: Hammer–pipe connection for Case 3. (a) a 915 mm diameter IHC S-280 hammer (b) observed hammer–pipe energy transfer efficiency distribution.

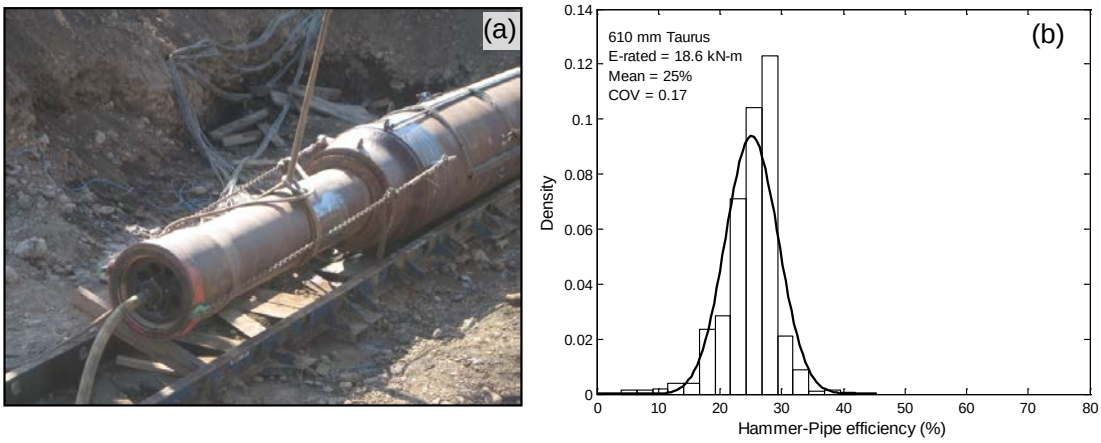

Figure 7.14: Hammer–pipe connection for Case 6. (a) a 610 mm diameter Grundoram Taurus hammer (b) observed hammer–pipe energy transfer efficiency distribution.

The second-moment sample statistics of the energy transfer efficiencies of the case histories are tabulated in Table 7.4. The mean and COV of the energy transfer efficiencies are observed to range from 23 to 50 percent and 0.10 to 0.22, respectively. The transfer of energy during pipe ramming can also depend on the tension within the chains or straps that holds the pipe and hammer in place and usage of support cradle during the pipe installation. The chain tension is an important factor as loose chains can result in significantly reduced transfer of energy. In the worst case scenario loose chains can result in a loss of seating of the hammer on the. Thus, the degree and frequency of chain tightening is a key issue that affects the transfer of the energy. For example, the hammer-pipe energy efficiency produced using the IHC S-280 hydraulic hammer was the largest of the hammers and connections investigated; however, this could be the result of the use of the motorized winch-based thrust. The usage of a support cradle (i.e. pipe cradle and hammer cradle) can assist in the positioning, aligning and leveling of the hammer with the pipe, which in turn improves the energy transfer from the hammer to the pipe. However, some projects utilize excavators to lift the hammer with aid of straps to the level of the pipe; this approach is not recommended, as variations in the excavator boom movement can cause significant variations in hammer-pipe energy transfer. For instance, the Taurus hammer in Case 6 was held horizontally by straps connected to the boom of an excavator that impacted the energy transfer between the hammer and the pipe (see Figure 6.1 and Figure 7.14a).

Table 7.4: Statistical summary of energy transfer efficiency for the case histories.

Projects	Hammer Type	Rated Energy (kN-m)	Energy transfer Efficiency (%)		Hammer–pipe Connection
			μ = Mean	COV	
Case 1	HammerHead	6.4	30	0.22	Collets with tensioned chains
Case 2	Apollo	40.5	46	0.19	Ram cone with tensioned chains
Case 3	IHC S-280	142	50	0.1	Ram cone and pipe cone with motorized winch
Case 6	HammerHead	6.4	23	0.22	Collets with pipe ram collars and tensioned chains
Case 6	Taurus	18.6	25	0.17	Ram cone and pipe cone with tensioned chains

7.5 SENSITIVITY ANALYSIS OF WAVE PROPAGATION MODELING

Wave propagation analysis requires the specification of various model inputs, including the pipe properties (diameter, length, wall thickness, modulus, and mass density), soil properties (static face and casing resistance, quake, and damping), and hammer properties (rated energy, energy transfer efficiency). The wave propagation analysis results in a predicted penetration rate (i.e., blow count) measured in blows per foot or blows per meter as a function total static and dynamic soil resistance (and presented in a drivability graph, for example) and the driving stresses induced in the pipe.

The effect of the magnitude of the model parameters on the wave propagation analysis was examined by performing a sensitivity analysis. The model parameters investigated included the soil quake for the face and casing, the Smith damping coefficients for the face and casing, the proportion of the static casing resistance (i.e., of the total static resistance), static thrust force and the hammer-pipe energy transfer efficiency. An open-ended steel pipe 600 mm in diameter, with 12.5 mm wall thickness, and 30 m in length was considered for the sensitivity analysis, which is similar to Case 1. The sensitivity analysis was performed using GRLWEAP® 2010. A 400 mm pneumatic HammerHead hammer, with an estimated maximum energy of 6.4 kN-m and impact rate of 231 blows per minute (bpm) was employed in the modeling. The sensitivity study considered the following baseline parameter values: hammer-pipe energy transfer efficiency, e = 0.3, shaft quake, Q_c = 2.5 mm, face quake, Q_f = 2.5 mm, casing damping, J_c = 2.6 mm, face damping, J_f = 2.6mm, and line force, F_L = 5 kN. The line force is required for the modeling of horizontal driving to keep the hammer and pipe under compression during driving. During the analysis, the model parameters were varied one at a time over the range of values, while holding the remaining parameters constant and equal to the baseline values. The results of the parametric study are presented in Figure 7.15. The drivability graph, which relates the penetration resistance for driving to the static soil resistance, appears insensitive to proportion of shaft resistance and the face quake and damping parameters on the lower tail of the curves, and show modest sensitivity at the upper tail of the curves (Figure 7.15a, c, and e). Similarly, the drivability graph is fairly insensitive to the shaft quake and damping values towards the lowest part of the curves, while modest to moderate sensitivity were observed on the upper part of the drivability curves. The drivability graphs also showed very little sensitivity to the line force, indicating that the drivability analysis for the physical system is relatively independent of the

application of the horizontal force required for numerical stability. On the other hand, the drivability was observed to be highly sensitive to the energy transfer efficiency for the range of static soil resistances examined. For instance, the energy transfer efficiency curves (Figure 7.15f) shows that the blow count increases from approximately 80 blows per meter to 240 blows per meter for a static soil resistance of 40 kN, and from 150 blows per meter to 530 blows per meter with a static soil resistance of 80 kN, as the hammer-pipe energy transfer efficiency reduces from 60 percent to 15 percent, respectively. This indicates a high sensitivity of the penetration rate to the energy transfer efficiency.

The model parameter values selected for evaluation of the sensitivity analysis were based on the values observed from the case histories. The drivability graphs demonstrated that the lower the magnitude of the dynamic soil parameters (i.e., quake and damping), the more easily the pipe is driven; in other words, the lower magnitudes of the dynamic soil parameters yields upper-bound penetration resistance curve (Figures 7.15a through 7.15e). Likewise, the higher the magnitude of the dynamic soil parameters, the more difficult the pipe penetration, and these higher parameter values produce a lower-bound penetration resistance curve. In contrast, the lower the value of the hammer-pipe energy transfer efficiency, the more difficult the pipe penetration, and use of lower efficiencies will produce lower-bound penetration resistance curves (Figure 7.15f). Given the statistical summary of quake and damping in Table 7.2, there is little room for error in their selection; however, the selection of the appropriate energy transfer efficiency is a critical task and must represent anticipated contractor equipment. Alternatively, specifications could be written so as to require a minimum energy transfer efficiency, thereby limiting the risk of pipe refusal.

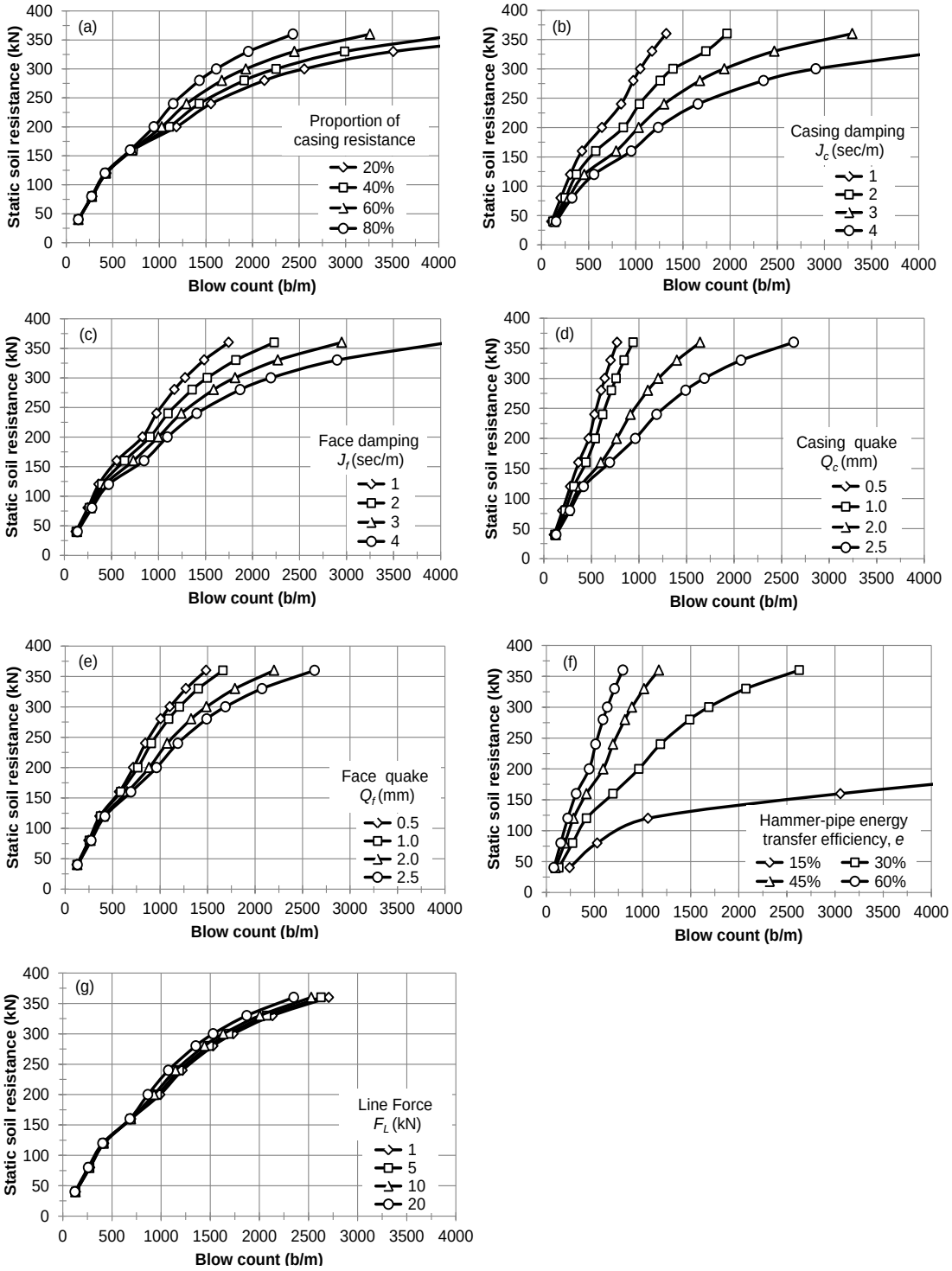

Figure 7.15: Sensitivity analysis of drivability modeling indicating the variation in blow count in blows per meter (b/m) as a function of static soil resistance, by varying (a) the percentage of casing resistance (b) casing damping (c) face damping (d) casing quake (e) face quake, (f) hammer-pipe energy transfer efficiency, and (g) line force.

7.6 DRIVABILITY ANALYSIS OF FIELD OBSERVATIONS

The analysis of pipe drivability is an important aspect of the engineering design of pipe ramming installations to assess the hammer energy needed to drive the desired length of the pipe. Drivability analyses present a means to compare the resistance that can be overcome by a given hammer to the resistance that the soil will offer to the pipe penetration. The drivability analysis consists of the computation of the penetration resistance, or the number of blows required to produce a unit of penetration distance, as a function of the assumed static soil resistance for a particular hammer-pi1e-soil system based on wave equation analysis (e.g., WEAP and WEAPRI). Drivability analyses were carried out for three production installations (Case 1 through 3) and the full-scale field experiment (Case 6), described in detail in Chapter 3. The simulation of the dynamic response of the pipes in each of the case histories was performed using the face and casing soil parameters (i.e., static soil resistance, quake, and damping coefficients) back-calculated through CAPWAP signal matching procedures discussed in Section 6.4.2 (in other words, the "measured" values). Stress wave traces are simulated and compared to the PDA force trace observations to validate the wave analysis models and examine their appropriateness for pipe ramming installations. The drivability analyses described here present the first comprehensive and data-informed effort to analyze the known installation performance of pipe ramming installations.

Table 7.1 presents the summary of soil parameters obtained from the CAPWAP analyses which were used in the drivability analysis for each case history. The energy transfer efficiencies used in the analysis were derived either from the CAPWAP back-calculations or the real-time Case Method solutions, depending on various factors. For example, the user can specify reasonable changes in the impact energy during the CAPWAP signal matching process to obtain the best fit to the observed stress wave (*R. Miner, personal communication, 2012*). In instances where the observed (i.e., the Case method) energy was altered during the CAPWAP simulation, the local average of the Case Method energies was adopted instead of the CAPWAP-based energies for the purposes of performing the drivability analysis. Pneumatic hammers can be modeled as External Combustion Hammers (ECH) since they rely on external source of mechanical energy derived from compressed air. These hammers need to be added to the Hammer database library (i.e., Appendix K) and a horizontal driving option (Appendix L) has to be selected for drivability modeling in WEAP.

Potential upper- and lower-bound penetration resistance curves were generated and are presented for each of the case histories in the subsequent sections in order to account for possible variability in dynamic soil parameters and energy transfer efficiencies. The sensitivity analysis performed in Section 7.5 demonstrated that lower-bound curves can be constructed by considering a combination of the following dynamic soil parameter values: maximum quakes, maximum damping coefficients, and the minimum energy transfer efficiency. On the other hand, the upper-bound curves can be produced by considering a combination of the minimum quakes, minimum damping coefficients, and a maximum energy transfer efficiency. Table 7.2 provides the minimum, maximum and average dynamic soil parameters used in the analysis to generate the bounds of the drivability graphs, intended to provide the possible ranges in the drivability curves for each scenario. The corresponding energy transfer efficiencies utilized in the analysis were extracted from statistical summaries provided on Table 7.4; the upper and lower bound curves were obtained by using the mean energy transfer efficiencies plus and minus one standard

deviation respectively. The proportion of the casing resistance used in the wave analysis was estimated based on the proposed static soil resistance model developed in Section 7.2 and assumed to be constant for the range of static soil resistances in the drivability analysis. The penetration resistance estimated by the model was compared to the static soil resistance observed in the field to evaluate the model accuracy.

In pipe ramming, the compressive stress is usually considered as the most important driving stress due to the nature of the impact (compression) and the presence of soil resistance. The wave propagation analysis provides an estimate of the maximum compressive stress corresponding to the assumed static soil resistance and dynamic soil properties. To evaluate the accuracy of the wave equation analyses, the estimated stresses are compared to the maximum measured stresses, obtained by dividing the measured maximum force by the cross-sectional area of the pipe for each hammer blow. In addition, the compressive stresses are estimated using Equation 6.29, which requires an estimate of the velocity of the hammer or the pipe, the impedance of the hammer and the pipe, and the actual hammer-pipe energy transfer. The average energy transfer provided in Table 7.4 can be assumed to represent the hammer-pipe energy transfer, whereas the ratio of the pipe and hammer impedances in Equation 6.30 can be represented by the ratio of their areas (Table 7.3). In general, the maximum compressive stress developed in the pipe should not exceed the limiting design strength of the pipe (i.e., the yield stress) to prevent damage, and should not exceed 90 percent of the yield stress for design purposes.

7.6.1 Case 1: Pressurized Water Pipe Installation, Wildish Sand and Gravel Co. Site, Eugene, Oregon

The drivability analysis for Case 1 was performed for the installation of the second segment of the pipe corresponding to the segment in which stress wave measurements were observed. Two hammer blows, specifically blow #42 at a penetration length of 11.9 m and blow #3304 at a penetration length of 20.3 m were selected for comparison with the drivability analysis. Figure 7.16 presents the observed and computed force time histories for blows #42 and #3304. The stress wave simulations were generated using CAPWAP-based soil parameters (provided in Table 7.1) and hammer-pipe energy transfer efficiencies. For blow #42 and blow #3304, the CAPWAP and Case Method resulted in identical energy transfer efficiencies of 31 and 19 percent respectively. Both of the wave propagation models provided a good match of the force traces for blows #42 (Figure 7.16a) and #3304 (Figure 7.16c), and indicated the suitability of these models for pipe ramming installations. The drivability graph for blows #42 (Figure 7.16b) and #3304 (Figure 7.16d) yielded the penetration resistance as a function of static soil resistance. These graphs demonstrate that the WEAP-based curves generally provide a lower blow count (i.e., driving resistance) compared to that provided by WEAPRI. Both models appeared to provide a very close estimate of the blow counts in the lower part of the penetration curves, however the differences between the models increased with increasing static soil resistance. For blow #42 where the CAPWAP-based static soil resistance equaled 224 kN (Table 7.1), the corresponding WEAP and WEAPRI driving resistance (blow counts per meter, b/m) was found to be 1,706 b/m and 3,766 b/m respectively. Similarly, for blow #3304, where the CAPWAP-based static soil resistance was 271 kN, the corresponding WEAP and WEAPRI driving resistance was found to be 3,730 b/m and 22,517 b/m respectively. In other words, for a blow rate of 231 bpm (e.g., the 400 mm HammerHead hammer) and for the scenario associated with

blow #42, the duration of driving would be approximately 7.4 and 16.3 min/m, and 16.2 and 97.4 min/m at blow #3304. The observed penetration resistance can be obtained from penetration length and driving time during installation assuming a constant rate of penetration. For the blow rate of 231 bpm and the penetration rate of 0.23 m/min (or 4.35 min/m), a penetration resistance of approximately 1000 b/m was found for blows #42 and #3304 which was lower than the penetration resistance estimated by both WEAP and WEAPRI. In other words, for Case 1, both WEAP and WEAPRI overestimated the penetration resistance.

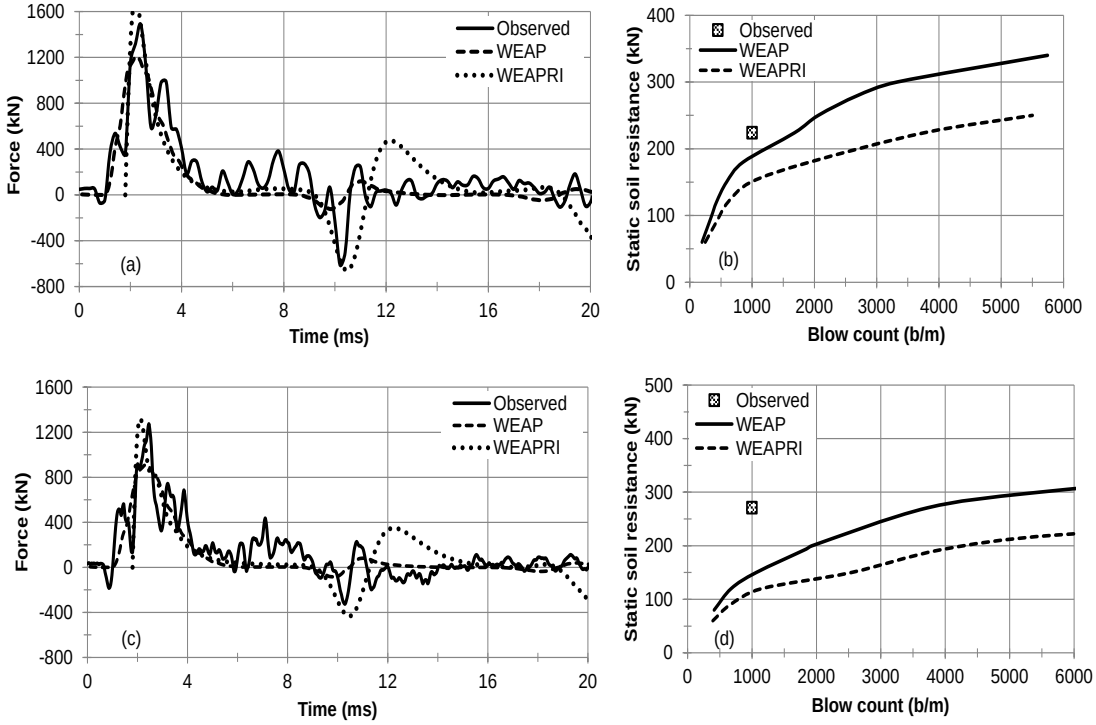

Figure 7.16: Observed and simulated force traces and drivability estimates: (a) force traces for blow #42, (b) drivability graph for blow #42, (c) force traces for blow #3304, and (d) drivability graph for blow #3304.

Figure 7.17 presents the average and potential upper- and lower-bound penetration resistance curves for blow #42 and #3304 based on WEAP. The graph clearly shows that for a given static soil resistance, the upper- and lower-bound curves widely bracketed the observed penetration resistance, and do not provide a confident range for estimating the likely penetration resistance. However, when using the average observed dynamic soil parameters, a reasonable and accurate estimate of penetration resistance can be obtained.

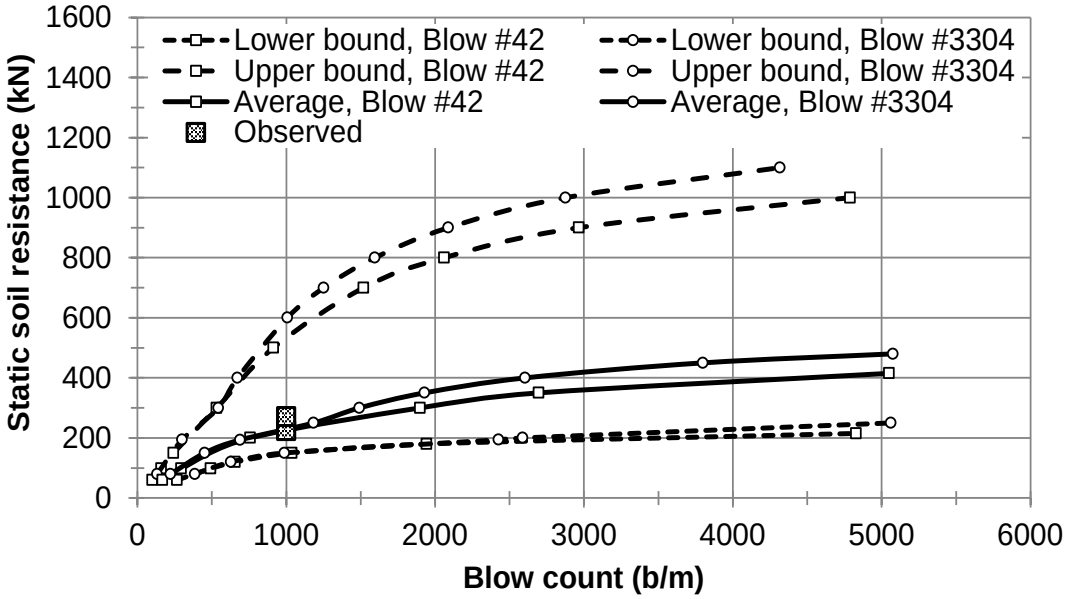

Figure 7.17: Comparison of observed penetration resistance to the average, lower- and upper-bound drivability curves simulated for blow #42 and #3304.

The model approximation of the compressive stresses using WEAP and WEAPRI for blow #42, corresponding to the observed static soil resistance of 224 kN and blow #3304 corresponding to the observed static soil resistance of 271 kN, are compared to the observed stresses in Figure 7.18. Both estimates of the compressive stresses are comparable to the observed stresses, with WEAPRI providing a conservative upper-bound estimate and WEAP delivering a lower-bound estimate. Therefore, relatively confident estimates of driving stresses can be obtained using WEAP and WEAPRI, provided that the hammer-pipe energy transfer efficiency can be reasonably estimated. The compressive stress can also be estimated based on Equation 6.29, which provided a compressive stress value 70 MPa assuming average energy transfer efficiency during installation. This estimate was found to be comparable to the observed stress. In general, the induced compressive stresses were found to be significantly smaller than the allowable compressive stress for the pipe, which was 241 MPa for the pipe used in Case

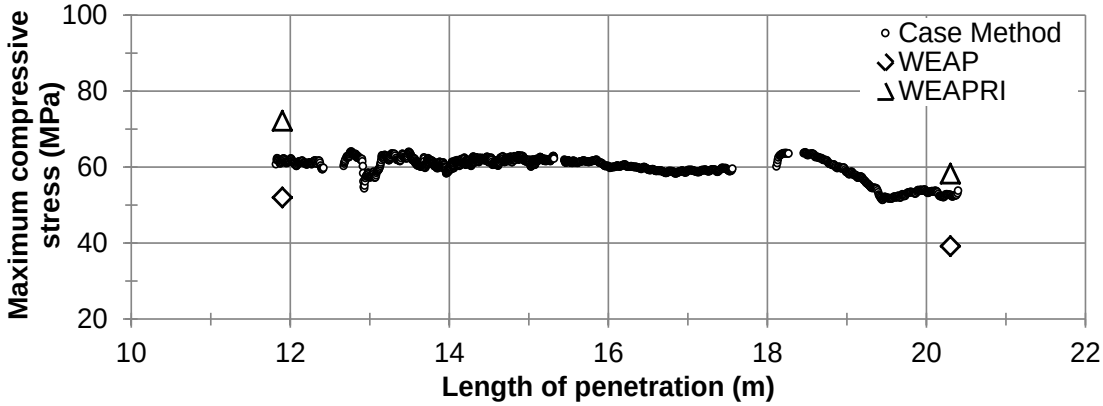

Figure 7.18: Maximum compressive stresses obtained from the Case Method solution to the PDA observations and those estimated using the drivability analyses for blow #42 and #3304.

7.6.2 Case 2: Corrugated Metal Pipe (CMP) replacement project under Highway 21 at Allan's Creek, Ontario

The drivability analysis for Case 2 was performed for two hammer strikes, corresponding to blow #14 and #1885 at penetration lengths of 8.2 m and 20.1 m, respectively. Blow #7673 and #9324 (i.e., at penetration lengths of 34.4 m and 36.6 m, respectively) were excluded from the analysis since these blows represent the ramming through buried concrete wing-walls. CAPWAP soil parameters (Table 7.1) and energy transfer efficiencies (Figure 6.8) were adopted in the wave propagation analysis to simulate the dynamic response of the pipe, and compared to the PDA measurements. Figure 7.19 presents the drivability analyses for blow #14 and #1885 using energy transfer efficiencies of 18 and 42 percent, respectively. The WEAPRI-based peak force in the computed force time history was over-estimated for blows #14 and #1885, whereas the WEAP-based simulations indicated relative agreement of the computed and observed force traces for blow #14 (Figure 7.19a), and an over-estimation of the peak force for blow #1885 (Figure 7.19c). Figure 7.19b and Figure 7.19d present the variation of penetration resistance with static soil resistance. Similar to Case 1, WEAP- and WEAPRI-derived drivability curves agreed closely in the lower portion of the curves and their differences increased with increasing static soil resistance. In general, the estimated penetration resistance at a given soil resistance computed using WEAP was lower than that derived using WEAPRI. The observed penetration resistance was calculated based on an observed penetration length and driving time assuming a constant rate of penetration, resulting in a penetration resistance of 550 b/m blow #42 and #1885 at the blow rate of 180 bpm (corresponding to the Grundoram Apollo pipe ramming hammer) and a penetration rate of 0.33 m/min (or 3 minutes per meter),. The WEAP and WEAPRI-based penetration resistance equaled 706 and 3,500 b/m, respectively, for blow #42 and corresponding to the observed static soil resistance of 400 kN. For blow #1885, the blow counts were computed to be 433 b/m and 780 b/m for the WEAP- and WEAPRI-based solution, respectively, corresponding to the observed static soil resistance of 622 kN. The duration of driving can be estimated for each blow based on the blow rate of 180 bpm. For blow #14, the duration of driving would be approximately 4.2 and 19.4 min/m, and 2.4 and 4.3 min/m for blow #1885, for WEAP- and WEAPRI-based drivability analyses, respectively. Therefore, WEAP provided a relatively good and consistent estimate of the penetration resistance at the observed soil resistance to driving, whereas WEAPRI generally over-estimated the penetration resistance.

Figure 7.20 presents the average and potential upper- and lower-bound penetration resistance curves generated for both blow #14 and #1885 based on the combination of the soil parameters as discussed above. The curves were produced based on soil parameters values provided on Table 7.2 and energy transfer efficiencies extracted from Table 7.4. The drivability graph shows that the observed penetration resistance can be reasonably estimated by the average and lower-bound curves.

Figure 7.21 presents the comparison of compressive stresses observed and computed based on the wave equation models for blow #14 and #1885. The WEAP model estimates were found to be very close to the observed stresses, as expected from the simulated force time histories in Figure 7.20. On the other hand, the estimates from the WEAPRI model slightly over-estimated the observed stresses. The estimate of compressive stress based on Equation 6.29 provided a value of 95 MPa, which is far larger than the stresses that were observed. Similar to Case 1, the

compressive stresses in Case 2 were considerably smaller than the allowable compressive stress for the pipe (i.e., 241 MPa).

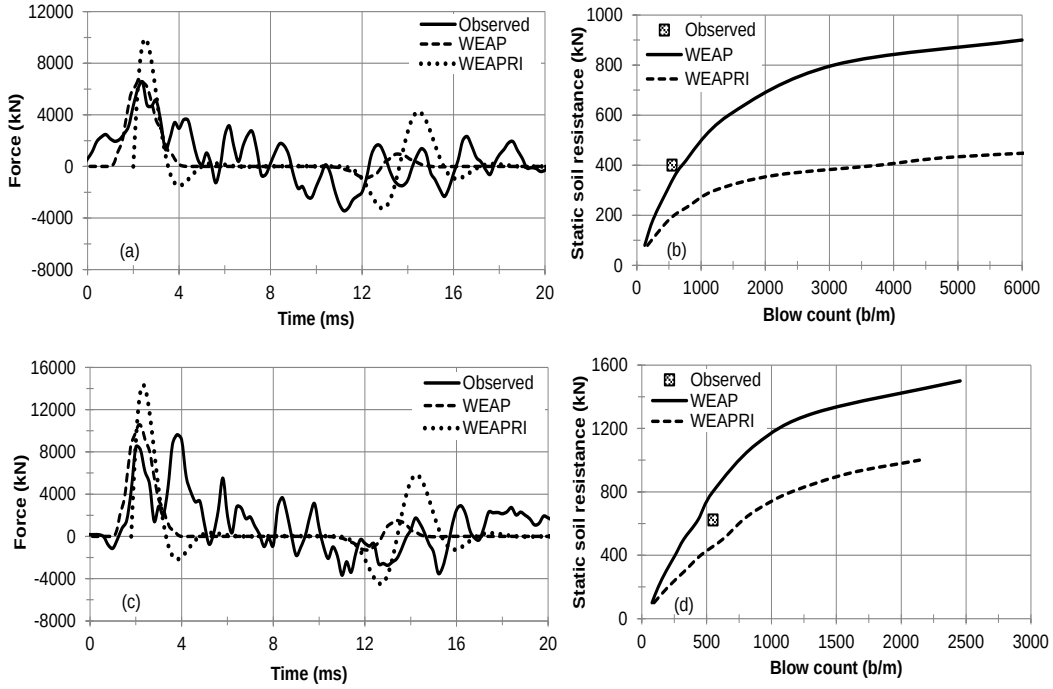

Figure 7.19: Observed and simulated force traces and drivability estimates: (a) force traces for blow #14, (b) drivability graph for blow #14, (c) force traces for blow #1885, and (d) drivability graph for blow #1885.

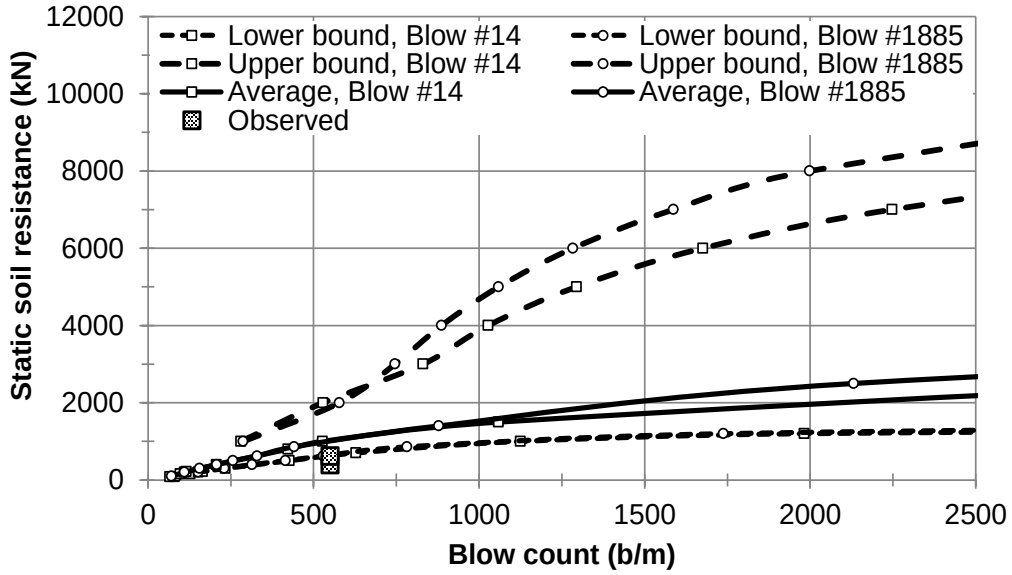

Figure 7.20: Comparison of observed penetration resistance to the average, lower- and upper-bound drivability curves simulated for blow #14 and #1885.

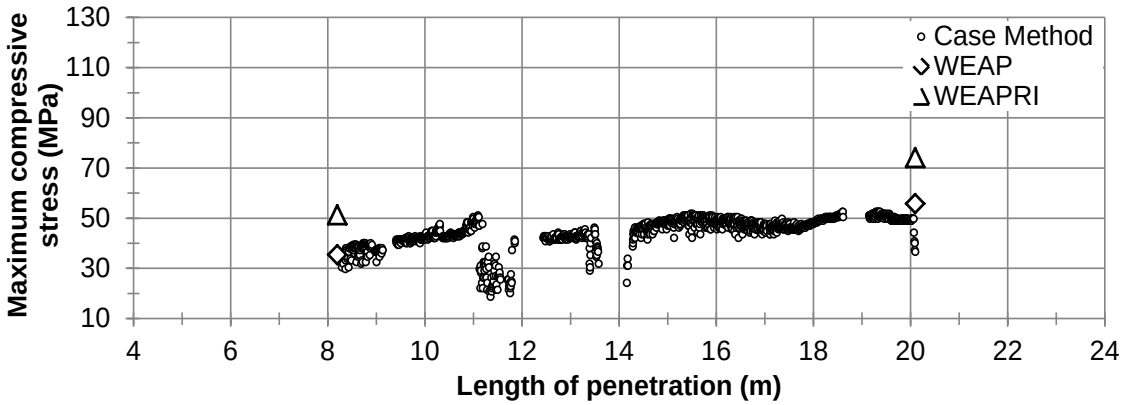

Figure 7.21: Maximum compressive stresses obtained from the Case Method solution to the PDA observations and those estimated using the drivability analyses for blow #14 and #1885 of production Case 2.

7.6.3 Case 3: Culvert replacement project under Interstate Highway 84 at Perham Creek, Oregon

The drivability analysis for Case 3 was performed for two specific IHC S-280 hammer strikes, corresponding to blow #4 and #3676 at penetration lengths of 52.7 m and 60.7 m, respectively. The IHC S-280 hammer was kept in contact with the pipe during driving through a system of winch, cable and blocks that maintained a hammer-pipe connection force of approximately 1,100 kN (*Miner 2003*). . Similar to other cases, the CAPWAP-based dynamic soil parameters (Table 7.1) and energy transfer efficiencies were used to simulate the dynamic response of the pipe, and subsequently compared to the PDA measurements. The energy transfer efficiencies were 31 and 50 percent for blow #4 and #3676, respectively. Figure 7.22 presents the drivability force time history simulations and observations, and drivability graphs for blow #4 and #3676. Both of the model calculations resulted in force simulations that under-estimated the peak force of the force traces by about 25 to 30 percent for blow #4 (Figure 7.22a) and #3676 (Figure 7.22c). The drivability graphs demonstrate that the models produced nearly similar penetration resistance curves for both blows (see Figure 7.22b and Figure 7.22d). Miner (*2003*) stated that ODOT personnel recorded approximate penetration resistances of 460 and 400 b/m for blow #4 and #3676 respectively. The corresponding WEAP and WEAPRI-based penetration resistances were 1350 and 1265 b/m for blow #4, where the static soil resistance equaled 7,340 kN, and 900 and 810 b/m for blow # 3676, where the static soil resistance was 6,984 kN. Therefore, both models over-estimated the penetration resistance for each of the blows considered. The duration of driving can be estimated for each blow based on the blow rate of 45 bpm for IHC S-280 hammer. For blow #4, the duration of driving would be approximately 30 and 28 min/m, and 20 and 18 min/m for blow #3676, for WEAP- and WEAPRI-based drivability analyses, respectively. This compares to the actual time of driving of 10 and 9 minutes per meter observed by ODOT personnel, for blows blow #4 and #3676, respectively.

Figure 7.23 presents the average, lower-, and upper-bound penetration resistance curves generated for blow #4 and #3676 based on the dynamic soil parameters provided in Tables 7.2 and 7.4. The penetration resistance observations represent approximate values obtained from Miner (*2003*). The observed penetration resistances were located outside of the bracketed resistances, but were close to the upper-bound curves.

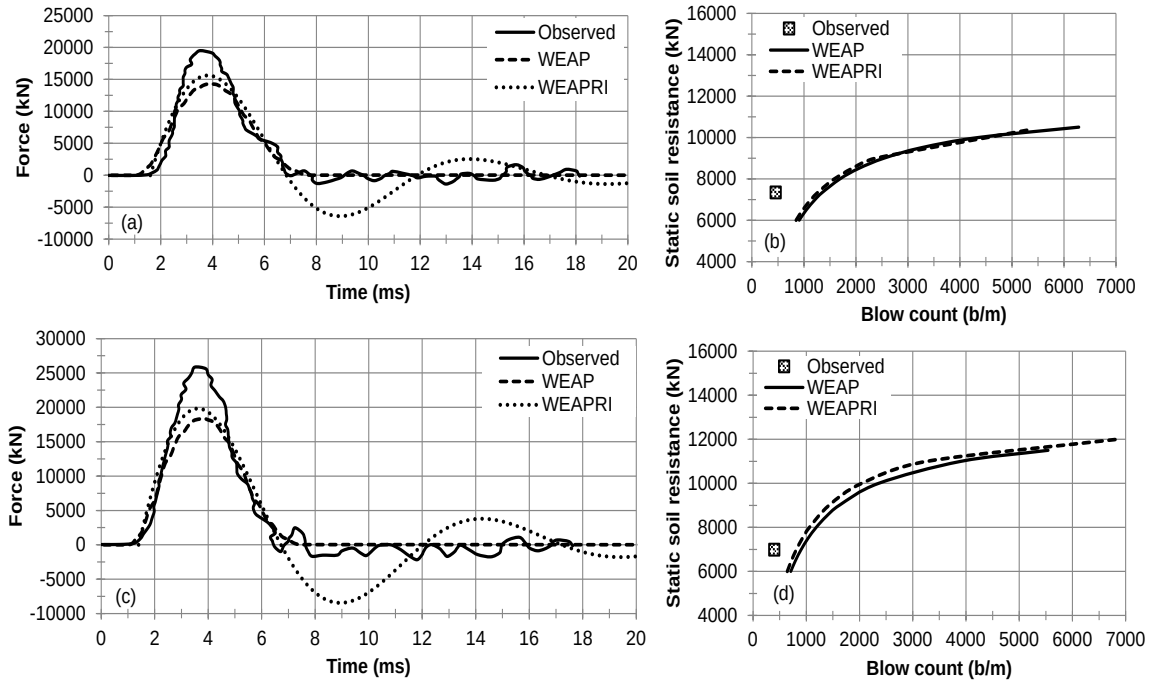

Figure 7.22: Observed and simulated force traces and drivability estimates: (a) force traces for blow #4, (b) drivability graph for blow #4, (c) force traces for blow #3676, and (d) drivability graph for blow #3676.

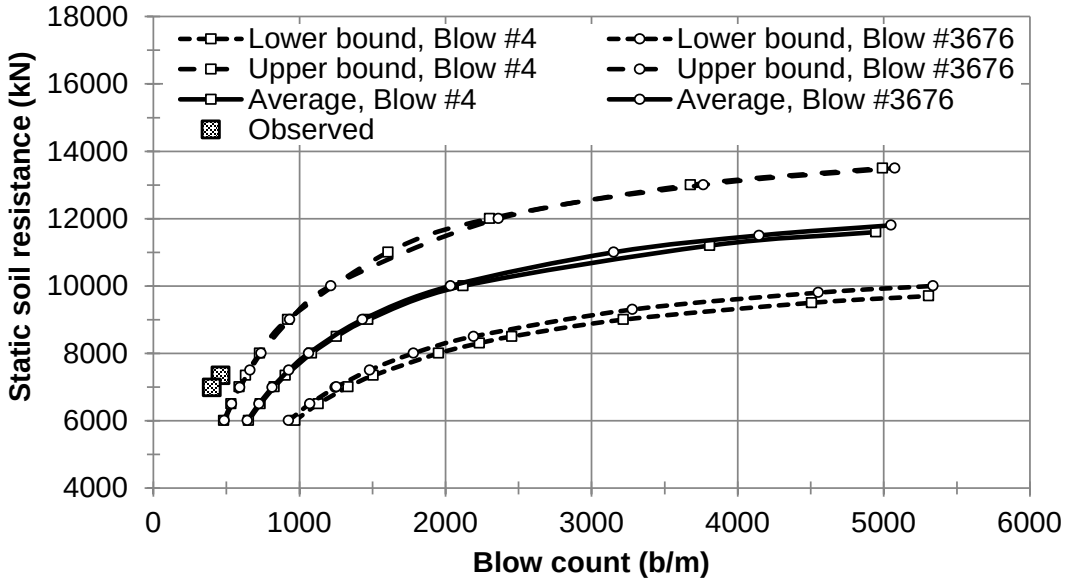

Figure 7.23: Comparison of observed penetration resistance to the average, lower- and upper-bound drivability curves simulated for blow #4 and #3676.

The observed compressive stresses were relatively constant, as described in Section 6.3.2, and equal to about 60 MPa over the observed penetration of 52 m to 61 m. The WEAP- and WEAPRI-computed compressive stresses were equal to 33 and 36 MPa for blow #4, and 42 and 46 MPa for blow #3676, respectively. Thus, both of the models under-estimated the observed stresses. The estimate of compressive stress based on Equation 6.29 provided a value of 85 MPa, about 42 percent larger than the observed stresses, though still reasonable in light of the

allowable stress. Similar to other cases histories, the actual and computed compressive stresses were substantially smaller than the allowable compressive stress in the pipe (i.e., 241 MPa).

7.6.4 Case 6: Full-scale Pipe Ramming Experiment at Emery & Sons, Inc., yard in Salem, Oregon

The evaluation of drivability for Case 6 was performed by selecting and analyzing two to three hammer strikes for each of the six pipe segments installed on the project (i.e., two hammer strikes each for pipe segments 1, 3, 5 and 6 and three hammer strikes each for pipe segments 2 and 4). The 14 hammer strikes, along with their penetration lengths, and corresponding CAPWAP-based soil parameters are provided in Table 7.1, and were utilized to simulate the dynamic response of the pipe. The CAPWAP and Case Method energy efficiencies are presented in Table 7.5, below, along with energy transfer efficiencies employed in the drivability analysis for the hammer blows considered. The Case Method energy was obtained by taking the local average of 50 blows before and after the selected impact blow. For blow #200 of the third pipe segment, both the CAPWAP and Case Method transferred energies were found to be insufficient to drive the pipe, and thus an overall average of the Case Method energy was adopted in the analysis. Similarly, both the CAPWAP and Case Method energies were insufficient to drive the pipe for the fifth pipe segment, and locally observed maximum efficiencies were adopted for the analysis.

The drivability analysis outcomes of each of the hammer blows for pipe segments 1, 2, 4 and 5 are reported in Appendix M while the analyses of pipe segment 3 and 6 are selected for discussion here. Figure 7.24 and Figure 7.25 presents the observed and computed force time histories for pipe segment 3 (i.e., blows #200 and #1991 with the 400 mm HammerHead hammer), and pipe segment 6 (i.e., blows #40 and #2404 with the 610 mm Grundoram Taurus hammer) respectively. For blow #200 and pipe segment 3, the actual hammer energy was insufficient to simulate the force trace corresponding to the CAPWAP static soil resistance of 224 kN when using both the WEAP and the WEAPRI code, and indicated pipe refusal. However, the pipe was actually driven successfully, and therefore the wave equation codes include occasional inherent limitations. To simulate the actual field behavior, the mean hammer energy and corresponding hammer-pipe efficiency was used in place of the instantaneous hammer energy, which allowed the drivability and force traces to be constructed as shown in Figure 7.24 for WEAP-based simulations, whereas WEAPRI-based simulations persisted in the result of pipe refusal with mean hammer energy.

Table 7.5: CAPWAP and Case Method energy transfer efficiencies (note, the rated hammer energy was 6.4 kN-m for segments 1 through 5 and 18.6 kN-m for segment 6).

Pipe segment	Blow number	Penetration length (m)	Static soil resistance (kN)	CAPWAP energy efficiency	Case Method energy efficiency	Energy efficiency used in analysis
1	406	2.2	113	0.08	0.14	0.08
	1154	4.6	201	0.11	0.15	0.11
2	512	6.7	202	0.21	0.23	0.21
	607	7.0	224	0.21	0.24	0.21
	2387	10.8	201	0.13	0.15	0.13
3	200	12.3	225	0.17	0.18	0.23*
	1991	17.3	247	0.30	0.26	0.30
4	8	18.3	266	0.19	0.25	0.25
	63	18.7	268	0.25	0.25	0.25
	1282	21.6	269	0.25	0.29	0.29
5	3067	26.1	516	0.23	0.26	0.30*
	4815	27.7	515	0.23	0.25	0.30*
6	40	29.3	669	0.22	0.22	0.22
	2404	33.5	735	0.28	0.29	0.28

* Instantaneous efficiency modified to equal mean observed efficiency due to simulated refusal of pipe.

The drivability graphs show the variation of penetration resistances with WEAP-based curves normally providing lower blow counts compared to WEAPRI. These models appeared to provide a very close estimate of the blow counts in the lower part of the penetration curves, however the differences between the models increased with increasing static soil resistance. For pipe segment 3, the observed penetration resistances were 2300 b/m for blow #200 and corresponding to an observed static soil resistance of 225 kN, and 1140 b/m for blow #1991 corresponding to an observed static soil resistance of 247 kN. The corresponding WEAP and WEAPRI penetration resistance were 2,610 b/m and infinity (i.e., the pipe exhibited refusal due to insufficient energy) for blow #200, and 1,260 and 5,840 b/m for blow #1991. Thus, the comparison of the penetration resistances generally shows a good estimate of the penetration resistances by WEAP and a general over-estimation by WEAPRI.

Similarly for pipe segment 6, the observed penetration resistances were 1,355 b/m for blow #40 corresponding to an observed static soil resistance of 669 kN, and 1,089 b/m for blow #2404 corresponding to an observed static soil resistance of 735 kN. The corresponding WEAP and WEAPRI penetration resistance were 1,032 and 1,659 b/m for blow #40, and 881 and 1,243 b/m for blow #2404. WEAP slightly underestimated the observed penetration resistance. WEAPRI slightly overestimated the penetration resistance. The duration of driving was estimated for each blow based on the blow rate of 231 bpm for pipe segment 3 where 400 mm HammerHead was used, and 180 bpm for pipe segment 6 where the 610 mm Grundoram Taurus was used. Table 7.6 provides the computed driving times for the blows observed in Case 6, and indicates that the penetration durations were reasonably estimated.

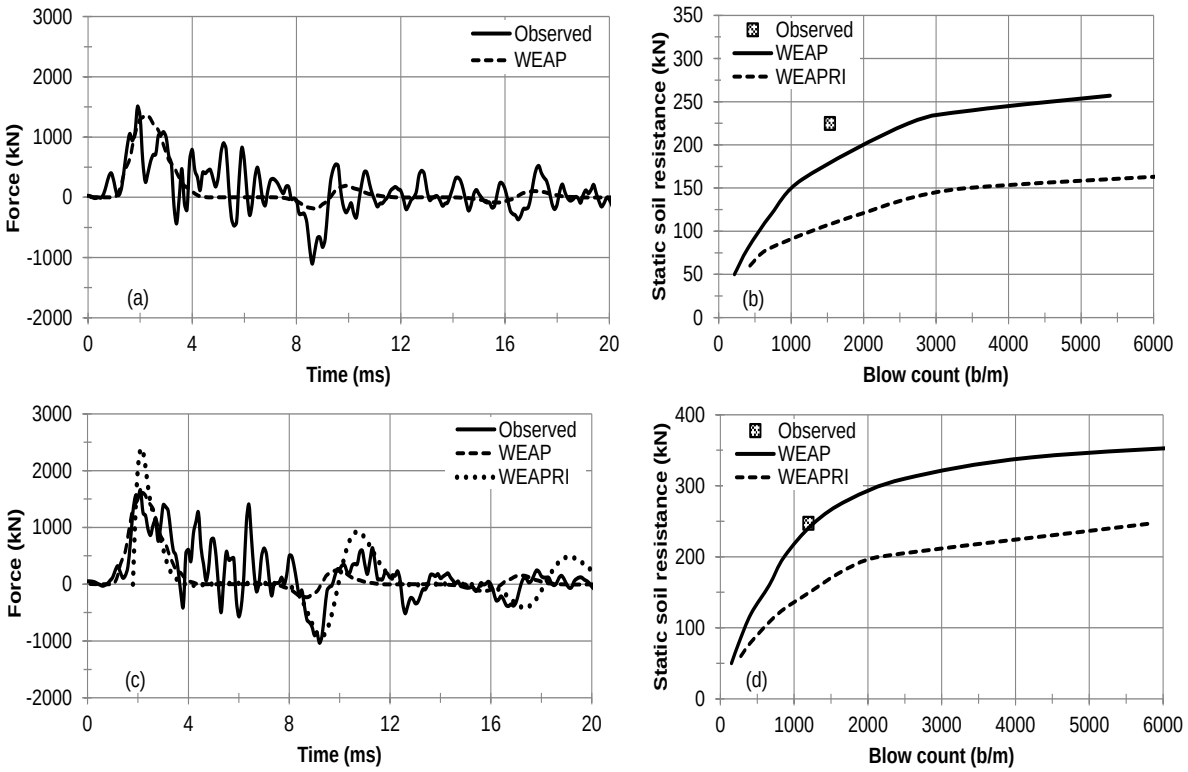

Figure 7.24: Observed and simulated force traces and drivability estimates of pipe segment 3 (a) force traces for blow #200 (b) drivability graph for blow #200 (c) force traces for blow #1991 (d) drivability graph for blow #1991.

Figure 7.26 and Figure 7.27 present an average and potential upper- and lower-bound penetration curves for pipe segment 3 (i.e., blows #200 and #1991) and pipe segment 6 (i.e., blows #40 and #2404) based on WEAP. The drivability graph apparently shows that for a given static soil resistance, the upper- and lower-bound curves widely bracketed the observed penetration resistance, and do not provide a confident range for estimating the likely penetration resistance. However, when using the average observed dynamic soil parameters, a reasonable and accurate estimate of penetration resistance can be obtained.

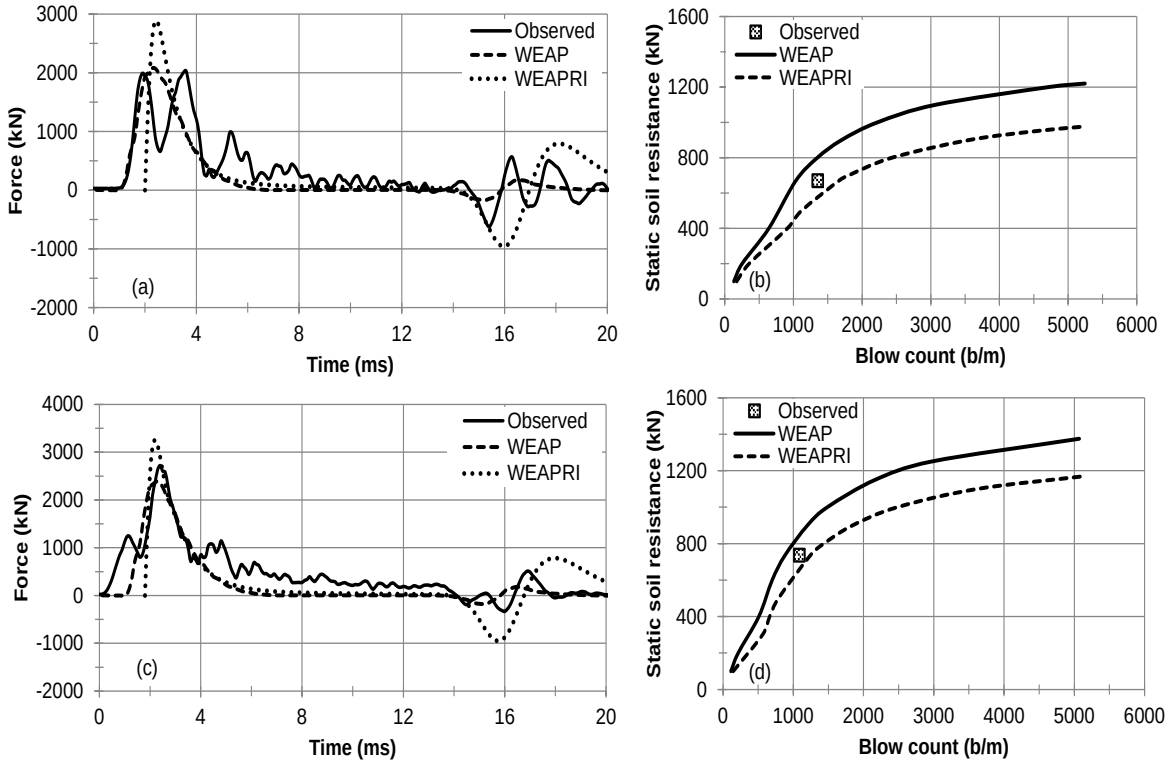

Figure 7.25: Observed and simulated force traces and drivability estimates of pipe segment 6: (a) force traces for blow #40, (b) drivability graph for blow #40, (c) force traces for blow #2404, and (d) drivability graph for blow #2404.

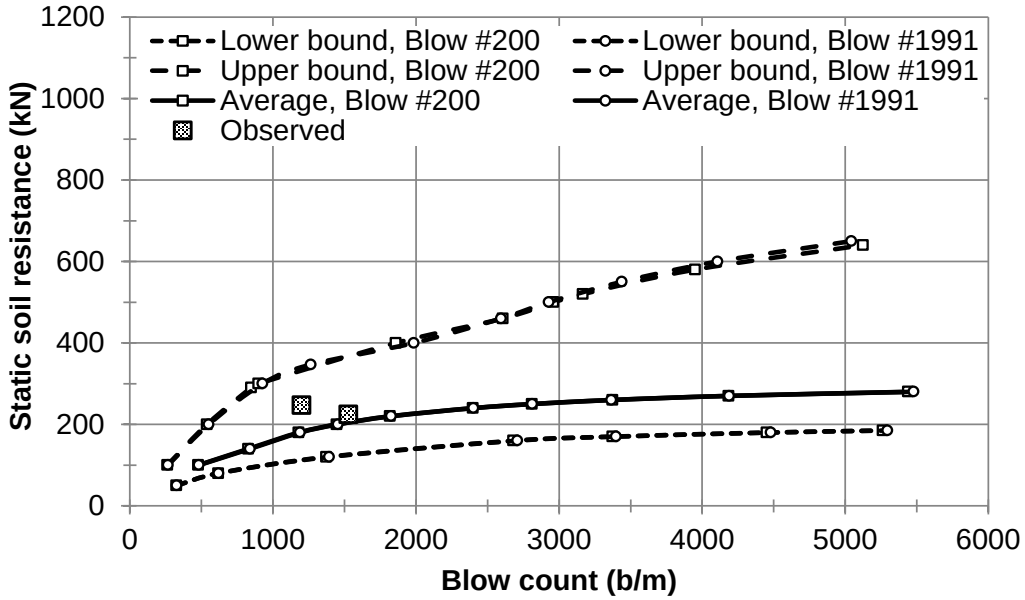

Figure 7.26: Comparison of observed penetration resistance to the average, lower- and upper-bound drivability curves simulated for blow #200 and #1991 of pipe segment 3.

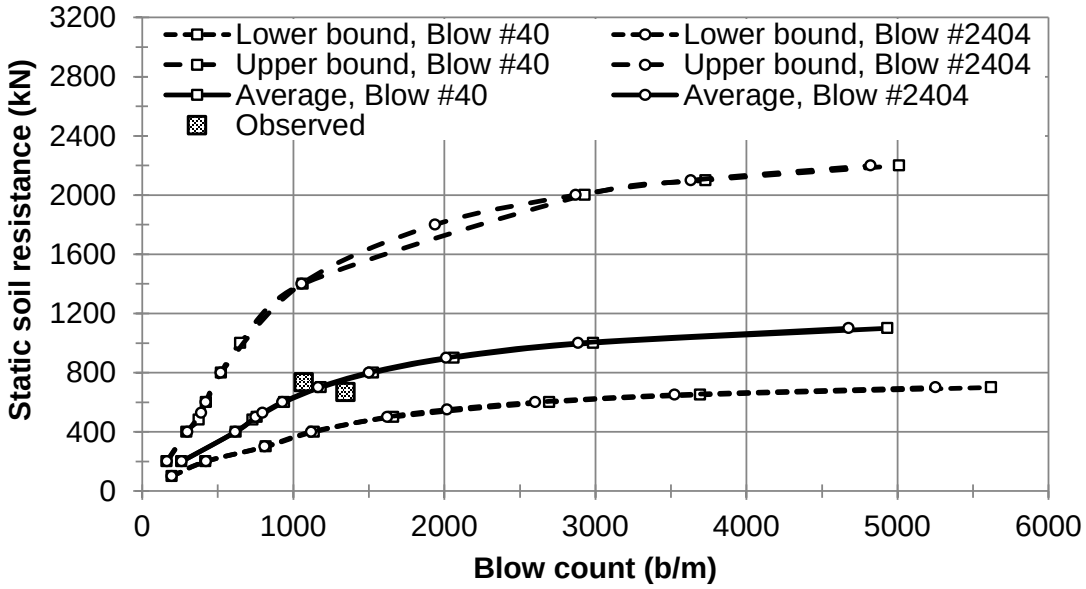

Figure 7.27: Comparison of observed penetration resistance to the average, lower- and upper-bound drivability curves simulated for blow #40 and #2404 of pipe segment 6.

Table 7.6: Computed driving times for blows of Case 6.

Pipe Segments	Blow number	Driving time (min/m)		
		Observed	WEAP	WEAPRI
1	406	5.8	3.0	6.6
	1154	6.4	16.0	–
2	512	7.5	6.3	43.3
	607	5.7	7.9	–
	2387	11.4	10.4	43.3
3	200	10.0	11.3	–
	1991	4.9	5.5	25.3
4	8	4.5	32.4	–
	63	7.4	21.8	–
	1282	7.0	19.2	–
5	3067	18.8	24.4	–
	4815	16.7	31.4	–
6	40	7.1	5.7	9.2
	2404	6.1	4.9	6.9

– Pipe refusal

Figure 7.28 presents the observed penetration resistances in blows per meter as a function of the length of penetration. The penetration resistance roughly followed a similar trend to that of the total soil resistance along the length of penetration (Figure 6.7c). The observed penetration resistances were compared to the WEAP and WEAPRI penetration resistances estimates for the hammer blows considered. Although WEAP overestimated the observed penetration resistance in some instances, good estimates of the observed penetration resistance were obtained for the majority of the cases. On the other hand, WEAPRI produced very high penetration resistances, predicting that the energy transferred was not sufficient to drive the pipe for most of the hammer blows, except for blow #406 of pipe segment 1, blow #1991 of pipe segment 3, and two of the blows for pipe segment 6. Although WEAP also uses the Smith model, the proprietary software

appears to include other elements that appear to generally capture drivability behavior better. WEAP's us of the predictor-corrector solution algorithm, as compared to the explicit solution of difference equations used by WEAPRI is an example of the differences.

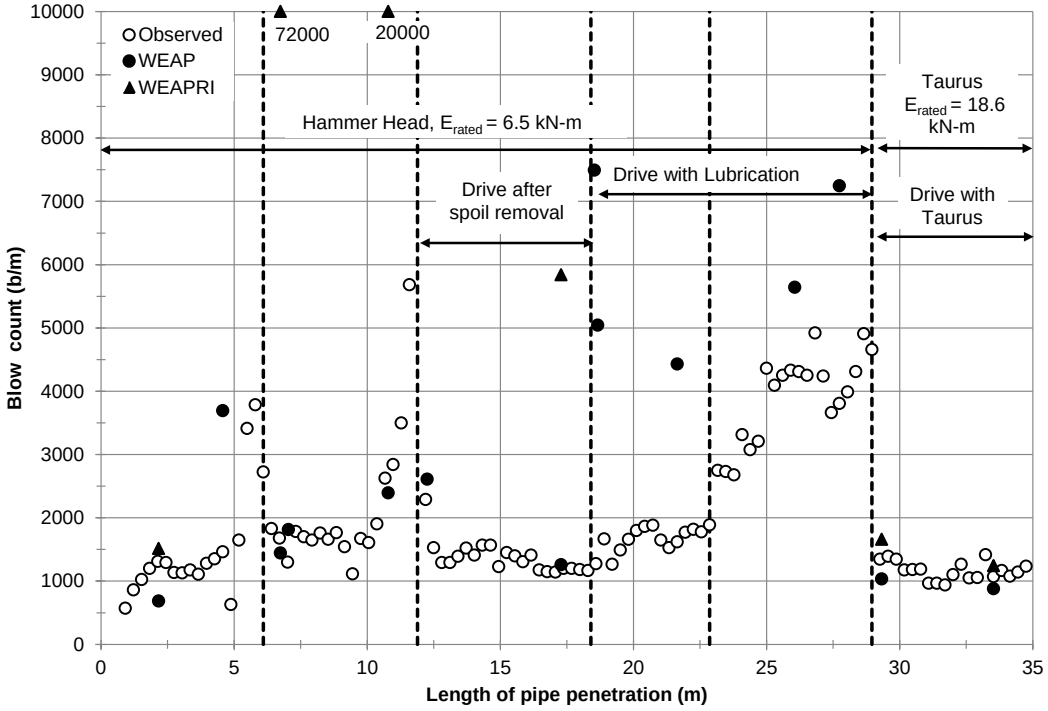

Figure 7.28: Pipe ramming log showing observed and simulated blow counts per meter.

The compressive stresses observed and estimated by the wave equation models are presented in Figure 7.29. The WEAP estimates of compressive driving stresses slightly under-estimated observed stresses for pipe segments 1 and 2. The observed stresses match the WEAP estimates fairly well for the remainder of the pipe segments. On the other hand, the WEAPRI calculations slightly over-estimated the observed stresses in most cases, although the computed stresses agreed with those observed during installation of pipe segment 1 and 2. The compressive stress was also computed using Equation 6.29, and resulted in 55 MPa and 80 MPa for pipe segments 1 through 5 and 6, respectively, indicating relatively good prediction of driving stress. However, as described above, the use of Equation 6.29 requires a good estimate of velocity of the hammer and the pipe, and impedance of the hammer and the pipe, as well as the actual hammer-pipe energy transfer. Generally, the compressive stresses were considerably smaller than the allowable compressive stress, which was 560 MPa, similar to the findings obtained in other cases.

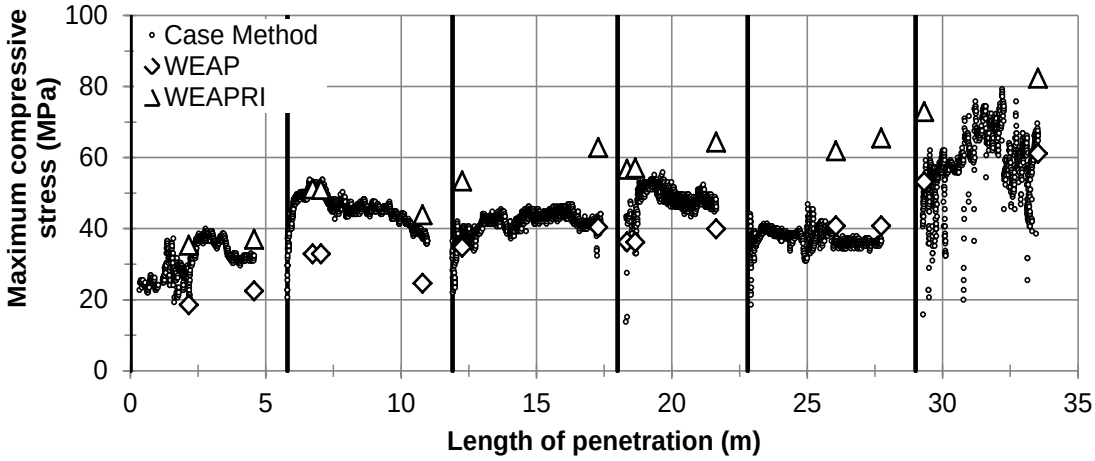

Figure 7.29: Maximum compressive stresses obtained from the Case Method solution to the PDA observations and those estimated using the drivability analyses.

7.7 RECOMMENDATIONS FOR CONDUCTING DRIVABILITY ANALYSES

Although this study evaluated the drivability of each of the instrumented pipes following installation, the intent of drivability analyses is to determine the appropriate level of energy required to drive the desired length of pipe in a safe and efficient way *prior to* the pipe installation in the planning phase of a project. The preceding sections described the static and dynamic soil properties and common energy transfer efficiencies associated with pipe ramming as observed in full scale projects. These data, and the models evaluated, should be used as the basis of regular drivability analyses. The following steps outline the proposed framework for the evaluation of the drivability of pipe ramming installations:

1. Gather information regarding the pipe planned to be driven. The information must include the pipe diameter, thickness, and length of the pipe, the desired length of drive, Young's modulus, specific weight, and yield strength of the pipe. Assumptions regarding the cutting shoe must be made in the event that the actual cutting shoe geometry is not known at this stage. Based on the case histories reported herein, a thickness of 10 to 12.5 mm (in addition to the pipe wall thickness) appears to provide a good initial estimate of shoe area for the purposes of face resistance estimation.
2. Gather information regarding the proposed subsurface alignment of the pipe. Perform soil borings with split-spoon sampling and appropriate laboratory tests to obtain soil index and design strength parameters. Document the static depth of the groundwater table at the time of drilling, and install monitoring wells to observe the seasonal fluctuation of the groundwater table.
3. Calculate the static soil resistance to driving as a function of penetration length, including the proportion of casing resistance. For granular soils, use Equation 7.1 and 7.4; these models estimate the face and casing resistance to ramming. Traditional pipe jacking equations may be used for installation in cohesive soils, albeit with unknown accuracy, until further information is obtained.
4. Based on known or estimated contractor equipment, determine the design value or bracket of values of the hammer-pipe energy transfer efficiency. The estimated energy efficiency can

be based on the type of connection between the hammer and the pipe, and usage of support cradle or excavator boom to lift the hammer during driving, and the degree of tension provided to restrain the hammer. Table 7.4 provides the statistical summary of the energy transfer efficiency for the four commonly used hammer-pipe connections based on case histories observed in this study. The mean energy transfer efficiency can be used for similar hammer-pipe connection conditions. The sensitivity of the drivability of the pipe can be readily investigated by varying the assumed energy transfer efficiency; the mean energy plus and minus the standard deviation in observed energy is recommended for bracketing the possible energy transfer efficiency. Alternatively, the project specifications can dictate the minimum required energy, independent of the hammer type or size, connection, or connection efficiency.

5. The dynamic face and casing soil parameters, including the quake and damping coefficients, should be selected based on the statistical summary of the case histories provided in Table 7.2. The average values of soil quake and damping coefficients are recommend for installation in medium dense to dense granular soils.
6. Using WEAP or WEAPRI, simulate the pipe drivability. Perform the drivability analysis over a range of static soil resistances to determine the drivability curve for various penetration lengths., For this step, select the proportion of casing resistance based on the computation of the proportion of resistance in Step 3 at a given penetration length. Compare the estimated static soil resistance to driving computed in Step 3 to the drivability curve to assess the feasibility of driving. The optimal hammer energy will produce reasonable penetration rates (penetration lengths per unit time) and resistances (blows per unit penetration length) without overstressing the pipe. Figure 7.30 indicates the approximate range in target penetration resistances, corresponding to the point of maximum curvature, that will produce the most efficient pipe ramming installations (provided the computed driving stresses are below allowable stresses, as described in Step 7). In cases where equipment availability is limited, or generally where hammer energy is insufficient to drive the required length of pipe, a static thrust force supplied by hydraulic actuators can supplement the dynamic driving force. In these cases, the drivability curve is simply shifted or offset by the magnitude of the thrust force at a given penetration resistance.

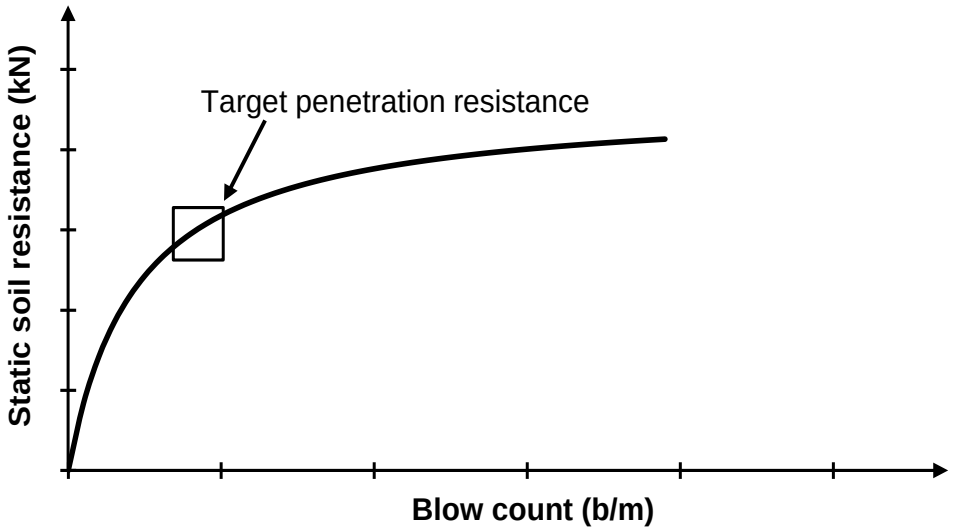

Figure 7.30: Conceptual sketch indicating target range of efficient penetration for pipe ramming.

7. Finally, compare the computed compressive driving stresses corresponding to the anticipated range of static soil resistance to the allowable stress of the pipe. The calculated driving stresses should not to exceed 90 percent of the design yield strength of the pipe to prevent any potential damage to the pipe.

Drivability analyses should be performed both during the planning stage of the project, and after the awarding of the contract. Analyses should be performed to evaluate the feasibility of the pipe ramming method during project planning. Once the contract for the project has been awarded, the selected contractor or sub-contractor should submit their proposed equipment, pipe geometry, and driving plan to the owner or owner's representative for review and acceptance. The owner or owner's representative should re-run the drivability analyses using the proposed equipment (e.g., the hammer) and pipe geometry (e.g., the proposed cutting shoe) to assess the acceptability of the equipment and pipe geometry. Details, such as the hammer-pipe connection, as well as the expected hammer-pipe energy transfer efficiency, should be provided in the contractor submittal for review.

7.8 SUMMARY

This chapter presents the drivability analysis of pipe ramming installations with the aim of assessing the constructability of a desired length of pipe with a given hammer in a safe and efficient manner. The analysis of drivability of a pipe is generally performed based on wave propagation models to develop a drivability curve that relates the penetration resistance to the range of static soil resistances for a specific hammer-pi1e-soil system. In addition to the penetration resistance, the drivability analysis produces driving stresses and stress wave traces that represent the dynamic response of the pipe. During pipe driving, the soil naturally offers dynamic and static resistances against the penetration due to forced impact driving. In Chapter 6, the static soil resistance to ramming was evaluated using the traditional quasi-static pipe jacking models. Generally, the models were observed to over-estimate the face resistance, and produce highly variable and biased estimates of the casing resistance. Hence, pipe ramming-specific static soil resistance models were developed in this chapter for both the face (Equation 7.1) and casing resistance (Equation 7.4).

Modeling the drivability of pipes requires specification of the dynamic soil parameters such as the soil quake and damping coefficients. The soil parameters were obtained from the back-analysis of the pipe driving records using CAPWAP signal matching. The soil parameters obtained from the case histories indicate that the soil face and casing quakes range from 1.8 to 2.8 mm while the Smith face and casing damping coefficients vary between 0.7 and 3 sec/m for granular soils. The hammer-pipe energy transfer efficiency is another critical parameter in pipe drivability investigations. Prior to this work, actual hammer-pipe energy transfer efficiencies have not been reported, hindering the analysis of pipe drivability. The energy transfer to the pipe generally depends on the magnitude of tension in the chains or winch, vertical support provided for the pipe and the hammer, and the hammer-pipe connection. The statistical summary of energy transfer efficiencies have been reported for four commonly used hammer and hammer connection types. The effect of varying the wave equation model parameters on the drivability analysis was examined by performing a sensitivity analysis. The analysis showed that the drivability curves were somewhat sensitive to the quake and damping values investigated.

However, in practice there is very little dispersion in the observed quake and damping. The drivability graphs were observed to have very little sensitivity to the assumed line force, whereas the energy transfer efficiency was found to have a significant effect on the drivability of a pipe.

Drivability analyses were performed for the case histories (i.e., Case 1, Case 2, Case 3, and Case 6) using WEAP and WEAPRI by simulating the force traces and drivability graphs. The WEAP model simulation generally provided a good match of the force traces in most cases although infrequent overestimation of the peak forces were observed in some instances. On the other hand, WEAPRI could not simulate the force traces for most of the blows due to insufficient energy transfer to drive the pipe. However in some cases, WEAPRI could also simulate force traces that provide a good match or overestimate the peak of the observed force traces. The drivability graphs show that WEAP-based penetration resistance curves mostly provide a lower blow count estimate compared to WEAPRI. Generally, the WEAP model was observed to produce more reasonable and accurate penetration resistances. In regard to the induced compressive stresses in the pipe, WEAP, WEAPRI, and Equation 6.29 usually produced reasonable estimates of the actual driving stresses. Both the observed and model estimates were found to be significantly smaller than the allowable compressive stress in the pipe for all the case histories, and indicate that the thickness of the pipes was likely excessive and therefore uneconomical. However, it is noted that unanticipated obstructions within the subsurface could result in higher compressive stresses, and that the models investigated are not able to simulate these possibilities. Therefore, a certain amount of caution is advised when the site geology is not known.

Finally, a framework for the assessment of pipe drivability was recommended. The use of the seven step framework and recommended soil and hammer properties should lead to the more economical and technically sound selection of the optimal pipe ramming hammer.

8 SUMMARY AND CONCLUSIONS

8.1 SUMMARY

Pipe ramming is an emerging trenchless technology for installation of new, and replacement of existing, buried pipes and culverts. Public agencies are increasingly embracing pipe ramming for culvert installation under roadways or other infrastructure due to its cost effectiveness and ability to mitigate problems associated with open-cut trenching. However, there has been little or no detailed technical guidance available for engineers to specify aspects of a pipeline or culvert installation, including the planning of feasible layouts, rates of penetration, pipe diameters, and hammers. This research was conducted to provide a reliable and comprehensive engineering framework to evaluate culvert installations at the planning phase. The engineering framework provides a means to assess the constructability of the required length and diameter of pipe with a given hammer, and evaluate the potential effect of pipe ramming-induced settlements and vibrations on existing adjacent infrastructures including roadways, railways, buildings, and buried utilities.

The development of engineering guidance requires the assessment of appropriate engineering calculations and validation against full-scale performance data. This study developed a pipe performance installation database based on the observation of five production installations and a full-scale experiment. Existing soil resistance, settlement, and vibration prediction models were adapted from pipe jacking, microtunneling, and pile driving models and examined for their applicability in pipe ramming installations. The principles of stress wave theory and stress wave measurements, routinely used in drivability analyses for pile foundations, were adopted for the evaluation of the dynamic response of pipes during pipe ramming installations. The development of these models should help owners, consultants, and contractors to appropriately plan pipe ramming installations.

8.2 CONCLUSIONS

The findings of this research on pipe ramming, including vertical ground settlements, ground vibrations, dynamic behavior of rammed pipes, static soil resistance to ramming, and drivability analyses, are summarized in the following sections.

8.2.1 Vertical Ground Movements

Vertical ground deformations observed during pipe ramming installations indicated that settlements and heave were relatively small, generally less than 15 mm and 10 mm, respectively. Approximately 97 percent of all settlements evaluated in the case histories were smaller than 10 mm; this indicates that the total magnitude of settlement resulting from pipe ramming was generally small, and sometimes negligible. The estimation of settlements was evaluated using the inverted normal probability distribution approach for tunneling and pipe jacking. Generally, these methods seemed to over-estimate the observed settlements close to the center of the pipes and under-estimate at radial distances away from center of the pipes. Therefore, a pipe-ramming-specific hyperbolic model was developed for better prediction of the vertical settlement

induced by pipe ramming in granular soils. The hyperbolic model was found to render a slightly conservative estimate of the settlement, with about 60 percent of the settlement estimates slightly higher than the measured settlements. Generally, the hyperbolic model provided a better estimate of the observed settlements both at the center and at radial distances away from the center of the pipe than the inverted normal probability distribution-based models.

8.2.2 Ground Vibration

Measurements of pipe ramming induced ground vibrations indicated that significant magnitudes of peak particle velocity, up to 100 mm/sec, are possible indicating that vibration can pose a potential hazard to adjacent structures; however, the vibration generally attenuated rapidly with radial distance away from the pipe. The vibration data was categorized into forward and lateral vibration propagation and their magnitude and frequency content were evaluated against USBM and OSM "safe" vibration threshold levels. Forward propagating vibrations were observed to be greater than laterally propagating vibrations, and may pose a hazard to existing structures or buried utilities when a pipe passes extremely close to these elements. Lateral vibrations were smaller, but attenuated more slowly with radial distance. The attenuation of ground vibration was modeled using the simple empirical approach proposed by Wiss (*1981*), which requires an estimate of energy of the hammer and the distance between the pipe and the point of interest. The model showed a reasonable estimate of the vibration after being calibrated based on the vibration data obtained from the full-scale field experiment, and can be used to predict vibrations for granular soils.

8.2.3 Dynamics of Pipe Ramming

The dynamic behavior of rammed pipes was investigated to form the basis of pipe drivability studies. Impact-induced stress waves were measured using specialty equipment to infer the total and static soil resistance to ramming, the energy transferred from the hammer to the pipe, and the driving stresses. The maximum compressive stresses for all the case histories were found to be considerably smaller than the allowable compressive stress of the pipe, indicating that present practice for the selection of pipe wall thickness is likely conservative. The maximum energy transfer was found to depend on the hammer alignment, the hammer-pipe connection, and the degree of tension in the restraining chains or cables. Accurate estimates of the soil resistance and dynamic soil parameters, such as the face and casing quake and damping, were obtained through rigorous CAPWAP signal matching analyses.

8.2.4 Static Soil Resistance to Ramming

The magnitude of static soil resistance to ramming must be estimated to perform drivability analyses of rammed pipes. The accuracy of existing static soil resistance models, developed for pipe jacking and microtunneling, was evaluated using the CAPWAP-based soil resistances. The quasi-static pipe jacking models over-estimated the face resistance, and produced highly variable and biased estimates of casing resistance, and indicated the need for pipe-ramming specific soil resistance models. Therefore, the pipe-ramming-specific static resistance models were developed in this study to adequately capture the observed face and casing soil resistances. The casing resistance model was calibrated separately for datasets with and without lubrication, to reflect the observed beneficial effect of lubrication to reduce casing resistance.

8.2.5 Drivability Analysis

The feasibility of a proposed pipe ramming installation can be effectively evaluated using drivability analyses that are based on stress wave propagation models. The aim of the drivability analysis is to determine the magnitude of driving stresses and to develop a drivability curve that relates the penetration resistance of a given pipe to the range of static soil resistances that are possible throughout the drive. Drivability analyses require the selection of dynamic soil parameters (i.e., soil quake and damping coefficients) and the hammer-pipe energy transfer efficiency. Representative dynamic soil parameters were developed from the back-analysis of stress wave measurements (i.e., CAPWAP signal matching), and statistically characterized to aid the selection of their value in practice. The effect of various hammer pipe connections and hammer supports on the energy transfer efficiency was evaluated and statistically characterized for direct use in drivability analyses. Based on the observed pipes, the average energy transfer efficiency ranged from approximately 25 to 50 percent of the rated energy, indicating the need for best practices for achieving and maintaining efficient hammer-pipe connections.

Drivability analyses were performed using a MATLAB® code (termed WEAPRI, found in Appendix D) and proprietary software (*GRLWEAP 2010*) for each of the case histories where dynamic measurements were available. This produced simulated force time histories for selected hammer blows and drivability curves. The WEAP model simulations generally agreed with the observed penetration resistances for most of the hammer blows analyzed, however the peak forces were under-estimated in some instances, resulting in under-prediction of compressive driving stresses. On the other hand, the open source WEAPRI code developed for this study often over-predicted driving resistance, but provided appropriately conservative estimates of driving stresses. Based on accepted practice for drivability of pile foundations, and the research conducted on rammed pipes herein, a seven step framework for performing the drivability of rammed pipes was recommended.

8.2.6 Recommendations for Future Study

The research performed herein provides a first step towards an improved understanding of the mechanics of pipe ramming installations. As such, there are a number of areas in which further study could increase the understanding of pipe ramming mechanics. Areas for further study include, but are not limited to:

1. Additional, carefully documented case histories to improve and extend the results of this research. Data of interest include the static soil resistance to ramming and dynamic soil parameters.
2. The development of an extensive library of pipe ramming hammer data that includes the manufacturer rated energy, internal hammer efficiency, ram mass, operational velocities and their variation as a function of hydraulic or pneumatic pressure and fluid flow rate, etc.) and the effect of various hammer-pipe connections on the energy transfer efficiency.
3. A comprehensive study of the mechanics of pipe ramming in cohesive soils. This study did not include observations in plastic fine-grained soils. Information on ground deformation, vibration, and static and dynamic soil parameters for ramming in cohesive soils is required.
4. Evaluation of the effect of high-frequency low energy impact blows on the drivability of rammed pipes. The stress wave theory used in this study was adapted directly from that used

for pile driving, in which the impact of high-energy pile driving hammers typically range from 36 to 50 blows per minute, significantly lower than the typical 180 to 240 bpm used with lower energy pneumatic hammers. Therefore, the installation mechanism of rammed pipes should be investigated assuming a hysteretic load-unload model that does not immediately assume plastic failure at the soil quake.

5. The wave equation analysis is commonly performed using variations of the Smith soil model with dynamic soil parameters including the quake and damping coefficient. The quake and damping coefficients are empirical parameters that are not correlated with any conventional soil mechanics parameters. Additionally, the damping coefficient represents a universal viscous damping without distinguishing between possible hysteretic, radiation, or viscous damping components. Moreover, laboratory testing has shown that actual viscous damping in the plastic zone is a power function of the static soil resistance, and is not linearly proportional. Soil models could be developed to address these limitations and implemented in drivability analyses.
6. Ramming-induced local liquefaction of loose coarse-grained soils is possible when ramming below the ground water table. Local liquefaction could be beneficial to the production rate, given the sharply reduced shear strength of the soil. Ramming-induced liquefaction should be investigated, and both beneficial and potential adverse consequences (e.g., ground failure, displacements) studied.

9 REFERENCES

Akkerman, M. *Pipe Jacking Equipment and Methods.* North American Society for Trenchless Technology, 2006, pp.1-13.

Ariaratnam, S., W. Chan, and D. Choi. Utilization of Trenchless Construction Methods in Mainland China to Sustain Urban Infrastructure. *Practice Periodical on Structural Design and Construction*, ASCE, Reston, VA, Vol. 11, No. 3, 2006, pp. 134-141.

ASTM. *Standard Test Method for Marsh Funnel Viscosity of Clay Construction Slurries*. Standard D6910, American Society for Testing and Measurement, West Conshohocken, PA. 2004.

ASTM. *Standard Practice for Classification of Soils for Engineering Purposes (Unified Soil Classification System*. Standard D2487, Annual Book of ASTM Standards, Denver, CO, Vol. 4, 2007, pp. 248–259.

ASTM. *Standard Test Method for High-Strain Dynamic Testing of Deep Foundations*. Standard D4945, American Society for Testing and Measurement, West Conshohocken, PA. 2008.

Atalah, A. *The Effect of Pipe Bursting on Nearby Utilities, Pavement, and Structures*. Technical Report TTC-98-01, Trenchless Technology Center, Louisiana Tech University. 1998.

Attewell, P.B. *An Overview of Site Investigation and Long-Term Tunnelling Induced Settlement in Soil.* Engineering Geology of Underground Movements, Bell et al. (eds.), Geological Society Engineering Geology Special Publication No. 5, 1998, pp. 55-61.

ATV. *Standard ATV-A 161E, Structural Calculation of Driven Pipes*. GesellschaftzurFörderung der Abwassertechnik (German Association for the Water Environment), Bonn, DE, 1990, pp.90.

Auld, F.A. Determination of Pipe Jacking Loads. Proceedings of the Pipe Jacking Association, Pipe Jacking Association, Manchester, UK. 1982.

Balthaus, H. Numerical Modeling of Pile Driving Based on an Automatic CAPWAP Search Procedure. Proceedings of the Third International Conference on the Application of Stress-Wave Theory to Piles. Vancouver: Bi-Tech Publishers. 1988, pp. 219-230.

Bennett Trenchless. Daily Inspection Log. 2010a.

Bennett Trenchless. Daily Inspection Log. 2010b.

Bennett, D., and K. Wallin. *Aeroject Groundwater Extraction and Treatment System Area 3 Wells and GET 'H" Pipeline: Highway 50 Crossing Feasibility Study*. Technical Memorandum, Folsom, CA. 2010.

Bennett, R.D. *Jacking Forces and Ground Deformations Associated with Microtunneling.* PhD Thesis, University of Illinois at Urbana-Champaign, IL, 1998, p.487.

Berardi, R., M. Jamiolkowski, and R. Lancellotta. Settlement of Shallow Foundations in Sands Selection of Stiffness on the Basis of Penetration Resistance. Proceedings of the Congress sponsored by the Geotechnical Engineering Division of the ASCE, Geotechnical Special Publication 27, 1991, pp.185 – 200.

Bolton, M.D. The Strength and Dilatancy of Sands. *Geotechnique*, Vol. 36, No. 1, 1986, pp. 65-78.

Borghi, F.X. *Soil Conditioning for Pipe-Jacking and Tunneling*. PhD dissertation, University of Cambridge, 2006, pp. 1-384.

Boyce, G., M. Wolski, R. Zavitz, and C. Camp. Chemistry and Physics Behind Microtunnel Slurries. Proceedings, No-Dig 2011, North American Society for Trenchless Technology, Washington D.C., 2011.

Brennan, A.J., and S.P.G. Madabhushi. Amplification of Seismic Accelerations at Slope Crests. *Canadian Geotechnical Journal*, Vol. 46, 2009, pp. 585–594.

Bush, G., and J. Simonsen. Rehabilitation of Underground Water and Sewer Line: The Costs beyond the Bid. CIGMAT Conference and Exhibition Proceeding, University of Houston. 2001.

Celestino, T.B., R.A.M.P. Gomes, and A.A. Bortolucci. Errors in Ground Distortions due to Settlement Trough Adjustment. *Tunnelling and Underground Space Technology*, Vol. 15, No. 1, 2000, pp.97–100.

Chapman, D.N., P.C.R. Ng, and R. Karri. Research Needs for On-Line Pipeline Replacement Techniques. *Tunnelling and Underground Space Technology*., Vol. 22, 2007, pp. 503 – 514.

Chapman, D.N. and Y. Ichioka. Prediction of Jacking Forces for Microtunnelling Operations. *Tunnelling and Underground Space Technology*, Vol. 14, Supplement 1, 1999, pp. 31 - 41.

Choe, J., and H.C. Juvkam-Wold. Pile Driving Analysis for Top Hammering and Bottom Hammering. *Journal of Geotechnical and Geoenvironmental Engineering*, Vol. 128, No. 2, 2002, pp.174-182.

Clarke, I. Hitting Harder. *Tunneling & Trenchless Construction*, Vol. 28, 2007, pp. 38-42.
Cording, E.J., and W.H. Hansmire. Displacement around Soft Ground Tunnels. Proceedings of 5th Pan American Congress on Soil Mechanics and Foundation Engineering, Buenos Aires, AR, 1975.

Coyle, H.M., and G.C. Gibson. Empirical Damping Constants for Sands and Clays. *Journal of Soil Mechanics and Foundation Division,* ASCE, Vol. 96, SM3, 1970, pp. 949-965.

Craig, R.N. A State-of-the-Art Review. *CIRIA Technical Note 112*. 1983.

Currey, J., G. Woodbridge, and E. Nicholson. On Grade, Large Diameter Pipe Ramming Installations. International No-Dig Show 2009. The North American Society (NASTT) and the International Society for Trenchless Technology (ISTT), Toronto, Canada, Paper D-1-04, 2009, pp. 1-8.

Farrell, R. *Tunnelling in Sands and the Response of Buildings*. PhD Thesis, University of Cambridge. 2011.

Federal Highway Administration. (FHWA) National Bridge Inventory (NBI). 2011. http://www.fhwa.dot.gov/bridge/nbi/strtyp11.cfm. Accessed on November 14, 2012.

Fellenuis, B.H. Basics of Foundation Design. Electronic Edition. 2011. www.Fellenius.net.

Gangavarapu, B.S., M. Najafi, and O. Salem. Quantitative Analysis and Comparison of Traffic Disruption Using Open-Cut and Trenchless Methods of Pipe Installation, New Pipeline Technologies, Security, and Safety. Proceedings of the ASCE International Conference on Pipeline Engineering and Construction, 2003, pp.1714-1724.

Goble G.G., G. Likins, and F. Rausche. *Bearing Capacity of Piles from Dynamic Measurements.* Final Report, Department of Civil Engineering, Case Western Reserve University, Cleveland, OH. 1975.

Goble, G.G., and F. Rausche. *Wave Equation Analysis of Pile Driving – WEAP Program*. U.S. Department of Transportation, FHWA, Washington, D.C., Implementation Package IP-76-14.1 – IP-76-14.4. 1976.

Goble, G.G., and F. Rausche. *Wave Equation Analysis of Pile Driving – WEAP Program.* Vol. 1, U.S. Department of Transportation, FHWA, Washington, D.C., Implementation Package IP-76-14.1, Updated: March, 1981.

Goble, G.G., F. Rausche, and G.E. Likins. The Analysis of Pile Driving – A State of the Art. Proceedings of the 1st International Seminar on the Application of Stress-Wave Theory on Piles, Stockholm, SE, 1980, pp. 131-161.

Golder Associated Ltd. *Foundation Investigation Report: Culvert Site 6-Station 13+405, Township of Colborne*. London, Ontario, Canada, 2010.

Goodman, A., and A. Cluett. Pipe ramming and the oil pipeline industry. The North American Society and the International Society for Trenchless Technology International No-dig Show 2009, Paper D-1-03, 2009, pp. 1-3.

GRLWEAP. *Background Report*. Pile Dynamics, Inc., Cleveland, OH, 2010.

Hannigan, P.J. *Dynamic Monitoring and Analysis of Pile Foundation Installations*. DFI Short Course Text. 1990.

Hannigan, P.J., G.G. Goble, and G.E. Likins. *Design and Construction of Driven Pile Foundations*. Reference Manual Vol. II. Publication No. FHWA NHI-05-043, Federal Highway Administration. 2006.

Hannigan, P.J., G.G. Goble, G. Thendean, G.E. Likins, and F. Rausche. *Design and Construction of Driven Pile Foundations*. Publication No. FHWA-HI-97-014, Workshop Manual. 1997.

Hashash, Y., and J. Javier. *Evaluation of Horizonal Directional Drilling (HDD).* Technical Report, FHWA-ICT-11-095. 2011.

Haslem, R.F. Pipe Jacking Forces: from Theory to Practice. Proceedings of Infrastructure, Renovation and Waste Control Centenary Conference, N.W. Association, Institute of Civil Engineering, 1986, pp. 173-180.

Hirsh, T.J., L. Carr, and L.L. Lowery. *Pile Driving Analysis – Wave Equation User's Manual*. Vol. 1, Texas Transportation Institute, Texas A&M Univ., College Station, TX, 1976.

Holcomb, D. Failing 96-inch Diameter CMP Replaced Utilizing Pipe Ramming Technology. No-Dig Show 2012, North American Society for Trenchless Technology, Nashville, TN, 2012, p.7.

Holloway, D.M. *Wave Equation Analyses of Pile Driving.* Technical Report S-75-, U.S. Army Engineer Waterways Experiment Station. 1975.

Howitt, M. Trenchless Construction in Practice. *Journal of Concrete Engineering*, Vol.8, No.1, 2004, pp. 40-41.

International Society for Trenchless Technology (ISTT). *Microtunneling Jacking Force*. Report from the Working Group No.3, 1994.

Iscimen, M. *Shearing Behavior of Curved Interfaces*. MSc Thesis. Georgia Institute of Technology, Atlanta, GA, 2004.

Iseley, T., M. Najafi, and R. Tanwani. *Trenchless Construction Methods and Soil Compatibility Manual*. 3rd Edition. National Utility Construction Association (NUCA). 1999.

Iseley, T., and S. Gokhale. *Trenchless Installation of Conduits Beneath Roadways – a Synthesis of Highway Practice*. National Research Council of Transportation Research Board, National Cooperative Highway Research Program NCHRP Synthesis 242. 1997.

Jaky, J. The Coefficient of Earth Pressure at Rest. *Journal Society Hungarian Architect and Engineering*, Vol. 7, 1944, pp. 355–358.

Jensen, N.W., D.S. Roy, and T. Wanless. Observations of Ground Movement during Pipe Ramming Operations under a Railway Embankment. Proceedings of Seventh International Symposium on Field Measurements in Geomechanics, ASCE. 2007.

Kim, D., and J. Lee. Propagation and Attenuation Characteristics of Various Ground Vibrations. *Soil Dynamics and Earthquake Engineering*. Vol.19, 2000, pp. 115–126.

Kramer, S.L. *Geotechnical Earthquake Engineering*. Prentice Hall. 1996.

Kulhawy, F.H., and P.W. Mayne. *Manual on Estimating Soil Properties for Foundation Design.* Report EL-6800. Electric Power Research Institute, Palo Alto, CA, 1990.

Leca, E., and B. New. Settlements Induced by Tunnelling in Soft Ground. ITA/AITES Report. *Tunnelling and Underground Space Technology*, Vol. 22, No. 2, 2007, pp. 119–149.

Lee, S., Y. Chow, G. Karunaratne, and K. Wong. Rational Wave Equation Model for Pile-Driving Analysis. *Journal of Geotechnical Engineering*, Vol. 114, No. 3, 1988, pp. 306–325.

Lidén, M. *Ground Vibrations due to Vibratory Sheet Pile Driving.* MSc Thesis. Royal Institute of Technology, Stockholm, SE, 2012.

Loukidis, D., R. Salgado, and G. Abou-Jaoude. *Assessment of Axially-Loaded Pile Dynamic Design Methods and Review of INDOT Axially-Loaded Pile Design Procedure*. Publication FHWA/IN/ JTRP-2008/06, Purdue University, West Lafayette, IN, 2008.

Lowe, J. Shear Strength of Coarse Embankment Dam Materials. Proceedings of 8th Congress on Large Dams, Transactions, Vol. III, International Commission on Large Dams, Paris, FR, 1964, pp. 745–761.

Lowery, L.L., Jr., T.J. Hirsch, T.C. Edwards, H.M. Coyle, and C.H. Samson Jr. *Pile Driving Analysis—State of Art*. Research Report No. 33-13, Texas A&M University, College Station, TX. 1969.

Mair, R.J., and R.N. Taylor. Bored Tunneling in the Urban Environment. Proceedings of 14th International Conference on Soil Mechanics and Foundation Engineering. Hamburg, DE. 1997, pp. 2353-2385.

Marshall, A.M., A. Klar, and R.J. Mair. Tunneling beneath Buried Pipes: View of Soil Strain and Its Effect on Pipeline Behavior. *Journal of Geotechnical and Geoenvironmental Engineering*, Vol.136, No. 12, 2010, pp. 1664–1672.

Marshall, M. *Pipe-Jacked Tunneling: Jacking Loads and Ground Movements*. PhD Thesis, Magdalen College, University of Oxford Trinity, UK, 1998.

Marshall, M.A. The Field Performance of a Pipe Jack in Glacial Till. Proceedings of International Exhibition and Symposium on Underground Construction (IESUC), London, UK, 2001, pp. 773-785.

Massarch K.R., and B.H. Fellenius. Ground Vibrations by Impact Pile Driving. Case Histories in Geotechnical Engineering, 6th International Conference, Arlington, VA, 2008.

Massarsch, K.R. Static and Dynamic Soil Displacements caused by Pile Driving. Keynote Lecture, Fourth International Conference on the Application of Stress Wave Theory to Piles, The Hague, NL, 1992, pp. 15-24.

Mayne, P.W., B.R. Christopher, and J. DeJong. *Subsurface Investigations – Geotechnical Site Characterization.* Report No. FHWA-NHI-01-031, National Highway Institute, Federal Highway Administration, Washington, D.C., 2002.

Meskele, T., and A.W. Stuedlein. Performance of an Instrumented Pipe Ramming Installation. Proceedings No-Dig 2011, North American Society for Trenchless Technology, Washington D.C., 2011.

Meyerhof, G. Shallow Foundations. *Journal of Soil Mechanics and Foundations Division*, Vol.91, SM2, 1965, pp. 21–31.

Meyerhof, G. Penetration Test and Bearing Capacity of Cohesionless Soils. *Journal of Soil Mechanics and Foundations Division*, Vol.82, SM1, 1956, pp. 1–19.

Milligan, G.W.E., and P. Norris. Pipe Jacking: Research Results and Recommendations. *Pipe Jacking Association*, London, UK, 1994, p.18.

Milligan, G.W.E., and P. Norris. Pipe-soil Interaction during Pipe Jacking. Proceedings of the Institution of Civil Engineers: Geotechnical Engineering, 1999, pp. 27-44.

Miner, R. *Dynamic Testing and Analysis of Perham Creek Culvert Project Report*. Robert Miner Dynamic Testing Inc., (RMDT). 2003.

Najafi M., B. Gunnink, G. Davis, and R. Humphreys. Field Testing of Major Trenchless Technology Methods for Road Crossings. Construction Research Congress - Wind of Change: Integration and Innovation, ASCE, Honolulu, HI, 2004, pp.1-8.

Najafi, M. *Pipe Ramming Projects*. ASCE Manuals and Reports on Engineering Practice, American Society of Civil Engineers, Reston, VA, No. 115, 2008, pp.1-71.

National Research Council. *Toward a Sustainable Future: Addressing the Long Term Effects of Motor Vehicle Transportation on Climate and Ecology*. National Academy Press, Washington, D.C., 1997.

NAVFAC. *Foundations and Earth Structures*. Design Manual DM 7-02, Naval Facilities Engineering Command, Alexandria, VA, 1986.

Norris, P. *The Behavior of Jacked Concrete Pipes during Site Installation.* PhD Thesis, Pembrook College, University of Oxford, Trinity, UK, 1992.

O'Connor, J.E., A. Sarna-wojcicki, K.C. Wozniak, D.J. Polette, and R.J. Fleck. *Origin, Extent, and Thickness of Quaternary Geologic Units in the Willamette Valley*. Oregon, U.S. Geological Survey Professional Paper 1620, Oregon Water Resources Department. 2001.

O'Reilly, M.P., and B.M. New. Settlements above tunnels in the United Kingdom-their magnitude and prediction. Proceedings of Tunneling, London, UK, IMM 173-181, 1982.

Oregon Department of Transportation (ODOT) *Perham Creek Culvert replacement Project. L*eaflet. 2010.

Orton, C. Pneumatic Pipe Ramming Solves Emergency Situation for Rail Corridor. Pipelines 2007: Advances and Experiences with Trenchless Pipeline Projects, ASCE. 2007a.

Orton, C. Lessons Learned From Large Diameter Sanitary Sewer Pipe Bursting Project: Conversion of Abandoned Gravity Sewer Main into Upsized Sanitary Force Main South San Fransisco, CA. Pipelines 2007: Advances and Experiences with Trenchless Pipeline Projects, ASCE. 2007b

Peck, R.B. Deep Excavations and Tunnelling in Soft Ground. Proceedings of 7th International Conference on Soil Mechanics and Foundation Engineering, Mexico City, MX, 1969, pp. 225–290.

Pellet-Beaucour, A.L., and R. Kastner. Experimental and Analytical Study of Friction Forces during Microtunneling Operations. *Tunneling and Underground Space Technology*, Elsevier Ltd, Oxford , UK, Vol.17, 2002, pp. 83-97.

Piehl, R. *Summary of Trenchless Technology for use with USDA Forest Service Culverts*. USDA Forest Service, San Dimas Technology and Development Center, San Dimas, CA, 2005, pp.1-15.
Potyondy, J.G. Skin Friction between Various Soils and Construction Materials. *Geotechnique*, Vol. 11, 1961, pp. 339-355.

Randolph, M.F., and H.A. Simons. An Improved Soil Model for One Dimensional Pile Driving Analysis. Proceedings of Third International Conference on Numerical Methods in Offshore Piling, Nantes, FR, 1986, pp. 3-17.

Rankine, W.J.M. On the Stability of Loose Earth. *Philosophical Transactions of the Royal Society of London*, Vol. 147, 1857, pp. 9–27.

Rausche, F., G. Goble, and G. Likins. Dynamic Determination of Pile Capacity. *Journal of Geotechnical Engineering*, Vol. 111, No. 3, 1985, pp. 367–383.

Rausche, F., G.E. Likins, L. Liang, and M.H. Hussein. Static and Dynamic Models for CAPWAP Signal Matching. *The Art of Foundation Engineering Practice*, Geotechnical Special Publication (GSP) No. 198, 2010, pp. 534-553.

Rausche, F., F. Moses, and G. Goble. Soil Resistance Predictions from Pile Dynamics. *Journal of the Soil Mechanics and Foundation Division*, ASCE, 1972, pp. 917-937.

Ripley, K.J. The Performance of Jacked Pipes. PhD Thesis, University of Oxford. 1989.

Roark, R.J., and W.C. Young. *Formulas for Stress and Strain.* McGraw-Hill, New York, NY, 1976.

Rogers, C., and D. Chapman. (1995) "Ground movements caused by trenchless pipe installation techniques," Transportation Research Record No. 1514, 1995, pp. 37-48.

Samson, C.H., T.L. Hirsch, and L.L. Lowery. Computer Study of Dynamic Behavior of Piling. *Journal of the Structural Division*, ASCE, Vol. 89, No.ST4, 1963, pp.413-449.

Schill, J. Contractor utilizes Trenchless Pipe Ramming, Slick Boring in Illinois. *Pipeline and Gas Journal*, 2003, pp.54-56.

Schmertmann, J.H. Measurement of In-situ Shear Strength. Proceedings of ASCE Geotechnical Division, Specialty Conference on In-Situ Measurement of Soil Properties, June 1 - 4, 1974, Raleigh, NC, Vol. 2,1975, pp. 57 - 138.

Schmertmann, J.H. Static Cone to Compute Settlement over Sand. *ASCE Journal Soil Mechanics and Foundation Engineering*, Vol.96, SM3, 1970, pp.1011-1043.

Schmidt, B. Settlements and Ground Movements Associated with Tunnelling in Soil. PhD Thesis, University of Illinois. 1969.

Schrank, J.S., M.D. Havekost, and S.M. Njoloma. Pipe Ramming under Three Active Railroad Lines in Difficult Soil Conditions. International No-Dig Show 2009. The North American Society (NASTT) and the International Society for Trenchless Technology (ISTT), Toronto, Canada, Paper F-2-05, 2009, pp. 1-10.

Simicevic, J., and R. Sterling. *Guidelines for Pipe Ramming*. Technical Report, Trenchless Technology Center of Louisiana Technological University, Ruston, LA, Vol. 4, 2001a, pp.1-21.

Simicevic, J., and R. Sterling. *Guidelines for Pipe Bursting*. Technical Report, Trenchless Technology Center of Louisiana Technological University, Vol. 2, 2001b, pp. 1- 55.

Smith, E.A.L. Pile Driving Analysis by the Wave Equation. *Journal of the Soil Mechanics and Foundation Engineering Division*, ASCE, Vol. 86, No. 4, 1960, pp. 35–61.

Staheli, K. *Jacking Force Prediction: An Interface Friction Approach Based On Pipe Surface Roughness*. Ph.D. Dissertation, Georgia Institute of Technology, Atlanta, GA, 2006.

Stantec . Freeway Monitoring Exhibit. 2010.

Stein, D. *Trenchless Technology for Installation of Cables and Pipelines*. Stein and Partner. Arnsberg, DE, 2005.

Stokoe, K.H., II, M.B. Darendeli, R.D. Andrus, and L.T. Brown. Dynamic Soil Properties: Laboratory, Field and Correlation Studies. Proceedings of 2nd International Conference on Earthquake Geotechnical Engineering, Lisbon, PT, Vol. 3, 1999, pp. 811–845.

Stuedlein, A.W., and T. Meskele. Preliminary Design and Engineering of Pipe Ramming Installations. *Journal of Pipeline Systems Engineering and Practice*, ASCE, Reston, VA, Vol. 3, No. 4, 2012, pp. 125-134.

Terzaghi, K. *Theoretical Soil Mechanics*. Wiley and Sons New York, NewYork, NY, 1943.

Tolouli, S., G. Boyce, and K. Barteaux. Pipe Ramming a 60-in. Casing under BART. International No-Dig show 2009, The North American Society and the International Society for Trenchless Technology, 2009, pp. 1-11.

Vorster, T.E.B., A. Klar, K. Soga, and R.J. Mair. Estimating the Effects of Tunneling on Existing Pipelines. *Journal of Geotechnical and Geoenvironmental Engineering*, Vol.131, No. 11, 2005, pp. 1399–1410.

Weber, W., and G. Hurtz. Ermittlung der Rohrreibung und Entwicklung eines Bohrgerätes. *Tiefbau, Ingenieurbau, Straßenbau*, Vol. 23, No. 8, 1981, pp. 550-555.

Wetter, L., K. Staheli, and P. Cohen. Trenchless Success saves a Trenchless Failure. International No-Dig Show 2009. The North American Society (NASTT) and the International Society for Trenchless Technology (ISTT), Toronto, Canada, Paper D-1-01, 2009, pp. 1-10.

Wiss, J.F. Construction Vibrations: State of the Art. *Journal of the Geotechnical Division*, ASCE, Vol. 107, 1981, pp. 167-181.

Wolff, T.F. Pile Capacity Prediction using Parameter Functions. *ASCE Geotechnical Special Publication*, No. 23, 1989, pp. 96–107.

Woods, R.S., and L.P. Jedele. *Energy-Attenuation Relationships from Construction Vibrations.* Vibration Problems in Geotechnical Engineering, Special Technical Publication, ASCE, New York, NY, 1985, pp. 187-202.

Woods, R.D. *Dynamic Effects of Pile Installation on Adjacent Structures.* Synthesis of Highway Practice 253, National Academy Press, Washington, D.C., 1997.

Yin, K., J. Peng, Q. Wang, R. Wang. Research on a Hydraulic Impact Hammer System for Pipe-Ramming. New Pipeline Technologies, Security and Safety*:* Proceedings of the ASCE International Conference on Pipeline Engineering and Construction, July 13-16, 2003, ASCE, Reston, VA, 2003, pp. 1194-1200.

Zhou, J.Q. *Numerical Analysis and Laboratory Test of Concrete Jacking Pipes*. PhD Thesis, Linacre College. University of Oxford, Trinity, UK, 1998.

Zubko, N. Pipe Ramming to the Next Level. *Trenchless Technology Magazine,* Benjamin Media, Peninsula, OH, 2003a.

Zubko, N. Tunneling Without a Trace: Emerging Technology Handles Environmental Issues with Ease. *Tunnel Business Magazine*, 2003b, pp.28-29.

9.1.1.1.1.1.1.1.1 APPENDIX A
BORING LOGS FOR CASE 2

9.1.1.1.1.1.1.1.2 APPENDIX B
BORING LOGS AND SONIC CORE PHOTOGRAPHS FOR CASE 5

9.1.1.1.1.1.1.1.3 APPENDIX C
BORING LOGS FOR CASE 6

9.1.1.1.1.1.1.1.4 APPENDIX D
WAVE EQUATION ANALYSIS PROGRAM FOR PIPE RAMMING INSTALLATIONS (WEAPRI)

9.1.1.1.1.1.1.1.5 APPENDIX E
CASE METHOD ANALYSIS FOR CASE 1

9.1.1.1.1.1.1.1.6 APPENDIX F
CASE METHOD ANALYSIS FOR CASE 2

9.1.1.1.1.1.1.1.7 APPENDIX G
CASE METHOD ANALYSIS FOR CASE 6

9.1.1.1.1.1.1.1.8 APPENDIX H
CAPWAP ANALYSIS FOR CASE 1

9.1.1.1.1.1.1.1.9 APPENDIX I
CAPWAP ANALYSIS FOR CASE 2

9.1.1.1.1.1.1.1.10 APPENDIX J
CAPWAP ANALYSIS FOR CASE 6

9.1.1.1.1.1.1.1.11 APPENDIX K
GRLWEAP NEW HAMMER INPUT

9.1.1.1.1.1.1.1.12 APPENDIX L
GRLWEAP HORIZONTAL PIPE DRIVING

9.1.1.1.1.1.1.1.13 APPENDIX M
DRIVABILITY ANALYSES OF CASE 6